

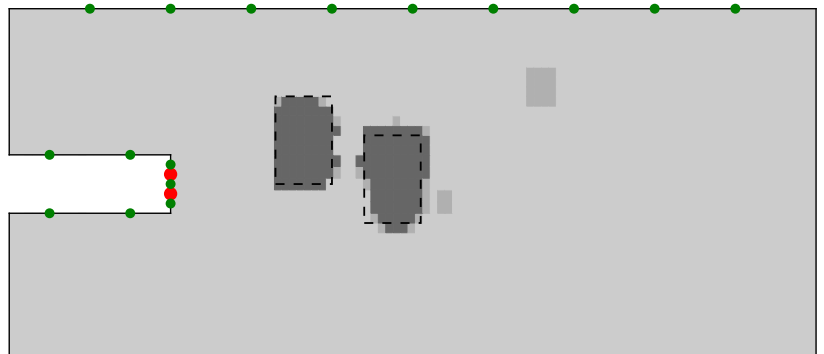
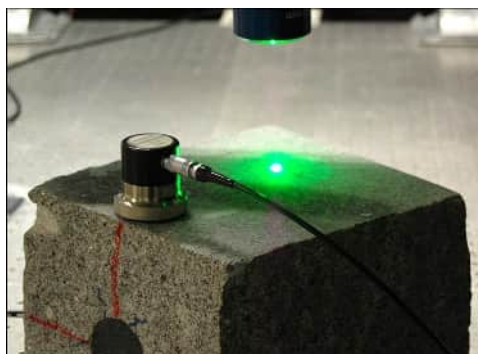
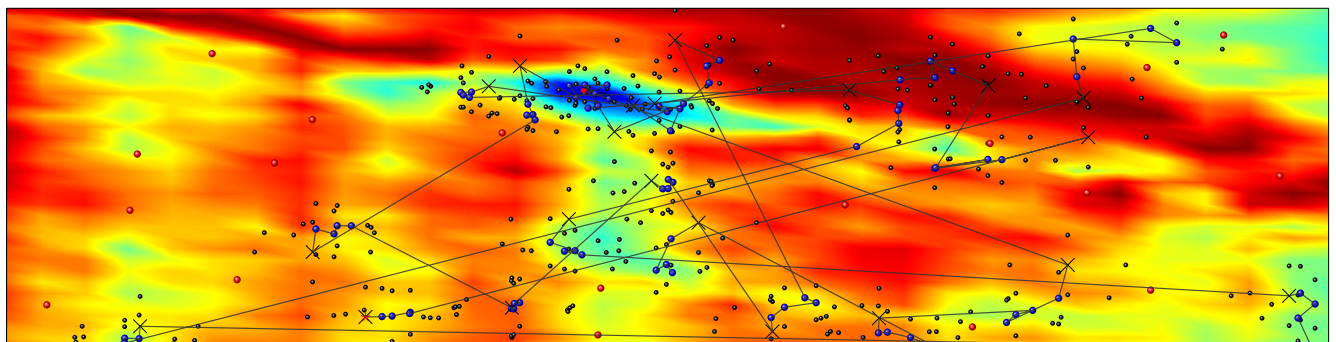


SFB 837
Interaction Modeling in
Mechanized Tunneling

Bayesian Full Waveform Inversion for Exploration During Mechanized Tunneling

A Numerical and Experimental Study

Maximilian Trapp



Dissertation

**Bayesian Full Waveform Inversion for Exploration During
Mechanized Tunneling**

A Numerical and Experimental Study

in Candidacy for the Degree of
Doctor of Engineering (Dr.-Ing.)
at the Faculty of
Civil and Environmental Engineering
Ruhr University Bochum

submitted by

Maximilian Trapp

Herausgeber (Publisher):

Institut für Mechanik

— Schriftenreihe —

Ruhr-Universität Bochum

D-44780 Bochum

ISBN 978-3-935892-67-4

This material is presented to ensure timely dissemination of scholarly and technical work. Copyright and all rights therein are retained by the copyright holders. All persons copying this information are expected to adhere to the terms and constraints invoked by the author's copyright. These works or parts of it may not be used to repost reprint/republish or for creating new collective works for resale or redistribution to servers or lists without the explicit permission of the copyright holder.

Dieses Werk ist urheberrechtlich geschützt. Die dadurch begründeten Rechte, insbesondere die der Übersetzung, des Nachdrucks, des Vortrags, der Entnahme von Abbildungen und Tabellen, der Funksendung, der Mikroverfilmung oder der Vervielfältigung auf anderen Wegen und der Speicherung in Datenverarbeitungsanlagen, bleiben, auch bei nur auszugsweiser Verwertung, vorbehalten. Eine Vervielfältigung dieses Werkes oder von Teilen dieses Werkes ist zulässig. Sie ist grundsätzlich vergütungspflichtig. Zuwiderhandlungen unterliegen den Strafbestimmungen des Urheberrechtsgesetzes.

©2022 Maximilian Trapp, Institut für Mechanik, Ruhr-Universität Bochum

Printed in Germany

Einreichung der Dissertation (thesis submission): 09. März 2022

Tag der mündlichen Prüfung (thesis defense): 02. Mai 2022

Erste Referentin (first referee):

Prof. Dr.-Ing. Tamara Nestorović

Zweiter Referent (second referee):

Prof. Dr. Wolfgang Friederich

Vorsitzende (committee chair):

Prof. Dr.-Ing. Annette Hafner

Acknowledgements

This thesis was developed during my work in the research group *Mechanics of Adaptive Systems* at the Ruhr University Bochum. First of all, I want to thank my supervisor Prof. Dr.-Ing. Tamara Nestorović for all her support, trust, advices, and for giving me the opportunity to work within her research team. I enjoyed these five years in your group. Secondly, I want to thank Prof. Dr. Wolfgang Friederich for reviewing this thesis as second supervisor and for sharing his valuable expertise with me over the years. Thirdly, I want to thank Prof. Dr.-Ing. Annette Hafner for her spontaneous agreement to become the chair of the doctoral committee.

Furthermore, I want to acknowledge the German Research Foundation (DFG) for funding my work within the framework of the collaborative research center SFB 837, subproject A2: *Interaction modeling in mechanized tunneling: Development of effective concepts for tunnel reconnaissance using acoustic methods*.

I want to thank all colleagues within my research group, especially Umaaran Gogilan for all the nice years of studying and working together, and Silvia Altevogt for her thorough organization and for spreading good mood. Additional thanks go out to our technician Daniel Lehmann for constructing the small-scale laser experiment, and to the members of SFB837, where I especially want to thank Christopher Riedel and Dr. Andre Lamert for the close, pleasant and successful teamwork.

Thanks go out to my beloved family for always being there, where I want to mention Mom, Norbert, Katha, Fabian and little Lotta. Furthermore, I want to greet my one and only Kronprinzen and further friends – can't imagine my life without you. Special thanks go out to Caro and Mike for support and encouragement in my final phase of writing and for having such great times together. Last but not least, I want to dedicate this work to the memories of my Dad and my friend Leopold, who I will always remember.

Abstract

The lack of effective exploration methods during mechanized tunneling can lead to a damage of the tunnel boring machine and to a delay in the excavation process. A promising instrument for the reconnaissance of soil properties is provided by exploration seismics, in which propagating waves deliver a detailed fingerprint that is to be decrypted. State-of-the-art exploration systems omit parts of the arriving information for the benefit of shorter computation times and therefore show deficiencies concerning precision and resolution. With exponentially increasing computational capacities, a methodology called *full waveform inversion* becomes attainable, in which the full recorded waveform is exploited. In the most common full waveform inversion methods, so-called adjoint methods, the inversion is performed with respect to a high number of unknowns (where the number of unknowns is also referred to as dimensionality of the inverse problem) since the material properties are variable all over the model domain – for instance at the nodes or elements. The inverse problem is then solved with gradient-based optimization. Due to the high dimensionality, these methods can provide a detailed image; however, a drawback is that they may easily tend to one of the local minima of the objective function. Possible consequences are inaccurate results, especially if measurement and modeling errors are included. An alternative is to reduce the dimensionality of the inverse problem. This can be achieved by implementing either a generally suitable but simplified parametrization of the subsoil model or a parametrization grounded on prior knowledge. On the reduced set of parameters, statistical inverse theory can be applied to find the optimal parameter set. This approach considers the non-uniqueness of inverse problems by assigning probability distributions to the model parameters revealing which parameter configurations are certainly or uncertainly describing a representation close to the true model. Based on all available prior information, the model is multiply updated with Bayesian inference. The final output is a complete statistical description of the model parameters, also enabling uncertainty quantification. This thesis starts here and further develops and applies two methods grounded on the principles of *dimensionality reduction of the inverse problem* and *statistical inverse theory based on Bayesian inference*. The investigations are to reveal if and how the methods can be considered for exploration during mechanized tunneling. Besides the validation of the methods with synthetic data, a meaningful part of this work is the validation with experimental data, where ultrasonic data is acquired in a *small-scale laser experiment*. This type of validation brings a significant gain compared to the validation with synthetic data since real data is processed. This data naturally induces noise, measurement errors and later modeling errors that also occur during field scenarios. Therefore, strategies are developed to maximize the quality of measurement and to achieve an adequate forward model. After developing the two Bayesian full waveform inversion approaches *unscented hybrid simulated annealing* and the *unscented Kalman filter-controlled parametric level-set method*, they are successfully applied to various synthetic and experimental examples in two and in three dimensions. It is shown that the methods can provide precise results with a certain robustness against noise, measurement errors, and modeling errors. The strategies and findings from the small-scale experiments are related to potential large-scale scenarios and on this basis, suggestions and challenges related to mechanized tunneling are outlined.

Contents

1. Introduction	1
1.1. Motivation	1
1.2. Non-seismic vs. seismic exploration	1
1.3. Full waveform inversion	3
1.4. Dimensionality reduction and statistical full waveform inversion	5
1.5. Goals and structure of the thesis	7
2. Fundamentals of seismic wave propagation	9
2.1. Elastic wave equations	9
2.2. Boundaries	10
2.3. Types of seismic waves	11
2.3.1. Body waves	11
2.3.2. Surface waves	12
2.4. Phase velocity, group velocity and dispersion	12
2.5. Numerical solution	13
2.5.1. The spectral element method	14
2.6. Attenuation	15
3. Methodologies – Full waveform inversion with Bayesian methods	17
3.1. The statistical inverse problem	18
3.2. The unscented Kalman filter (UKF)	19
3.3. Method 1: Unscented hybrid simulated annealing (UHSA)	22
3.4. Method 2: UKF-controlled parametric level-set method (UKF-PaLS)	25
3.5. The multi-scale approach	28
3.6. Parameter tuning	29
4. Small-scale laser experiment	31
4.1. Setup	31
4.2. Ultrasonic transducers	33
4.3. Laser signal response	34
4.3.1. Validation of reflectors	36
4.3.2. Repeatability and signal-to-noise ratio	38
4.3.3. Noise	40
5. Synthetic inversion scenarios in 2D and 3D	43
5.1. UKF-PaLS in 2D	43
5.1.1. Generation of seismic measurements	43
5.1.2. Full waveform inversion	45
5.2. UKF-PaLS in 3D	50
5.2.1. Generation of synthetic measurements	50
5.2.2. Full waveform inversion	51
5.3. Short summary and discussion	54

6. Imaging of a hole in an aluminum block	55
6.1. The experiment	55
6.2. The forward model	57
6.3. Full waveform inversion	60
6.3.1. UHSA	60
6.3.2. UKF-PaLS	64
6.4. Comparison to results of adjoint full waveform inversion	69
6.5. Short summary and discussion	71
7. Imaging of anomalies in concrete plates	73
7.1. The experiment	73
7.2. The forward model	75
7.3. Full waveform inversion - UHSA	76
7.3.1. Hole localization	79
7.3.2. Detection of a linear material change	81
7.3.3. Detection of a rectangular disturbance	84
7.4. Short summary and discussion	86
8. Imaging of a layer change in a concrete block	87
8.1. The experiment	87
8.2. The forward model	91
8.3. Full waveform inversion	92
8.3.1. Source-receiver configurations and source functions	93
8.3.2. UHSA	95
8.3.3. UKF-PaLS	98
8.4. Comparability to large-scale models	101
8.5. Short summary and discussion	103
9. A three-stage concept	105
9.1. Reconstruction of a boulder	105
9.1.1. Supervised machine learning	106
9.1.2. Acquisition of seismic data	106
9.1.3. UHSA FWI	107
9.1.4. Adjoint FWI	109
9.2. Short summary and discussion	110
10. Discussion	111
10.1. Comparability of the experiments to large-scale scenarios and their additional value	111
10.2. Challenges in mechanized tunneling	111
10.3. Sources and receivers	112
10.4. Gains and restrictions of the applied FWI methods	113
10.5. Computation time	115
10.6. Supervised machine learning for the creation of metamodels	116
11. Summary and conclusion	117
A. Appendix A	119
B. Appendix B	125

1. Introduction

1.1. Motivation

Underground tunnels are a key to the creation of an effective infrastructure. In densely populated cities with lack of space, they may be the only possibility to extend the road system and to provide fast and effective journey times. Both in and apart from cities, tunnels allow overcoming obstacles like water or mountains. Over time, different strategies for the excavation of tunnels have evolved. Conventional tunneling is a category of methods in which the rock is loosened in a non-automated way with explosives and tools like hammers and diggers. Although this methodology is still widely used, it suffers from several disadvantages like a comparatively low construction velocity and a restriction to hard rock due to the lack of active support of the tunnel face (Jetschny, 2010). Unlike in conventional techniques, the field of mechanized tunneling provides a more automated way of tunneling by making use of tunnel boring machines (TBMs). TBMs include a big cutting wheel at the front, enabling to excavate the whole diameter of the tunnel at once. Different working steps are automated, for instance the removal of the soil and – dependent on the architecture of the TBM – the stabilization of the tunnel face or the attachment of the tunnel lining. TBMs can drill through almost all kinds of rocks with velocities higher than the velocities reached with conventional tunneling techniques. Due to the shield excavation and the immediate stabilization, the impact on surrounding buildings by induced settlements is minimized. Furthermore, TBMs are comparatively environment-friendly and safe for the workers (Maidl *et al.*, 2011). Although the dangers concerning settlements and humans are rather low, a detailed knowledge of the subsoil properties prior to drilling is beneficial for several reasons: firstly, if the TBM drills into voids or water-filled fractures, a pressure imbalance may be released (Kneib *et al.*, 2000). Secondly, drilling into abrupt soil changes can lead to high wear or a blocking of the cutting wheel, where all of the described cases can lead to expensive damages or delays in the construction process. With detailed prior knowledge, the cutting tools can be changed, or the excavation velocity can be adapted accordingly. Induced settlements can be further minimized by adapting the excavation velocity of the TBM. The following section gives an overview of current methods in the context of seismic and non-seismic exploration and identifies their deficiencies.

1.2. Non-seismic vs. seismic exploration

A coarse estimation of the subsoil properties is performed prior to construction when the tunnel trajectory is planned. Thereby, also techniques are utilized which are not related to wave propagation, referred to as non-seismic exploration techniques. An extrapolation of the geological situation from the Earth's surface to its interior is usually used in order to predict the soil properties along the planned tunnel track. The obtained image can be enhanced by additional geophysical measurements (Jetschny, 2010). However, the estimation is not

necessarily correct. For instance, boulders may easily be missed by this procedure and the course of a layer change may be misinterpreted. Exploratory drillings provide a reliable method in order to obtain a locally precise image but are, however, time-consuming and costly – especially for larger overburdens – and can therefore only sparsely be used. One possibility for exploration during construction is to conduct exploratory drillings through the tunnel face, but this procedure, too, is time-consuming and costly. Furthermore, it requires direct access to the tunnel face, which needs to be considered when building the TBM. Another possibility for exploration is constructing an exploratory tunnel parallel to the main tunnel trajectory, which has been performed during the construction of the Brenner Base tunnel (Bergmeister & Reinhold, 2017). The advantage in the case of the Brenner Base is that it has been planned to be utilized as a drainage tunnel when the construction period is finished. However, the costs for the exploratory tunnel of the Brenner Base add up to about 1.5 billion euro, which is about 15 % of the project volume, showing that the method is highly expensive and cannot always be applied.

An effective instrument for exploration is the field of exploration seismics, where knowledge about the subsoil is gained on the basis of wave propagation. Seismic surveys can be conducted from the Earth’s surface even before the excavation of the tunnel starts; however, difficulties may arise, especially in urban areas (due to buildings and infrastructure) or in the case of large overburdens (due to large distances to the tunnel trajectory). Surveys from the tunnel site bring a different exploration angle and varying distances to anomalies, which may be advantageous for the imaging. During a seismic survey, seismic sources trigger elastic waves which propagate through the soil and eventually provide information about the soil properties. The sources can for instance be explosives (Sattel *et al.*, 1992), pneumatic impulse hammers, or sweep vibrators (Borm *et al.*, 2003). These kinds of sources can be placed anywhere inside the tunnel, in boreholes, or, in the case of shallow tunnels, even at the Earth’s surface. Alternatively, the vibrations induced by the cutting head of the TBM may be utilized as a passive seismic source (Petronio *et al.*, 2007). If the traveling waves encounter material property changes, they are e.g. reflected, refracted, scattered, or converted. A part of the energy is arriving back at seismic receivers, which can be placed, same as the seismic sources, inside the tunnel, in boreholes, or at the Earth’s surface. The waveforms may be analyzed with seismic techniques in order to estimate the subsoil properties. The working principle of seismic exploration during mechanized tunneling described above is visualized in Figure 1.1.

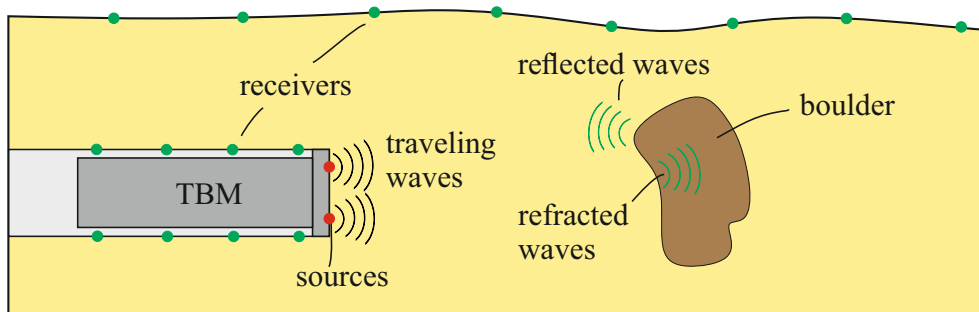


Figure 1.1.: Working principle of seismic exploration during mechanized tunneling. Sources (red) and receivers (green) can potentially be placed anywhere; however, in state-of-the-art methods they are usually placed inside the tunnel only.

The state-of-the-art of seismic methods for mechanized tunneling is based on seismic tomography methods. These methods commonly evaluate just parts of the seismic wave-

forms, extracting and processing reflected waves or applying migration techniques. Sources and receivers are usually placed inside the tunnel only. Some of the typically used systems are Sonic Softground Probing (SSP) (Kneib *et al.*, 2000), Integrated Seismic Imaging System (ISIS) (Borm *et al.*, 2003), Tunnel Seismic Prediction (TSP) (Sattel *et al.*, 1992), and True Reflection Tomography (TRT) (Otto *et al.*, 2002). SSP is used for exploration in soft rock. In this method, sources and receivers are located at the cutting wheel of the TBM. Reflected compressional waves are extracted from the recorded seismic data and the subsoil properties are estimated with a technique based on 3D migration. In contrast to SSP, ISIS is used in hard rock. Pneumatic hammers are placed directly at the tunnel wall and the signal responses are recorded with 3-component receivers in rock anchors along the tunnel wall. Also here, migration of reflected waves is utilized for subsoil imaging, in this case on the basis of reflected tunnel surface waves. In TSP, explosive charges and 3-component receivers are placed in boreholes along the tunnel wall. The technique separates compressional and shear waves and applies various geotechnical techniques which evaluate the reflected waves. TRT uses explosive charges or pneumatic hammers at the tunnel face as seismic sources and seismic receivers placed in boreholes along the tunnel walls. The evaluation of the seismic records is, as the name of the system says, based on reflection tomography.

Due to the different working principles of the tomography methods mentioned, ranges and resolutions vary. According to Schmitt *et al.* (2004), SSP has a range of about 40 m, TRT of about 60 – 100 m, TSP of 150 – 200 m, and ISIS of about 200 m. However, resolutions decrease and uncertainties increase with increasing distance to the tunnel face. Dickmann & Sander (1996) specify that the TSP error margin in the predicted distance to the boundary of an anomaly amounts to 5 % for an investigation range of 0 – 50 m, to 10 % for an investigation range of 50 – 200 m, and to at least 20 % for higher distances. Schmitt *et al.* (2004) state that none of the systems can bring an absolutely safe prediction and indicate the resolutions of TRT and SSP to lie at about 1 m in the region directly behind the TBM, decreasing rapidly with increasing distance to the tunnel face.

1.3. Full waveform inversion

The quality of the seismic prediction can be improved with full waveform inversion (FWI). A FWI exploits – as its name implies – the full waveforms recorded at the seismic receivers. In this method, a so-called misfit functional is defined that expresses the difference of the measured seismic records to synthetic waveforms generated with a computational model of the subsoil. During the inversion, the model is altered with the aim to minimize the misfit functional. The model with the minimum misfit is then considered for an estimation of the subsoil properties. FWI in general can gain a resolution of about half a wavelength of the operating waves (Virieux & Operto, 2009); however, this relation strongly depends on the applied measurement setup. With advantageous source-receiver configurations, the range of FWI is expected to be much more far-reaching with a resolution much more precise than of the above-mentioned tomography methods – with limitations rather caused by applied working frequencies and technical issues. Still, the greatest technical restriction lies in the computational cost. Although FWI in general became applicable in many fields – experiencing an exploding number of publications since the years after the turn of the millennium (Igel, 2017) – the methods are still distant from delivering results close to real-time or during a time which would be necessary for an application during mechanized tunneling. However,

with exponentially growing computational power, FWI may become applicable in the sector in a few years.

Early FWI approaches exist in time-domain (Tarantola, 1984) and in frequency-domain (Pratt & Worthington, 1990). In its first decades, FWI was rather limited to 2D and acoustic cases due to the computational cost. Nowadays, the field of applications is large – also in 3D elastics – ranging from laboratory scales up to local scales, continental scales, and global scales. Examples for FWI on local scales give the works of Sirgue *et al.* (2010) and Schiemenz & Igel (2013), who investigate the Valhall data set with FWI, both providing high resolutions of the territory. Colli *et al.* (2013) provide an example for FWI on a continental scale, where adjoint FWI is applied to data sets of the upper mantle in the South Atlantic region. Another famous example for FWI on the continental scale is the work of Fichtner & Villaseñor (2015), who create a full waveform tomographic model of the western Mediterranean crust and mantle. In recent years, computational resources even enabled FWI on global scales, where examples are provided by French & Romanowicz (2015) and Lei (2019). Note that the above-mentioned references are only some prominent examples from a large and continuously growing pool of literature. This thesis, however, focuses on smaller scales than the above-mentioned. In mechanized tunneling, scales ranging from a few decades of meters to the kilometer scale are interesting. Publications in this range also exist but are, however, less frequent. Romdhane *et al.* (2011) apply FWI in order to characterize shallow structures. Smith *et al.* (2019) use their FWI approach in order to detect an underground tunnel. The current research is concerned with even smaller scales since the methods shall be directly validated on the laboratory scale with the aid of ultrasonic measurements. An example in this order of magnitude is provided by Bretaudeau *et al.* (2013), who apply FWI in order to reconstruct anomalies in epoxy resin models with FWI – similarly, with the aim to draw conclusions about the performance of the algorithm on larger scales. Another example is provided by Rao *et al.* (2016), who utilize FWI for the reconstruction of wall thicknesses in aluminum plates.

Few approaches exist that are designed for an application during mechanized tunneling. A frequency-domain adjoint gradient method for FWI in a tunnel environment is proposed by Musayev *et al.* (2013). The performance of this FWI approach in the context of 2D and 3D acoustic synthetic examples is investigated in detail by Riedel *et al.* (2021a), who later extend the approach to elastic wave modeling cases (Riedel *et al.*, 2021b). Bharadwaj *et al.* (2017) provide a time-domain 2D adjoint FWI approach for application in soft soil, which is designed to be applied to 3D data directly with the help of certain transformation techniques. The method is validated with synthetic data as well as with surrogate field experiments. Lamert & Friederich (2018) provide another 2D adjoint FWI approach in time-domain for application in mechanized tunneling, which is later extended to 3D (Lamert, 2019). The approach is based on the nodal discontinuous Galerkin method, where tetrahedral elements allow a regular meshing in the tunnel environment and thus also the implementation of a comparatively large time step. The approach is tested on several synthetic examples as well as on laboratory-generated data, which is generated in Trapp *et al.* (2019) and also used for the validation of our FWI methods (see Chapter 6).

1.4. Dimensionality reduction and statistical full waveform inversion

Most of the recent FWI methods are based on a gradient search within the frame of so-called adjoint methods. These methods usually include a high number of unknowns since the material properties are variable (e.g. at the nodes or elements) all over the model domain, where the number of unknowns is also referred to as the dimensionality of the inverse problem. Due to the high dimensionality, adjoint methods are in general able to supply a more or less exact image of the subsoil. However, the occurring inverse problem is highly ill-posed with a high number of minima in the misfit functional. As a consequence, adjoint methods are often trapped in one of the local minima, especially if the initial model is not close to the real model. The results of the inversion may then be blurred reconstructions with underestimated material property changes. In scenarios, where due to source-receiver configurations only reflected waves are considered (for instance in a tunneling scenario, where sources and receivers are only placed inside the tunnel), the non-uniqueness of the inverse problem combined with the high dimensionality makes a reconstruction of the anomaly behind the first upcoming boundary of the anomaly (seen from seismic sources and receivers) difficult. One possibility to overcome the above-mentioned problems is to reduce the number of unknowns of the inverse problem by implementing either a generally suitable but simplified parametrization of the subsoil model or a parametrization grounded on prior knowledge. This *dimensionality reduction* or *inversion parameter space reduction* is central to this work. The procedure reduces the complexity of the misfit functional, providing a smoother function. As a consequence, the risk of ending up in one of the local minima is lowered since many of the local minima, in which classical methods may be trapped, do not exist since the parametrization of the model does not allow them. The disadvantage of a dimensionality reduction is that certain details are missed out if the computational model cannot approximately describe the real model due to the simplification, or, in the extreme case, a failure of the inversion if the parametrization is not valid. However, if the computational model with the reduced dimensionality is able to approximately describe the real model, inversion results may be highly precise, which will be shown in the further course of this work.

A methodology which can tackle the parameter estimation of the resulting reduced model is statistical inverse theory (e.g. Tarantola 2005). This approach considers the non-uniqueness of the solution of inverse problems by assigning probability distributions to the model parameters revealing which parameter configurations are certainly and which are uncertainly describing a representation that is close to the true model. Prior knowledge about measurement and modeling uncertainties may be implemented prior to inversion. Starting from a prior guess with initial uncertainties, parameter configurations are sampled and the model parameters and uncertainties are updated until a satisfactory small misfit functional is reached for the current mean value of the model parameters. The result of the inverse problem is a statistical description of the model parameters. The mean value of the parameters may then be used to define the model that is most probably representing a model which is close to the true model. Note that, due to the finite number of parameters and due to assumptions and approximations, a computational model can never fully illustrate the true model but rather output a computational model which is, if all assumptions are to large parts valid, certainly close to the true model. The final covariance of the model parameters can be used to perform uncertainty quantification in order to find out where anomalies may potentially be missed or where estimated objects may be falsely imaged. The two main FWI methods used in this work are based on the above-mentioned principles of dimensionality reduction and statistical inverse theory based on Bayesian inference.

Statistical inverse problems commonly require more forward simulations than gradient-based approaches. Since forward simulations in FWI are computationally demanding, statistical FWI is usually combined with dimensionality reduction – same as in this work. Numerous recent examples in which those two ideas are combined can be found in literature. Again, the following examples are only some recent ones out of a large pool. Statistical FWI is often applied to coarsened velocity grids of subsoil models. Sajeva *et al.* (2016) use a gridded parametrization and apply a genetic algorithm for FWI, where the final model is improved with descent-based FWI. Another example is provided by Wang *et al.* (2019), where the ensemble Kalman filter is integrated into a semi-random framework for FWI. Gebraad *et al.* (2020) apply a Hamiltonian Monte Carlo approach to solve for gridded velocity models. Besides the approach of gridded models, also a problem-specific parametrization may be defined. Visser *et al.* (2019) apply Markov chain Monte Carlo (MCMC) to a parametrization of dipping layers. Hunziker *et al.* (2019) apply MCMC to a reduced geostatistical model based on relative permittivity and electric conductivity. Statistical approaches for FWI with a problem-oriented application in mechanized tunneling are – besides the two methods explained in the following – not found in literature.

The first method to be applied in this work is *unscented hybrid simulated annealing* (UHSA), introduced by Nguyen & Nestorović (2016). UHSA combines two algorithms – simulated annealing (SA) (Kirkpatrick *et al.*, 1983) and the unscented Kalman filter (UKF) (Julier & Uhlmann, 2004), with SA being the global and the UKF being the local optimization algorithm. The resulting algorithm is a non-deterministic global optimization algorithm. The method is based on the implementation of prior knowledge in order to achieve the dimensionality reduction. Prior knowledge about the subsoil may be available from several sources. As previously explained, a coarse estimation of the subsoil properties is already provided prior to excavation when the tunnel trajectory is planned by extrapolation of the geological situation from the Earth’s surface to its interior, additional geophysical measurements, exploratory drillings and prior seismic surveys. Even before, geological maps can provide knowledge. Another approach to gain prior knowledge is described in the three-stage concept in Chapter 9, where a supervised machine learning algorithm provides information. Gained prior knowledge can for instance be the knowledge about the existence of a boulder or a layer change, with unknown/uncertain location and size or angle. In urban areas, it is also conceivable that knowledge about the existence of further obstacles like slurry walls or steel beams is available. This knowledge may be implemented in the form of a parametrization of the disturbance. The parametrization of a layer change could for instance include location coordinates, angles around all spatial directions, and material properties. A (cuboid) boulder could be specified with a parametrization defining location coordinates, edge lengths, and material properties. With a given set of parameters, the disturbance can then be exactly specified inside the model domain and a misfit functional can be computed. The aim of the inversion is to find the optimal parameter configuration (which is the set of parameters with the lowest misfit functional). Due to the global search nature of UHSA, a parameter configuration close to the global minimum will be found if the number of cycles is high enough and if the parametrization of the disturbance is valid. It is noted that if no prior knowledge can be supplied, UHSA is difficult to apply.

The second method to be applied is the *UKF-controlled parametric level-set method* (UKF-PaLS) introduced by Nguyen & Nestorović (2018). Two methods are combined here as well: the UKF and the parametric level-set method (PaLS) (Aghasi *et al.*, 2011). In contrast to UHSA, UKF-PaLS is a deterministic method with the UKF as the optimization algorithm and PaLS as the parametrization algorithm used for the definition of anomalies.

The level-set parametrization is implemented in a numerical model of the subsoil, enabling the definition of the shapes and the material properties of disturbances. The UKF minimizes the misfit functional in order to find the optimal parameter configuration of the implemented parametrization. The method allows to flexibly define irregularly shaped objects but is still based on parameter space reduction, where also prior knowledge can be implemented: firstly, the region of investigation is restricted to a predefined area. Secondly, also a resolution determining the smallest possible size of an object that still can be imaged is implemented by the user. Thirdly, the examples in this work reduce the number of possible disturbance materials to one. Ideas on how these criteria could be loosened if they are too restrictive will be presented in Section 10.4.

1.5. Goals and structure of the thesis

The two major goals of this work are (1) the further development of UHSA and UKF-PaLS and (2) their application to seismic data, where also several side goals exist, which are explained in the following. Some of the developments include the extension of the inversion methods to 3D, the implementation of a multi-scale approach, the provision of methods for parameter tuning and a parallelization of forward simulations. The performance of UHSA is to be tested against other comparable global optimization methods. Furthermore, a variation of source-receiver configurations is to be tested in order to be able to make statements about possible configurations for field applications. Besides the application to synthetic data, a special focus of this work lies in the application to experimental data. Since adequate field data is difficult to obtain, a *small-scale laser experiment* is set up in which ultrasonic experiments can be performed in order to acquire seismic data. For that purpose, special specimens are constructed and excited with ultrasonic transducers in order to release seismic waves. A laser interferometer is integrated which is capable of measuring displacements in the nanometer range over time at different locations of the specimens, providing the data for inversion. The idea of this procedure is to scale down the dimensions of field models in accordance with operating wavelengths, obtaining data that is in a certain sense comparable to field measurements. This is also the idea in the work of Bretaudeau *et al.* (2011), where a similar setup is used. The usage of experimental data bears several challenges, which will be addressed in the course of the work. Some of them are directly related to the measurement itself, for instance it needs to be investigated how the signal quality may be maximized and how a measurement on porous surfaces becomes realizable with the sensitive laser interferometer. Others are related to the representation of the experiment with a numerical model. In this context, the greatest challenges lie in the characterization of material properties and in the estimation of the transducer source function. The application of the FWI approaches to the experimental seismic data finally shows if the methods are robust against remaining modeling and measurement errors. The fulfillment of the main and side goals is expected to reveal if and how the parameter reduction methods can be deployed for exploration during mechanized tunneling.

The work is structured as follows: in Chapter 2, fundamentals of seismic wave propagation are introduced, characterizing the forward problem and methods to find out its (numerical) solution. Chapter 3 focuses on the inverse problem by explaining the FWI methods in detail. The small-scale laser experiment is described in Chapter 4, including essential investigations on repeatability, signal-to-noise ratio and the characteristics of noise. A first validation of

UKF-PaLS with synthetic data is performed in Chapter 5, where an improved version of the method is validated with synthetic 2D examples before it is extended to 3D. The next three chapters include validations with experimental scenarios. The first experimental validation of the methods is conducted in Chapter 6, where both UHSA and UKF-PaLS invert seismic data acquired on an aluminum block with the aim to image a drilling. The results of both methods are compared to the results of an adjoint approach inverting the same data. Furthermore, UHSA is compared to particle swarm optimization. The difficulty of the experimental FWI is increased in Chapter 7, where various concrete plates with anomalies are manufactured and investigated, bringing a more rock-like behavior. UHSA is tested on three different inversion scenarios and compared to a genetic algorithm for one scenario. Chapter 8 is the final phase of experimental investigation in this work. Here, an experimental model, also consisting of concrete but having more similarities to a tunneling field model, is designed. The experiment is designed in such a way that simulations may be conducted in 2D for the benefit of a shorter calculation time, allowing to make investigations on different source-receiver configurations as well as to validate both UHSA and UKF-PaLS. Chapter 9 presents a three-stage concept, where UHSA is coupled with two different methods, namely with an approach based on supervised machine learning and the adjoint method. The discussion part in Chapter 10 analyzes the applied methods, shows similarities between the conducted experiments and large-scale cases, and reveals potential challenges during mechanized tunneling, also regarding sources and receivers and their placement. Furthermore, the chapter presents an approach for creating a substitute metamodel for simulation models based on supervised machine learning. In the last chapter of this work, the results are summarized and concluded.

2. Fundamentals of seismic wave propagation

2.1. Elastic wave equations

A wave equation is a second-order partial differential equation that describes the propagation of waves. In the case of seismic exploration during mechanized tunneling, where a rather small amount of energy is released by seismic sources, the soil behavior may be assumed to be elastic – meaning that the induced strains are in the range of elastic material behavior, for which elastic wave equations can be applied. Counter-examples are for instance large earthquakes, where material behavior can be plastic. The aim of a forward seismic wave propagation problem is to calculate the response of a model to a seismic signal triggered by a seismic source. The displacement field $\mathbf{u}(\mathbf{x}, t)$ (or its time derivative, the velocity field) is the unknown to be estimated for a formulation in time-domain. Vector \mathbf{x} specifies a location inside the model. A synthetic seismogram is obtained by specifying a location \mathbf{x} inside the model and evolving the displacement during time t . With the displacement field, the strain field $\boldsymbol{\epsilon}(\mathbf{x}, t)$ may be derived; and the strain field determines the stress field $\boldsymbol{\sigma}(\mathbf{x}, t)$. The equations that connect the external forces with stresses, strains, and displacements are the balance of momentum in continua, Hooke's law, and a strain-displacement relation. Detailed information is for instance provided by Udias & Buforn (2017). The balance of momentum for continua may be written as follows:

$$\rho \ddot{\mathbf{u}} = \nabla \cdot \boldsymbol{\sigma} + \mathbf{f}, \quad (2.1)$$

where $\rho(\mathbf{x})$ is the density and $\mathbf{f}(\mathbf{x}, t)$ are the seismic sources characterized by volumetric forces (Igel, 2017). ∇ is the nabla operator containing the partial derivative operators in all spatial directions. Note that seismic sources may also be characterized by a seismic moment tensor. The stress field is calculated with Hooke's law. In the case of linear elastic and isotropic media, the relation

$$\boldsymbol{\sigma} = \lambda \operatorname{tr}(\boldsymbol{\epsilon})\mathbf{I} + 2\mu\boldsymbol{\epsilon} \quad (2.2)$$

applies, where $\lambda(x)$ and $\mu(x)$ are the Lamé constants and where \mathbf{I} is the identity tensor. The strain tensor for small strains is derived by

$$\boldsymbol{\epsilon} = \frac{1}{2} [\nabla \mathbf{u} + (\nabla \mathbf{u})^T]. \quad (2.3)$$

The three equations above make up the elastic wave equation in the displacement form for linear elastic isotropic media. For homogeneous media with constant λ and μ , these equations may be merged into one equation (Udias & Buforn, 2017):

$$(\lambda + \mu)\nabla(\nabla \cdot \mathbf{u}) + \mu\nabla^2 \mathbf{u} + \mathbf{f} = \rho \ddot{\mathbf{u}}. \quad (2.4)$$

Note that ∇^2 is also referred to as the Laplace operator. A special form, the acoustic wave equation, can be derived assuming a vanishing shear modulus. This equation describes the

propagation of compressional waves only and may be used for the full description of wave propagation in media like fluids and gases, but not for elastic media. For the implementation of anisotropy, the general form of Hooke's law

$$\boldsymbol{\sigma} = \boldsymbol{C} : \boldsymbol{\epsilon} \quad (2.5)$$

needs to be considered, where the double dot denotes the Frobenius inner product and \boldsymbol{C} is a fourth-order tensor with 81 elastic constants in the 3D case. These constants can be reduced to 21 independent elements due to symmetry conditions and thermodynamical arguments (Igel, 2017). With symmetries of materials, the number of constants can be further reduced, with 9 constants for an orthorhombic crystal, with 5 for a hexagonal structure, and 3 for cubic symmetry (Mouhat & Coudert, 2014), where the most commonly used system for seismic wave propagation if considering anisotropy is hexagonal symmetry (Igel, 2017). For isotropic media, one obtains only two independent constants μ and λ as shown in Eq. 2.3. In this work, no anisotropy is considered as the investigated materials (aluminum and concrete) can be sufficiently described considering the assumption of isotropic material properties.

2.2. Boundaries

The solution of the elastic wave equations depends on the boundaries of the model. Boundaries may be classified into free boundaries, internal boundaries, and absorbing boundaries. The implementation of the free and internal boundaries leads to the realization of reflection, refraction, diffraction, conversion, and scattering – phenomena, which would not occur within an infinite homogeneous space. At a free surface, the free surface boundary condition applies, meaning that the tractions in normal directions are zero. This condition leads to the formation of surface waves (see Section 2.3.2). At internal boundaries, the material properties change, but the displacements and tractions remain continuous. However, the continuity does not have to be explicitly implemented into numerical solvers, except if fluid-structure implementations are utilized (Igel, 2017). The last category of boundaries, the absorbing boundary conditions, are implemented in order to decrease the size of the computational model. Instead of designing a large model in a way that no reflections arrive at seismic receivers from free boundaries, which limit the computational model, absorbing boundaries may be implemented. The aim of the implementation is that no reflections arise from these boundaries. The implementation of efficient absorbing boundaries has been intensively researched and a large number of methods have been developed (Igel, 2017). Very

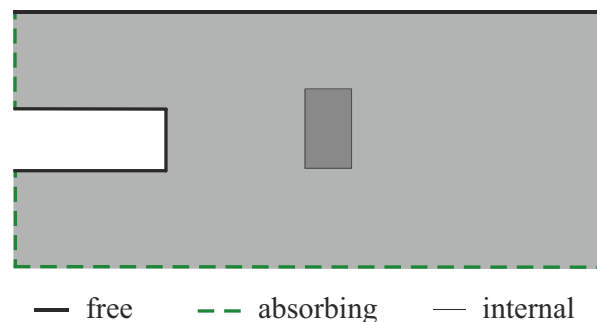


Figure 2.1.: Schematic illustration of free, internal, and absorbing boundaries in a 2D shallow tunnel environment including a boulder. For deep tunnels, the top boundary would obtain absorbing boundary conditions.

widely used are perfectly matched layers (PMLs), originally implemented by Berenger *et al.* (1994). This method features a high effectivity, meaning that the absorption is high while reflections are low; however, a drawback is an increase of computation time. For the examples in this work (where absorbing boundaries are only used for the synthetic examples), Stacey absorbing boundary conditions (Stacey, 1988) are utilized, which are less effective than PMLs (meaning that slight reflections occur) but require smaller computational capacities. The boundaries can be selected in the forward wave propagation codes that will be used in this work (see Section 2.5.1). Figure 2.1 illustrates the boundaries in a typical tunneling simulation model in 2D with a rectangular-shaped boulder. The same rules apply to 3D structures. Free surfaces are implemented at the air-soil interfaces and consequently at the Earth's surface as well as at the tunnel walls. Absorbing boundaries are assigned to all other outer boundaries since in those directions, seismic waves spread further. Their implementation induces the assumption that no reflections arrive at the receivers from outside of the boundaries in the corresponding real model, which is to be considered by the user. The illustration applies to shallow tunnels, where the top boundary is the Earth's surface. Considering deep tunnels, the top boundary would obtain absorbing boundary conditions.

2.3. Types of seismic waves

The solutions of the wave equations are superpositions of different types of waves. Basically, seismic waves may be categorized into body waves, which travel through the interior of the earth, and surface waves, which travel along the surface of the earth. The following two subsections cover the fundamentals of body waves and surface waves, respectively. Once more it is noted that detailed information is for instance provided by Udias & Buforn (2017).

2.3.1. Body waves

The solution of a wave propagation problem in infinite homogeneous elastic media consists of two types of seismic waves – compressional or primary waves (P-waves) and shear or secondary waves (S-waves). P-waves are the fastest occurring waves, vibrating longitudinal in direction of wave propagation with velocity

$$v_p = \sqrt{\frac{\lambda + 2\mu}{\rho}}. \quad (2.6)$$

S-waves are transverse waves, vibrating perpendicular to the direction of wave propagation with velocity

$$v_s = \sqrt{\frac{\mu}{\rho}}. \quad (2.7)$$

They may be partitioned into horizontally polarized (SH-waves) and vertically polarized (SV-waves) components. In classical mechanics, often, the Young's modulus E and the Poisson's ratio ν are utilized to describe linear elastic isotropic materials. These parameters may be derived from the Lamé parameters as follows:

$$E = \frac{\mu(3\lambda + 2\mu)}{\lambda + \mu}, \quad \nu = \frac{\lambda}{2(\lambda + \mu)}. \quad (2.8)$$

The Poisson's ratio can be derived from the body wave velocities as follows

$$\nu = \frac{v_p^2 - 2v_s^2}{2(v_p^2 - v_s^2)}. \quad (2.9)$$

A widely-specified range of the Poisson's ratio is $0 < \nu < 0.5$, although there exist very few materials with a negative Poisson's ratio. A common range for rock materials lies between 0.2 and 0.3, and nearly all kinds of rocks are covered within a range of $0.05 < \nu < 0.45$ (Gercek, 2007). The Poisson's ratio will later be used in order to check if pairs of wave velocities are reasonable and in order to set limitations during the inversion.

2.3.2. Surface waves

A different type of seismic waves are surface waves. If body waves arrive at a free surface, a part of the energy is transformed into surface waves. With propagating distance x , the energy of body waves decays with $1/x^2$ due to geometrical spreading, where the energy of surface waves decays only with $1/x$. This is the reason for the property that surface waves are typically most destructive during an earthquake. The most important types of surface waves are Rayleigh- and Love-waves. Rayleigh waves travel a little slower than shear waves with elliptical but significantly higher particle motion, causing distinctly higher amplitudes on the surface in vertical direction than body waves. The Rayleigh wave velocity may be estimated as follows (Freund, 1998):

$$v_r = v_s \cdot \frac{0.862 + 1.14\nu}{1 + \nu}. \quad (2.10)$$

Thus, for a variation of ν between 0 and 0.5, the Rayleigh wave velocity varies between $0.862 v_s$ and $0.955 v_s$. Moving particles excited by Love waves vibrate perpendicular to the direction of wave propagation with horizontal polarization. Love waves only exist in layered media (Igel, 2017, p. 30) (and consequently, they do not exist in a homogeneous half space) with a velocity lower than P- and S-waves but higher than Rayleigh-type surface waves.

2.4. Phase velocity, group velocity and dispersion

There are two types of velocities to be distinguished – the phase velocity and the group velocity. The phase velocity is the velocity, with which the phase of a single frequency component of the wave travels. The phase velocity is given as

$$v_{\text{phase}} = \frac{\lambda}{T} = \lambda f, \quad (2.11)$$

where λ is the wavelength, T is the time period and f the frequency component. If the phase velocity is a function of frequency, the medium is said to be dispersive. This is for example the case in attenuating media. Furthermore, surface waves are dispersive in layered media; in a homogeneous half space they are non-dispersive (Igel, 2017, p. 30). As a consequence of dispersion, the different frequency components of the wave travel with different velocities. The group velocity is the velocity, with which the overall shape of the amplitudes of the waves (the envelope) propagate through the domain. Despite physical dispersion, there

exists numerical dispersion. Numerical dispersion is an unwanted effect that occurs if the model is discretized with an insufficient number of grid points per wavelength (Fichtner, 2010). This effect should be avoided with an adequate meshing, which is described in the next section.

2.5. Numerical solution

In order to compute forward seismic wave propagation, an adequate scheme needs to be selected. Analytical solutions only exist for special cases, for example for a homogeneous full- or half-space. Besides analytical methods, there are seismic methods that are based on certain assumptions, where a prominent example is ray theory. The drawback of this method is that it only works for smooth media and in the case that inhomogeneities are considerably larger than the operating wavelengths (Fichtner, 2010). In the context of full waveform inversion, the full waveform for complex media is required, where a solution for the set of partial differential equations Eq. 2.1-Eq. 2.3 can only be provided with the aid of numerical methods. There are numerous numerical methods that have advantages and disadvantages; this section focuses on a description of the fundamentals of the *spectral element method* and the method from which it originates, the *finite element method*. Other methods which were intensively used were the *finite difference method*, which was the first method that was widely applied, the *pseudospectral method*, and the *discontinuous Galerkin method*. The first two methods lost their popularity since they suffer from certain disadvantages, where for instance the finite difference method requires a high number of grid points while the pseudospectral method shows problems facing parallelization. However, the most significant disadvantage of both methods is the restriction to comparatively smooth geometries (Fichtner, 2010; Igel, 2017). Although the pseudospectral method is rarely used nowadays, a basic idea of this method was implemented in the spectral element method, which is the idea of using a specific set of collocation points for interpolation inside the elements (Igel, 2017), which will be referred to below. The discontinuous Galerkin method is, same as the spectral element method, still widely used and will also be shortly introduced in the course of the following text.

The *finite element method* (FEM) overcomes the main weakness of the finite difference method and the pseudospectral method with the ability to describe complex structures. Since it is able to deal with various boundary conditions, it is a widely used method, especially for engineering applications, where probably the largest fields are structural and solid mechanics for stress and strain calculations. Other related fields are fluid mechanics, heat transfer, electromagnetics, geomechanics, and numerous more. As previously explained, the unknowns of interest (so-called field variables) are governed by partial differential equations. These equations, together with the boundary conditions, are referred to as the strong form. It is noted that, considering the wave equations Eq. 2.1-Eq. 2.3, the assumption that the displacement is not dependent on time directly leads to the governing equations of static elasticity. The starting point of FEM is the formulation of an integral form of the wave equation multiplied with so-called test functions. This form is referred to as the weak form. The spatial model is discretized with non-overlapping elements connected at nodes. The gain of this discretization is that the partial differential equations do not have to be defined continuously but only over a finite number of discrete elements. Inside the elements, the displacement field is computed with a linear combination of basis functions with the same

shape as the test functions, where this procedure is called the Galerkin method. Substituting this formulation of the displacement field into the weak form of the differential equation, the latter becomes a matrix equation for each element. These matrix equations are assembled into one large matrix equation, which is then solved with linear algebra methods respective to the induced boundary conditions. The matrix to be inverted is either a stiffness matrix or a mass matrix, where in the case of static elasticity the stiffness matrix needs to be inverted. Usually, for time-dependent problems, a finite difference scheme is implemented for the second time derivative of the displacement field, which then enables to propagate the equations with time in order to compute time-dependent wave propagation. In this case, the mass matrix needs to be inverted, which typically is sparse and banded in FEM, but not diagonal. Detailed information regarding FEM is for instance provided by Zienkiewicz *et al.* (2005). In its classical formulation, FEM is rarely used for waveform modeling. The reasons for that lie in a large numerical dispersion resulting from low-order polynomial approximations inside the elements as well as in large computational expensiveness (Fichtner, 2010) compared to the method described in the following, which reduces the computational effort with a formulation that leads to a diagonal mass matrix.

2.5.1. The spectral element method

The spectral element method (SEM), which is sometimes also referred to as the spectral finite element method, is a formulation of the FEM with ideas used in the pseudospectral method. Same as in FEM, the wave equation is solved in its weak form and the displacement field is computed with a linear combination of basis functions inside the elements. The fundamental difference lies in the shape of the basis functions, where high-order polynomials are used inside the elements. Often (and also in the codes that are utilized in this work), Lagrange polynomials are used as basis functions. These polynomials are collocated at the so-called Gauss-Lobatto-Legendre (GLL) points and a method called Gauss-Lobatto-Legendre quadrature is utilized in order to approximate the integrals of the weak form of the differential equation. The great advantage of this procedure is that the mass matrix that needs to be inverted in the forward problem becomes diagonal for quadrilateral (2D) and hexahedral (3D) meshes. The spectral element method is not restricted to quadrilateral or hexahedral elements per se, but for geometries that may not be meshed with these kinds of elements but with tetrahedrons, *discontinuous Galerkin methods* are more commonly used. These methods are also formulations of the FEM based on the Galerkin principle, where certain discontinuities at the element boundaries are allowed by the implementation of numerical fluxes (Fichtner, 2010). Back to SEM, the advantage of a diagonal mass matrix for quadrilateral or hexahedral elements lies in its trivial inversion and thus in a reduction of computational demand. Since all spatial models in this work can be meshed with quadrilaterals or hexahedrons, 2D simulations are performed with SPECFEM2D (Tromp *et al.*, 2008) and 3D simulations with SPECFEM3D (Komatitsch *et al.*, 2012). Both codes are open-source. The meshing of the 2D spatial models is conducted with the open-source program Gmsh 2.10.1 (Geuzaine & Remacle, 2007), while the meshing of 3D spatial models is performed with Trelis 15.2 (American Fork, 2015). In order to ensure that all frequencies of interest are contained in the numerical solution and that the time stepping is stable, an adequate meshing and the selection of an appropriate time step is necessary. According to Komatitsch & Vilotte (1998), who are among others the founders of SPECFEM2D and SPECFEM3D, a grid sampling of about 5 points per minimum wavelength is found very accurate for SEM. Since the predefined number of GLL points on an element edge in the two

codes is $N_{\text{GLL,edge}} = 5$, the basis for the mesh generation in this work is

$$\Delta h_{\text{max}} < \frac{v_{\text{min}}}{f_{\text{max}}} \quad (2.12)$$

since in this case, at least 5 points per minimum wavelength are used. Δh_{max} is the largest occurring element edge length in the mesh (specified by the smallest occurring wavelength) and v_{min} is the smallest occurring wave velocity in the model. f_{max} is the highest significant frequency defining the upper bound of the frequency range of interest, meaning that if the mesh size is chosen so that Eq. 2.12 is fulfilled, all frequencies are incorporated adequately by the mesh with at least 5 points per minimum wavelength. Komatitsch & Vilotte (1998) propose to set f_{max} at least to the frequency at which the spectral amplitude falls to 5% of the maximum spectral amplitude of the source function, which, for the Ricker wavelet, is the case at about $f_{\text{max}} = 2.5f_0$. For the Ricker wavelet, more than 99% of the energy of the Ricker source function is contained within the frequency range of 0 and $f_{\text{max}} = 2.5f_0$. Both SPECSEM2D and SPECSEM3D output the maximum resolved frequency, which is used as a control value in order to check if the meshing is performed accurately. The condition for the time step is the Courant-Friedrichs-Lewy criterion

$$\Delta t < C \cdot \frac{\Delta x_{\text{min}}}{v_{\text{max}}}, \quad (2.13)$$

where Δt is the time step for the numerical simulation, C is the Courant (or CFL) number, v_{max} is the maximum occurring wave velocity in the model and Δx_{min} is the smallest occurring grid interval in terms of the collocation points. The SPECSEM-codes try to evaluate the optimal value of Δt for empirically chosen Courant numbers $C \approx 0.3$ as described in the SPECSEM3D user manual (Computational Infrastructure for Geodynamics, 2020, p.30). When generating the databases, a maximum time step is suggested. A slightly lower value is used as the basis for the implementation of the time steps in this work.

2.6. Attenuation

In nature, propagating seismic waves continuously lose energy, for instance due to friction, converting the energy of motion into heat. This so-called intrinsic attenuation is measured with the dimensionless quality factor Q , which is defined as the ratio of the energy of the seismic wave per cycle to the energy loss per cycle as follows (Igel, 2017):

$$Q = -\frac{2\pi E}{\Delta E}, \quad (2.14)$$

where E is the peak strain energy and ΔE the energy loss per cycle. Hence, attenuation increases with decreasing values of Q . Typical values range from 10 to several 1000 in the Earth's crust and mantle. Knopoff (1964) gives examples for possible values of sandstone ($Q \approx 21$), limestone ($Q \approx 110$) or aluminum ($Q > 10000$); however, general values for Q cannot be given as the values differ strongly due to microcracks, pressure, dry or saturated state, weathering and numerous other aspects (Barton, 2006). The quality factor typically increases with increasing velocity – therefore, most often two Q -factors are given, which correspond to the attenuation of P-waves (Q_p) and to the attenuation of S-waves (Q_s) and which are usually considered independent of frequency. In SPECSEM2D and SPECSEM3D, the quality factors are specified with bulk (Q_κ) and shear (Q_μ) attenuation. Thereby, Q_μ

is equal to Q_s and Q_κ can be transformed to Q_p as described by Dahlen & Tromp (1998, p. 350). The decay in amplitude for a monochromatic plane wave is given as follows (Igel, 2017, p. 23)

$$A(x) = A_0 e^{-\frac{fx}{2vQ}}, \quad (2.15)$$

where A_0 is the initial amplitude, f the frequency of the plane wave, v the propagation velocity and x the propagation distance. The formula shows that amplitudes with high frequencies are more damped than amplitudes with lower frequencies, consequently altering the shape of the waveform. As a possible example for tunneling scenarios, Figure 2.2 shows the decay of the amplitude in terms of a relative amplitude in dependency of the propagated distance of the wave with an exemplary wave velocity of $v = 3000 \frac{m}{s}$ and a frequency $f = 200$ Hz for a variation of quality factors between 20 and 1000. The idea for the figure is inspired by Igel (2017, p. 23). The curves and the formula show that the amplitude decay caused by attenuation is strongly dependent on the intrinsic attenuation of the investigated material, the frequencies applied and the propagated distance of the seismic wave, which is proportional to the time the wave propagates. Applying no attenuation could be conceivable for scenarios in e.g. hard rock with small intrinsic attenuation, smaller frequencies, and short periods of investigation. Otherwise, Q -factors will have to be determined experimentally. For the examples in this work, the observed time periods will be rather short, most notably due to the high computational effort of simulations. For this reason, no attenuation needs to be applied. For the example of the concrete block in Chapter 8, a variation of Q -factors will be tested and it will be found that the numerical simulation fits better to the measurements if no attenuation is applied.

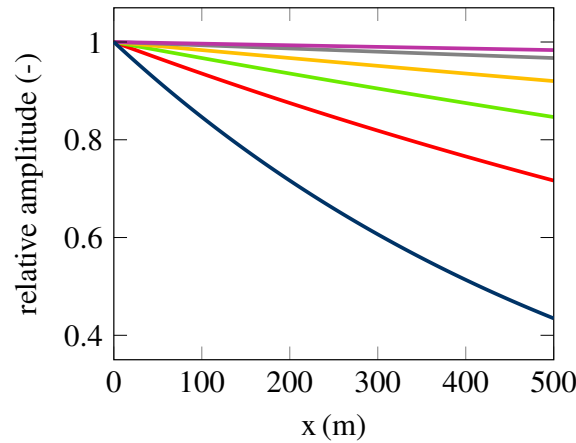


Figure 2.2.: Amplitude decay due to attenuation for variations of $Q = \{20, 50, 100, 200, 500, 1000\}$ (from the bottom curve to the top curve) for a scenario with plane wave velocity $v = 3000 \frac{m}{s}$ and frequency $f = 200$ Hz. The idea for the figure is inspired by Igel (2017, p. 23)

3. Methodologies – Full waveform inversion with Bayesian methods

Given a reliable description of a physical system, measurements can be predicted with a model. This is the task of the so-called *forward problem*, in which the causes are known and the effects are calculated. As previously mentioned, a forward simulation in the applied context is the numerical simulation of the propagating waves for a certain numerical model. In an *inverse problem*, effects are recorded in order to calculate their causes. Measurements are inverted with the aim to find the parameters that characterize the physical system. In the case of FWI, seismic waveform measurements are given as a basis for the determination of the inner structure of the soil. The aim is to find a numerical model that describes the anomalies inside the observed domain sufficiently well. For that purpose, typically a large number of forward simulations needs to be performed. The inversion process may be subdivided into the following three steps (Tarantola, 2005):

1. Parametrization of the model: choose parameters that are able to sufficiently describe the system
2. Forward modeling: set up a numerical model in order to be able to calculate the synthetic waveforms for a given set of parameters
3. Inverse modeling: change the set of parameters in a way that differences between measurements and synthetic waveforms, expressed by the misfit functional, are minimized

The part of the numerical model, whose material properties remain unchanged during inversion and hence maintain initial material properties, is referred to as the *background domain* in the following. The other part is referred to as the *disturbance domain*. The two regions in sum constitute the *model domain*. In a first step, a parametrization of the model $\mathbf{m} \in \mathbb{R}^n$ (where n is the number of model parameters) is selected, which shall be able to sufficiently describe the anomalies inside the model domain. As explained in Section 1.4, the parametrization of the disturbance is, for the examples in this work, dependent on the method used as well as on available prior knowledge. Once a parametrization of the disturbance is selected, a forward model is constructed. Forward modeling consists, for instance, of the assignment of material properties, the implementation of boundaries, the meshing, and their implementation in the numerical solver. For the experimental case, e.g. also geometries, material properties and the source function are to be determined and implemented. The parametrization and the forward modeling are dependent on the specific inversion problems and therefore are discussed in the chapters treating the application scenarios. The task of the inversion algorithm is to find a set of parameters, which describes the disturbance domain sufficiently well, or which, in other words, minimizes the misfit functional. A specified set of parameters will also be referred to as a parameter configuration or as a sample in the following.

FWI problems are *ill-posed problems* (Virieux & Operto, 2009) since their solution can be *non-unique* – there may be different distributions of material properties that give the same or a similar prediction of the measurement at a seismic receiver. The strategy which is applied in this work in order to deal with the non-uniqueness is the previously described dimensionality reduction (see Section 1.4), which is the main difference to classical adjoint FWI methods and which may also be referred to as regularization through parametrization. In order to find a parameter configuration close to the global minimum, the application of a multi-scale approach may be necessary, referring to a method which implements a low-pass filter with a stepwise increasing cutoff frequency (see Section 3.5). By resolving larger structures in early iterations and smaller structures in later iterations, chances increase that the inversion converges to a solution close to the global minimum. The term which expresses how well the reference model generally can be reconstructed out of the seismic data is referred to as the resolution, which is mainly affected by data coverage, data quality, and applied frequencies (Fichtner, 2010). In order to achieve a high resolution, it is important that the region of interest is well covered with seismic sources and receivers (or, in other words, that sources and receivers are rather close to the region of interest) and that output traces are of high quality. If these criteria are fulfilled, FWI can generally bring a resolution of about half a wavelength of the operating waves (Virieux & Operto, 2009). Whether the computed representation is realistic or not then depends to a large part on the chosen description of the physics of the model and on the chosen parametrization in the frame of the dimensionality reduction.

The working principles of UHSA and UKF-PaLS are already explained in Section 1.4. The current chapter focuses on the detailed mathematical formulation of the methodologies. Section 3.1 focuses on the Bayesian formulation of the inverse problem, including the formulation of the misfit functional. As the UKF is a relevant ingredient for both FWI methods, the UKF is discussed in Section 3.2 before the two FWI methods are explained. Section 3.3 discusses the first FWI method, UHSA and Section 3.4 deals with the second FWI method, which is UKF-PaLS. Subsequently, the multi-scale approach is addressed (Section 3.5) before it is explained how the input parameters of the two methods may be tuned (Section 3.6).

3.1. The statistical inverse problem

Instead of using a gradient-based formulation, the inverse problem may be formulated with the help of Bayesian inference, sometimes referred to as the statistical inversion approach (Kaipio & Somersalo, 2006). Bayesian inference is the key concept of Kalman filters. The approach tries to tackle the problem of the non-uniqueness of inverse problems, outputting a complete statistical description of the parameter values via the posterior probability distribution, considering uncertainties in the data, in the model, and in prior estimates (Martin *et al.*, 2012). The Bayesian approach is based on updating a prior probability distribution of the model parameters with new information in order to produce a posterior model estimate. This posterior probability density function expresses the degree of confidence in \mathbf{m} for representing a model close to the real model with output \mathbf{d}_{obs} (which is, in the context of FWI, waveform data measured at seismic receivers) and is given as (Gebraad *et al.*, 2020):

$$p(\mathbf{m}|\mathbf{d}_{\text{obs}}) = \frac{p(\mathbf{d}_{\text{obs}}|\mathbf{m})p(\mathbf{m})}{p(\mathbf{d}_{\text{obs}})}. \quad (3.1)$$

$p(\mathbf{m})$ is the prior probability density function of the model parameters which represents the confidence in prior information on the model parameters independent of the observations (Martin *et al.*, 2012). The term $p(\mathbf{d}_{\text{obs}}|\mathbf{m})$ is called the likelihood and is the probability that the observed data \mathbf{d}_{obs} can be reproduced with the model \mathbf{m} . The denominator is a normalization factor referred to as the evidence, where $p(\mathbf{d}_{\text{obs}}) = \int_{-\infty}^{\infty} p(\mathbf{d}_{\text{obs}}|\mathbf{m})p(\mathbf{m})d\mathbf{m}$. This term secures that the posterior probability density function is a true probability density function integrating to one (Hunziker *et al.*, 2019). Since only relative probabilities are relevant for our case and since the term is difficult to compute, Eq. 3.1 can be rewritten as follows:

$$p(\mathbf{m}|\mathbf{d}_{\text{obs}}) \propto p(\mathbf{d}_{\text{obs}}|\mathbf{m})p(\mathbf{m}), \quad (3.2)$$

where \propto denotes proportionality. The likelihood can be written as an exponential of a misfit functional $S(\mathbf{m})$ (Eq. 3.6) as

$$p(\mathbf{d}_{\text{obs}}|\mathbf{m}) \propto e^{-S(\mathbf{m})}. \quad (3.3)$$

Kalman filters maximize the posterior probability density function for multivariate normal distributions. According to Eq. 3.2 and Eq. 3.3, the maximization of the posterior is equivalent to a minimization of the misfit function. In this work, the misfit functional $s_j \in \mathbb{R}$ between a measured and synthetic seismogram at a receiver location \mathbf{x}_j with $j \in \{1, 2, \dots, r\}$ is defined as

$$s_j(\mathbf{m}) = \frac{1}{2} \int_0^T (\mathbf{h}(\mathbf{m}, \mathbf{x}_j, t) - \mathbf{d}_{\text{obs}}(\mathbf{x}_j, t))^2 dt, \quad (3.4)$$

where $\mathbf{h}(\mathbf{m}, \mathbf{x}_j, t)$ stores the model outputs for a given parameter configuration \mathbf{m} during the time window $t \in [0, T]$ and where $\mathbf{d}_{\text{obs}}(\mathbf{x}_j, t)$ is the corresponding measurement. r is the number of receivers, also including measurements from varying sources. The misfit vector includes the misfit functionals at all seismic receivers as follows:

$$\mathbf{s}(\mathbf{m}) = \{s_1, s_2, \dots, s_r\}. \quad (3.5)$$

A total value of the misfit functional can be obtained by summing up the vector components according to:

$$S = \sum_{j=1}^r s_j. \quad (3.6)$$

In the next section, the unscented Kalman filter is introduced, which is, as already stated, a recursive Bayesian filter for multivariate normal distributions.

3.2. The unscented Kalman filter (UKF)

The UKF (Julier & Uhlmann, 1997) is a state estimator for parameters of nonlinear dynamic state-space models. A large field of application is the state estimation of time-dependent systems; however, by reformulation of the state-space representation, it can also be used for parameter estimation of stationary systems. Furthermore, the UKF can be used for the estimation of system parameters that may not be directly measured. This also applies to the scenarios in this work, where the observed waveforms are an indirect measure for the

inner structure of the subsol. The reformulation of the estimation problem is performed in such a way that the state vector is composed of the parameters describing the disturbance zone, where those parameters are affecting the value of the misfit functional. The UKF shall be applied in order to find the optimal state, that is the set of parameters \mathbf{m} for which the components of the misfit vector \mathbf{s} are minimized. The UKF is an extension of the Kalman filter (Kalman, 1960), which is named after Rudolf E. Kálmán. The original Kalman filter is limited to linear systems. The most commonly used extensions of the Kalman filter for the estimation of nonlinear systems are the extended Kalman filter (EKF) and the UKF. EKFs essentially linearize the function to be estimated around the current mean, resulting in a poor approximation for highly nonlinear systems. UKFs operate differently – instead of calculating Jacobians, UKFs approximate a probability distribution with the so-called unscented transform. Simon (2006) gives a detailed description of various algorithms of the Kalman filter family. The procedure of the UKF may be abstracted in a simplified way:

1. select certain parameter configurations (so-called sigma points)
2. propagate sigma points through the nonlinear function (compute misfit functionals)
3. calculate mean and covariance of the sigma points and of the propagated sigma points and their cross covariance
4. update mean and compute covariance of the new guess

Related to the FWI problem in this work, the method can be explained as follows: Starting from the current state or mean, which is the current parameter configuration describing the disturbance domain in the numerical model (and which is to be optimized), a set of sigma point vectors is defined. The current state is the first sigma point vector, the other sigma point vectors are parameter vectors distributed around the mean. The distribution is dependent on the covariance of the mean value, which is either calculated in the previous UKF run or, prior to the first run, initialized. Thereupon, each of the sigma points is propagated through the numerical simulation so that for each of the sigma points, a misfit vector is obtained, containing the misfit functionals at each seismic receiver. With the help of these vectors, a mean and covariance of the misfit vectors is computed. On the basis of the mean and covariance of the sigma points, the mean and the covariance of the misfit vectors, and the cross-covariance of sigma points and misfit vectors, a new mean and covariance is calculated – seeking to minimize the misfit at each receiver. This new mean and covariance are utilized for the next Kalman filter run. In order to use the UKF for parameter estimation, a pseudo-dynamic state-space representation is formulated as follows (Attarian *et al.*, 2013):

$$\mathbf{m}_k = \mathbf{m}_{k-1} + \mathbf{w}_{k-1}, \quad (3.7)$$

$$\mathbf{s}_k = \mathbf{s}(\mathbf{m}_k) + \mathbf{v}_k, \quad (3.8)$$

where $\mathbf{m}_k \in \mathbb{R}^n$ is the searched state which is assumed to be a stationary process with process noise $\mathbf{w}_{k-1} \in \mathbb{R}^n$ and where the calculation of $\mathbf{s}(\mathbf{m}_k) \in \mathbb{R}^r$ follows the definition in Eq. 3.5. $\mathbf{v}_k \in \mathbb{R}^r$ includes the summed modeling and measurement uncertainty. Both $\mathbf{v}_k \in \mathbb{R}^r$ and $\mathbf{w}_{k-1} \in \mathbb{R}^n$ are assumed to be drawn from a zero-mean multivariate normal distribution $p(\mathbf{w}_k) \sim \mathcal{N}(0, \mathbf{Q})$ and $p(\mathbf{v}_k) \sim \mathcal{N}(0, \mathbf{R})$. The process noise covariance matrix \mathbf{Q} and the modeling and measurement covariance matrix \mathbf{R} are fixed during Kalman filtering. \mathbf{R} can be understood as a summation of a measurement uncertainty \mathbf{R}^{meas} and a modeling uncertainty $\mathbf{R}^{\text{model}}$ according to $\mathbf{R} = \mathbf{R}^{\text{meas}} + \mathbf{R}^{\text{model}}$ (Tarantola, 2005). With

this quantity, prior knowledge about these uncertainties may be implemented. Matrix \mathbf{Q} is set in order to add an amount of Gaussian noise to the covariance of the parameters and therefore has an impact on the spread of the sigma points during the UKF process. Tuning this matrix, the user can prevent the distances between the sigma points from becoming too small during the inversion process. The tuning of the matrices \mathbf{Q} and \mathbf{R} and the various other parameters is described in Section 3.6. The UKF operates as follows. A set of $2n + 1$ sigma-point vectors $\tilde{\mathbf{m}}_i$ (parameter configurations) is computed:

$$\tilde{\mathbf{m}}_0 = \hat{\mathbf{m}}, \quad (3.9)$$

$$\tilde{\mathbf{m}}_i = \hat{\mathbf{m}} + \left(\sqrt{(n + \kappa) \mathbf{P}^m} \right)_i, \text{ for } i = 1 : n, \quad (3.10)$$

$$\tilde{\mathbf{m}}_{n+i} = \hat{\mathbf{m}} - \left(\sqrt{(n + \kappa) \mathbf{P}^m} \right)_i, \text{ for } i = 1 : n, \quad (3.11)$$

where $\hat{\mathbf{m}}$ is the current state with n model parameters and covariance \mathbf{P}^m . $(\cdot)_i$ is the i -column of the matrix. Cholesky factorization is used to calculate the square root of \mathbf{P}^m . For the first cycle, the quantities are initialized to $\hat{\mathbf{m}} = \mathbf{m}_0$, and $\mathbf{P}^m = \mathbf{P}_0^m$ in the form of a Gaussian distribution $p_0(\mathbf{m}) \sim \mathcal{N}(\mathbf{m}_0, \mathbf{P}_0^m)$. The parameter κ is a scaling factor that has an impact on the spread of the sigma points and can be used to fine tune the higher order moments of the mean and covariance approximation in order to reduce the overall prediction error (Simon, 2006; Julier & Uhlmann, 2004). Its values can be defined by the user where both positive and negative values are explicitly allowed. However, Julier *et al.* (2000, Appendix I) suggest to tune it to $\kappa = 3 - n$ since in this case, the differences between the moments of a normal distribution and the sigma points are minimized up to the fourth moment. Note that if this relation is applied, the respective term $n + \kappa$ in Eq. 3.9 and Eq. 3.13 amounts to 3. Misfit vectors $\tilde{\mathbf{s}}_i$ are calculated by evaluation of Eq. 3.4 at each sigma-point:

$$\tilde{\mathbf{s}}_i = \mathbf{s}(\tilde{\mathbf{m}}_i), \text{ for } i = 0 : 2n, \quad (3.12)$$

so that for each sigma-point, a misfit vector $\tilde{\mathbf{s}}_i \in \mathbb{R}^r$ containing the misfit values at each seismic receiver r is obtained. Each sigma-point is associated with a weight W_i so that the sum of the weights is one:

$$W_0 = \frac{\kappa}{n + \kappa}, W_i = W_{i+n} = \frac{1}{2(n + \kappa)}, \text{ for } i = 1 : n. \quad (3.13)$$

The mean of the misfit is approximated by weighted summation of the misfit vectors:

$$\hat{\mathbf{s}} = \sum_{i=0}^{2n} W_i \tilde{\mathbf{s}}_i. \quad (3.14)$$

The covariance of the parameters \mathbf{P}^m , the covariance of the misfit \mathbf{P}^s and the cross-covariance \mathbf{P}^{ms} between the two covariances is updated as follows:

$$\mathbf{P}^m = \sum_{i=0}^{2n} W_i (\tilde{\mathbf{m}}_i - \hat{\mathbf{m}}) (\tilde{\mathbf{m}}_i - \hat{\mathbf{m}})^t + \mathbf{Q}, \quad (3.15)$$

$$\mathbf{P}^s = \sum_{i=0}^{2n} W_i (\tilde{\mathbf{s}}_i - \hat{\mathbf{s}}) (\tilde{\mathbf{s}}_i - \hat{\mathbf{s}})^t + \mathbf{R}, \quad (3.16)$$

$$\mathbf{P}^{ms} = \sum_{i=0}^{2n} W_i (\tilde{\mathbf{m}}_i - \hat{\mathbf{m}}) (\tilde{\mathbf{s}}_i - \hat{\mathbf{s}})^t. \quad (3.17)$$

The posterior mean $\hat{\mathbf{m}}_+$ and its covariance \mathbf{P}_+^m are calculated as follows:

$$\hat{\mathbf{m}}_+ = \hat{\mathbf{m}} + \mathbf{K} (\mathbf{s}_{\min} - \hat{\mathbf{s}}), \quad (3.18)$$

$$\mathbf{P}_+^m = \mathbf{P}^m - \mathbf{K} \mathbf{P}^s \mathbf{K}^t, \quad (3.19)$$

with the Kalman gain

$$\mathbf{K} = \mathbf{P}^{ms} (\mathbf{P}^s)^{-1}. \quad (3.20)$$

$\mathbf{s}_{\min} - \hat{\mathbf{s}}$ is the innovation term and \mathbf{s}_{\min} is the expected minimum misfit which can be set to zero or tuned as described in Section 3.6. For both of the upcoming methods, the UKF is usually run multiple times with number N_k in each cycle to increase the accuracy of the state estimation.

3.3. Method 1: Unscented hybrid simulated annealing (UHSA)

This section deals with UHSA, which is one of the main FWI methods used in this work. UHSA is introduced and applied to synthetic data by Nguyen & Nestorović (2016). Applications to experimental data follow in Trapp *et al.* (2019), Trapp & Nestorović (2020), and Trapp & Nestorović (2021). UHSA is a global optimization technique, which combines the metaheuristic search algorithm simulated annealing (SA) with the UKF. SA operates as the global search algorithm, while the previously explained UKF serves for local minimization. Kirkpatrick *et al.* (1983) introduce SA into statistical mechanics, whereas the underlying procedure, the Metropolis algorithm, was founded early by Metropolis *et al.* (1953). The algorithm is based on calculating an energy change to decide if the sampled point is accepted or not – or, related to the FWI problem, on calculating a misfit difference in order to decide if the parameter configuration is accepted or not. SA is explained in the context of UHSA directly in order to achieve a better understanding for the overall method. A simplified illustration of the principle of UHSA is shown in Figure 3.1. Firstly, a parametrization of the disturbance domain \mathbf{m} is to be implemented in the numerical model. For instance, if prior knowledge allows the assumption of an occurring boulder with cuboid shape somewhere in the model domain, its parametrization could consist of location coordinates, spatial dimensions, and material properties. A specific parameter configuration then defines the disturbance, for which a numerical model is set up. After performing the corresponding numerical simulation, the output waveforms are used to compute a misfit functional. UHSA seeks to find a parameter configuration which corresponds to the global minimum of the misfit functional (Eq. 3.6). For the inversion examples of this work, the model is remeshed for every new sample. Prior to inversion, the user may either select an initial parameter configuration or set random values. For this configuration, the misfit functional is calculated, expressed by point (1) in Figure 3.1. Thereupon, the UKF is run for a predefined number of cycles in order to reach a parameter configuration with a lower misfit functional (1'). In a next step, SA proposes the next parameter configuration, for which the misfit functional is calculated (2). The further the progress of UHSA, the closer the proposed parameter configuration statistically is to the current parameter configuration (1'), which is the parameter configuration with the minimum misfit found up to that point. The new sample (2) is accepted although the misfit functional is less favorable than the current result. This is one of the key concepts of SA (and therefore also of UHSA), leading to a more intense exploration of the misfit landscape. The probability of acceptance of a worse solution decreases with the progress of

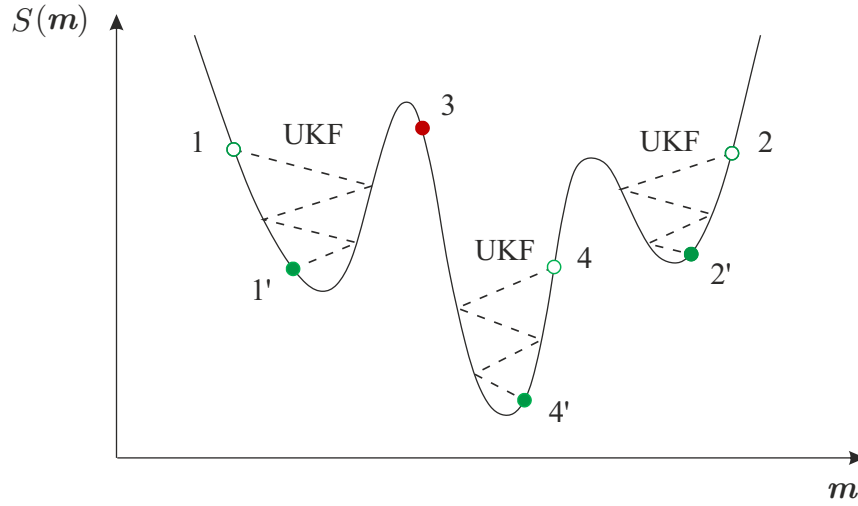


Figure 3.1.: Concept of UHSA illustrated on the example of three cycles. The curve visualizes a misfit functional over possible parameter configurations. The accepted sample and therefore also the initial sample of the UKF is illustrated with the empty green dot, the determined sample after UKF minimization is illustrated with the filled green dot. The red dot visualizes a rejected UHSA cycle.

UHSA as well as with an increasing misfit functional compared to previous average misfit functionals. After local minimization (2'), a next random sample (3) is proposed. In this case, the sample is rejected since the probability of acceptance is lower due to the further progress of UHSA and because the misfit functional is high compared to previous average misfit functionals. The next proposed parameter configuration (4) lies in the global minimum region and due to its comparatively low misfit functional, it is accepted. After UKF minimization, a parameter configuration close to the global minimum is found. Note that in a real UHSA inversion, the number of UHSA cycles is selected much higher. The higher the number of UHSA cycles, the higher the probability a parameter configuration close to the global minimum is found.

The algorithm is constructed as described below, following the description of Nguyen & Nestorović (2016) to large parts. The progress of the inversion is expressed by the so-called annealing temperature. This quantity plays a key role in proposing a parameter configuration as well as in determining a probability of acceptance. In this work, the cooling schedule is selected to be linear as proposed by Blum & Roli (2003):

$$T_c = \zeta T_{c-1}, \quad (3.21)$$

where T_c is the annealing temperature in cycle c and where the cooling parameter $\zeta \in (0, 1)$ is free to tune. However, for the purpose of an intuitive selection of ζ , the annealing temperature in the first cycle T_0 and the annealing temperature in the last cycle T_e are tuned by setting the probability of acceptance for a slightly worse solution in the beginning of UHSA and the probability of acceptance for a slightly worse solution in the end before calculating ζ :

$$T_e = -\frac{1}{\ln(p_e)} \quad (3.22)$$

$$T_0 = -\frac{1}{\ln(p_0)}, \quad (3.23)$$

$$\zeta = (T_e/T_0)^{1/(N_c-1.0)}. \quad (3.24)$$

N_c is the number of UHSA cycles set. As previously mentioned, prior to the first cycle, the user can either set a random sample or select a parameter configuration incorporating prior assumptions. Based on this sample, the UKF conducts a local search for a predefined number of cycles. The following cycles start with a parameter configuration proposal

$$m_{c_i} = m_{\min_i} + y_i (U_i - L_i), \quad (3.25)$$

where m_{\min} is the parameter configuration with the lowest misfit functional (Eq. 3.6) up to the current UHSA cycle. U_i and L_i contain the upper and lower boundaries for the parameter configuration m_{c_i} with $i = 1, \dots, n$, where n is the number of parameters. $y_i \in [-1, 1]$ is the parameter determining how close the proposed parameter configuration is to the current parameter configuration. Based on a proposal by Ingber (1993), it is set to

$$y_i = \text{sgn} \left(u_i - \frac{1}{2} \right) T_c \left[\left(1 + \frac{1}{T_c} \right)^{|2u_i-1|} - 1 \right], \quad (3.26)$$

where $u_i \in [0, 1]$ is the uniform distribution variable. As the current annealing temperature decreases with the progress of UHSA, y_i decreases as well, meaning that (as already referred to above) proposed parameter configurations are statistically closer to the current parameter configuration with increasing progress of UHSA. Eq. 3.25 is repeated until all components of m_c are in between the allowed bounds of U and L . If the misfit of the proposed parameter configuration S_c is smaller than the lowest misfit computed up to that point S_{\min} , the sample is accepted for local minimization with the UKF. Otherwise, a probability of acceptance is calculated similarly to the proposal by Balling (1991)

$$P = \exp \left(-\frac{\Delta S}{\Delta \bar{S} T_c} \right), \quad (3.27)$$

where $\Delta S = S_c - S_{\min}$ is the misfit difference between the proposed move and the parameter configuration with the lowest misfit value up to that point. $\Delta \bar{S}$ is the average of all ΔS

Algorithm 1: UHSA

```

// Initialization
General settings for UHSA:  $m_0, U, L, N_c, p_0, p_e$ 
Settings for the UKF:  $N_k, P_0^m, R, Q, s_{\min}$ 
// run  $N_c$  cycles of SA
for  $j = 1..N_c$  do
    Select random configuration  $m_c$  according to Eq. 3.25
    Calculate acceptance probability  $P$  according to Eq. 3.27
    Compute uniform distribution variable  $u_i \in [0, 1]$ :
    if  $u_i < P$  or  $S_c < S_{\min}$  then
        // Run the UKF for  $N_k$  iterations
        Set initial estimate for the UKF  $\hat{m}_0 = m_c$ 
        for  $k = 1..N_k$  do
            |  $\hat{m}_k, P_k = \text{UKF}(\hat{m}_{k-1}, P_{k-1}, R, Q)$ 
        end
    end
    In the case of an improvement, store new  $m_{\min}$ 
    Lowering temperature  $T_c$ : Eq. 3.21
end

```

computed by then. With the help of the probability of acceptance, it is decided (computing a random variable) if the current parameter configuration is accepted for local minimization with the UKF. If it is accepted, UKF is run for N_k cycles. If not, the next UHSA cycle is started. At the end of every UHSA cycle, the annealing temperature is lowered according to Eq. 3.21. The algorithm is summarized in Algorithm 1. The quantities to be tuned for UHSA are \mathbf{m}_0 , \mathbf{U} , \mathbf{L} , N_c , p_0 , p_e , N_k , \mathbf{P}_0^m , \mathbf{Q} , \mathbf{R} , s_{\min} where the last five parameters correspond to the UKF.

3.4. Method 2: UKF-controlled parametric level-set method (UKF-PaLS)

The second main method to be applied in this work is UKF-PaLS, in which the UKF (see Section 3.2) is combined with the parametric level-set method proposed by Aghasi *et al.* (2011). UKF-PaLS is introduced by Nguyen & Nestorović (2018) with 2D applications to synthetic data and applied to experimental data in Trapp & Nestorović (2021). As already explained in the introduction, the parametric level-set method serves for the parametrization of the disturbance, while the UKF minimizes the misfit function. The parametrization of the disturbance is achieved by the distortion of so-called bumps, which are able to flexibly define the geometry of irregularly shaped objects. The concept of UKF-PaLS is illustrated in Figure 3.2 on a 2D example. The measurements are generated synthetically with the model referred to as the true model. The disturbance is, in this case, a quadratic boulder. The measurements are seismic waveforms resulting from some source-receiver configuration, where an exemplary waveform is illustrated. The user defines the forward model and the centers of the bumps, which are fixed during the inversion (note that, however, a loosening could be a subject of future studies for a gain described in Section 10.4). The centers are illustrated with black dots in the top image referred to as the parametrized model. By defining the placement of the bumps, the user determines the region of investigation as well as the resolution. It is noted that the current method can only work properly, if there is at least one bump placed inside the actual disturbance. Furthermore, the method works better if bumps are not located at the border of the actual disturbance only. Therefore, the distance of the bumps is approximately equivalent to the resolution of the method but should be selected slightly smaller than the desired resolution in order not to miss potential disturbances. The selected number of bumps is proportional to the computational demand. Each bump is distorted by two parameters – α_i and β_i , which are to be initialized prior to inversion. β_i is the decisive factor in controlling the radial size/diameter of the current bump – the higher the value, the larger the radial size. Factor α_i controls the magnitude or direction of the bumps and may be in some sense interpreted as a magnet attracting or repelling the neighboring bumps seen from bump i . The initial model, which is defined by a set of parameters \mathbf{m}_0 , is shown in the bottom left. In this work, the initial level-set parameters are tuned so that small pieces of material are visible. Due to this procedure, a prediction about material properties becomes possible already in the first cycle as well as a prognosis if an appearance of no material, few material or a larger amount of material is probable at a bump. Note that in all of the illustrations of the initial model in this work, the bumps seem to be aligned irregularly with different sizes since the mesh is not discretized in accordance with the locations of the bumps. For UKF inversion, a set of sigma points is computed based on the initial covariance \mathbf{P}_0^m . The sigma points are samples distributed around the initial set of parameters \mathbf{m}_0 . After the computation of the misfit vectors (Eq. 3.5) for the $2n + 1$ sigma points of an iteration, corresponding covariances are computed and an updated mean value (which is

the new guess) and a covariance is determined by the UKF. Starting from that, a new set of sigma points is computed. After a predefined number of iterations, the UKF is stopped. The bottom part of the figure shows the mean estimates after 2, 5 and 23 iterations.

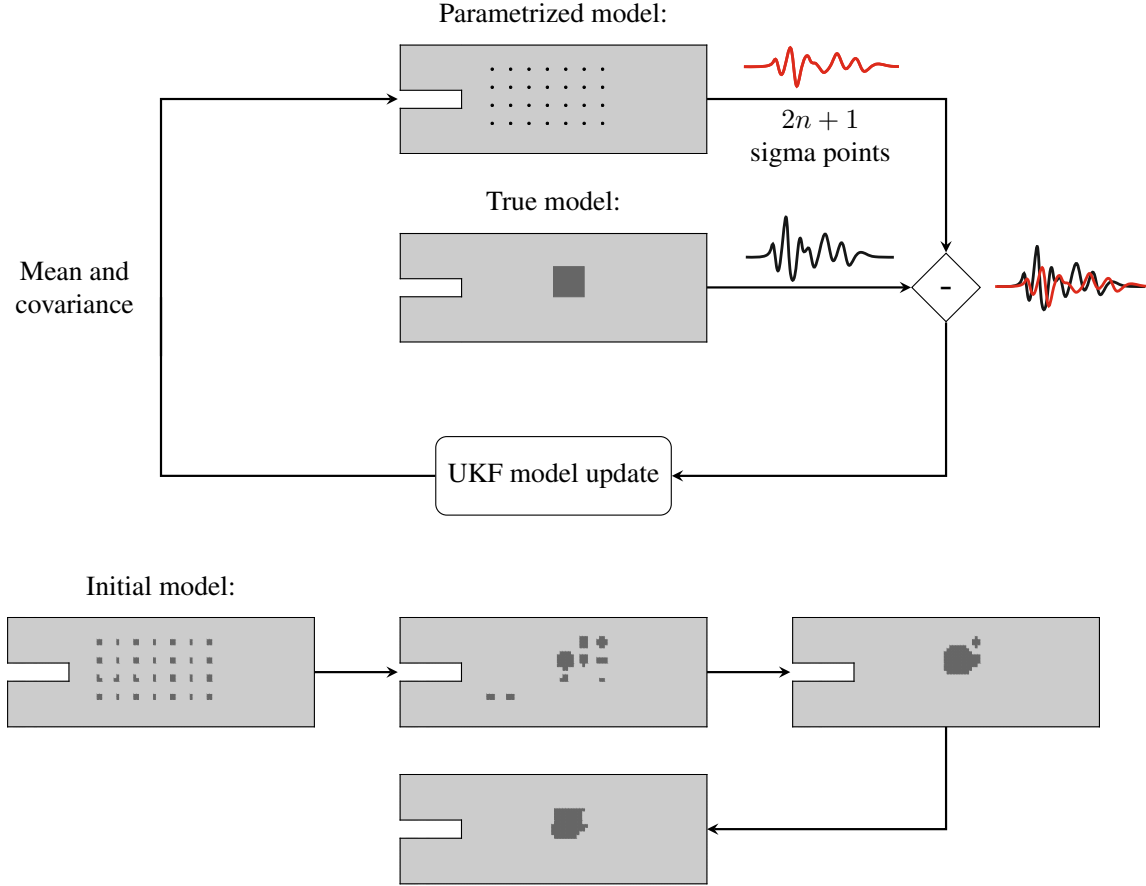


Figure 3.2.: Working principle of UKF-PaLS. Concept at the top, exemplary course of the estimates at the bottom. The UKF updates the model based on the mean and covariance of the sigma points and the corresponding misfits in order to compute a new optimal mean and covariance.

More specifically, UKF-PaLS operates as described below, where the definition to large parts follows the formulation of Nguyen & Nestorović (2018). The user defines the centers

$$\mathbf{x}_{\text{rbf}} = \{\mathbf{x}_1, \mathbf{x}_2, \dots, \mathbf{x}_{N_b}\} \quad (3.28)$$

of a set of N_b bumps, which in the mathematical sense are centers of radial basis functions (RBFs). Vector \mathbf{x}_i in $i \in 1, 2, \dots, N_b$ contains the coordinates of the center of the respective RBF. Since each RBF is controlled by the two parameters α_i and β_i , the parameters to be determined by the UKF-PaLS inversion are

$$\mathbf{m} = \{\alpha_1, \alpha_2, \dots, \alpha_{N_b}, \beta_1, \beta_2, \dots, \beta_{N_b}, \mathcal{X}_d\}, \quad (3.29)$$

where \mathcal{X}_d contains the material properties of the disturbance. Prior to inversion, the parameter vector is initialized. In order to determine if an element obtains background material properties or disturbance material properties, a level-set function $\phi : \Omega \mapsto \mathbb{R}$ is introduced. The function is defined on $\mathbf{x} \in \Omega$, which is the spatial domain of the model, and follows the

definitions of Aghasi *et al.* (2011). The function is written as

$$\phi(\mathbf{x}) = \sum_{i=1}^{N_b} \alpha_i \psi \left(\frac{1}{\beta_i^2} \|\mathbf{x} - \mathbf{x}_i\| \right), \quad (3.30)$$

where \mathbf{x}_i are the centers of the RBFs and $\psi(\cdot)$ is the RBF, which is chosen to be the Wendland's function following Wendland (1995):

$$\psi(r) = \begin{cases} (1-r)^4(4r+1), & \text{if } 0 \leq r \leq 1 \\ 0, & \text{if } r > 1. \end{cases} \quad (3.31)$$

With the help of the previous definitions, a value $\phi(\mathbf{x})$ for each spectral element center is determined. The criterion to decide whether the element has background material properties or disturbance material properties is

$$\begin{cases} \phi(\mathbf{x}) > c, & \forall \mathbf{x} \in D, \\ \phi(\mathbf{x}) = c, & \forall \mathbf{x} \in \partial D, \\ \phi(\mathbf{x}) < c, & \forall \mathbf{x} \in \Omega \setminus D, \end{cases} \quad (3.32)$$

meaning that if the value of the radial basis function for the current element is larger than c , the element belongs to the disturbance domain D , otherwise it obtains background material properties. Parameter c is free to tune but can be set to zero also. In this work, it is tuned so that the level-set parameters of the initial model become slightly greater than zero. The material definition $\mathcal{X}(\mathbf{x})$ for the whole spatial domain Ω is assigned with the help of the Heaviside function $H(\cdot) = 0.5(1 + \text{sign}(\cdot))$

$$\mathcal{X}(\mathbf{x}) = \mathcal{X}_d(\mathbf{x})H(\phi(\mathbf{x}) - c) + \mathcal{X}_b(\mathbf{x})\left(1 - H(\phi(\mathbf{x}) - c)\right), \quad (3.33)$$

where \mathcal{X}_b are the material properties for the background domain. The minimization occurs during a predefined number of UKF cycles N_k . The quantities to be tuned for UKF-PaLS are \mathbf{m}_0 , N_k , \mathbf{P}_0^m , \mathbf{Q} , s_{min} and \mathbf{R} .

Algorithm 2: UKF-PaLS

```
// Initialization
Settings for the UKF:  $\mathbf{m}_0$ ,  $N_k$ ,  $\mathbf{P}_0^m$ ,  $\mathbf{Q}$ ,  $s_{min}$ ,  $\mathbf{R}$ 
Set the centers of the RBFs (bumps) according to Eq. 3.28
Initialize vector  $\mathbf{m}_0$  Eq. 3.29
// run  $N_k$  cycles of UKF
for  $k = 1..N_k$  do
    | For each sigma point, apply Eq. 3.32 and assign material properties
    |  $\hat{\mathbf{m}}_k, \mathbf{P}_k = \text{UKF}(\hat{\mathbf{m}}_{k-1}, \mathbf{P}_{k-1}, \mathbf{R}, \mathbf{Q})$ 
end
```

3.5. The multi-scale approach

In order to prevent the inversion from moving into one of the local minima of the misfit functional, a multi-scale approach is commonly implemented into adjoint FWI methods (Fichtner, 2010; Virieux & Operto, 2009). This approach takes advantage of the circumstance that the complexity of the misfit functional decreases with increasing wavelengths. Incrementally increasing working frequencies during the inversion increase the resolution, where in the first cycles, a rough picture is evolved and in later cycles, further details are imaged. To achieve this, a low-pass filter with a step-wise increasing cutoff frequency is applied to the output data in this work. The method is implemented for UKF-PaLS only since UHSA is a global optimization strategy already, meaning that the optimum will be found anyways for a high number of cycles. Nonetheless, an implementation could also be tested for UHSA since it may decrease the number of necessary forward simulations. The principle of the multi-scale approach is illustrated in Figure 3.3 on the example of three stages, where the idea for the figure is inspired by Fichtner (2010, p. 135).

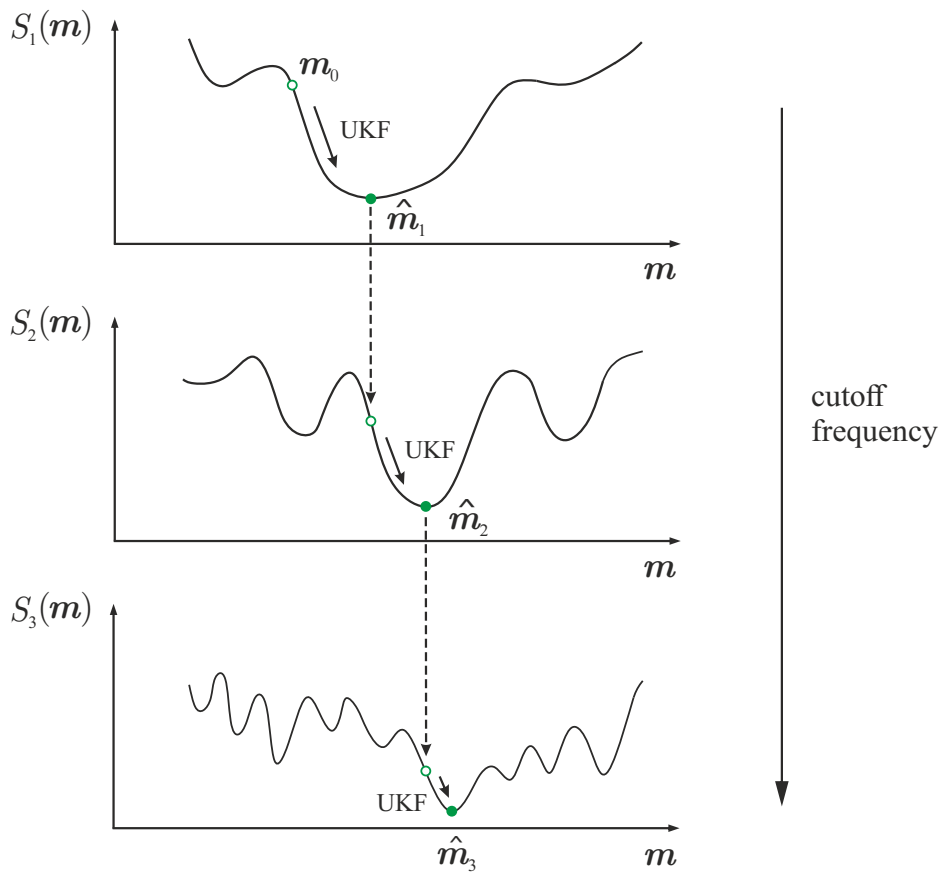


Figure 3.3.: Illustration of the multi-scale approach. The complexity of the misfit functional increases with an increasing cutoff frequency. During each stage, the cutoff frequency is maintained and an optimization is performed with the UKF. The final model is used as the initial model for the next stage. The idea for the figure is inspired by Fichtner (2010, p. 135).

The top part of the figure shows the misfit functional for low resolutions. Since the data are filtered with a low-pass filter with a small cutoff frequency, less and broader local minima are contained in the functional. Starting from the initial model \hat{m}_0 , the UKF seeks to

minimize the misfit functional within a predefined number of cycles and finds a parameter configuration $\hat{\mathbf{m}}_1$. In the next step, the cutoff frequency is increased, leading to narrower and more frequent local minima. Since the parameter configuration from the first stage is used as the initial model for the second stage, the parameter configuration is already on the incline towards the optimum. After UKF minimization, parameter configuration $\hat{\mathbf{m}}_2$ is found. Again, the cutoff frequency is increased (or instead, no low-pass filter is applied), leading to various other narrow local minima in the third stage. However, since the parameter configuration is already corresponding to a misfit functional in the global minimum region, the optimization succeeds.

3.6. Parameter tuning

The parameters to be tuned for the UKF are \mathbf{m}_0 , N_k , \mathbf{P}_0^m , \mathbf{Q} , \mathbf{s}_{\min} and \mathbf{R} . These parameters are to be tuned for both UHSA and UKF-PaLS as both methods include the UKF. N_k is set according to the desired grade of local exploration. It is suggested to increase N_k with the number of inversion parameters since with this number, also the complexity of the inversion problem increases. In UHSA, the UKF is the local minimization scheme only and therefore N_k is usually set lower here than for UKF-PaLS. Commonly used values in this work are for instance $N_k = 4$ for UHSA and $N_k = 25$ for UKF-PaLS. Parameter \mathbf{P}_0^m determines the initial spread of the sigma points. This parameter can be set rather intuitively since this covariance is adapted by the UKF throughout the inversion. Anyways, it should be set so that the sigma points differ significantly, but not overmuch. A higher distance between the sigma points leads to larger jumps during a UKF cycle. A visualization of the spread of the sigma points will be shown in Figure 6.7, where the sigma points are composed of two location coordinates only.

For the adjustment of the best expected result \mathbf{s}_{\min} and the measurement covariance matrix \mathbf{R} in a rather intuitive way, a strategy is developed for the examples in this work. With a precise knowledge of \mathbf{R} , inversion results could be improved. For the small-scale experiments, a general suitable estimation of the measurement covariance is not possible since the quality of measurement is to the largest extent dependent on the reflection behavior of the laser beam at a specific point. However, the following strategy considers this issue of local changes in quality, where the strategy could also be used in field scenarios. A numerical simulation corresponding to an undisturbed specimen (a specimen without a disturbance, obtaining only background material parameters) is conducted. Afterwards, a vector \mathbf{s}_u is determined, containing the misfit values between the experimental data (of the real model) and the simulation data of the undisturbed specimen at each receiver. It is trivial that the misfit functional after inversion should be significantly lower than the sum of the elements of vector \mathbf{s}_u as the model corresponding to \mathbf{s}_u does not incorporate any disturbance. Thus, two optional parameters $a, b \in [0, 1]$ are used to set $\mathbf{s}_{\min} = a\mathbf{s}_u$ and $\mathbf{R} = b\mathbf{s}_u \cdot \mathbf{I}_r$, where $\mathbf{I}_r \in \mathbb{R}^{r \times r}$ is an identity matrix of dimension equal to the number of receivers. With the help of this method, the quality of the measurement at each receiver point is considered, avoiding that too much emphasis is put on low-quality receiver points with a high misfit functional (for instance due to a measurement on a grain). Furthermore, an intuitive tuning is enabled. In order to further adjust the parameters a and b , an option is implemented into the code. The user may select if the code stops in the end of the first UKF cycle in order to enter the two parameters. Depending on the entered values, the code outputs the resulting first sigma

point, to which the algorithm would jump in the next UKF run. The user can then either confirm the entered values or disapprove and enter new values until a reasonable size of the jump is reached. Note that parameter a can also be set to zero, leading to a zero vector for s_u , in which case only the measurement covariance matrix \mathbf{R} is tuned. This method is used in the later progress of the research since a tuning is faster. Note that with the method explained above, a careful fine-tuning is not needed. The methods are tested with many different parameter configurations leading to only slightly changing inversion results. The covariance matrix in the UKF, which is automatically updated, usually manages a convergence to a meaningful minimum. The last parameter to be tuned for the UKF is the process noise covariance matrix \mathbf{Q} . With this matrix, the user can prevent the distances between the sigma points from becoming too small when the misfit functional becomes smaller and thus also prevents the algorithm from converging too slowly. For the examples in this work, the matrix is varied between $0.1 \mathbf{P}_0^m \leq \mathbf{Q} \leq 0.5 \mathbf{P}_0^m$ with a success for all of the applied examples.

The additional parameters to be tuned for UHSA are N_c , p_0 and p_e . N_c should be adjusted depending on the number of inversion parameters and the desired precision. Furthermore, it depends on the difference between the upper and lower borders of the inversion parameters U and L (which need to be set inversion-specific and are based on prior knowledge). If the allowed range of the inversion parameters is rather small, a misfit functional close to the global minimum is likely to be found early – allowing for a smaller value for N_c . Values in this work vary between $15 \leq N_c \leq 200$. With the parameters p_0 and p_e , the user can tune how intense the inversion parameter space is explored. For instance, a configuration of $p_0 = 0.8$ and $p_e = 0.01$ implies a relatively strict annealing scheme, meaning that many parameter configurations are rejected during the course of UHSA. Such a scheme is convenient in the case of a rather small number of inversion parameters or if the allowed range of the inversion parameters is set rather small due to prior knowledge. A rather intense exploration of the parameter space is for example implied by a setting $p_0 = 0.9$ and $p_e = 0.1$, which should be applied if the complexity of the inversion is higher. The initial configuration \mathbf{m}_0 for UHSA can be either set to fixed starting values or to a random configuration. For the reasons already explained, \mathbf{m}_0 for UKF-PaLS is set so that small pieces of material are visible as shown in Figure 3.2. The tuning of the level-set parameters is dependent on parameter c , which however can be set arbitrarily. In this work, it is tuned so that the level-set parameters of the initial model become slightly greater than zero. The examples in this work can be used as reference values for all of the parameters for upcoming scenarios.

4. Small-scale laser experiment

For the purpose of validating the previously explained FWI methods with real data, a small-scale laser experiment is constructed. A validation with experimental laboratory data brings a significant gain compared to a validation with synthetic data since sources of noise as well as measurement errors are naturally included. Furthermore, also modeling errors come into play when building the model. All of these error types also occur in an application in mechanized tunneling, but not in synthetic tests. Self-evidently, the number one way to validate the methods would be an application to in-situ (field) data; however, rich field data is difficult to get since a close cooperation with a tunneling company would have to be required. Creating specimens and generating data in a laboratory is comparatively simple and cheap and enables the possibility to perform inversion scenarios with a broad variety in order to prepare the methods in the best possible way for a later in-situ application.

The laser laboratory enables the realization of ultrasonic experiments, where a laser interferometer enables the contact-free acquisition of waveform displacement data which is utilized for FWI. In order to preserve a similarity to real field scenarios, the idea is to introduce a scaling factor k that reduces the dimension of a field model d_f to a small-scale model d_s in the form of $d_s = k^{-1}d_f$. A reduction of the dimension requires a reduction of the operating wavelengths as well according to $\lambda_s = k^{-1}\lambda_f$ in order to maintain the relations, which implies an increase of operating frequencies $f_s = kf_f$. The scaling factor is thought to have values between about 100 and 500, but is strongly dependent on the selected inversion scenario. An example for the scaling factor is given in Section 8.1, which treats the scenario closest to a field scenario in this work.

4.1. Setup

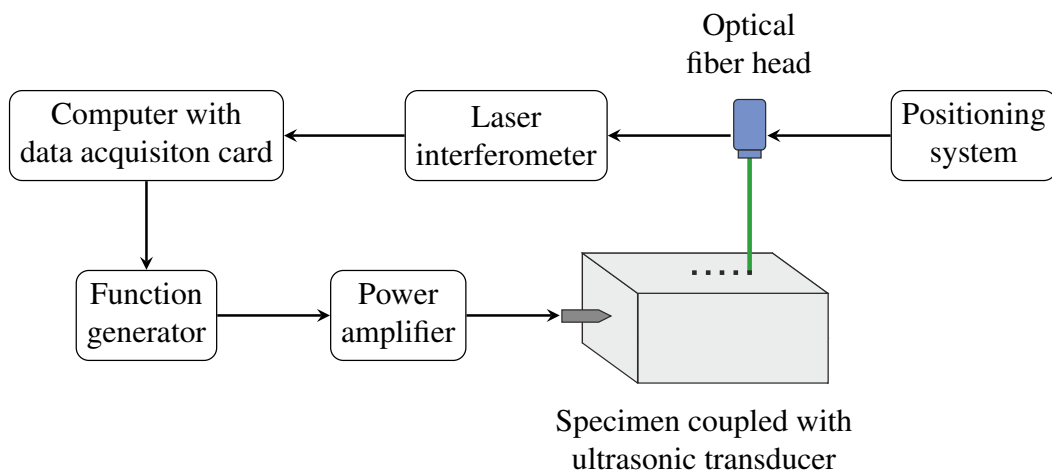


Figure 4.1.: Measurement chain of the small-scale experiment

The flow of a measurement scenario is sketched in Figure 4.1. The starting point of the investigation is a computer, where the source input signal is specified. The input signal is sent to the function generator that transforms the discrete function into an electrical signal. This signal is sent to a power amplifier before it arrives at the ultrasonic transducer where it is transformed into a mechanical waveform. Thereby, the transducer applies a force on the specimen and seismic waves are released that propagate inside the specimen and interact with potential anomalies and boundaries. The laser interferometer records the seismic responses contactless at predefined locations within the desired time window, where a positioning system enables to move the optical fiber head of the interferometer along predefined lines or areas. Measurements are recorded sequentially, meaning that for every record of a seismic response, a new signal is excited. The interferometer signal is forwarded to the computer for the purpose of data acquisition. The whole setup is placed on an optical table in order to decouple the experiment from vibrational influences from the environment. A picture of the experiment with a labeling of the single components is shown in Figure 4.2.

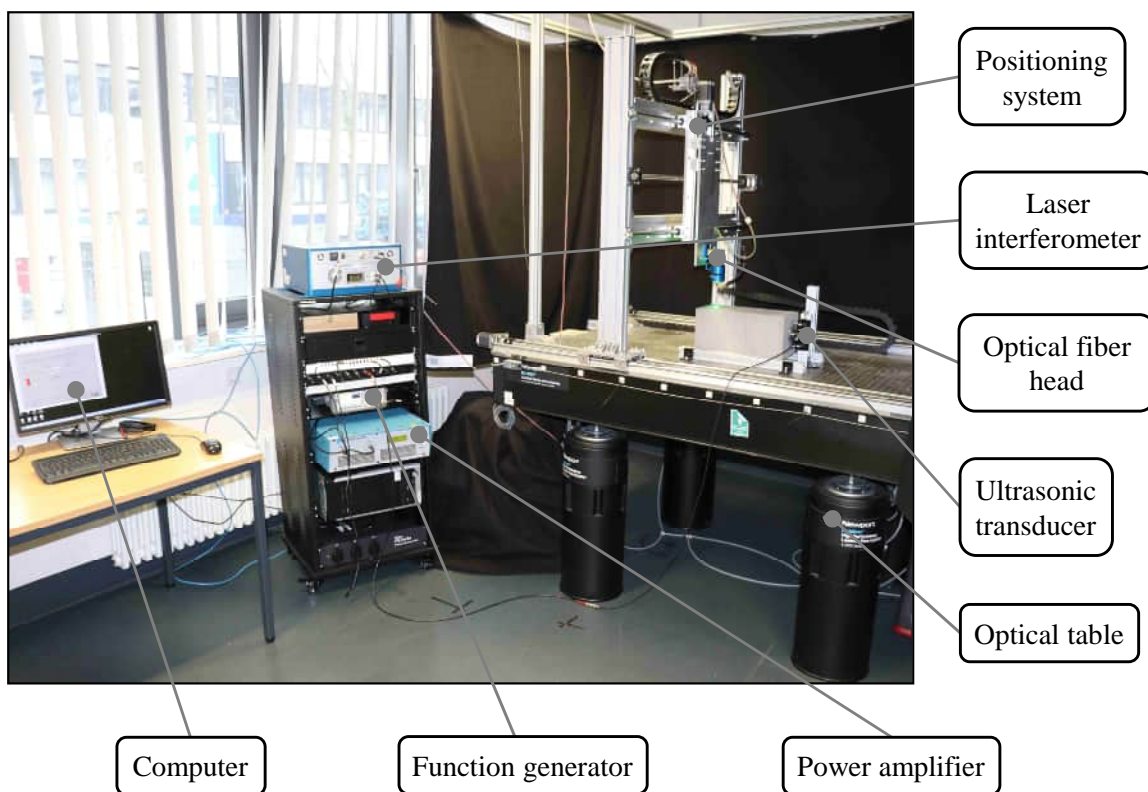


Figure 4.2.: Picture of the setup with its components

The technical components of the system are

- Laser interferometer: BNT-QUARTET-500 linear by Bossa Nova Technologies, frequency range 50 kHz - 50 MHz, measurements of displacements in the sub-nanometer range
- Ultrasonic transducers: Various transducers in a frequency range of 50 kHz - 2 MHz manufactured by Karl Deutsch, General Electrics and Olympus.
- Optical table: Newport M-RS2000-46-8

- Power amplifier: Electronics & Innovation 1040L
- Function generator: Keysight 33500
- Acquisition hardware: National instruments PCI-5922
- user interface built with MATLAB (MATLAB, 2019)

4.2. Ultrasonic transducers

In the following, the two ultrasonic senders which are utilized during the progress of this work are presented. The first one is transducer B 0.1NN manufactured by GE Measurement & Control Solutions (Figure 4.3a, left). This transducer is tapered at its end and therefore transmits the applied force almost pointwise. The nominal frequency is indicated with 100 kHz. The second transducer is transducer S 24 HB 0.2-0.6 manufactured by Karl Deutsch (Figure 4.3b, left). This sender shows a circular contact face of about 28 mm di-

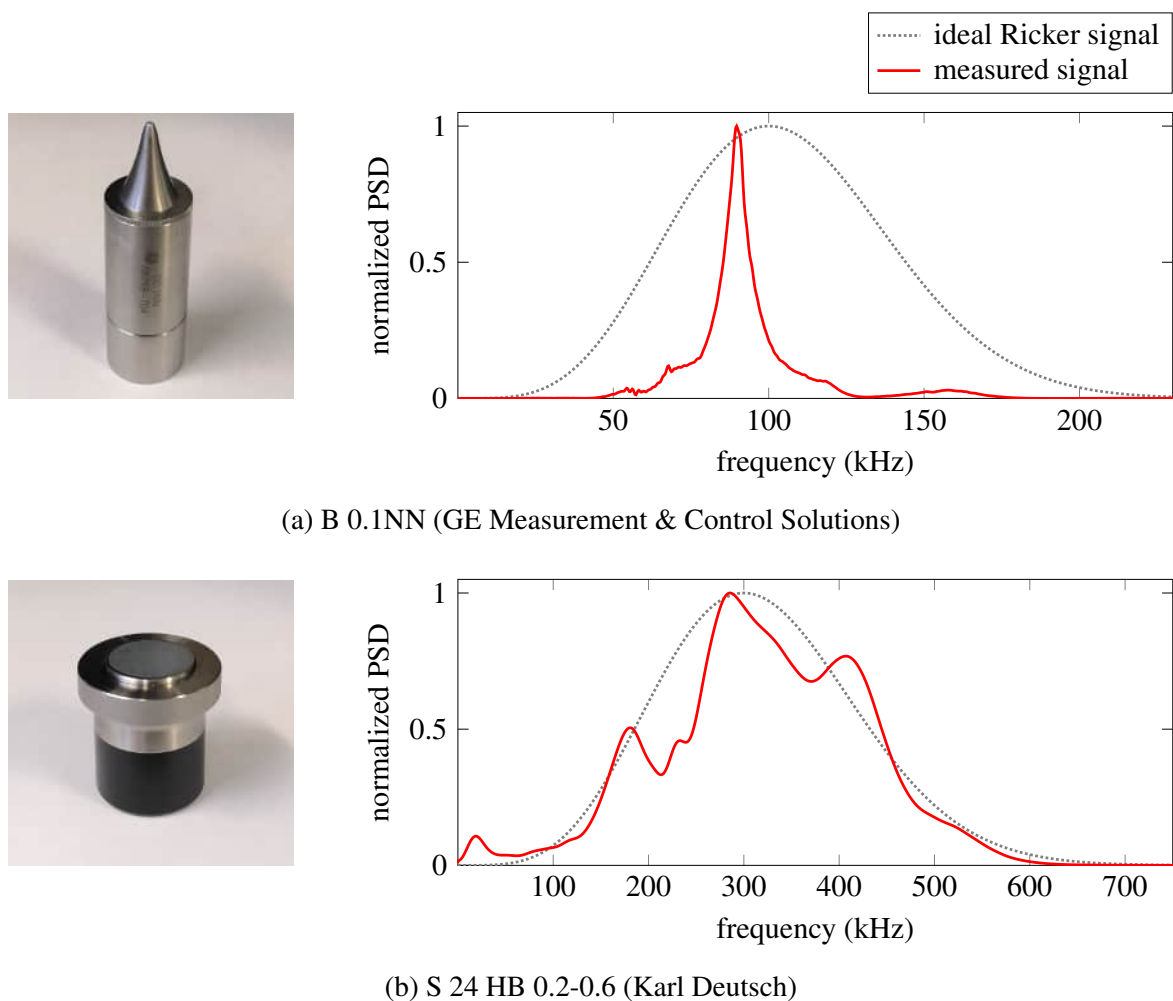


Figure 4.3.: Power spectral densities (PSD) of the ideal Ricker signals and the measured signal responses of the ultrasonic transducers. The PSDs are normalized with their maximum value.

ameter with a nominal frequency range of 200 - 600 kHz. For the upcoming experiments, a characterization of the oscillation behavior in dependency of frequencies is crucial in order to choose a source function. In seismics, Ricker signals are frequently used since these signals excite a broad frequency range. Therefore, the transducers' signal responses to Ricker signals are to be recorded and investigated in the following. For the first transducer, a Ricker with 100 kHz central frequency is utilized, while for the second transducer, a 300 kHz Ricker is used. The laser is positioned so that it points at the contact face of the corresponding transducer. Accordingly, for the first transducer, the laser beam is pointed directly at the vertex of the cone (peak). For the second transducer, the beam is directed at the contact face, where 15 measurements are acquired along a line distributed over the diameter of the face. At every point of measurement, 100 single responses to the source input signal are recorded and stacked in order to increase the signal-to-noise ratio. For the resulting signals as well as for the respective ideal Ricker signals, the power spectral densities (PSD) are computed, where the ones acquired at the flat transducer are averaged. The PSDs are normalized with their maxima in order to achieve an illustrative comparison (Figure 4.3a, right and Figure 4.3b, right). It is observed that the tapered transducer has a highly narrow frequency range with a peak at around 90 kHz, which shows that a Ricker signal may not be the optimum input signal for this sender since the output function differs distinctly from the input function. Therefore, a signal with a more narrow frequency range – a tone burst signal – will be applied when using this transducer. The narrow frequency range may be seen as a disadvantage of the transducer since it increases the difficulty of the FWI due to less occurring working frequencies. An advantage of the transducer is the tapered end, which makes the numerical modeling more trivial. The second transducer shows a more broad frequency range, covering nearly all of the frequencies of the input function. In the lower frequency region below 50 kHz some unwanted frequencies occur, which can be eliminated with a high-pass filter. The broad frequency range is the advantage of this transducer. The disadvantage is the flat contact face increasing the modeling complexity. For both transducers, it is observed that the shapes of the PSDs differ distinctly from the ideal Ricker PSD shapes, which illustrates the importance of an adequate source function estimation if the transducer is coupled to a structure.

4.3. Laser signal response

A key factor for the evaluation of the small-scale experiment is the repeatability of the seismic measurements. Repeatability is the degree of the agreement of successively taken measurements acquired under identical conditions. A measure for the similarity of two seismic signals is the normalized correlation coefficient, for instance described by Ohm & Lüke (2015, p. 205) as follows:

$$r_{1,2} = \frac{\int_{-\infty}^{\infty} d_1(t)d_2(t) dt}{\sqrt{E_{d_1}E_{d_2}}}, \quad (4.1)$$

where $d_1(t)$ and $d_2(t)$ are two seismic signals with energies E_{d_1} and E_{d_2} according to

$$E_{d_i} = \int_{-\infty}^{\infty} d_i^2(t) dt, i \in \{1, 2\}. \quad (4.2)$$

The coefficient expresses the similarity between $d_1(t)$ and $d_2(t)$ by a value smaller than 1. A value of 1 results in the case of perfect agreement $d_1(t) = d_2(t)$ or, due to the normalization with the energies, if the two signals differ in a factor k according to $d_1(t) = k \cdot d_2(t)$, $k \in \mathbb{R}^{>0}$. In the case of negative correlation $d_1(t) = -k \cdot d_2(t)$, $k \in \mathbb{R}^{>0}$, the coefficient becomes -1 . The value becomes 0 if the numerator in Eq. 4.1 becomes 0, which is the case if the two signals are orthogonal. For orthogonal signals, there is no linear dependence, resulting in the largest possible dissimilarity.

An important measure for the quality of a measurement is the signal-to-noise ratio (SNR), which describes the ratio between the signal power P_{signal} and the background noise power P_{noise} according to:

$$\text{SNR} = \frac{P_{\text{signal}}}{P_{\text{noise}}}, \quad (4.3)$$

or, in logarithmic decibel scale:

$$\text{SNR}_{\text{dB}} = 10 \log_{10} \left(\frac{P_{\text{signal}}}{P_{\text{noise}}} \right). \quad (4.4)$$

There are two main actions taken in this work in order to secure a high grade of repeatability – firstly, the stacking of measurements at receiver points and secondly, the application of a reflector. The stacking of measurements is necessary due to a high amount of random noise in single measurements. This is illustrated in Figure 4.4a, where two successively acquired measurements are compared, which are acquired with the laser interferometer pointing directly at a concrete surface within a setup which will be described in the next section. Figure 4.4b shows two measurement sets with $n_{\text{stack}} = 500$ stacked single measurements each. It is observed that the single measurements contain a noticeable level of noise in terms of both low- and high-frequency noise. The waveforms until $1.5 \cdot 10^{-4}$ s, which are clearly visible in Figure 4.4b, cannot be observed in Figure 4.4a as they fully disappear in noise. The stacking of the measurements naturally removes most of the noise contained in the seismic records and makes these waveforms visible. As a consequence, the two signals in Figure 4.4b show a high degree of accordance.

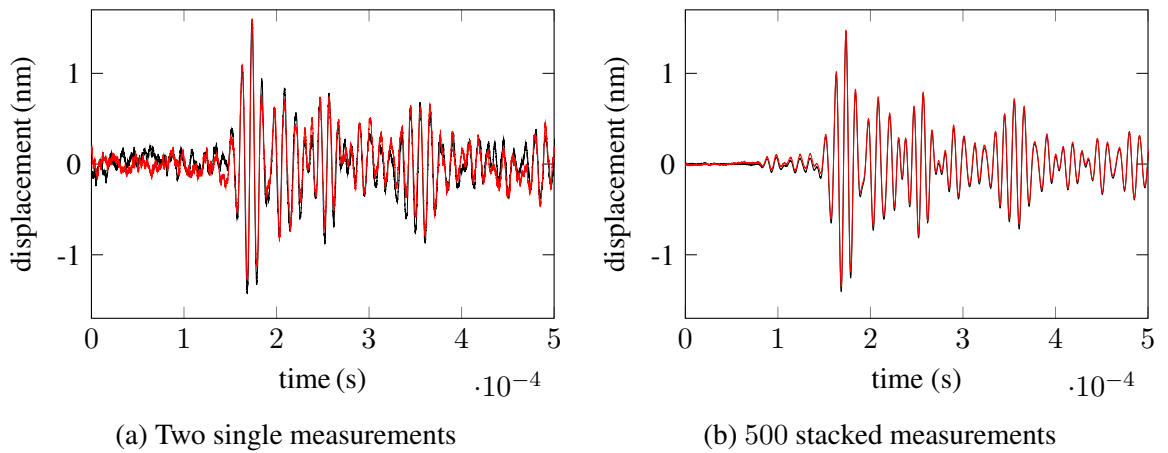


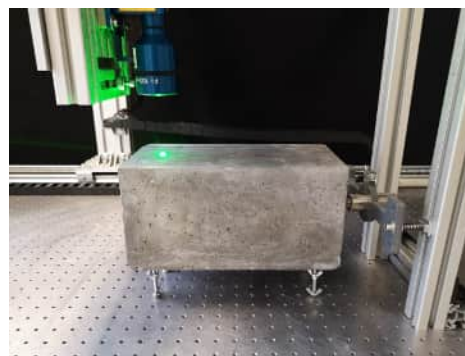
Figure 4.4.: Comparison of two successively taken measurement sets acquired on a concrete surface

In order to further improve the repeatability, a reflector is applied if measuring on porous, sandy or uneven surfaces, where the reflection of the laser beam is weak. Its attachment

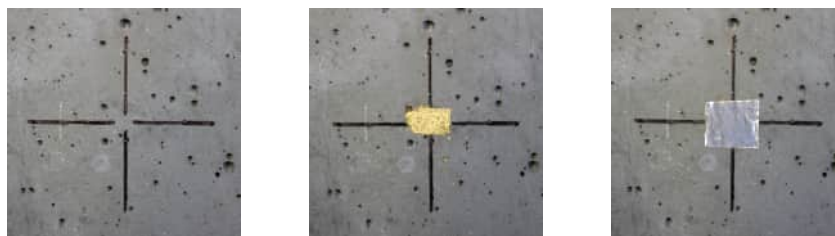
reduces the number of necessary stacked measurements until a satisfying measurement is reached since the reflection of the laser beam is substantially improved. In the experiment conducted in Chapter 7, leaf gold is applied to the surfaces of the concrete plates. This is done by grinding the surface and subsequently applying a water-based gilding size in order to secure the adhesion of the gold at the surface before the leaf gold itself is applied. In the further progress of research, aluminum tape is found to be more practicable and is thus used for the experiment conducted in Chapter 8. The advantages in applying aluminum tape instead of leaf gold are a faster attachment and a better performance if e.g. measuring on sand grains, where the first method may provide erroneous records. Furthermore, the SNR becomes substantially larger, which is to be shown in the next sections. In Section 4.3.1, the usage of the reflectors applied to concrete is validated. In Section 4.3.2, the repeatability and the SNR of all of the three reflection cases are analyzed for a specific experimental setup.

4.3.1. Validation of reflectors

Before making use of a reflector, it is necessary to investigate if the additional layer may alter the seismic records. The thickness of the leaf gold is $0.1\ \mu\text{m}$; however, there is a dried gilding size below with unknown and varying thickness. The thickness of the aluminum tape, which also has an adhesive at its bottom, is $50\ \mu\text{m}$. Since the wavelengths in the small-scale experiments conducted in this work all lie in the millimeter to centimeter range, the impacts of the additional layers are already expected to be low as they are distinctly smaller. In order to test this issue in the form of a comparison of each of the three cases (direct, leaf gold, aluminum tape), an experiment is constructed, which is shown in Figure 4.5. Note that descriptions concerning transducer holdings and bearings are to be given later on.



(a) Experimental setup



(b) Reflectors from left to right: no reflector (direct); leaf gold, aluminum tape

Figure 4.5.: Experiment for the investigation of the impact of the reflectors

The investigated specimen is a concrete block. The ultrasonic transducer B 0.1NN (see Section 4.2) is placed in the middle of one of the smaller surfaces of the specimen and

triggers a signal induced by a source function in the form of a 3.5-cycle Hanning windowed tone burst signal with a central frequency of 100 kHz. The laser measures at one location at the top surface of the specimen as shown in Figure 4.5a with the three different reflectors as shown in Figure 4.5b. In the first case, the measurement is acquired directly at the specimen. In the second case, leaf gold is applied to the same location and in the third case, aluminum tape is attached. For each of the three cases, two measurement sets are acquired with $n_{\text{stack}} = 500$ stacked measurements each for a duration of $5 \cdot 10^{-4}$ s. With these sets, it is tested if the attachment of a reflector is valid. Figure 4.6 shows a measurement set for each type of reflector.

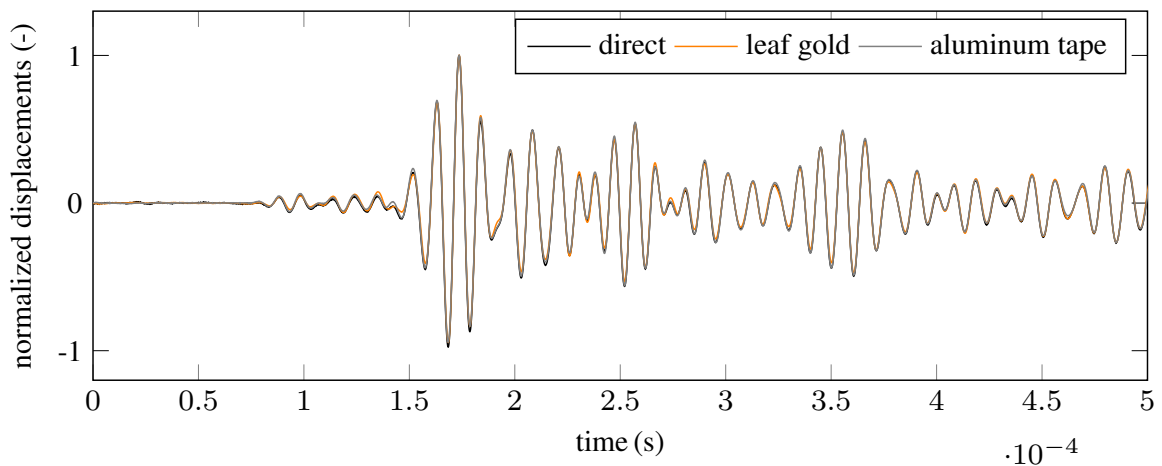


Figure 4.6.: Comparison of the waveforms resulting from 500 stacked single measurements for the three different reflector cases. The measurements are normalized with their maxima.

As the measurement sets differ slightly in amplitudes due to the different grades of reflection, the amplitudes are normalized with their maxima. A first observation of the figure shows a high degree of accordance between the waveforms. Slight differences may be observed in amplitude relations only. For an evidence of this observation, normalized correlation coefficients are computed according to Eq. 4.1 between the direct measurement sets and between the direct and leaf gold/aluminum measurement sets, respectively. The average correlation coefficients are shown in Table 4.1.

	average correlation coefficient		
n_{stack}	direct/direct	gold/direct	aluminum/direct
500	0.9961	0.9976	0.9982

Table 4.1.: Correlation coefficients for pairs of measurement sets with 500 stacked measurements

The results show a high correlation coefficient for each of the three cases. The decisive factor for judging the attachment of a reflector to be valid is that the correlation coefficients for gold/direct and for aluminum/direct are in the same region as the coefficient for direct/direct. In this case, these coefficients are even higher, showing that the measurement sets with reflectors correlate even more with the direct measurement sets than the direct measurement sets correlate with other direct measurement sets. This is due to the lower level of noise induced by a better reflection. Even after the stacking of 500 single measurements, the noise is still prominent in the direct measurement. Based on the investigations of this section, the attachment of both reflectors is judged to be valid.

4.3.2. Repeatability and signal-to-noise ratio

Based on the prior findings, the question arises how many stacked measurements are needed in order to obtain a satisfying signal for each of the three reflection cases. The repeatability of measurements can be quantified with the correlation coefficient of successively taken measurement sets, while the quality of the measurement may be judged with the SNR. It is noted that the following investigations are exemplary, meaning that for every experimental setup, the number of necessary measurements needs to be judged again since the signal quality is strongly dependent on the utilized transducer, applied frequencies and the material and size of the specimen. A judgment may be performed by acquiring sets of measurements at various points at the specimen and investigating after which number of stacked measurements the waveform does not change severely anymore. A high number of stacked measurements is always desirable; however, a compromise between time of measurement and signal quality needs to be found. For an exemplary investigation of correlation coefficients and SNRs, the experiment of Section 4.3.1 is repeated acquiring $n_{\text{total}} = 5000$ single measurements for each reflector with a duration of 2 ms. The source signal is excited after 1 ms, so that the period until about 1 ms contains noise only which will be relevant for the computation of the SNR.

In the first step, average correlation coefficients between successively acquired measurement sets are to be determined (according to Eq. 4.1) with relation to the number of stacked measurements n_{stack} . Therefore, for $1 \leq n_{\text{stack}} \leq 1000$, measurements are separated into the maximum possible number of groups of n_{stack} single measurements $n_{\text{groups}} = \lfloor n_{\text{total}}/n_{\text{stack}} \rfloor = \lfloor 5000/n_{\text{stack}} \rfloor$, where $\lfloor \xi \rfloor$ denotes the floor of ξ . For instance, 2500 groups with 2 single waveforms each are set up for $n_{\text{stack}} = 2$, while 5 groups with 1000 waveforms each are set up for $n_{\text{stack}} = 1000$. In each of the groups, the measurements are stacked so that one waveform is obtained. Finally, correlation coefficients between the waveforms of the groups are computed and averaged. For their computation, only the second half of the waveform is utilized (since the first half includes, as stated above, only noise). Figure 4.7 shows the curves of the resulting average correlation coefficients for $1 \leq n_{\text{stack}} \leq 200$ as well as the measurement time (defined as the time from the first signal release on the computer until final signal saving), which is linearly increasing and lasts about 98 s for 200

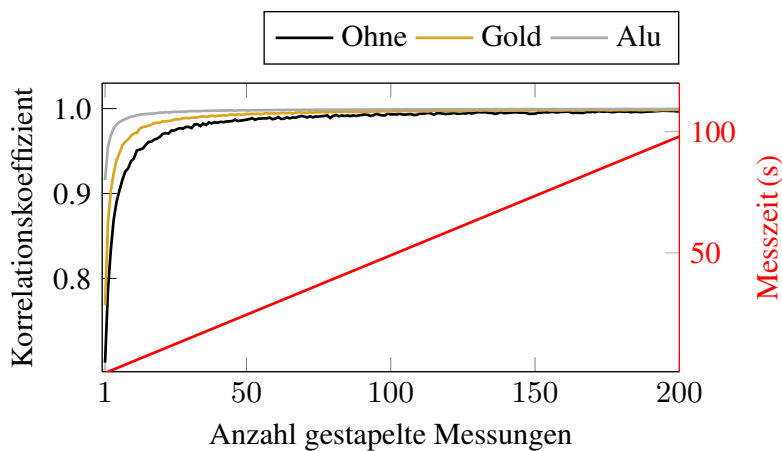


Figure 4.7.: Average correlation coefficients dependent on the number of stacked measurements n_{stack} for each of the three reflectors. The red curve shows the measurement time, which is linearly increasing.

acquired single measurements. It is observed that the values of the average correlation coefficients for each of the three reflectors converge quickly towards 1, whereas, however, the curve corresponding to aluminum converges much faster than the curve for gold, and the curve for gold converges faster than the curve corresponding to the direct measurement. The average correlation coefficients for various values of n_{stack} are given in Table 4.2. It is observed that the correlation coefficient for one single measurement acquired on aluminum tape is higher than after multiple measurements acquired on gold or concrete.

n_{stack}	corr			SNR (-)			SNR (dB)		
	direct	gold	alu	direct	gold	alu	direct	gold	alu
1	0.70	0.7681	0.9159	11.3	10.9	68	10.6	10.4	18.3
2	0.7863	0.8654	0.9549	15	18	108	11.8	12.6	20.3
5	0.8905	0.9393	0.9812	26	40	223	14.2	16.0	23.5
10	0.9381	0.9680	0.9903	46	76	407	16.6	18.8	26.1
20	0.9668	0.9834	0.9954	81	148	781	19.1	21.7	28.9
50	0.9869	0.9937	0.9979	194	370	1805	22.9	25.7	32.6
100	0.9930	0.9968	0.9989	373	716	4322	25.7	28.6	36.4
150	0.9940	0.998	0.9994	571	981	5700	27.6	29.9	37.6
200	0.9967	0.9985	0.9995	752	1397	8170	28.8	31.5	39.1
1000	0.9991	0.9994	0.9998	3724	6582	25903	35.7	38.2	44.1

Table 4.2.: Average correlation coefficients and signal-to-noise ratios for various values of the number of stacked measurements n_{stack} .

A similar procedure as explained above is conducted in order to determine the SNR dependent on the number of stacked measurements. For $1 \leq n_{\text{stack}} \leq 1000$, measurements are again separated into the maximum possible number of groups $n_{\text{groups}} = \lfloor 5000/n_{\text{stack}} \rfloor$. In each of the groups, the waveforms are stacked and corresponding SNRs are computed according to Eq. 4.3 and Eq. 4.4, respectively. For the determination of P_{noise} , the first half of the signal is used while for the determination of P_{signal} , the second half of the signal is used. Finally, the SNRs of all groups corresponding to a value of n_{stack} are averaged. Figure 4.8 shows the SNRs for each of the three reflectors. The top illustration shows the dimensionless SNR, the bottom illustration shows the SNR converted into decibel. Based on the data points which are visible in the right figures, fitting curves are computed. For the dimensionless illustration, a polynomial of degree two is used to fit the data and for the decibel illustration, a two-term power series of shape $an_{\text{stack}}^b + c$ is utilized. The right sides of the figure show the SNRs for $1 \leq n_{\text{stack}} \leq 1000$ with the data points and the fitting curves, the left sides show zoom-ins to $1 \leq n_{\text{stack}} \leq 200$ with the fitting curves only. Values for the SNRs for various values of n_{stack} are given in Table 4.2. Note that the SNR of a single direct measurement ($n_{\text{stack}} = 1$) is slightly higher than the SNR of the single measurement on gold. This is probably due to few outliers in the gold measurement set. The results show that the usage of gold as a reflector can almost double the SNR compared to the SNR of the direct measurement. The usage of aluminum tape can almost increase the SNR tenfold.

The results of this section show that the usage of aluminum tape is desirable if measuring on concrete since it increases both the repeatability and the SNR drastically. However, it is shown that also the layer of gold is advantageous compared to a direct measurement. In this work, around $n_{\text{stack}} = 100$ measurements will be acquired for both reflectors since with this

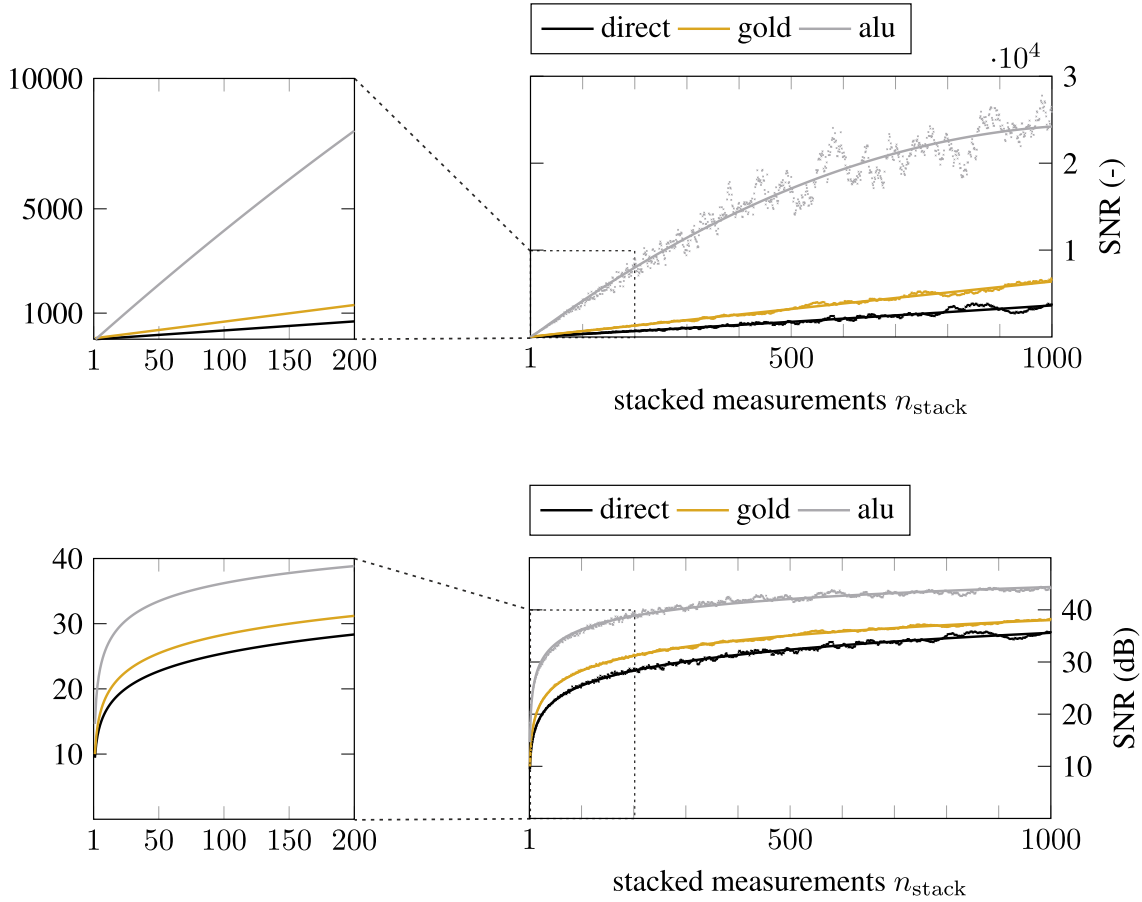


Figure 4.8.: Signal-to-noise ratios of the three reflector cases with single data points and fitting curves. The bottom illustration is in decibel.

value, a good compromise between signal quality and time of measurement is achieved. For the example in this section, $n_{\text{stack}} = 100$ brings a correlation coefficient of 0.9968 for gold and a value of 0.9989 for aluminum and a SNR of 716 (28.6 db) for gold and 4322 (36.4 db) for aluminum (see Table 4.2), which can be evaluated to be satisfyingly high. The time of measurement for one receiver point with $n_{\text{stack}} = 100$ amounts to 49 s, where however the acquired signal is comparatively long.

4.3.3. Noise

The optical table is incorporated into the system in order to reduce seismic noise. It decouples the experiment from vibrational influences of the environment, for instance induced by human activities and machines or electronics inside the room and building. However, there are still numerous sources of noise that may be contained in the seismic signal, for example induced by the electronics on the table, vibrations caused by air, or polluted air worsening the reflection of the laser beam. The characteristics of the seismic noise included in the system is to be analyzed with the noise measurement data acquired in the previous section. Since the investigations in Section 4.3 induce a suggestion of about 100 stacked single measurements if measuring on concrete, also this value is used for the investigation of the seismic noise. Thus, one waveform composed of $n_{\text{stack}} = 100$ single measurements

of noise is created for each reflector. For each of the waveforms, the PSD (dB) is computed, which is shown in Figure 4.9a. Here, it is directly observed that the reflectors can reduce noise. Between 40 kHz and 800 kHz, a relatively flat spectrum of the spectral amplitude is observed, with the tendency to increase slightly moving to lower frequencies. Below about 40 kHz, there is a sudden increase for all of the three reflectors. The source of this is unknown; anyways it may not be expected to contaminate the signals to a high amount since the SNR was shown to become satisfyingly high making use of a reflector and multiple single measurements in Section 4.3. However, the noises will be further reduced by the application of bandpass filters. Figure 4.9b shows the statistical distribution of the amplitude in the form of a probability density (integral sums to 1). The shape of the probability densities show similarities to centered Gaussians, which indicates that the distribution of the noise approximately is of Gaussian random nature with zero mean. The shapes nicely show that the reflectors, especially the aluminum tape, decrease the noise massively since the histogram becomes more narrow.

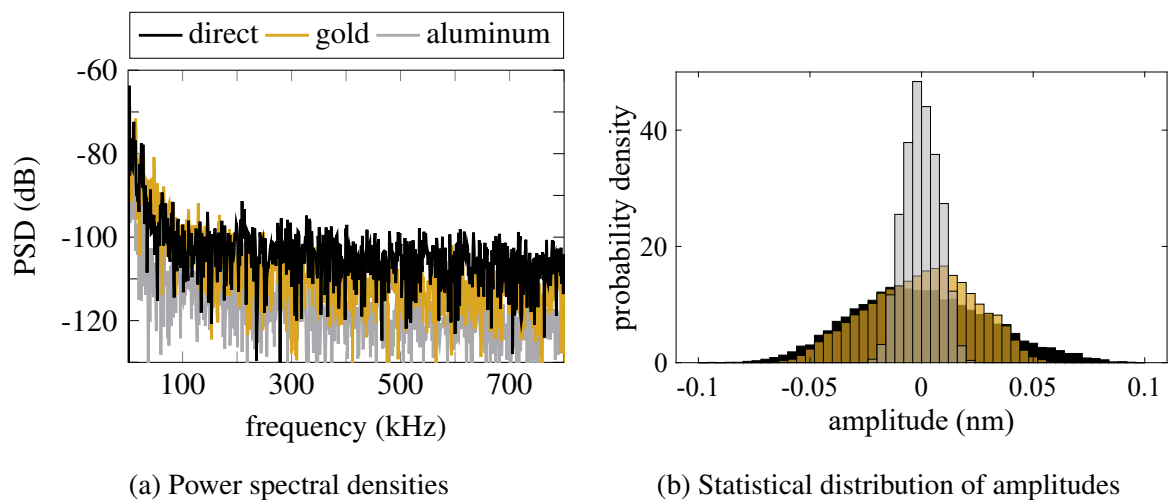


Figure 4.9.: Characteristics of the seismic noise for the three reflection cases computed with a signal containing 100 stacked single measurements.

5. Synthetic inversion scenarios in 2D and 3D

In this chapter, UKF-PaLS is applied to synthetic 2D and 3D examples. The reference model for each of the scenarios is created with an exact definition of the borders of the disturbance and not with the PaLS parametrization. This is necessary in order to avoid *inverse crime*, which would occur if the synthetic reference data were generated with a model comprising the same conditions as the forward model used for inversion (Colton *et al.*, 1998). Inverse crime is to be avoided in order to provide a validation of the methods. Note that as a consequence of the exact definition of borders, a zero misfit will not be possible since a different mesh is utilized during inversion. Preliminary investigations show that the implementation of the multi-scale approach brings remarkable improvements concerning the ability of UKF-PaLS to converge to a physically meaningful minimum of the misfit functional. Other essential novelties include the parameter tuning and the parallelization of the simulations during one iteration. After considering 2D examples, the algorithm is extended to 3D and applied to 3D synthetic examples.

5.1. UKF-PaLS in 2D

5.1.1. Generation of seismic measurements

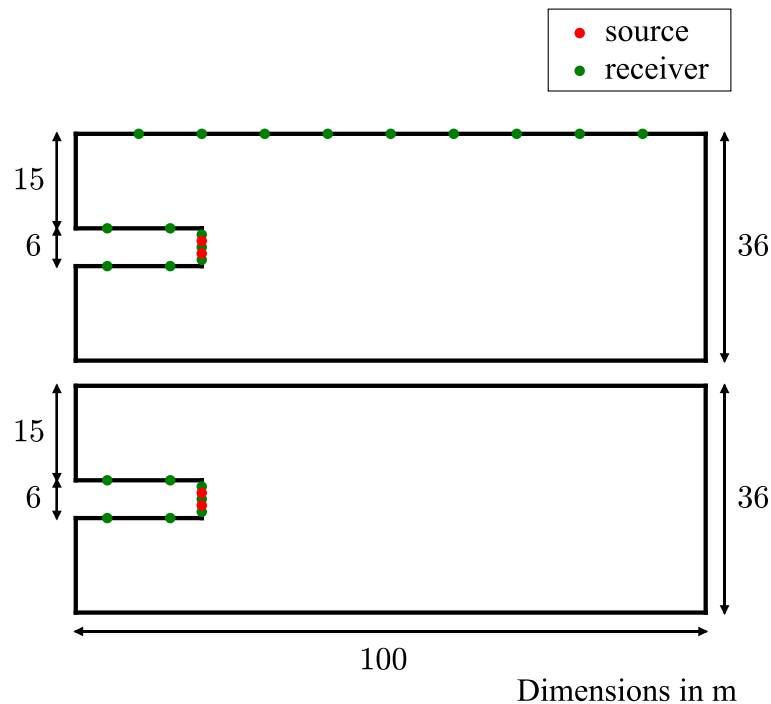


Figure 5.1.: Model dimensions and source-receiver configurations for the 2D synthetic tests. Top: Configuration 1. Bottom: Configuration 2.

Two different source-receiver configurations are utilized for the application of the synthetic 2D examples (see Figure 5.1). The first configuration consists of 2 sources and 16 receivers, where 9 of the seismic receivers are placed at the Earth's surface, 4 are placed at the tunnel walls and 3 are placed at the tunnel front. The second source-receiver configuration contains only the receivers inside the tunnel but is apart from that equal to the first configuration. The source function for all of the seismic sources is a Ricker wavelet with a central frequency of $f_c = 300$ Hz. The lower source transmits a force in excavation direction, the upper source points in top direction in order to increase the shear wave content in excavation direction. The overall model has a length of 100 m and a height of 36 m with a tunnel of 6 m height, 20 m length and 15 m overburden. The model boundaries are set as explained in Section 2.2 considering shallow tunnels. The background velocities are set to $v_{p,b} = 4000 \frac{\text{m}}{\text{s}}$, $v_{s,b} = 2400 \frac{\text{m}}{\text{s}}$ and $\rho_b = 2500 \frac{\text{kg}}{\text{m}^3}$, where the Poisson's ratio amounts to $\nu_b = 0.21875$ according to Eq. 2.9. The material is considered to be elastic with no attenuation in order to save computational power. For the generation of the measurements, 5 different models are set up, which can be observed in Figure 5.2. Note that in this example, the density is considered to be constant all over the model domain. In a real tunneling surrounding, the density of the disturbance may be an additional material property to be determined. However, if the density values can be expected to be close to each other, the influence of varying densities can probably be neglected, which will also be done for the experimental examples in Chapter 7 and Chapter 8.

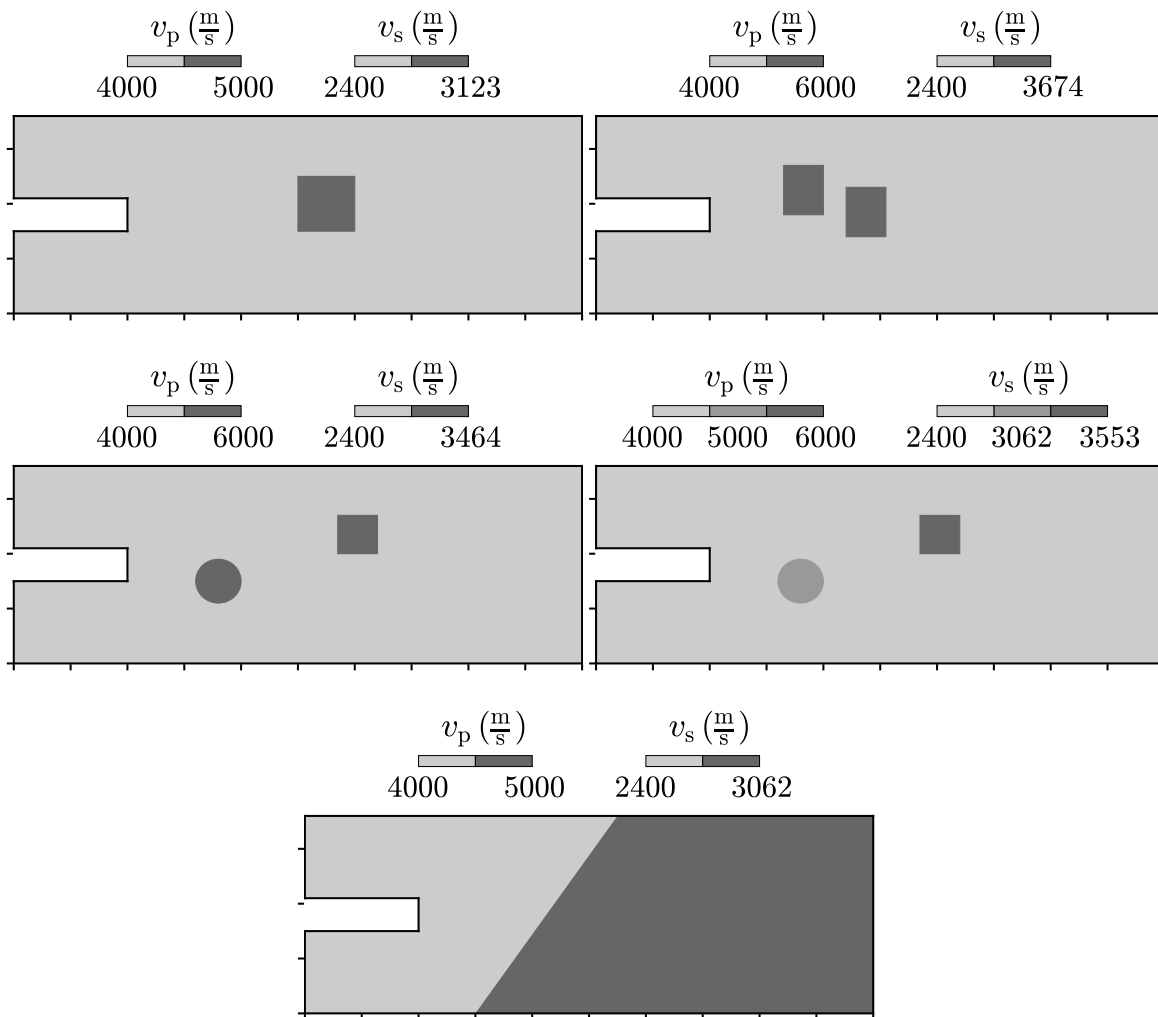


Figure 5.2.: True models for scenarios 1 to 5 (left to right, top to bottom). Ticks are in distances of 10 m.

Scenarios 1 to 3 (left to right, top to bottom) are designed in order to test the ability of UKF-PaLS to determine single and multiple objects with varying sizes, shapes, distances to each other, distances to the tunnel face, and material properties. Scenarios 4 and 5 are test scenarios for cases in which the chosen parametrization of UKF-PaLS is not fully able to determine the structure. The disturbances in scenario 4 have the same structure as the disturbances in scenario 3, but however, the two anomalies have different material properties. Since UKF-PaLS will only invert for one material, the scenario serves to examine if the two objects may still be resolved. The anomaly in scenario 5 is a layer change. In this case, the distribution of the bumps will not cover the whole model (which will be shown in the following) so that a fully correct inversion remains difficult. Note that for all of the examples, the disturbance material properties are chosen stiffer than the background material properties since doing so, the same mesh and initial model can be selected for all of the scenarios with no need of remeshing during inversion. This procedure has only practical and illustrative reasons and does not decrease the difficulty of inversion; an experimental example for UKF-PaLS where the disturbance wave velocities have smaller values than the background wave velocities will be investigated in Section 8.3.3. The simulation time window in SPEC2D is set to 1.3 s. For each of the scenarios, measurements for both source-receiver configurations (Figure 5.1) are generated. Accordingly, the scenarios are referred to as scenarios 1.1, 1.2, ..., 5.1, 5.2.

5.1.2. Full waveform inversion

The numerical model for the inversion scenario is discretized according to Eq. 2.12 so that the largest element in the mesh is able to consider frequencies up to $f_{\max} = 2.5f_c = 750$ Hz (where $f_c = 300$ Hz is the central frequency of the Ricker), resulting in 3675 quadrilateral 4-node elements. $N_b = 28$ bumps are centered on a regular grid of 36×18 m with distances of 6 m to each other. Consequently, also the resolutions amount to about 6 m, where the maximum size of the disturbances in the true models was 7 m. Instead of determining a shear wave velocity of the disturbance $v_{s,d}$ directly during inversion, a Poisson's ratio ν_d is determined. The advantages are that the shear wave velocity can be controlled better during optimization since it is coupled to the compressional wave velocity and that boundaries of the Poisson's ratio may be set in order to keep the ratio between reasonable values for rock material. Note that, however, in the following, the shear wave velocity is used in illustrations for the purpose of a more trivial imaging. According to Eq. 3.29, the dimension

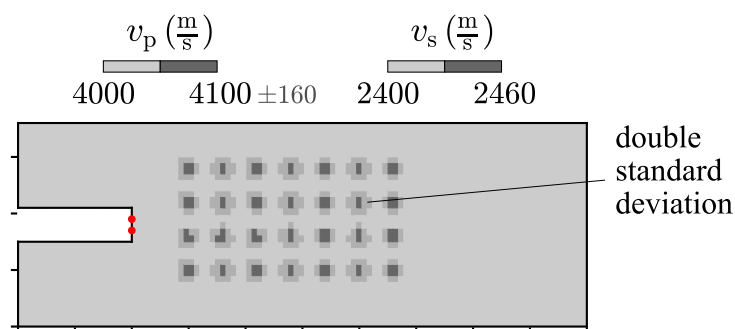


Figure 5.3.: Initial model for all scenarios. The double standard deviations of the initial parameters are illustrated by the medium dark grey tone (see marking). Ticks are in distances of 10 m.

of the inversion problem amounts (with its $N_b = 28$ bumps and two disturbance material properties) to $n = 58$ (with 28 dimensions for α , 28 dimensions for β , 1 for $v_{p,d}$ and 1 for ν_d). Thus, there are $2n + 1 = 117$ sigma points to compute in each iteration. The initial model is defined by setting a vector $\mathbf{m}_0 \in \mathbb{R}^n$, where the parameters may be found in Table 5.1. The initial compressional wave velocity is set to $4100 \frac{\text{m}}{\text{s}}$, where already a tendency to material with higher wave velocities is implemented in order to achieve faster convergence. During field measurements, travel time observations could probably deliver a prediction of whether the disturbance material has higher or lower wave velocities than the background material. Otherwise, the first cycle should be performed with both higher and lower initial wave velocities in order to determine for which case the misfit functional decreases more. The general settings of the UKF in terms of \mathbf{P}_0^m , \mathbf{s}_{\min} , \mathbf{R} and \mathbf{Q} are tuned as explained in Section 3.6. The parameter settings stay the same for the 10 scenarios, which shows that the method is not dependent on a fine parameter tuning. A more illustrative representation of the initial parameters is shown in Figure 5.3, where the initial model is plotted. The medium dark grey area (see marking in the figure) visualizes the positive double standard deviation of \mathbf{P}_0^m , which is the 95% confidence interval, and is thought of as a measure of uncertainties during inversion. Note that the double standard deviation could also be plotted in negative direction, which would mean a potential material loss at the reconstructed anomaly. However, the positive direction is more meaningful for an application in mechanized tunneling since it is more important to know where additional disturbances could be located than to know where they could possibly not be located. The interval of the standard deviation of the compressional wave velocity is also plotted, denoted by ± 160 . Prior to inversion, the uncertainty measure determines the spread of the sigma points and does not long for any physical interpretation since the covariance is adapted by the UKF during optimization. For each of the scenarios, UKF-PaLS is run for 25 iterations. The multi-scale approach is implemented in the form of a low-pass filter with a step-wise increasing cutoff frequency ranging from 200 Hz to 750 Hz with an increase every 3 cycles up to iteration 21, after which no filtering is applied anymore.

Parameter	Configuration
N_b	28
\mathbf{m}_0	$\{\alpha_0, \beta_0, (v_{p,d})_0, (\nu_d)_0\}$
α_0	$0.2 \mathbf{J}_{N_b,1}$
β_0	$3 \mathbf{J}_{N_b,1}$
$(v_{p,d})_0$	$4100 \frac{\text{m}}{\text{s}}$
$(\nu_d)_0$	0.21875
c	0.1
N_k	25
\mathbf{P}_0^m	$\text{diag}(\mathbf{P}_0^\alpha, \mathbf{P}_0^\beta, P_0^{v_{p,d}}, P_0^{\nu_d})$
\mathbf{P}_0^α	$0.3^2 \mathbf{J}_{N_b,1}$
\mathbf{P}_0^β	$0.3^2 \mathbf{J}_{N_b,1}$
$P_0^{v_{p,d}}$	80^2
$P_0^{\nu_d}$	0.001^2
\mathbf{s}_{\min}	$0 \cdot \mathbf{s}_u$
\mathbf{R}	$0.05 \mathbf{s}_u \cdot \mathbf{I}_r$
\mathbf{Q}	$0.3 \mathbf{P}_0^m$

Table 5.1.: Initial model parameters and input parameter configuration for UKF-PaLS. $\mathbf{J}_{N_b,1}$ is a vector of ones of the size of the number of bumps $\mathbb{R}^{N_b \times 1}$

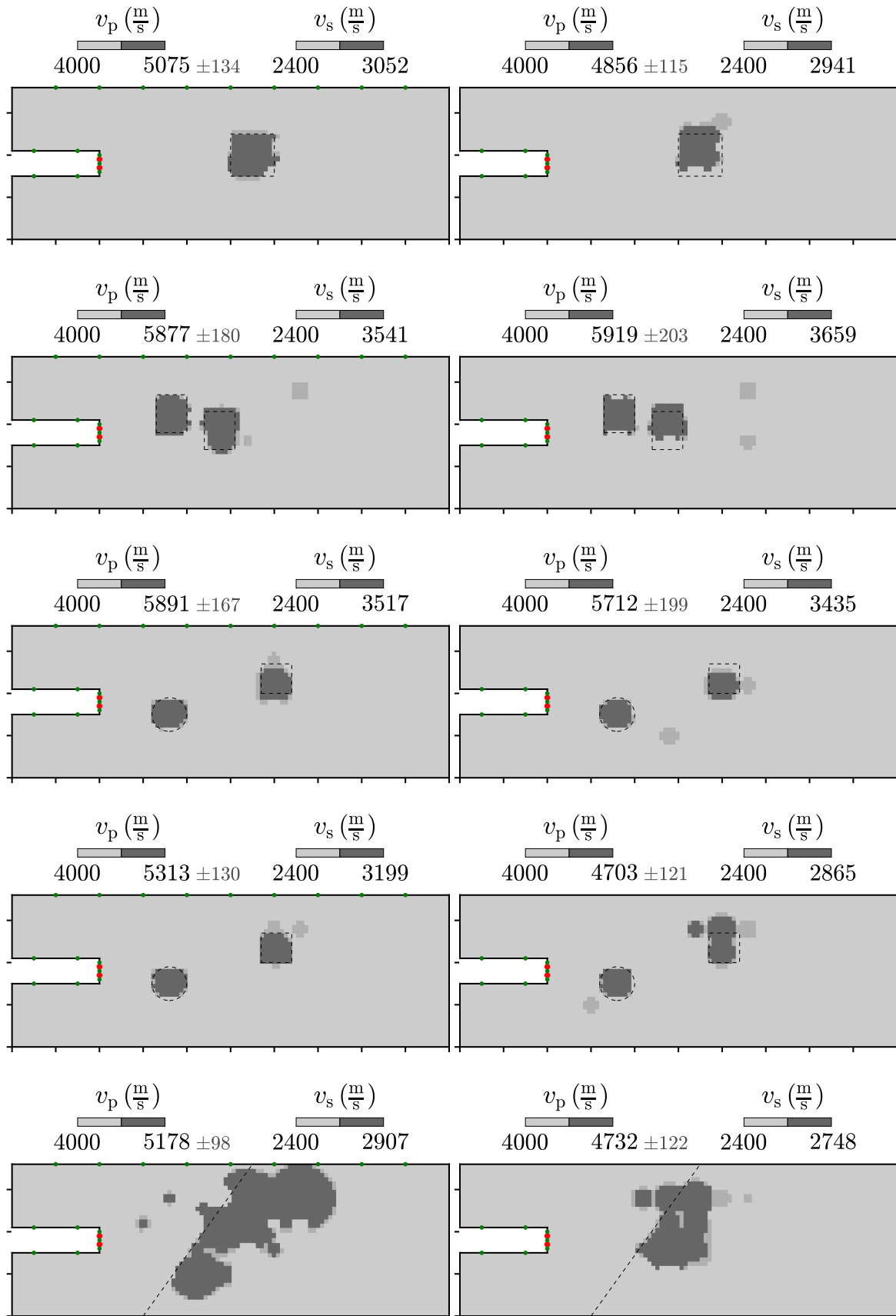


Figure 5.4.: Best estimate during inversion for scenarios 1.1, 1.2, ..., 5.2 (left to right, top to bottom). The double standard deviations are plotted in medium dark grey. Ticks are in distances of 10 m. Sources are illustrated in red, receivers in green.

The best estimates of UKF-PaLS during the 25 iterations for scenarios 1.1 – 5.1 are shown in Figure 5.4. The borders of the true disturbances are illustrated by black dashed lines. Again, the double standard deviations are plotted in medium dark grey. A first analysis of the results is performed for scenarios 1.1–3.2, which are the scenarios where the UKF-PaLS parametrization may be able to invert the measurements to a high grade. For all of these scenarios, the inversion performs greatly accurate. Front borders and rear borders (seen from direction of seismic sources) are well resolved, although – due to the meshing of the true models with an exact definition of the borders – the inversion model cannot fit the model entirely. Furthermore, in scenarios 2.1 and 2.2 both objects are clearly resolved without melting together. The scenarios with source-receiver configuration 1 perform slightly better than the scenarios with source-receiver configuration 2. However, the differences remain small – only the top and bottom borders of the anomalies are determined slightly worse since no information of transmitted waves arrives at the seismic receivers. This emphasizes the advantage of the parameter reduction since the resolving of rear boundaries of anomalies based only on reflected waves is a difficult FWI problem. Besides the good reconstruction of geometries, also the determined material properties are close to the true values. The uncertainties in terms of the double standard deviations show where potential objects could be missed by the inversion. These uncertainties lie, for all of the examples, in the 'shadow' of the reconstructed objects. At these locations, the reconstruction can be considered the most unreliable since the occurrence of a disturbance would only bring a slight change in the misfit functional here. The uncertainties could presumably be eliminated by incorporating a seismic source at the Earth's surface with a horizontal distance equal or larger than the horizontal distance of the 'shadows' to the tunnel. Incorporating the double standard deviation for the compressional wave velocity, most of the resulting intervals include the true value – if not, it is only slightly apart.

Observing the results for scenarios 4.1 and 4.2 in Figure 5.4, it is found that the reconstruction of the shapes of both anomalies is accurate, although the correct inversion in terms of material properties is not possible since UKF-PaLS is defined so that it only determines one set of material properties. The only aggravation compared to the scenarios 3.1 and 3.2 occurs at the top disturbance in scenario 4.2, where some additional material appears. The determined compressional wave velocity of the disturbance lies with $5313 \frac{\text{m}}{\text{s}}$ relatively centered between the true values of $5000 \frac{\text{m}}{\text{s}}$ and $6000 \frac{\text{m}}{\text{s}}$. It is noted that a reconstruction of the disturbances with only one set of material properties is only expected to be successful if the disturbances have both lower or both higher wave velocities, which is the case in the current scenario. The inversion results of scenarios 5.1 and 5.2 show a good reconstruction of the front border of the layer change. For scenario 5.2, this only applies in excavation direction. The back part of the layer change is not reconstructed since the bumps do not spread all over the model. In both scenarios, some small areas of material appear at locations where the true model has background material properties only. The reason for this is not apparent, but it is assumed that the areas compensate for a mismatch at the seismic receivers above the tunnel originating from reflected waves from the back end of the disturbance in the determined model. A better result can be expected if the bumps are located all over the model domain, where an example for this case will be given in Section 8.3.3 in the context of an application to experimental data. However, the results show that the inversion may also be satisfactory if the region of investigation is selected to be small. Each of the inversion scenarios is solved in less than 6 hours on a 26-core computer with 2.4 GHz each and 96 GB RAM, consuming $25(2n + 1) = 2925$ forward simulations per source.

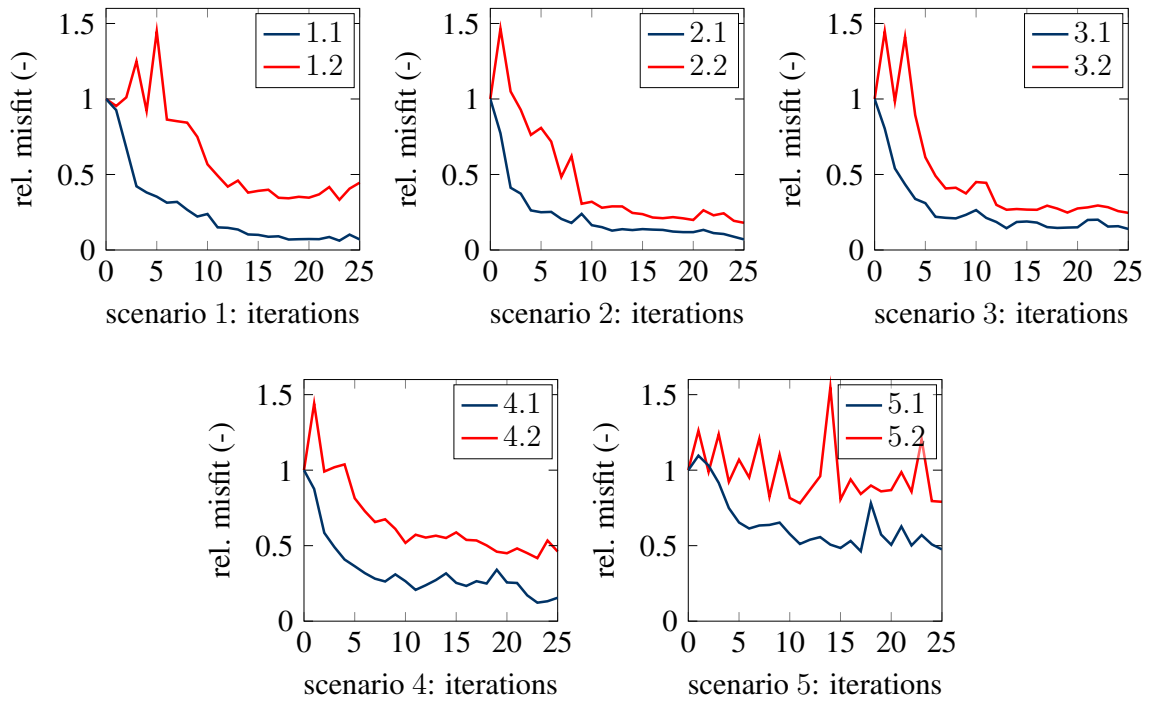


Figure 5.5.: Relative misfit functionals of the corresponding unfiltered data. The plotted value is the UKF estimate of the respective iteration. The misfit functionals are normalized with the misfit value of the respective initial model.

The corresponding courses of the misfit functionals are shown in Figure 5.5, where for illustration purposes, the misfit functional of the unfiltered data is computed and utilized. Due to the step-wise increasing cutoff frequency of the multi-scale approach, the misfit functional is continuously increasing since higher frequencies come into play, which makes a plot of the unfiltered functional more trivial. For scenarios 1.1 – 3.2, the misfit functionals are distinctly decreased, with values up to more than 90%. However, for the scenarios corresponding to source-receiver configuration 2, the misfit functional is lowered less intense due to the increased complexity of the inverse problem caused by the incorporation of fewer receivers. Still, it is lowered for more than 60% for all of the three scenarios. Scenarios 4.1 – 5.2 show a much smaller decrease, especially in scenarios 5.1 and 5.2, since the restricted parametrization of the disturbance domain hinders UKF-PaLS to decrease the misfit functional to a higher amount. Observing the course of the misfit functionals, it is noticeable that a low level is already reached after a few cycles. Accordingly, also the illustrations of the best estimates after 5, 10, 15 and 20 iterations are observed and attached in Appendix A, where it becomes visible that most of the disturbances are already reconstructed after 5 iterations. However, at this stage, some additional areas of material are visible, and the observed uncertainties are comparatively large. After 10 iterations only, most of the images provide a reliable estimation of the disturbance domain. This shows that, if computational resources are limited, also fewer iterations could be conducted for a prediction. Another opportunity is to observe the results of the iterations during inversion already, where results become more reliable if a convergence of the misfit functional can be noticed. After 15 and 20 iterations, the uncertainties become smaller, which is a consequence of the incorporation of higher frequencies since in the case of smaller occurring wavelengths, small appearances of material in the model have a more significant impact on the misfit functional.

5.2. UKF-PaLS in 3D

5.2.1. Generation of synthetic measurements

In the following, a model including a boulder is set up that is again tested on two source-receiver configurations. The investigations are restricted to these two scenarios since the computational effort is much larger for the 3D inversion than it is for the 2D inversion. The first configuration is illustrated at the left of Figure 5.6 and includes 3 seismic sources and 88 seismic receivers. Two of the seismic sources are placed at the tunnel front, the bottom one pointing in x -direction and the top one pointing in z -direction. The other source is placed on the Earth's surface pointing in z -direction. 39 of the seismic receivers are placed inside the tunnel and 49 are placed at the Earth's surface. The second configuration, illustrated at the right of Figure 5.6, includes only the receivers inside the tunnel and is apart from that equal to configuration 1. Accordingly, it consists of 2 seismic sources and 39 receivers. The source functions of the seismic sources are Ricker wavelets with central frequencies of $f_c = 300$ Hz. The ground model has a dimension of 100 m in x -direction and 20 m both in y - and z -direction. A cylindrical tunnel with a diameter of 8.5 m, 15.75 m overburden and 25 m excavation length in x -direction is included into the model. In a distance of 24 m to the front face of the tunnel, the front face of the boulder is located. Basis of the boulder is a brick with a dimension of 15 m in x -, 17 m in y - and 17 m in z -direction with its center located at (6.5, 0, 1.5) m, where the dimensions are chosen comparatively large for the first test. At the top right corner of the boulder seen from the tunnel face, material in the form of a brick with dimensions of 7 m in y - and 3 m in z -direction is removed all over the x -direction in order to test the ability of the algorithm to reconstruct small structural changes. Material properties are considered to be homogeneous elastic with background material properties $v_{p,b} = 4000 \frac{\text{m}}{\text{s}}$, $v_{s,b} = 2400 \frac{\text{m}}{\text{s}}$ and $\rho_b = 2000 \frac{\text{kg}}{\text{m}^3}$ and disturbance material properties of $v_{p,d} = 6000 \frac{\text{m}}{\text{s}}$, $v_{s,d} = 3600 \frac{\text{m}}{\text{s}}$ and $\rho_d = 2000 \frac{\text{kg}}{\text{m}^3}$, where same as in the previous section the density is considered to be constant all over the model. According to the defined material properties, the Poisson's ratio for both materials amounts to $\nu_b = \nu_d = 0.21875$ (Eq. 2.9). The boundaries are defined as explained in Section 2.2 for shallow tunnels. Corresponding to the two source-receiver configurations, two sets of measurement are generated with a signal duration of 0.1 s, referred to as scenarios 1 and 2 in the following.

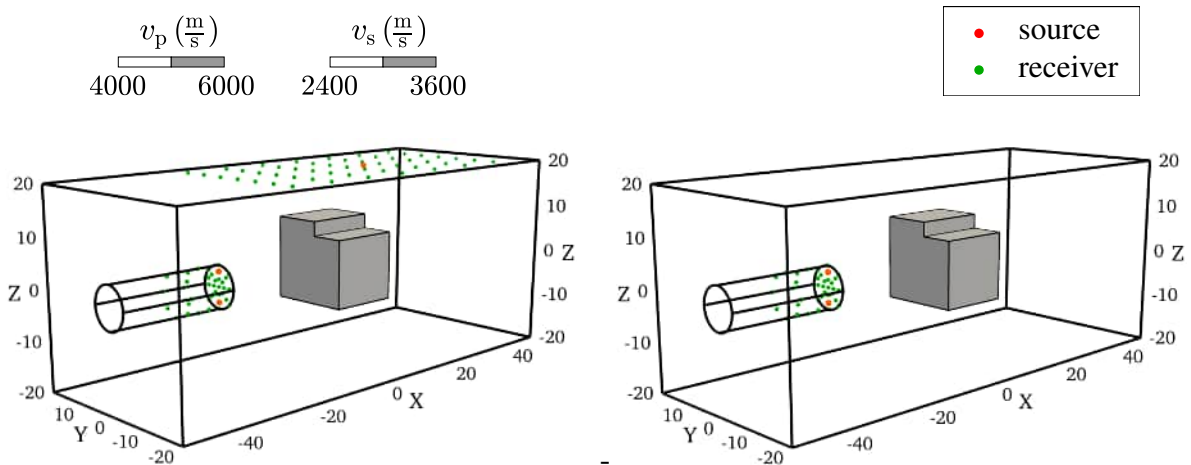


Figure 5.6.: True models for scenarios 1 and 2, where the only difference lies in the source-receiver configuration. Dimensions are in m.

5.2.2. Full waveform inversion

The numerical model for the inversion scenario is discretized according to Eq. 2.12 so that the largest element in the mesh is able to consider frequencies up to $f_{\max} = 2.5f_c = 750$ Hz, resulting in 52520 hexahedral 8-node elements. 80 bumps are aligned on a regular grid within a domain of $30 \times 20 \times 20$ m with distances of 7.5 m to each other. In order to save computation time, only the compressional wave velocity is determined; the shear wave velocity is computed based on the Poisson's ratio $\nu_d = \nu_b = 0.21875$. Therefore, the dimension of the inversion scenario amounts to $n = 161$ (with 80 dimensions for α , 80 dimensions for β and 1 for $v_{p,d}$) resulting in $2n + 1 = 323$ sigma points to compute in each iteration. The initial model and the general settings of the UKF are, for both inversion scenarios, tuned according to Table 5.2. The corresponding initial distribution of the disturbance domain is shown in Figure 5.7. In the 3D case, no uncertainty measure is plotted. The reason for this is that the region of investigation is, compared to the size of the boulder, relatively small in this scenario. Therefore, uncertainties can only appear in the region directly around the

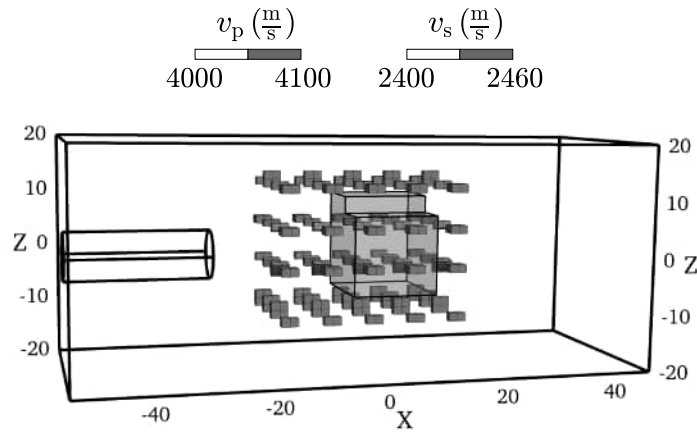


Figure 5.7.: Initial model of UKF-PaLS with borders of the true disturbance in light grey.

Parameter	Configuration
N_b	80
\mathbf{m}_0	$\{\alpha_0, \beta_0, (v_{p,d})_0\}$
α_0	$0.2 \cdot \mathbf{J}_{N_b,1}$
β_0	$4 \cdot \mathbf{J}_{N_b,1}$
$(v_{p,d})_0$	$4100 \frac{\text{m}}{\text{s}}$
c	0.1
N_k	25
\mathbf{P}_0^m	$\text{diag}(\mathbf{P}_0^\alpha, \mathbf{P}_0^\beta, P_0^{v_{p,d}})$
\mathbf{P}_0^α	$0.2^2 \cdot \mathbf{J}_{N_b,1}$
\mathbf{P}_0^β	$0.2^2 \cdot \mathbf{J}_{N_b,1}$
$P_0^{v_{p,d}}$	40^2
\mathbf{s}_{\min}	$0 \cdot s_u$
\mathbf{R}	$0.01 \cdot s_u \cdot \mathbf{I}_r$
\mathbf{Q}	$0.4 \cdot \mathbf{P}_0^m$

Table 5.2.: Initial model parameters and input parameter configuration for UKF-PaLS. $\mathbf{J}_{N_b,1}$ is a vector of ones of the size of the number of bumps $\mathbb{R}^{N_b \times 1}$.

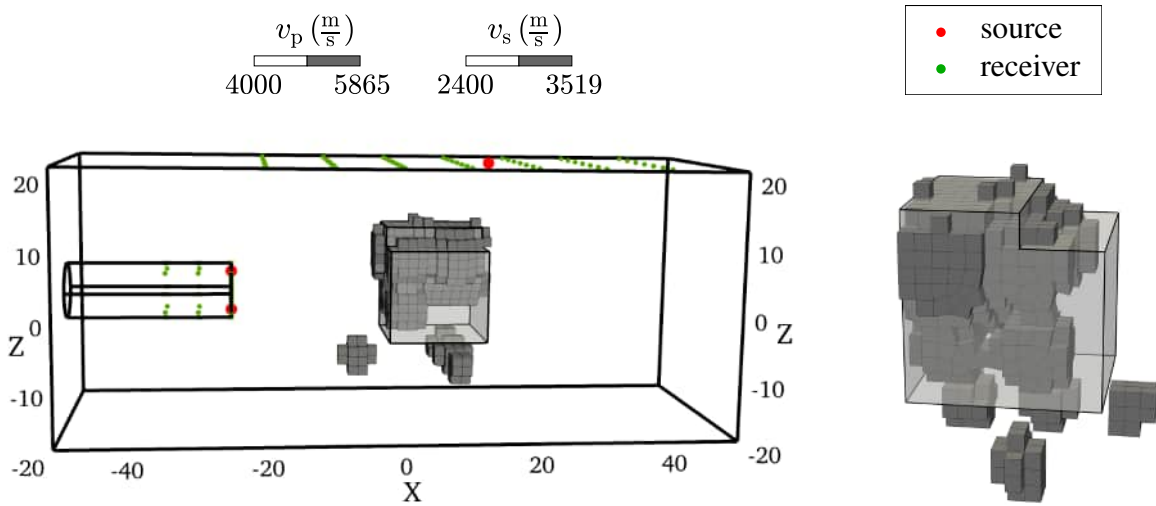


Figure 5.8.: Inversion result for scenario 1 from two points of view: Model corresponding to parameter configuration with minimum misfit compared to the borders of the true disturbance in light grey.

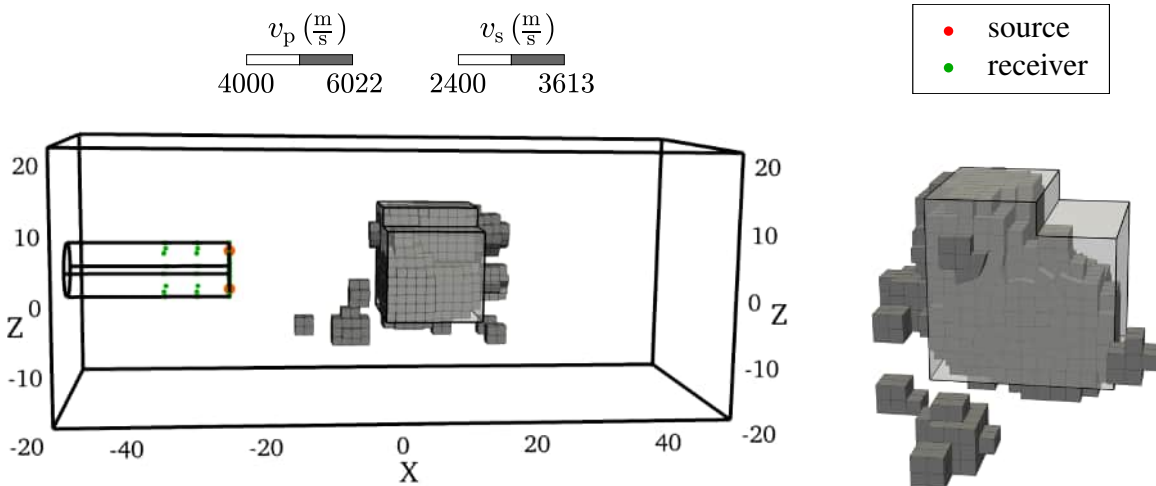


Figure 5.9.: Inversion result for scenario 2 from two points of view: Model corresponding to parameter configuration with minimum misfit compared to borders of the true disturbance in light grey.

boulder, which does not allow for very valuable uncertainty quantification. Furthermore, the 3D illustration would look less clear. Nonetheless, an estimation should be performed for future cases where the computational resources allow for larger regions of investigations. For both inversion scenarios, UKF-PaLS is run for 25 iterations. Same as in the previous section, cutoff frequencies are increased step-wise from 200 Hz to 750 Hz with an increase every 3 cycles up to iteration 21, after which no filter is applied anymore. The model corresponding to the parameter configuration with the lowest misfit functional during the overall course of UKF-PaLS for scenario 1 is found during iteration 24 and is visualized in Figure 5.8. The borders of the true disturbance are illustrated in light grey. It is found that the core of the boulder as well as its top border are reconstructed well and that at the location of the boulder, where material is removed, the structure vanishes. Also the front boundary of the boulder and the rear boundary seen from tunnel face direction are precisely deter-

mined. However, most notably at the bottom and the right side of the boulder, the shape is less well reconstructed. Furthermore, below the bottom of the disturbance, some areas of disturbance material occur. This is most probably due to the occurrence of seismic sources and receivers at the top surface, meaning that the top of the boulder is screened with transmitted waves. The bottom is not affected by transmitted waves which later arrive at seismic receivers, which increases the rate of failure at these locations. An approach that could eliminate these occurrences of material is proposed at the end of the chapter. Altogether, the boulder is determined precisely. With the inversion result, the location of the boulder can be exactly determined and the shape may be estimated. It is expected that with a higher number of seismic sources, the shape could be reconstructed even more precisely. Also the determined compressional wave velocity $v_{p,d} = 5865 \frac{\text{m}}{\text{s}}$ is close to the true value. The computation takes about 13 days on a computer cluster if occupying 600 cores with 2.4 GHz each and about 700 GB RAM, where $25 \cdot 2(n + 1) = 8075$ forward simulations per source are computed.

The model corresponding to the parameter configuration of the disturbance with the lowest misfit functional during inversion scenario 2 is found during iteration 17 and visualized in Figure 5.9. It is observed that the boulder is reconstructed similarly detailed as in scenario 1. The bottom side is even reconstructed better, while the top surface is determined slightly worse. The reason for this is that the surface receivers and the surface source are missing, leading to a less good reconstruction at the top but to a higher focus on reflected waves, incorporating also the bottom part to a higher grade. Same as in the previous scenario, some material occurs at locations where the model is not well covered by reflected waves, where also here, the approach proposed at the end of the chapter could provide a remedy. The compressional wave velocity is precisely determined with a value of $v_{p,d} = 6022 \frac{\text{m}}{\text{s}}$. The computation of this scenario takes about 9 days on the computer cluster described above, where also here $25 \cdot 2(n + 1) = 8075$ forward simulations per source are computed. Figure 5.10 shows the course of the relative misfit functional over the number of iterations of UKF-PaLS, where same as in the previous section the misfit functional of the unfiltered data is computed and utilized. The plotted value refers to the lowest misfit functional of the respective iteration. During scenario 1, the misfit functional is lowered for more than 70%, while during scenario 2, the misfit functional is decreased for more than 40%.

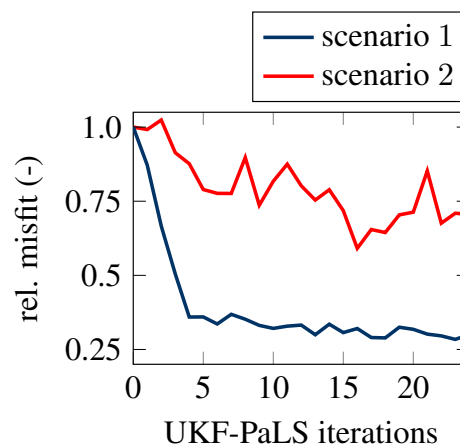


Figure 5.10.: Relative misfit functionals of the corresponding unfiltered data. The plotted value refers to the lowest misfit functional of the respective iteration. The misfit functionals are normalized with the misfit value of the respective initial model.

Same as for the 2D examples, it is observed that a low level of the misfit functional is already reached within the first 5 cycles. Therefore, also here, the illustrations of the best estimates after 5, 10, 15 and 20 iterations are observed and attached in Appendix B. The observations agree to the greatest extent with the observations made in the previous section: The core of the boulder becomes visible already after 5 iterations, where however additional pieces of disturbance material appear. During the further course of inversion, most of this material vanishes. This shows once more that a first prediction can be performed already after a few iterations, where also less iterations with lower working frequencies could be performed.

5.3. Short summary and discussion

The investigations of this chapter show that UKF-PaLS can provide precise inversion results both in 2D and 3D. The multi-scale approach brings a fast convergence and precise results. The gain of the approach becomes visible if the results of scenario 2 are compared to the results of Nguyen & Nestorović (2018), where a separation of two objects with a comparatively small distance to each other was not possible although twice as many sources and more than three times as many receivers (placed even in boreholes) were used. For all of the scenarios in this chapter, accurate results are already achieved after much less than the conducted 25 cycles, which shows that either a first prediction can be performed early or that less iterations with lower working frequencies could be performed if computational resources are limited. It is found that even if the level-set parametrization is not chosen fully optimal in the sense that it is not able to fully describe the disturbance domain, inversion results can still be satisfactory. The covariance of the computed mean value can be used to perform uncertainty quantification in order to analyze where anomalies could potentially be missed by the inversion. Regarding source-receiver configurations it is found that an exclusive placement of sources and receivers inside the tunnel already brings accurate results, where the differences to scenarios in which additional receivers are distributed at the Earth's surface remain small. Due to the increased computation time, only two inversion scenarios are tested in 3D. Scenarios with different types of disturbances with varying distances to the tunnel face, larger regions of investigation and varying source-receiver configurations are to be tested in future works. An approach that could further improve the results by removing additional occurrences of disturbance material (which are especially visible for the 3D cases) is *Tikhonov regularization* (Tikhonov & Arsenin, 1963), where Fichtner (2010) provides a short and comprehensive overview. The approach is based on the assumption that the subsoil model is most probably simplistic, with rather small deviations from the background model. Therefore, a quadratic term is added to the misfit functional that increases if the current model departs from a reference model, which may be for instance the initial model. It is probable that the additional areas of disturbance material, which appear in the discussed 3D examples, vanish if Tikhonov regularization is applied. However, the approach requires tests where probably also an investigation of a tuning of parameters is to be performed, which is too costly for the 3D case regarding the available computational resources.

6. Imaging of a hole in an aluminum block

This chapter deals with the localization of a drilling hole in an aluminum block with both UHSA and UKF-PaLS, where the scenarios serve as a first validation of the two methods with experimental data. The advantage in choosing aluminum is a more straightforward modeling compared to specimens composed of rock material as the isotropic and elastic assumption is more valid for aluminum, leading to a smaller mismatch between measured and synthetic waveforms. Therefore, strategies may be more easily developed, especially concerning the forward modeling in terms of material property finding and the source function estimation. After the acquisition of measurement data and the creation of the forward model, both FWI methods are applied to the data and investigated on two source-receiver configurations. UHSA is tested against particle swarm optimization and the results of UHSA and UKF-PaLS are compared to the results of an adjoint approach, where the latter are achieved by Lamert (2019). The contents up to the results of UHSA are similar to the contents published in Trapp *et al.* (2019); however, the work is rewritten and the pictures and figures are changed or edited substantially. Furthermore, additional content is added and the inversion scenarios for UHSA are recomputed. The part corresponding to the supervised machine learning approach is left out since these contents are written by the co-authors Can Boguclu and Dirk Roos. However, the value of using supervised machine learning for the creation of metamodels will be emphasized in Section 10.6.

6.1. The experiment

In order to create the ultrasonic data needed for the forward modeling as well as for the inversion scenario, two cuboid aluminum specimens with dimensions $200.4 \times 103 \times 100$ mm are utilized. Into one of the blocks, a hole is drilled, while the other one remains undis-



(a) Photo of measurement setup 1

(b) Photo of measurement setup 2

Figure 6.1.: Measurement setup for the undisturbed and the disturbed specimen.

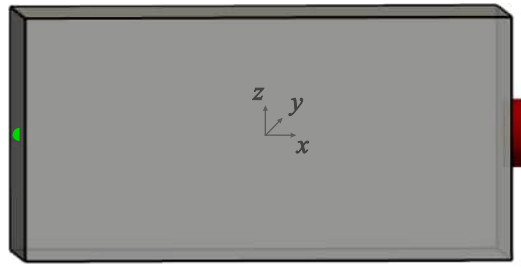
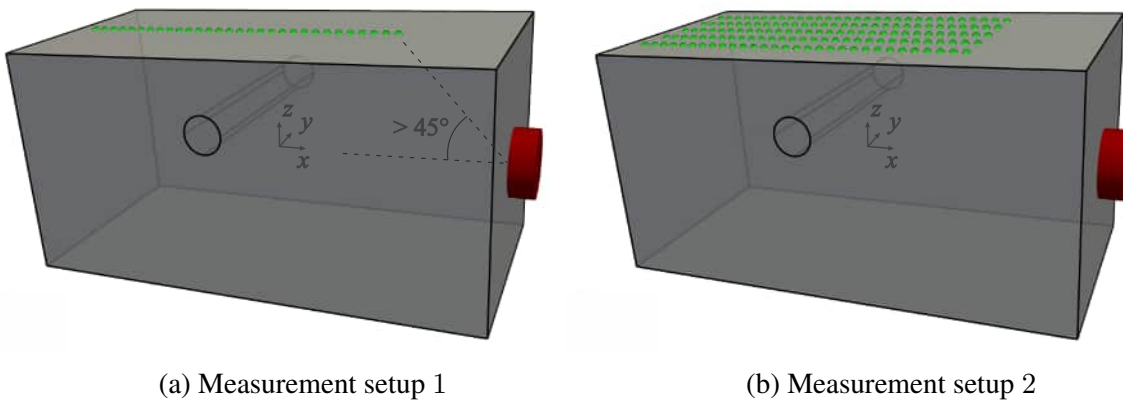


Figure 6.2.: Undisturbed specimen with measurement configuration. The red cylinder illustrates the ultrasonic transducer. The green dot marks a single-point laser measurement.



(a) Measurement setup 1

(b) Measurement setup 2

Figure 6.3.: Disturbed specimen with measurement configurations. The red cylinder illustrates the ultrasonic transducer. The green dots mark the points of laser measurements.

turbed. Corresponding coordinate systems are placed in the respective center of mass of the ideal block (without a drilling). The undisturbed specimen, which is shown in Figure 6.1a and illustrated in Figure 6.2, serves for investigations concerning material properties and the source signature. Into the second specimen, which is shown in Figure 6.1b and illustrated in Figure 6.3, a hole of 16 mm diameter is drilled with its center aimed at position $(-10, y, 20)$ mm all over the y -direction. Wave excitation is conducted with transducer S 24 HB 0.2-0.6 (see Section 4.2). The flat contact area is for both specimens aimed to be placed at $(100.2, 0, 0)$ mm, where the source is illustrated with the red cylinder. The source input signal is a Ricker function with $f_c = 300$ kHz central frequency. When acquiring measurements with the laser, it is observed that the signal strength becomes weaker measuring close to the transducer (or, in other words, for higher values of x). The reason for this is that signal directivities of ultrasonic transducers are usually not constant, where a study of Bretaudeau *et al.* (2011) investigates this issue. Based on preliminary investigations, the angle between the x -axis and the line connecting the middle of the transducer with the last upcoming receiver in x -direction is chosen to be larger than 45 degrees (see Figure 6.3a). The corresponding measurement setups are illustrated in Figure 6.2 and Figure 6.3. On the undisturbed specimen, a single-shot measurement is acquired at $(-100.2, 0, 0)$ mm, where the location of the laser measurement is illustrated with the green dot. The measurement is achieved with a mirror redirecting the laser beam (see Figure 6.1a). On the disturbed specimen, measurement data for two receiver sets are acquired, where the source location remains unchanged. For measurement setup 1, the data is acquired on the top surface at $z = 50$ mm (xy -plane) along line $y = 0$, that is the line in the middle of the surface parallel

to the x -axis. 30 points of measurement are acquired along a 145 mm long line in distances of 5 mm. For measurement setup 2, four additional line measurements are conducted which are parallel to the one acquired above with distances of -15 , 15 , -30 and 30 mm in y -direction. The resulting measurement setup consists of 5 parallel line measurements with $5 \cdot 30 = 150$ points of laser measurements. The number of stacked single measurements is with $n_{\text{stack}} = 200$ comparatively large, which is possible in this case since the number of receivers is rather low. During measurement acquisition, the specimens are placed on threaded bars, which are sharpened in order to accomplish a minimum contact face. In order to achieve a good transducer-structure coupling, a holder is built, where the transducer is fixed in a PVC structure which is pressed into the direction of the specimen with the help of two springs. To apply a contact pressure, two counterbalances are built and placed at the opposite side of the specimen. The counterbalances are made up of circular cutouts of PVC plates, attached eccentrically on threaded bars. The contact pressure is tuned by spinning the counterbalances. For a different view on the bearing in a different setup, readers are referred to Figure 7.2. Preliminary investigations show that the impact of the contact pressure on the output signal is low if the coupling with the structure is secured. Therefore, it is sufficient if the springs of the holder are compressed for a small amount only. During the creation of the setup, the impact of the bearing as interfering objects is aimed to be minimized. The threaded bars, on which the plates are placed, are close to having a point contact only, while the circular cutout almost induce a line contact only. Thus, the impacts can be considered rather low. The largest impact is expected to be caused by the transducer itself due to the comparatively large contact face. However, since a modeling of the transducer would be complex and since the inner structure would have to be known, it is left out of this study. The offsets of the acquired traces are removed by subtracting the average amplitude before waveform arrival. Bandpass filters are applied with cutoff frequencies of 50 and 800 kHz.

6.2. The forward model

The first stage of forward modeling is made up of a careful measurement of the dimensions of the aluminum blocks and the implementation of the 3D geometrical model into Trellis, where all of the surfaces are defined as free boundaries. In a second step, material properties are to be determined. The material is chosen to be elastic as on the one hand, the attenuation in aluminum may be expected to be rather small and as on the other hand, also the time window of observation is selected to be rather short so that the amplitudes do not decay greatly anyways. As a consequence, the material properties are reduced to density ρ , compressional wave velocity v_p and shear wave velocity v_s . The density is determined to $2775 \frac{\text{kg}}{\text{m}^3}$ and implemented into the computational model. However, it could also obtain any arbitrary value since the amplitudes of the simulation are scaled anyways. Since for homogeneous media, a variation of the density only scales amplitudes in the elastic wave equation, the shape of the waveform stays the same for different densities if only one material is considered. A first estimation of the compressional wave velocity is obtained with the help of travel time measurements. Subsequently, a first value of the shear wave velocity is obtained with this compressional wave velocity and with an assumed value for the Poisson's ratio $\nu = 0.34$ (which is a common value for aluminum). The values for the wave velocities are then refined with a sampling investigation. Therefore, forward simulations corresponding to the model in Figure 6.2 are set up with a gridded variation of v_p and v_s in an interval of $10 \frac{\text{m}}{\text{s}}$ around the first estimation. The misfit functional (Eq. 3.6) for each pair of wave velocities is calculated

incorporating the single-point measurement acquired in the previous section. Amplitudes of the simulation data are aligned to the amplitudes of the experimental data by calculating the factor leading to the minimum gap. Finally, the pair according to the minimum misfit value is chosen, which is $v_p = 6340 \frac{\text{m}}{\text{s}}$ and $v_s = 3110 \frac{\text{m}}{\text{s}}$. The creation of a gridded database has the advantage of an offline evaluation, where observation times can be varied and where waveform matches can be observed carefully. Since the finding of material properties turns out to be not fully trivial for many cases (especially for different materials than aluminum), this method is found to be useful. A comparison of the measurement (black) and synthetic data (grey dotted) generated with the estimated wave velocities and the ideal Ricker signal is illustrated in Figure 6.4. It is observed that the two waveforms already have a strong agreement, particularly in terms of phases, which is seen as a hint that the material properties are close to the real material properties. However, especially in terms of amplitudes, the match may still be improved by an estimation of the source signature. Due to the coupling of the source with the structure, the specific frequency of the ultrasonic transducer (Section 4.2) and its inertia, the displacement function of the transducer's contact face differs from the source input. For this reason, a strategy is utilized in order to estimate this function, which may be derived as follows. The synthetic signal response in frequency-domain $S_{\text{syn}}(\omega)$ to the ideal source function in frequency-domain $R_{\text{syn}}(\omega)$ (in this case, the ideal Ricker signal) may be derived with the help of a transfer function $M(\omega)$ according to

$$S_{\text{syn}}(\omega) = M(\omega) \cdot R_{\text{syn}}(\omega). \quad (6.1)$$

Assuming that the numerical model captures all properties of the experimental model, the same relation is valid for the experimental data:

$$S_{\text{exp}}(\omega) = M(\omega) \cdot R_{\text{exp}}(\omega), \quad (6.2)$$

where $S_{\text{exp}}(\omega)$ is the measured waveform expressed in frequency-domain and $R_{\text{exp}}(\omega)$ is the sought real source function in frequency-domain. Capturing all properties of the experimental model is, of course, impossible. However, the assumption is considered sufficient in

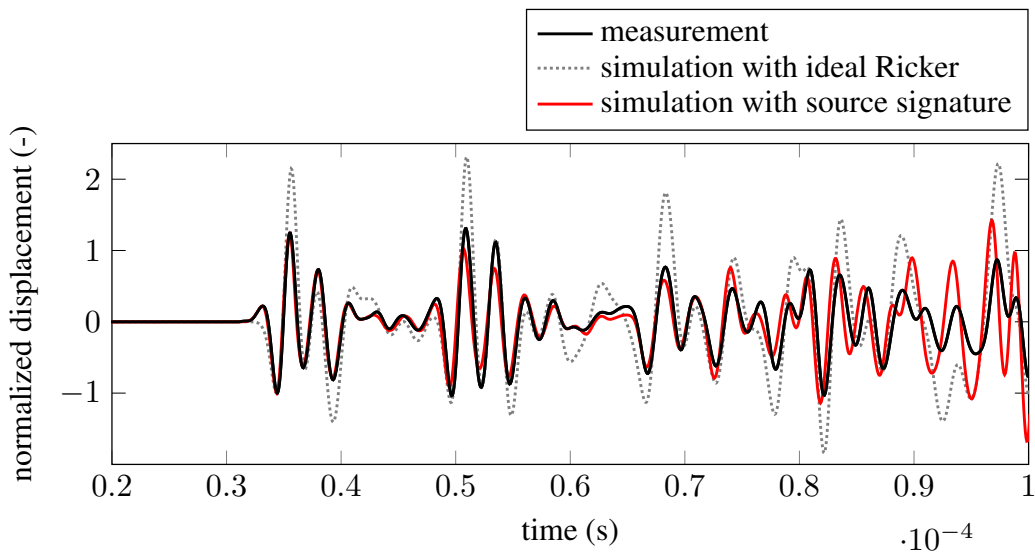
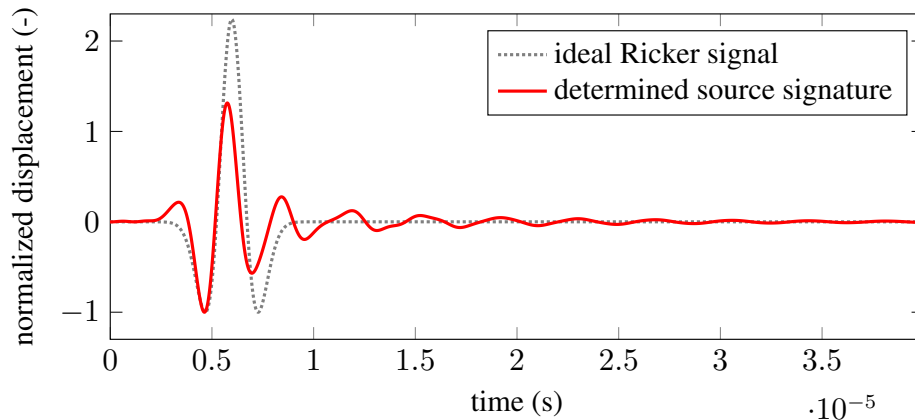


Figure 6.4.: Comparison of the measured waveform, a synthetic waveform generated with an ideal Ricker source function, and a synthetic waveform generated with the determined source signature Figure 6.5a. The wavelets are normalized with their first minima.

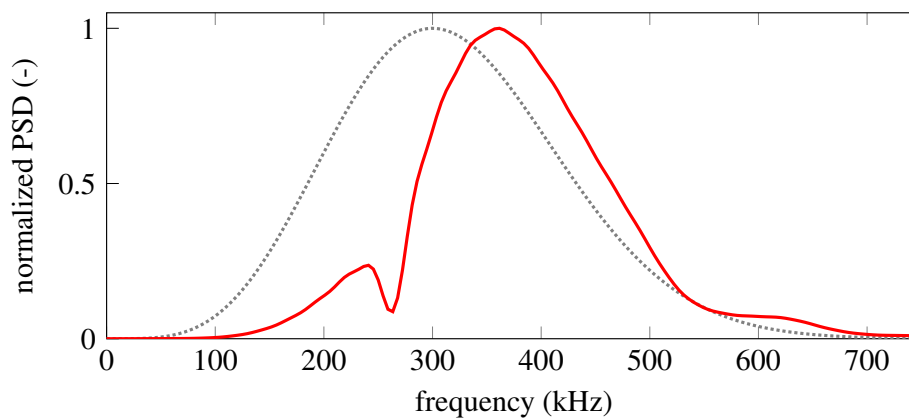
this case since the ideal signal and the experimental signal already have a good agreement. Finally, from Eq. 6.1 and Eq. 6.2 it follows that

$$R_{\text{exp}}(\omega) = \frac{S_{\text{exp}}(\omega)}{S_{\text{syn}}(\omega)} \cdot R_{\text{syn}}(\omega), \quad (6.3)$$

which shows that with the help of the experimental signal response, the synthetic signal response and the ideal source signal, one can derive an estimation of the real source signal in frequency-domain. The source signal in time-domain is obtained by performing an inverse Fourier transform on $R_{\text{exp}}(\omega)$. The result of the source signal estimation is shown in Figure 6.5a, where the derived source function (red) is compared to the ideal source function (grey dotted). Again, the signals are normalized with their first minima. In Figure 6.5b, the PSDs of these signals are illustrated. Note that the shape of the PSD of the source function differs from the PSD determined in Section 4.2. Due to the coupling with the structure, the spectrum is observed to be shifted to higher frequencies. The derived source function in time-domain serves as the input signal for a new simulation with the previously derived model. The red wavelet in Figure 6.4 shows the synthetic signal response. It is observed that the agreement to the measured waveform is improved substantially compared to the wavelet generated with the ideal Ricker signal. The success in achieving a good agreement is a sign of well-fitting material properties and a well-estimated source signature. For the past and



(a) Displacement time data normalized with maximum amplitude.



(b) Power spectral densities normalized with maximum value.

Figure 6.5.: Determined source signature and ideal source signal in time and frequency. The time data is normalized with the first minimum of the wavelets. The PSDs are normalized with their maxima.

the upcoming numerical simulations, the mesh is generated so that Eq. 2.12 is fulfilled, with a maximum frequency of $f_{\max} = f_c \cdot 2.5 = 750$ kHz, where $f_c = 300$ kHz is the central frequency of the Ricker signal. In order to consider the effect of the flat transducer, 50 seismic sources are regularly applied along the contact area of the transducer (see red dots in Figure 6.11)

6.3. Full waveform inversion

6.3.1. UHSA

The main goal of this section is the application of UHSA to the experimentally gained data. UHSA is applied to measurement setup 1 only (Figure 6.3a) in order not to go beyond the scope of this work. An application to measurement setup 2 can be expected to bring a less complex misfit functional due to more seismic receivers and therefore also a distinctly faster convergence. The parametrization of the drilling hole is defined with two center coordinates in the form of $\mathbf{m} = (x, z)$ according to the coordinate system shown in Figure 6.3, where the drilling spreads entirely across the specimen in y -direction. The radius of the hole is not determined as the occurrence of only two inversion parameters brings two advantages for this section – on the one hand, the inversion time remains comparatively low and on the other hand, a visualization of the corresponding misfit landscape is enabled. The working steps of this section are segmented as follows: in the first step, an image of the misfit landscape is generated on the basis of computed misfit functionals for sampled pairs of coordinates. Secondly, UHSA is applied with two different input parameter settings. Thirdly, UHSA is tested against particle swarm optimization (PSO). A single simulation takes 7–8 minutes on average on a 26-core computer with 2.4 GHz each and 96 GB RAM. Since the model domain is remeshed each time a parameter configuration is proposed, the number of elements varies, with an approximate number of 58000 spectral elements. Same as in the previous section, the amplitudes of the simulation are aligned to the amplitudes of the measured data with the factor leading to a minimum gap. The investigated time window is set to $8.8 \cdot 10^{-5}$ s as Figure 6.4 shows a good fit of experimental and synthetic waveforms during that time.

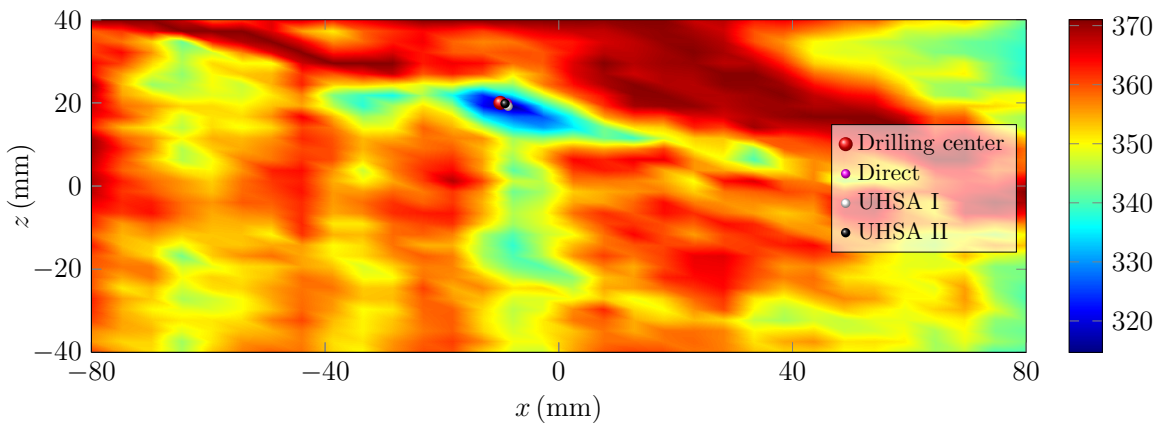


Figure 6.6.: Linear interpolation of the misfit landscape with 1024 parameter configurations and visualization of the determined drilling hole coordinates of each applied method.

The misfit landscape shown in Figure 6.6 is determined by a linear interpolation of 1024 sampled points between bounds of $x \in [-80, 80]$ mm and $z \in [-40, 40]$ mm. The abscissa corresponds to the x -axis in Figure 6.3 and the ordinate to the z -axis. The expected center of the boring at position $(x, z) = (-10, 20)$ mm is marked with the red dot. The inversion outcomes of UHSA with two different settings and the inversion outcome of PSO (which will be generated in the course of the section) are illustrated as well. It is observed that there is a steep global minimum close to the expected center of the boring. Additionally, there are several local minima with, however, distinctly higher misfit functionals. Before starting the inversion, input parameter configurations are set up, where the tuning is explained in Section 3.6. Two examples of UHSA are created with the parameter configurations shown in Table 6.1.

Parameter	UHSA I	UHSA II
\mathbf{m}	(x, z)	(x, z)
\mathbf{U}	$[80, 40]$	$[80, 40]$
\mathbf{L}	$[-80, -40]$	$[-80, -40]$
N_c	40	120
p_0	0.9	0.7
p_e	0.2	0.1
N_k	4	2
\mathbf{P}_0^m	$\text{diag}(4^2, 4^2)$	$\text{diag}(2^2, 2^2)$
\mathbf{Q}	$0.1\mathbf{P}_0^m$	$0.1\mathbf{P}_0^m$
\mathbf{s}_{min}	$0.8\mathbf{s}_u$	$0.7\mathbf{s}_u$
\mathbf{R}	$0.2\mathbf{s}_u \cdot \mathbf{I}_r$	$0.1\mathbf{s}_u \cdot \mathbf{I}_r$

Table 6.1.: Input parameter configurations for UHSA

Configuration 1, also referred to as UHSA I, is set with the aim to find the global minimum during a small number of UHSA cycles. Therefore, both the grade of local exploration and the spread of the sigma points are set relatively high. Furthermore, the general settings of UHSA are set so that many cycles are accepted. Configuration 2, also referred to as UHSA II, is set with a much higher number of UHSA cycles, but a lower grade of local exploration. The UHSA settings in this example are set strict, meaning that many cycles will be rejected during inversion. Thus, in order to find the global minimum, the proposed configuration has to be close to the region of the global minimum as the strict annealing cycle would hinder it from being accepted instead. However, as the number of UHSA cycles is quite high and the minimum region around the global minimum is quite large as well, the global minimum is expected to be found. Figure 6.7 shows the courses of the algorithms on the misfit landscapes for both parameter configurations of UHSA, where the working principle of UHSA can be observed. In regions with a lower misfit functional, more samples are accepted for a local minimization. For most of the accepted parameter configurations, it is observed that the UKF succeeds in moving closer to the neighboring local minimum. This also applies for accepted samples close to the global minimum as these samples move directly into the direction of the hole coordinates. During the later stage of the inversions, the global minimum is intensively explored as the annealing temperature becomes smaller, meaning that computed parameter configurations are more likely close to the parameter configuration with the lowest misfit functional. This effect is more visible for UHSA II as the annealing parameters are set more strictly. Figure 6.8 shows the courses of the misfit functionals and the inversion parameters over the number of UHSA cycles. With Figure 6.7a and Figure 6.8a, the course of UHSA I is analyzed. Due to the applied settings in this example, the rate of acceptance

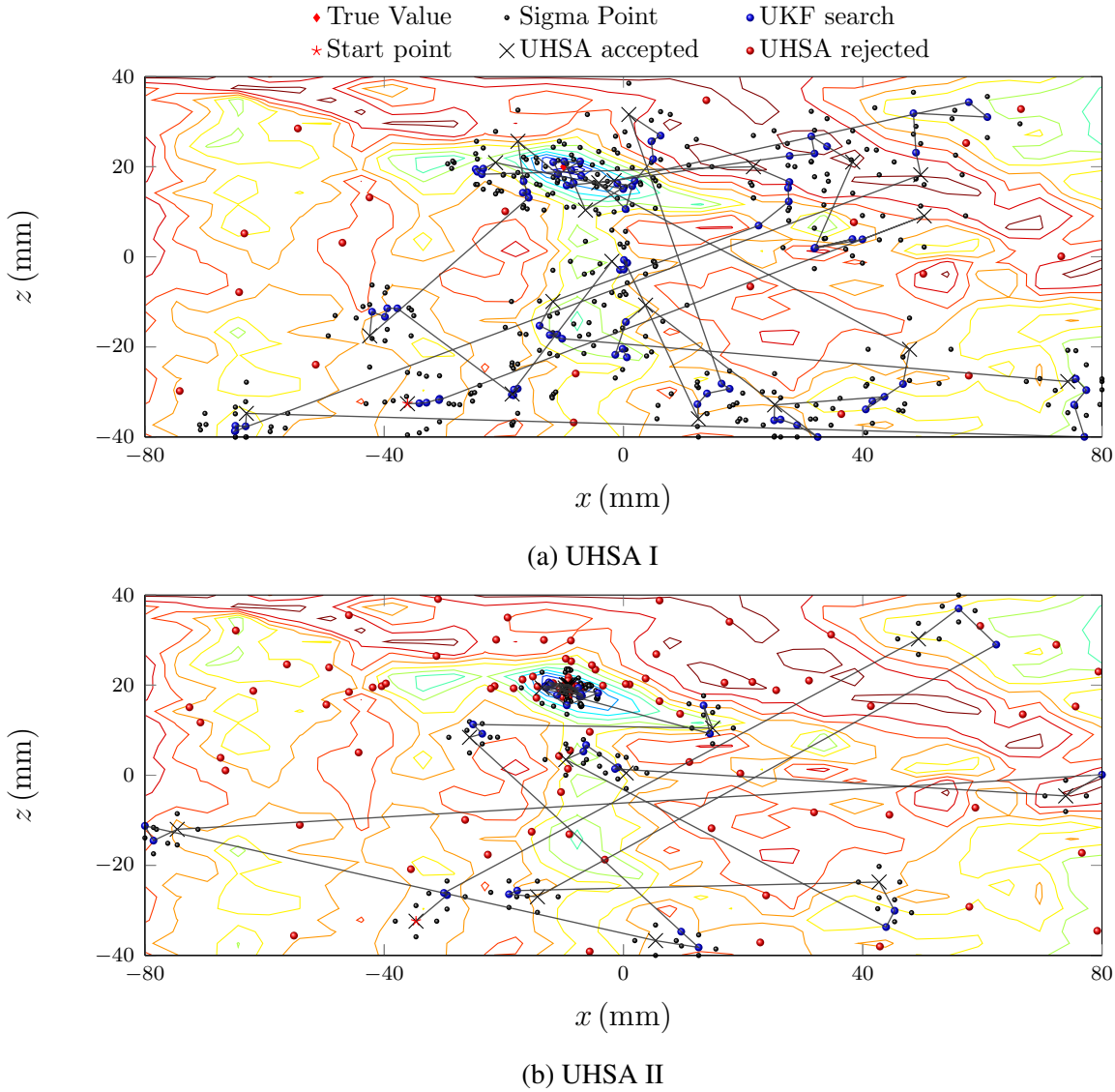


Figure 6.7.: Course of UHSA in the parameter space, plotted onto the predicted misfit landscape

is quite high with 0.55. A parameter configuration close to the global minimum is already found after 14 cycles. However, after 28 cycles, a parameter configuration with an even lower misfit functional is found. During the entire inversion, 460 forward simulations are consumed in about 55 hours of computation time on a 26-core computer with 2.4 GHz each and 96 GB RAM. The course of UHSA II is analyzed with Figure 6.7b and Figure 6.8b. The strict annealing schedule leads to a low acceptance rate of 0.12. After 33 cycles, a parameter configuration close to the global minimum is found. During the further course of the inversion, many parameter configurations with even lower misfit functionals are found. This is a consequence of the strict annealing schedule as the annealing parameter Eq. 3.26 becomes small during the inversion, which leads to many parameter configuration proposals close to the current optimum. The parameter configuration with the lowest misfit functional is found after 106 cycles. During the inversion, 305 forward simulations are consumed during about 35 hours of computation time on the computer described above. The inversion results for both configurations are summarized in Table 6.2. It is found that with both parameter configurations, the global optimum is found with a high precision. The misfit functional is slightly lower for configuration 2 and furthermore, the determined parameter configuration is slightly closer to the expected true coordinates of $(-10, 20)$ mm.

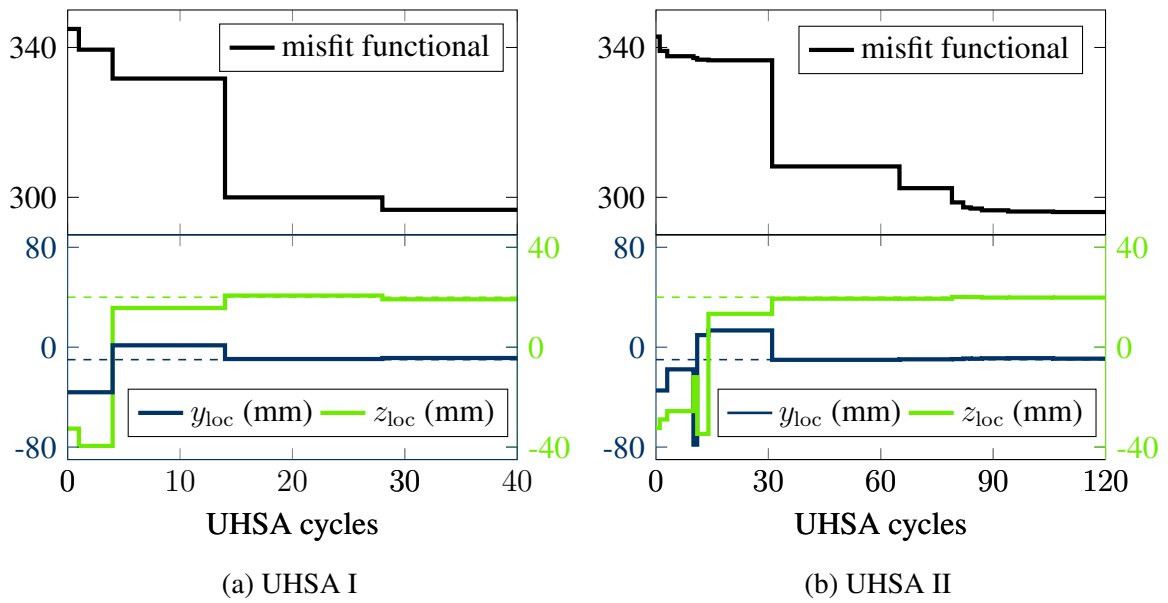


Figure 6.8.: Courses of misfit functionals and inversion parameters over the number of UHSA cycles for configuration 1 and 2. The dashed lines illustrate the respective estimated true values.

Strategy	Coordinates (mm)	Misfit	No. of calculations
UHSA I	(-8.68, 19.17)	296.66	460
UHSA II	(-9.20, 19.84)	296.07	305
PSO	(-8.79, 19.96)	296.91	600

Table 6.2.: Results of the optimizations

In a next step, UHSA is compared to PSO (Eberhart & Kennedy, 1995). PSO belongs to the class of evolutionary algorithms and is inspired by biological swarm intelligence. Same as UHSA, it is a metaheuristic global search approach. The algorithm is implemented as proposed by Garrett (2014) with the same geometric bounds as used for UHSA. The number of generations is set to 12 with a population size of 50. During the inversion, 600 forward simulations are consumed during about 70 hours calculation time on the computer described above. The performances of UHSA and PSO are compared with the final results given in Table 6.2 and with the course of the misfit functionals for all of the three inversion

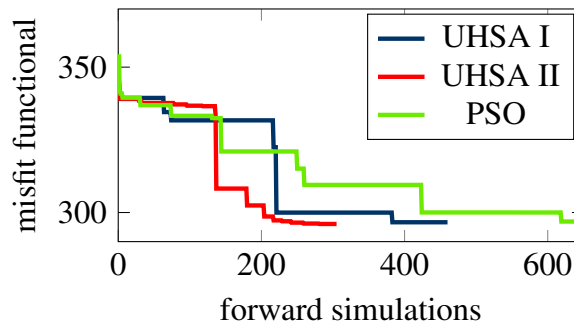


Figure 6.9.: Courses of the misfit functional of UHSA I, UHSA II and PSO over the number of forward simulations.

scenarios shown in Figure 6.9. It is found that the final misfit functional gained with PSO is slightly higher than for both UHSA scenarios, although nearly 1.5 (UHSA I) and 2 (UHSA II) times as many simulations are consumed. The course of the misfit functionals shows better performances of UHSA as well. It is observed that UHSA I and UHSA II reach a level below a misfit functional of 300 after 221 or 204 forward simulations, respectively. PSO needs 424 forward simulations to reach a level slightly higher than 300. Hence, UHSA is found to be more effective than PSO.

6.3.2. UKF-PaLS

This section deals with the application of UKF-PaLS to the acquired data. Thereby, three tests are performed, where in the first scenario, UKF-PaLS is applied to measurement setup 1 (Figure 6.3a) and in the second scenario to measurement setup 2 (Figure 6.3b). In the third scenario, the initial model is changed in terms of the positions of the bumps and UKF-PaLS is applied to measurement setup 2 again. The model domain is discretized with 31250 hexahedral 8-node elements, where the number of elements is much smaller than for UHSA due to the regular meshing. A single simulation takes about 1.5 minutes on a 26-core computer with 2.4 GHz each and 96 GB RAM. For scenarios 1 and 2, $N_b = 150$ bumps are aligned to a regular grid with a dimension of $50 \times 80 \times 40$ mm with a distance of 10 mm to each other in x - and z -direction (where the diameter of the drilling to be detected was 16 mm) and with a distance of 20 mm to each other in y -direction. Prior knowledge is implemented in the form that the disturbance is implemented as a cavity, meaning that elements belonging to the disturbance domain are deleted from the mesh. This secures a rather fast inversion with a relatively coarse mesh as no material properties need to be determined. The dimension of the inversion scenario amounts to $n = 300$ (150 parameters for α and 150 for β), resulting in $2n + 1 = 601$ sigma points to compute during each iteration. The initial parameter configuration is defined by setting the vector $\mathbf{m}_0 \in \mathbb{R}^n$, where the initial parameters and settings of the UKF are given in Table 6.3. The resulting initial model is shown in Figure 6.10. In this figure, it becomes visible that the placement of bumps is advantageous since certain bumps almost lie in the perfect center of the drilling. Note again that the bumps seem to be aligned irregularly since the mesh is not discretized in accordance with the bumps. The upcoming results are produced without a multi-scale approach. An implementation is also

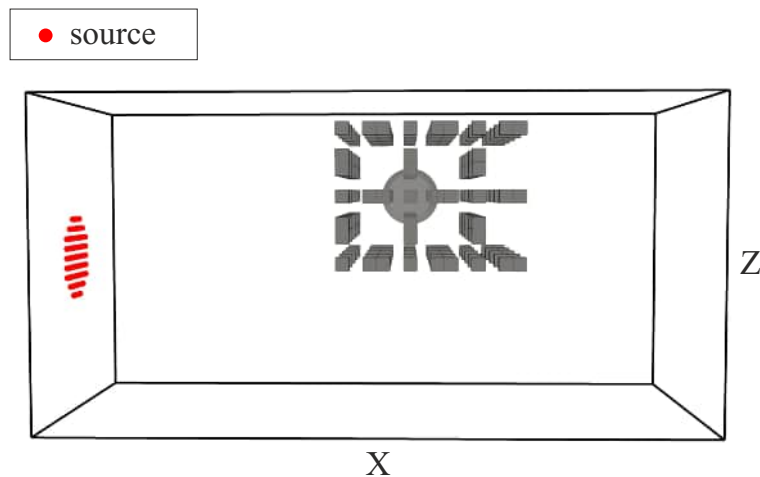


Figure 6.10.: Initial model of UKF-PaLS with borders of the actual drilling hole.

Parameter	Configuration
N_b	150
\mathbf{m}_0	$\{\boldsymbol{\alpha}_0, \boldsymbol{\beta}_0\}$
$\boldsymbol{\alpha}_0$	$1\mathbf{J}_{N_b,1}$
$\boldsymbol{\beta}_0$	$2\mathbf{J}_{N_b,1}$
N_k	20
\mathbf{P}_0^m	$\text{diag}(\mathbf{P}_0^\alpha, \mathbf{P}_0^\beta)$
\mathbf{P}_0^α	$1^2\mathbf{J}_{N_b,1}$
\mathbf{P}_0^β	$0.3^2\mathbf{J}_{N_b,1}$
s_{\min}	$0s_u$
\mathbf{R}	$0.01s_u \cdot \mathbf{I}_r$
\mathbf{Q}	$0.5\mathbf{P}_0^m$

Table 6.3.: Initial model parameters and input parameter configuration for UKF-PaLS. $\mathbf{J}_{N_b,1}$ is a vector of ones of the size of the number of bumps $\mathbb{R}^{N_b \times 1}$

tested; however, the results are less successful than the upcoming. The reason is that, compared to previous examples, the disturbance is smaller (16 mm in diameter) in relation to the operating wavelengths (approximately 1 – 2 cm for the central frequency of the Ricker and the P- and S-wave velocities), so that the higher frequencies are most important for the optimization. Therefore, it is disadvantageous to filter these frequencies until later stages of inversion. Also an uncertainty quantification is left out for the same reasons as in the 3D synthetic examples explained on page 51. In order to prevent double calculations, it is checked prior to each simulation if the current model was already computed before, where this applies to more than half of the computed samples. The current examples are the only examples of this thesis for which this works, where the reason is that no material properties are determined. UKF-PaLS is started for scenarios 1 and 2 with a preset number of iterations $N_k = 20$.

The model corresponding to the parameter configuration with the minimum misfit for scenario 1 is found during iteration 13 and compared to the actual shape of the drilling in light grey in Figure 6.11. It is observed that the core of the drilling is well reconstructed around $y = 0$, where the determined geometry has a similar diameter like the drilling. However, moving towards positive or negative direction of y , the geometry is not well reconstructed. Outside the actual drilling, most of the elements satisfactorily vanish; especially in positive x -direction or in direction of the sources. In negative x -direction, there are more appearances of disturbance material that are not correct. Still, the reconstruction of the middle part of the cylinder is in accordance with the expectations since receivers are placed in plane $y = 0$ only, lacking to bring unambiguous information about the model sides. During the inversion, 4122 forward simulations are consumed, where the inversion takes about 5 days on a 26-core computer with 2.4 GHz each and 96 GB RAM.

Figure 6.12 shows the model corresponding to the parameter configuration with the minimum misfit for scenario 2, which is found during iteration 7 already. The results show a good reconstruction of the drilling all over the dimension of y . Nearly all of the elements outside the disturbance domain vanish, while the elements inside the region of the disturbance domain appear. Even the diameter of the cylinder is well reconstructed. During the inversion, 4066 forward simulations are consumed during a similar computation time as above. For scenario 3, the position of the bumps is changed to a disadvantageous position,

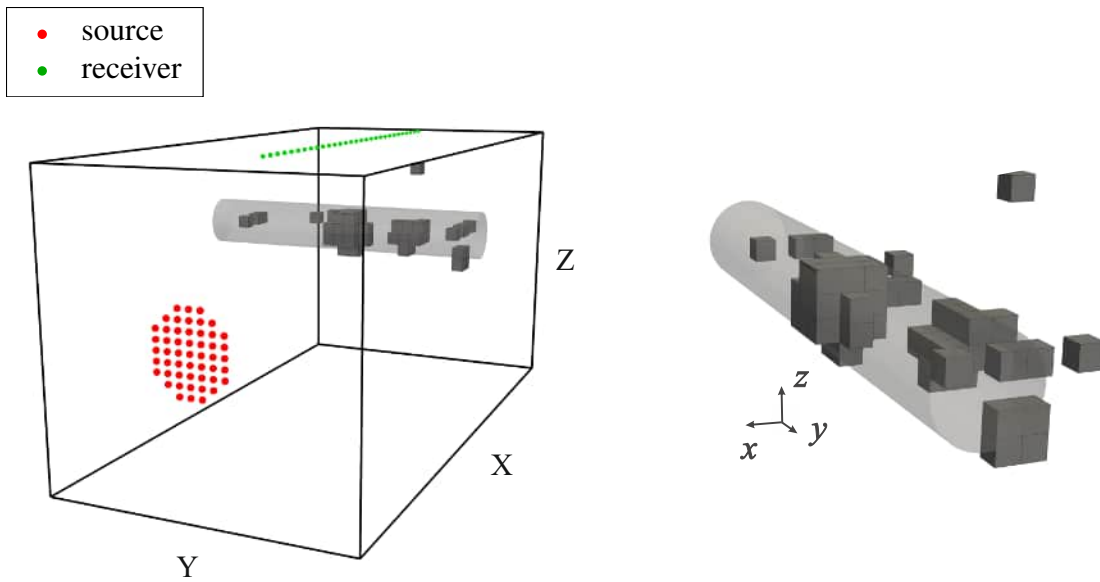


Figure 6.11.: Scenario 1: model corresponding to the parameter configuration with the minimum misfit from two points of view, compared to borders of the actual drilling hole.

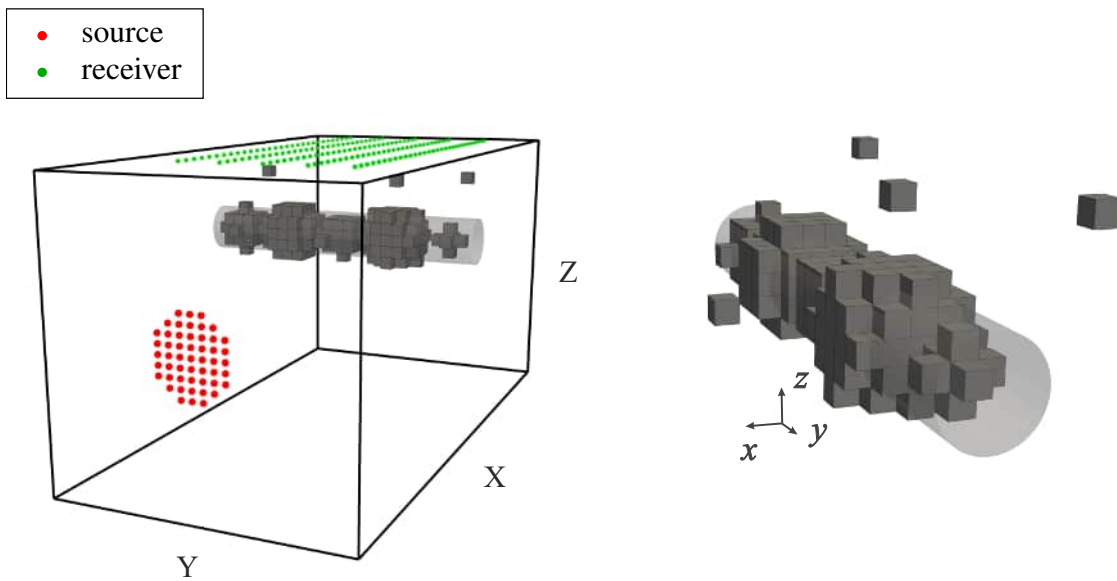


Figure 6.12.: Scenario 2: model corresponding to the parameter configuration with the minimum misfit from two points of view, compared to borders of the actual drilling hole.

where all bumps are moved 5 mm in positive x -direction and 5 mm in positive z -direction. Thereby, the centers of the bumps move to the edge of the drilling hole, which is shown in Figure 6.13 and which has the effect that the corners of the elements are slightly outside of the shape of the true drilling. The settings for the inversion scenario stay the same as in the previous two scenarios. The parameter configuration with the minimum misfit is found after 16 iterations and is visualized in Figure 6.14. It is observed that due to the position of the bumps at the edges of the true disturbance, the drilling is less accurately reconstructed than in scenario 2. Furthermore, most of the material appears in positive y -direction, where the

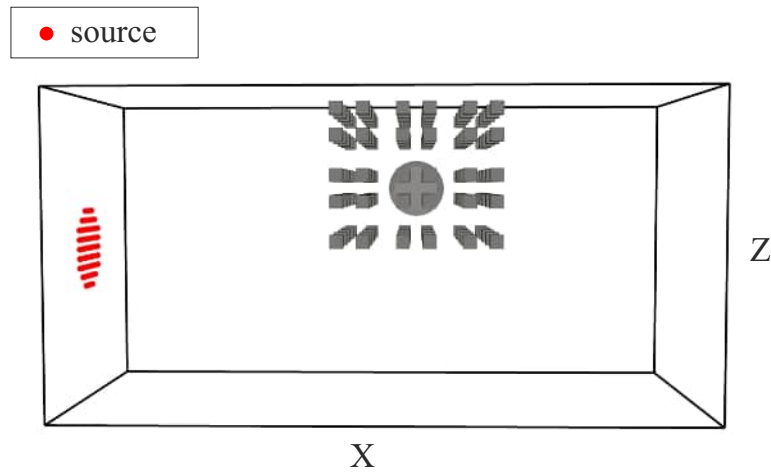


Figure 6.13.: Initial model for UKF-PaLS for scenario 3 with borders of the actual drilling hole.

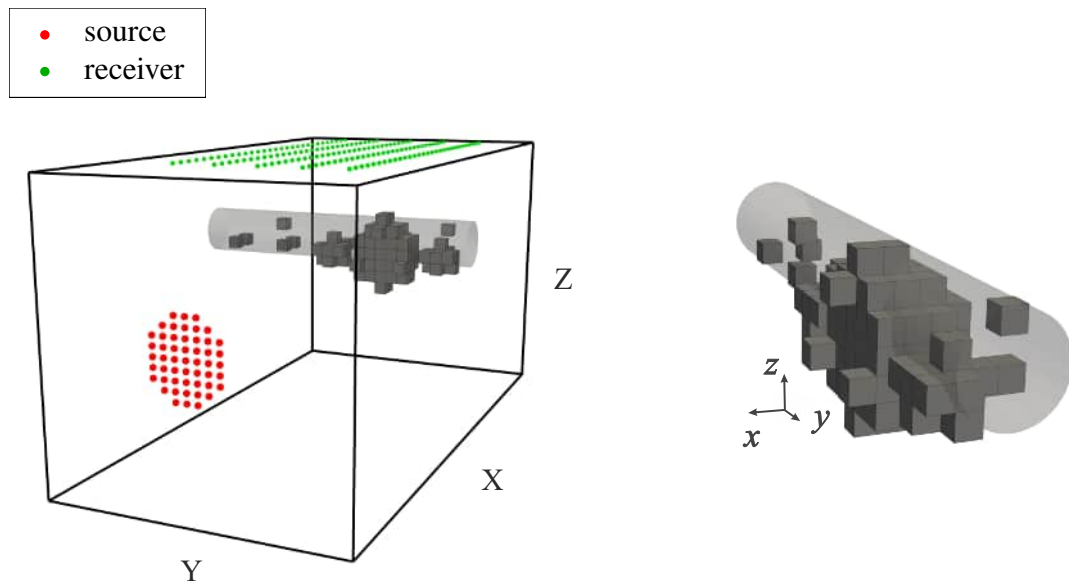


Figure 6.14.: Scenario 3: model corresponding to the parameter configuration with the minimum misfit compared to borders of the actual drilling hole.

origin is unclear. With the determined disturbance domain, the location of the drilling can only be approximately estimated, but is not completely misinterpreted. Therefore, the example shows that a good placement of the bumps is advantageous for the inversion, but that a disadvantageous placement may still bring satisfactory results. If the bumps are placed at the edges of the disturbance only, the filling of the inner core is mathematically complex with the level-set representation. For the current scenario, it is noted that the element size is quite large in relation to the disturbance. In a tunneling setting, the element size is probably much smaller than the disturbance, so that in the case of a high chosen resolution, the placement of the bumps would have a minor impact given that the actual disturbance lies inside the region of investigation. During inversion scenario 3, 4044 forward simulations are consumed. Figure 6.15 shows the courses of the relative misfit functionals over the number of iterations, where the respective misfit functional corresponds to the lowest misfit functional of the respective iteration. For all of the three scenarios, it is observed that the misfit

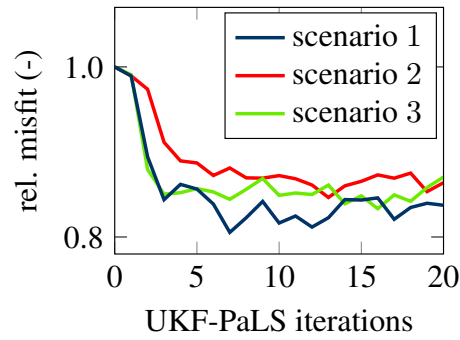


Figure 6.15.: Course of the relative misfit functionals after each iteration of UKF-PaLS. The misfit functionals are normalized with the misfit value of the respective initial model. The plotted value refers to the lowest misfit functional of the iteration.

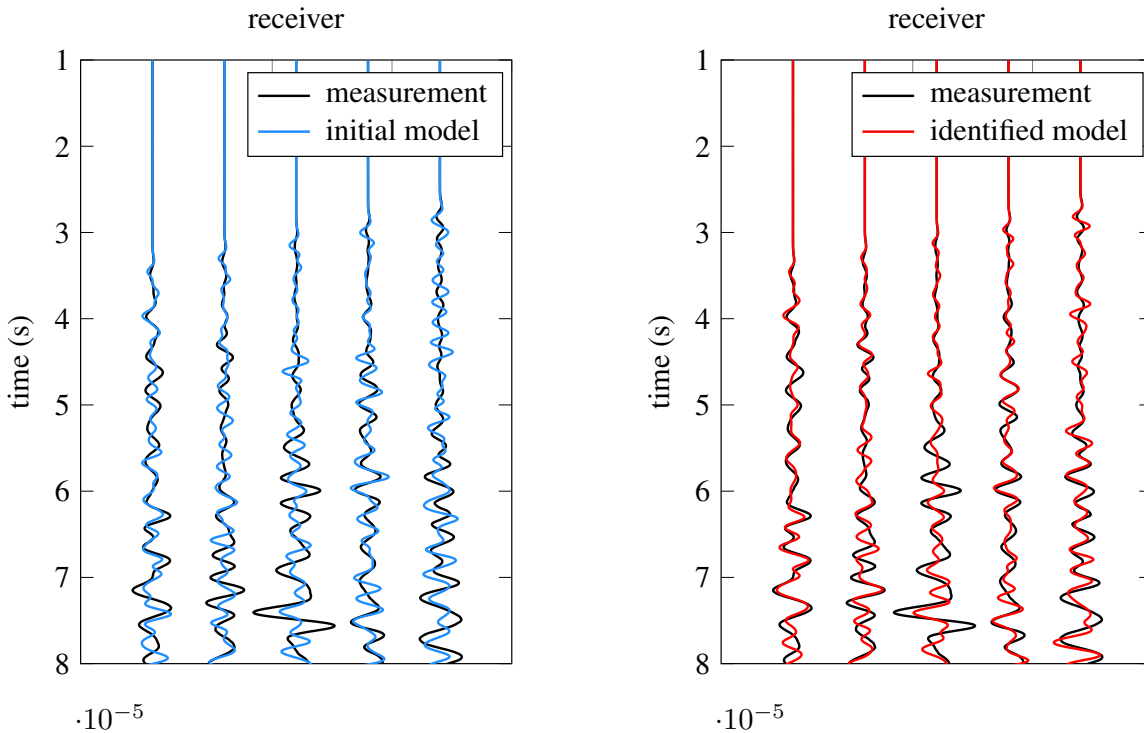


Figure 6.16.: Selected waveforms of the measurement, the initial model, and the identified model resulting from scenario 2. The receiver points are located at positions $(x = \{-90, -80, -70, -60, -50\}, y = 0, z = 50)$ mm

functional is decreasing quickly within the first 5 iterations and then does not change significantly anymore. These observations are in accordance with the findings of the previous chapter, where it turned out that a meaningful minimum is usually found early. Analysis of the results after certain iterations (like in the previous chapter) is left out in this chapter since the scenarios are not very similar to tunneling scenarios compared to the upcoming scenarios. On the example of the model of scenario 2, a comparison of selected waveforms of the initial model, the identified model and the measurement is provided in Figure 6.16. It is observed that the mismatch of the synthetic waveforms and the measured waveforms is substantially reduced in the identified model, although there is still a significant mismatch due to measurement and modeling errors.

6.4. Comparison to results of adjoint full waveform inversion

In this section, the results of UHSA and UKF-PaLS are compared to the results of an adjoint approach. The results of the latter originate from Lamert (2019), where measurement setup 1 (Figure 6.3a) is used as the data set to be inverted. The utilized source function is the one determined previously (red curve in Figure 6.5a); the initial model is a homogeneous model with the dimensions of the aluminum block (Figure 6.2) and with the material properties determined for the background model (see Section 6.2). The elastic wave equation is solved with the nodal discontinuous Galerkin method with a mesh consisting of 285588 tetrahedral elements. As tetrahedrons are utilized, the number of elements is distinctly higher than in the previous examples (around 58000 for UHSA and 31250 for UKF-PaLS). The computation time for one single simulation on a machine with two Intel Xeon E5-2698 v4 processors with 20 cores each and 256 GB RAM on 40 threads is approximately 1.35 hours, which is distinctly larger than for the described methods in this work (around 7.5 minutes for a single simulation in UHSA and around 1.5 minutes for a simulation in UKF-PaLS on a 26-core computer with 2.4 GHz each and 96 GB RAM). Certainly, the computation times cannot be directly compared as the simulations are run on different machines; however, the advantages

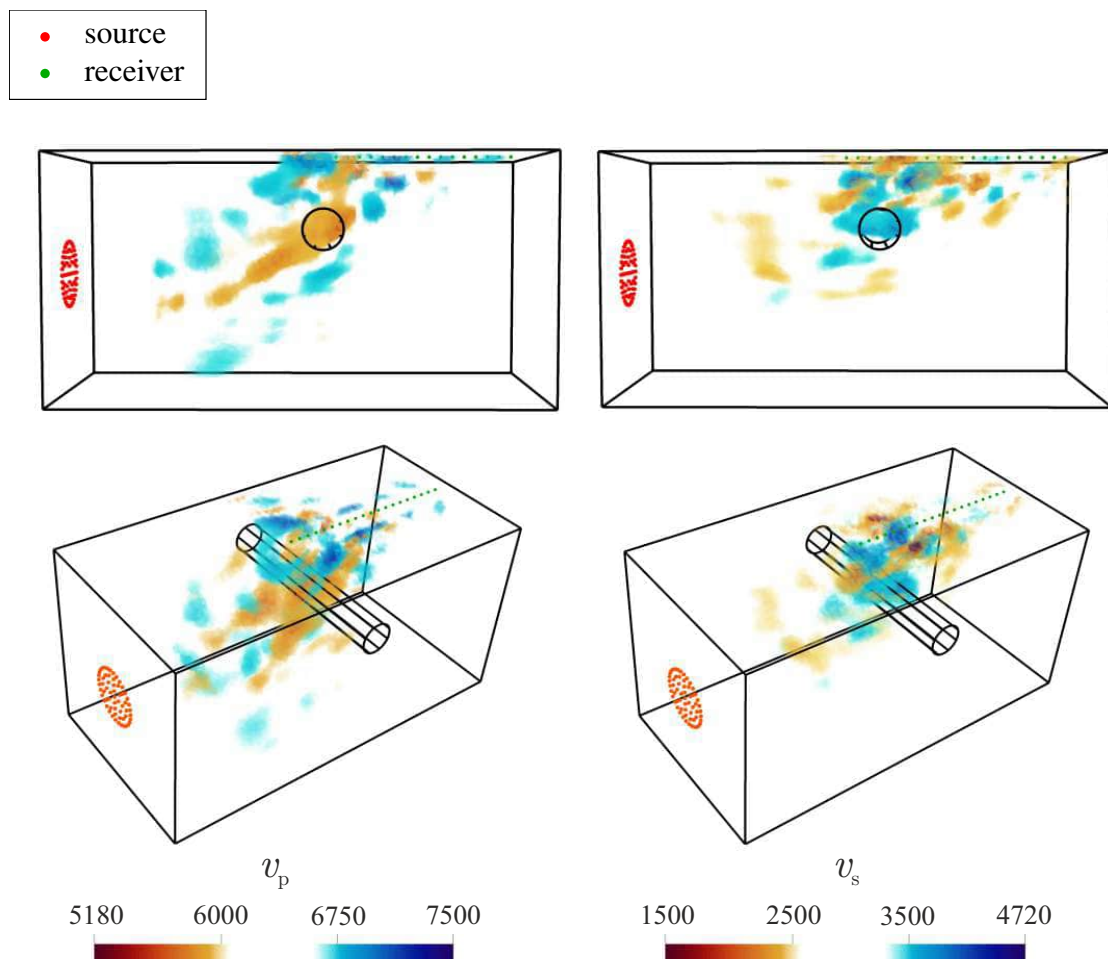


Figure 6.17.: Inversion results with the adjoint method from two points of view, where the true shape of the drilling is illustrated by black lines. The left column illustrates the determined compressional wave velocities and the right column the shear wave velocities.

of the spectral element method in combination with hexahedral elements (Section 2.5.1) lead to the fast computation times of UHSA and UKF-PaLS. Contrary to the two methods applied in this work, no prior knowledge is implemented and no dimensionality reduction is applied in the adjoint approach, so that material properties may vary all over the model domain. Figure 6.17 shows the inversion results of the adjoint approach, where the determined compressional and shear wave velocities are illustrated from two points of view. The true drilling is illustrated by black lines. Around the region of the true position of the drilling, a decrease of the compressional wave velocity is observed. Furthermore, various additional regions of altered wave velocities are visible, especially in the direction from sources to the true position of the drilling. These alterations occur because travel time discrepancies of simulated and experimental waveforms at receivers in source-drilling direction can also be compensated with a reduction of wave velocities somewhere on the path from source to drilling. In the shear wave velocity model, an increase is observed around the region of the true drilling. Assumptions for why an increase rather than a decrease occurs are provided by Lamert (2019). With the two wave velocity models, an inhomogeneity could be indicated, lying in the region of the true drilling. Lamert (2019, p. 100) makes an estimate of the center lying at $(x, z) = (-15.5 \text{ mm}, 24.5 \text{ mm})$ with a radius of 6.5 mm, while the real center is located at $(x, z) = (-10 \text{ mm}, 20 \text{ mm})$ with a radius of 8 mm. The inversion results of UHSA and UKF-PaLS for measurement setup 1 are summarized again in Figure 6.18 in order to gain a better overview. The results for UHSA are those generated with UHSA II since the misfit functional is slightly lower here. Same as for the adjoint illustration, the true shape of the drilling is illustrated by black lines. The inversion results are shown in grey. For UHSA, the reconstruction of the drilling is close to exact with only a very small error. Same as the adjoint method, UKF-PaLS can only reconstruct the object close to $y = 0$ due to the placement of receivers. Here, the location and the radius of the drilling may be estimated well if the reconstructed cube directly below the line of measurement is considered. Also the shape of the drilling is determined quite precisely, with limitations caused by the element size. However, it is noted again that the placement of the bumps was advantageous for the shown case. The number of consumed forward simulations is 485 for the adjoint approach, 305 for UHSA and 4066 for UKF-PaLS (where the optimum is found after 2643 iterations).

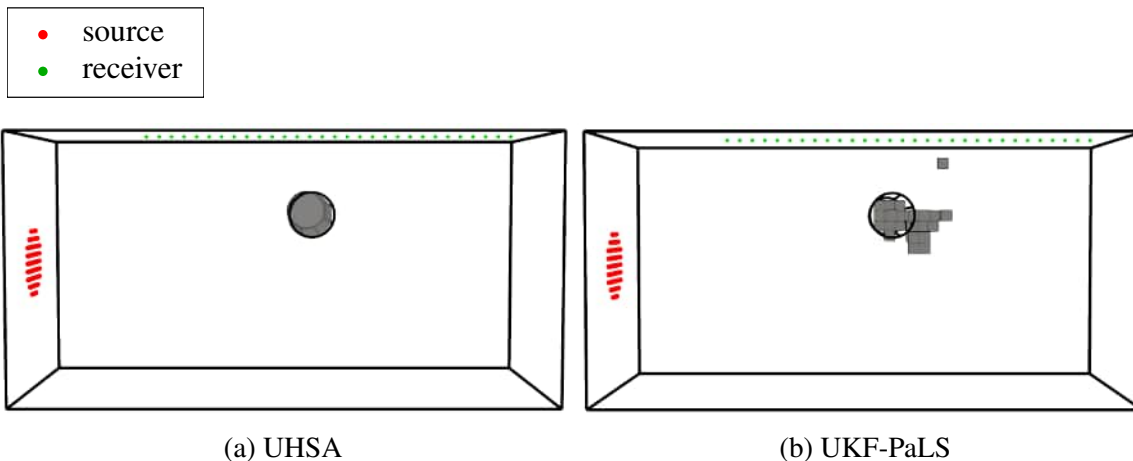


Figure 6.18.: Inversion results of UHSA and UKF-PaLS for measurement setup 1. The true shape of the drilling is illustrated by black lines. The inversion results are illustrated in grey.

A comparison of the methods demonstrates the advantages as well as the limitations of UHSA and UKF-PaLS compared to adjoint methods. The advantage of the two parameter reduction methods is the increased accuracy, which is close to being exact for UHSA and

high for UKF-PaLS. As shown in Figure 6.12, the accuracy for UKF-PaLS may be further improved if more receivers are utilized. Unfortunately, this is not tested for the adjoint approach. The limitations of the non-gradient methods lie in the parameter reduction. For UHSA, a parametrization of the disturbance needs to be derived that specifies the shape of the drilling. Therefore, prior knowledge is necessary, which may not always be available. For UKF-PaLS, no prior knowledge about the shape of the disturbance is necessary. However, prior knowledge is implemented in the form that the marked elements directly implement a cavity (which would, of course, be different in a tunneling scenario). Furthermore, the bumps need to be positioned by the user, determining the region of investigation and a resolution. The method seems quite restrictive and dependent on prior knowledge when considering the current scenario, but is however less restrictive for real tunneling environments where the element size would be much smaller in relation to the disturbance. There, the placement of the bumps would have a minor impact if the resolution would be selected high enough and if the disturbance would lie inside the region of investigation (see the examples of Chapter 5). Gains and restrictions of the methods, also in regard of further improvement, will be further discussed in Section 10.4. Both for UHSA and UKF-PaLS it can be stated that with the conducted dimensionality reduction, the exactness of the inversion is improved compared to the adjoint approach. However, a parameter reduction, especially as applied for UHSA, might not always be applicable. Due to the utilization of the spectral element method, UHSA and UKF-PaLS perform distinctly faster than the adjoint approach, where however the number of forward simulations is distinctly higher for UKF-PaLS than for the adjoint approach. For UHSA, it is slightly lower.

6.5. Short summary and discussion

This chapter deals with the first validation of UHSA and UKF-PaLS with experimental data. The object of investigation is an aluminum block with a drilling to be determined. Ultrasonic measurement data are acquired and an adequate forward model is constructed, including a successful strategy in order to estimate the source signature. With the applied parameter reduction in UHSA, a nearly exact determination of the drilling hole center coordinates is achieved. Compared to a standard PSO, the computational effort remains low. With the parameter reduction applied in UKF-PaLS, a good approximation of the drilling is found as well, improving substantially if more receivers are utilized. A good placement of bumps is shown to be advantageous, but a disadvantageous placement may still bring satisfying results in terms of approximately locating the object. For both scenarios, low minima in the misfit functional are found early, which shows once more that a prediction of the subsoil properties may happen early as well. The comparison with the adjoint approach shows that a parameter reduction may improve the inversion result if applicable. For a more representative comparison, the methods should be compared based on tunnel environment examples. A comparison of UKF-PaLS to the adjoint approach for 2D synthetic scenarios is provided by Lamert *et al.* (2018), where however, the multi-scale approach was not included in UKF-PaLS. Therefore, the inversions performed quite long and the results were not that accurate.

7. Imaging of anomalies in concrete plates

This chapter deals with the imaging of structural anomalies in concrete plates with UHSA. This is one step further towards FWI in mechanized tunneling since firstly, concrete may be seen as a rock-like material and secondly, not only the shapes, but also material properties are determined. Three concrete plates are poured in order to validate the method with experimental data. The reasons for manufacturing concrete plates instead of larger specimens are firstly a fast manufacturing process and secondly fast simulation times. Similar to the procedure in the previous chapter, ultrasonic measurements are performed and an adequate forward model is constructed before UHSA is applied to the data. In order to validate the performance of UHSA again, the algorithm is compared to a genetic algorithm for one of the specimens. The results are published in Trapp & Nestorović (2020); however, the work is rewritten and the pictures and figures are changed or edited substantially. An investigation with UKF-PaLS is left out of this study since the first implementation of this method was conducted later (first in Chapter 8 for the 2D case and then in Chapter 5 and Chapter 6 for the 2D and 3D cases), where the stage of validation of UKF-PaLS is already judged high.

7.1. The experiment

The basis of the investigations are three self-manufactured concrete plates with dimensions $0.5 \times 0.5 \times 0.024$ m. Into each concrete plate, a different anomaly is included. Figure 7.1 shows the concrete plates in a 2D view. The disturbance of the first specimen has the shape of a cylindrical hole with no material inclusion. The second specimen includes two materials that are separated by a linear material change. The third specimen shows a material inclusion of approximate rectangular shape. In preliminary tests, various concrete mixtures are poured before their corresponding material properties are determined. Thereupon, two

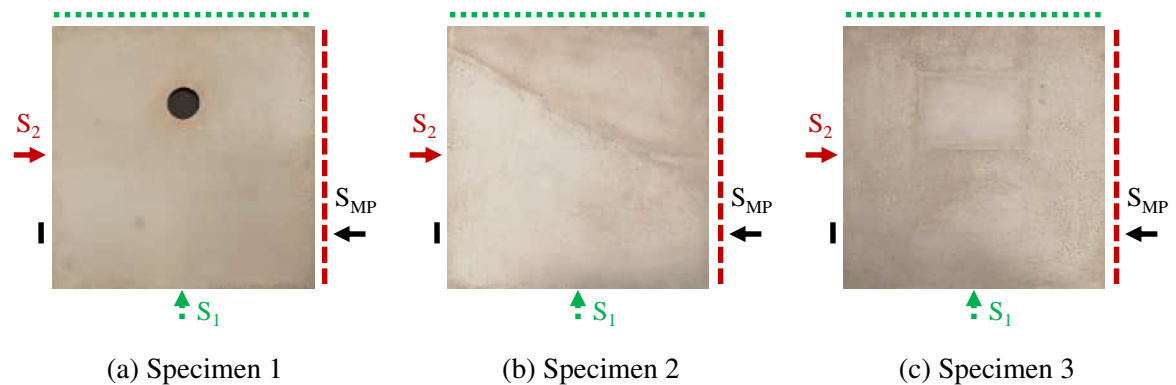


Figure 7.1.: Investigated concrete plates with measurement configurations illustrated by green dotted and red dashed lines. The black measurement setup serves for the determination of the background material properties.

mixtures for the background and disturbance materials are selected, which are to differ distinctly in the determined wave velocities in order to induce a clear material contrast, but also not overmuch since a large difference would lead to a large computational demand during FWI. The selected background material is a concrete topping with a mixture ratio *cement/sand/gravel/water* of about 0.5/1/1/0.25 with sand grains from 0 to 1 mm and gravel grains from 1.2 mm to 8 mm. The selected disturbance material is a combination of a mortar for brickwork mixture (mixture ratio *cement/limestone/dust/sand/water* of about 0.12/0.07/1/0.42) and the above-mentioned concrete mixture in the ratio *concrete/mortar* 1/0.7. The compressional wave velocities of the two materials differ in about $750 \frac{\text{m}}{\text{s}}$, with a slower velocity for the disturbance material which is a consequence of the higher amounts of sand and water. The disturbance material is used to pour an additional but homogeneous plate in order to be able to estimate the material properties as exact as possible for validation purposes. Figure 7.2 shows two perspectives of the experiment.

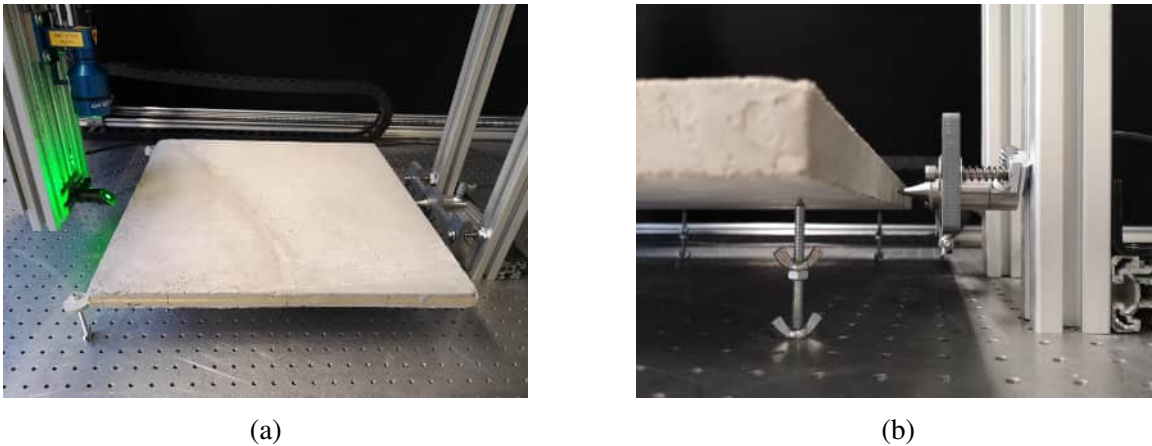


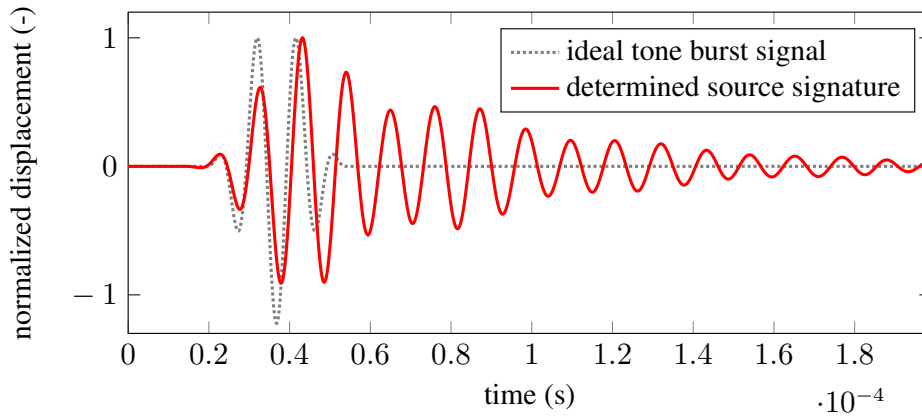
Figure 7.2.: Photos of the experiment from two perspectives

In order to increase the repeatability and the SNR, leaf gold is applied to the side surfaces of the concrete plates as validated and investigated in Section 4.3. The reason for the choice of gold is that the idea of using aluminum tape as a reflector occurred later. Same as in Chapter 6, the concrete plates are placed on sharpened threaded bars and a holding with springs serves for the application of a contact pressure, where counterbalances are placed at the opposite side of the specimen. Similarly, also here, the impact of the bearing on the measurements can be expected to be low (see page 57), where even the impact of the transducer as an interfering object is expected to be low due to the point contact. On each concrete plate, two measurement setups are acquired, consisting of 2 sources and 982 receiver locations in total. The measurement setups are illustrated in Figure 7.1. The sources are placed in the middle of the side surfaces and represented by the green dotted (S_1) and red (S_2) arrows. The laser measurements are acquired along two 0.49 m long lines in 1 mm distances, illustrated by the green dotted and the red dashed lines. The laser focus is aimed to run along the middle of the side surfaces with the height of the contact point of the ultrasonic transducer. The measurement is achieved with a mirror redirecting the laser beam. An additional measurement setup is acquired on each plate in order to be able to determine the material properties of the background material. These sets are illustrated in black (source S_{MP}) and consist of 41 measurements along 0.04 m long lines. As one can observe in the figures, the configurations are chosen so that direct waves are distant to the disturbance in order to perform a suitable background material property determination. The source signal for each measurement setup is a 3.5-cycle Hanning windowed tone burst signal with a central frequency of 100 kHz excited with the ultrasonic transducer B 0.1NN by GE Measurement &

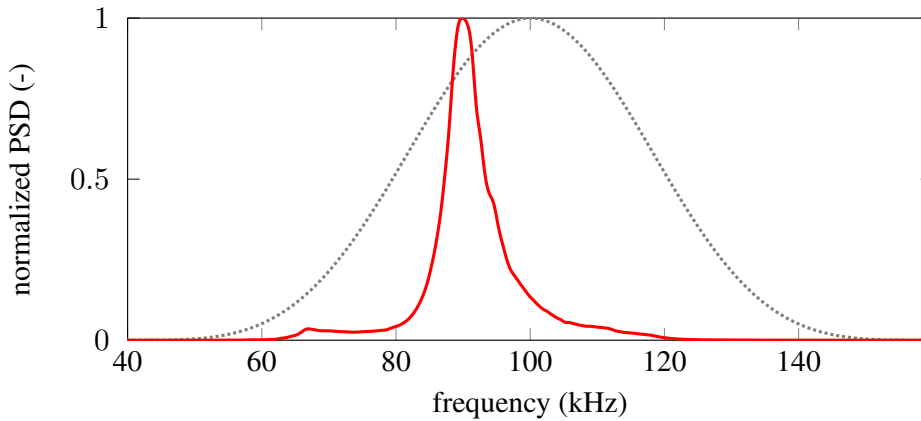
Control Solutions, where the reasons for choosing this kind of signal are explained in Section 4.2. Although the characteristic peak of the transducer was found to be slightly lower, the 100 kHz tone burst is utilized in order to increase the amount of higher frequencies in the signal. According to the findings of Section 4.3, measurements are repeated about 100 times and stacked. However, there are still some poor measurements that arise due to the measurement on porous surfaces. Moving over grains and pores, the focus of the laser varies, and the reflection can be weak. Therefore, traces are carefully observed and deleted if they are apparently poor. Note that this problem can be reduced applying aluminum tape instead of leaf gold (which, as explained above, had not yet been established at the time of conducting the experiment). The offsets of the traces are removed by subtracting the average amplitudes before waveform arrival. Furthermore, bandpass filters are applied with cutoff frequencies of 10 and 170 kHz.

7.2. The forward model

Same as in the previous chapter, the geometrical model is built and implemented into Trelis, where all model boundaries obtain free boundary conditions. The determination of the source signature is performed differently since an estimation as proposed in Section 6.2 is found to be difficult for the current scenarios. The reason is that the match between synthetic and measured waveforms is not high enough. Thus, the source signature is estimated experimentally by a transducer-on-source measurement. The peak of a second transducer, which is also a B 0.1NN, is placed at the peak of the source transducer in order to measure the source function directly. The advantage in using such a signal compared to a laser-on-source measurement is that the transducer is coupled with a structure already. However, a laser-on-source measurement incorporates the time delay or dead time of the measurement system. For this reason, the obtained transducer-on-source measurement is aligned to a laser-on-source measurement on the time axis. Implementing this aligned signal into the simulation, the time delay of the system is incorporated into the simulation and no adaption along the time axis needs to be performed. Figure 7.3 shows the experimentally determined source signature compared to the ideal source signal in time and frequency. It is observed that the frequency content of the estimated source signature is shifted slightly to lower frequencies, which is expected to be mainly due to the lower frequency range of the transducer. After the experimental estimation of the source signature, the background material properties are to be determined. The determination is conducted with the aid of the black measurement setups in Figure 7.1. As explained before, the measurement setups were chosen to be distant from the anomalies to minimize their influence on the data. Therefore, a model of an undisturbed (homogeneous) model is set up for the material property determination. Since the durations of the signals are set to a small time window in which amplitudes do not decay much, the material is again chosen to be elastic, where the gain is a reduced computational demand. Same as in Section 6.2, a database with a gridded variation of v_p and v_s is created and the material property set with the minimum misfit functional is selected. The determined compressional wave velocities of all the three concrete plates lie between $3550 \frac{\text{m}}{\text{s}}$ and $3690 \frac{\text{m}}{\text{s}}$ with shear wave velocities between $2330 \frac{\text{m}}{\text{s}}$ and $2360 \frac{\text{m}}{\text{s}}$. A comparison of synthetic and experimental measurements for the measurement setup generated with source S_{MP} for specimen 1 is shown in Figure 7.4. It is observed that the overall agreement of measured waveforms and synthetic waveforms is high despite numerous sources of errors, which are explained in the upcoming section. For the past and the forthcoming



(a) Displacement time data normalized with maximum amplitude.



(b) Power spectral densities normalized with maximum value.

Figure 7.3.: Experimentally determined source signature and ideal source signal in time and frequency.

numerical simulations, the mesh is generated so that Eq. 2.12 is fulfilled with a maximum frequency of $f_{\max} = 150$ kHz, where f_{\max} is chosen so that most of the energy of the signal is contained within the frequency range between 0 and f_{\max} (compare Figure 7.3b). The observation time window is set to $3 \cdot 10^{-4}$ s.

7.3. Full waveform inversion - UHSA

In the following, UHSA is applied to the previously gained data sets. For each of the scenarios, a parametrization of the disturbance is set up, which is expected to be able to approximately describe the disturbance. For the hole in specimen 1 those are two location coordinates and the size of the hole in terms of the radius. For the definition of the linear change in specimen 2, the parametrization is set to a location coordinate defining the center of the linear change, the angle of the linear change with respect to a reference line and the disturbance material properties. For the rectangular disturbance in specimen 3, it is set to two location coordinates of the geometric center of the disturbance, two edge lengths and the disturbance material properties. For the description of the latter, a simplification is made which was also applied in Section 5.2.2. During inversion, only the compressional wave velocity of the disturbance $v_{p,d}$ is determined where the shear wave velocity is computed with an assumed value for the Poisson's ratio of $\nu_d = 0.15$. This value is chosen since it is

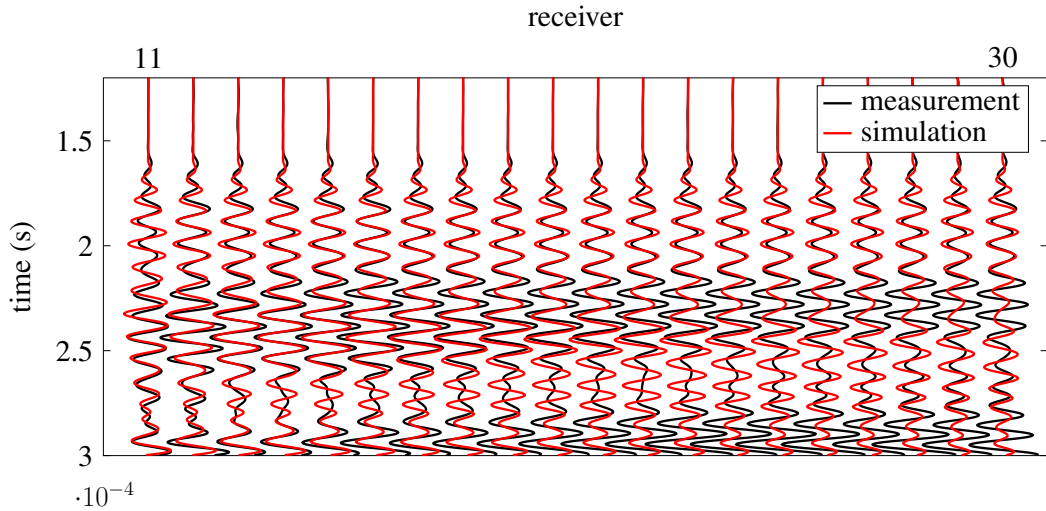


Figure 7.4.: Comparison of experimental (black) and synthetic (red) waveforms for the middle 20 receivers of the measurement setup generated with source S_{MP} for specimen 1 according to Figure 7.2

a common value for concrete and since it is close to the Poisson's ratio of the background material. Thereby, the number of material properties to be determined is reduced to one, also decreasing the computational demand. The compressional wave velocity of the homogeneous specimen with the disturbance material of specimens 2 and 3 (see Section 7.1) is estimated with the same technique as described in the previous section and determined to lie at $v_{p,d} = 2856 \frac{m}{s}$. This value is referred to as the expected true value of the disturbance material compressional wave velocity in the following. Besides the above-mentioned simplification, a second one is made, where the density of the disturbance material is set to the same value as the density of the background material, which again reduces computational demand. This is expected to be valid since the disturbance material consists of a similar material. The two simplifications may cause some errors in the form of both amplitude mismatches and smaller phase errors. However, these errors are expected to be rather small. Depending on the inversion scenarios, both simplifications could also possibly be made during an application in mechanized tunneling.

Prior to the inversion, the whole simulation data set is scaled with a factor in such a way that the largest simulation amplitudes are similar to the amplitudes of measurements at measurement points with a rather low displacement. This leads to lower amplitudes of simulations compared to measurements for most of the waveforms, which can be observed in Figure 7.7. The reason for this procedure is that if simulation amplitudes are scaled higher than the amplitudes of measurements, it is observed that the inversion may tend towards wrong results with late waveform arrivals (where late waveform arrivals are for instance caused by large anomalies with low wave velocities). This issue is explained with aid of Figure 7.5. The black lines illustrate an exemplary waveform measurement at one receiver point, where both subfigures show the same black curve. The red lines illustrate two exemplary simulation waveforms, where their effect on the misfit shall be compared. The waveforms on the left-hand side show a perfect normalized correlation, where the simulation is scaled with a scaling factor of slightly larger than 2 respective to the measurement. The resulting misfit functional (Eq. 3.6) amounts to $S_1 = 1$, where the waveform difference is marked with grey color for illustration purposes. The right-hand side shows a lately arriving simulation signal. Although the normalized correlation between measurement and simulation is bad, the misfit is, with an amount of $S_2 = 0.87$, lower than for the left-hand case (where the grey area

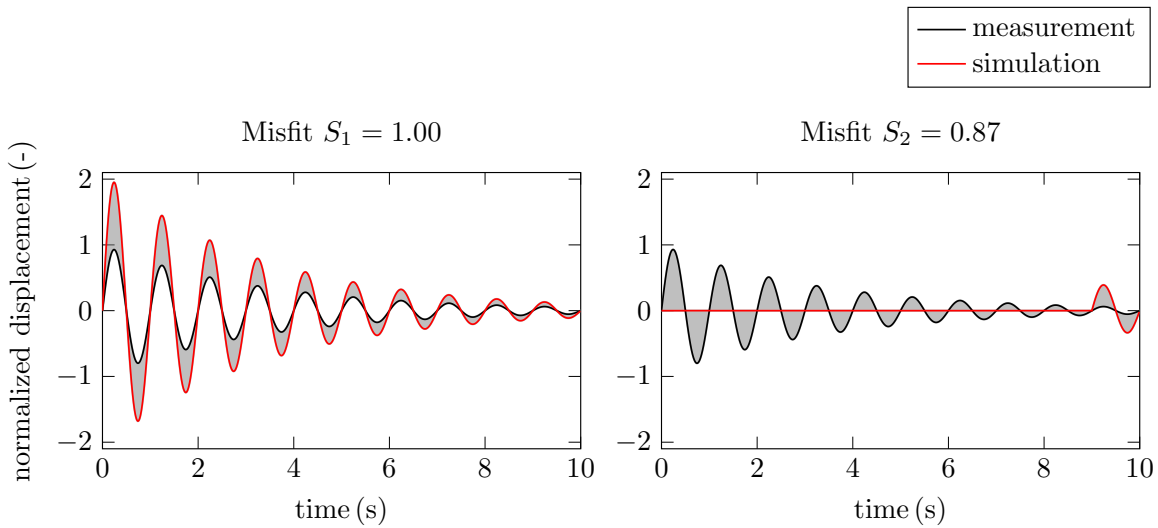


Figure 7.5.: Illustration of misfit values for two scenarios with the same exemplary measurements. On the left, the misfit functional is higher despite a perfect normalized correlation. Choosing a high scaling factor can hence bring the inversion to false results with late waveform arrivals (like on the right-hand side).

is larger). Hence, if the scaling illustrated on the left-hand side would be applied, UHSA would tend to results with lately arriving signals like shown on the right-hand side due to the lower misfit functional. Note that this effect becomes stronger if the normalized correlation is not perfect. Furthermore, since many receivers with varying amplitudes are used for the UHSA inversion, a scaling to comparatively low simulation amplitudes is necessary.

In order to test the performance of UHSA in the case of a disadvantageous initial model, the parameters of the initial model are set distant from the expected real parameters. Input parameter configurations for all of the three scenarios are given in Table 7.1. For all of the inversion scenarios, there are numerous sources of errors or inaccurate results, which are all related to modeling and measurement errors. The primary sources of error are (List 7.1):

- imprecise approximations of the background material properties
- imprecise approximations of the source signature
- an inaccurate simulation model in terms of geometry and source/receiver locations
- inhomogeneities, anisotropies, attenuation and dispersion effects of the real model which are not imaged by the simulation model
- errors related to the measurement (e.g. weak signal due to porous surfaces)
- noise contained in the measurements
- inaccurate approximations of the expected true parameters
- an insufficient parametrization: the parametrization of the disturbance may not be able to capture all details of the experimental model
- small numerical errors

List 7.1.: Main sources of error during inversion

	specimen 1	specimen 2	specimen 3
\mathbf{m}	$[y_{\text{loc}}, z_{\text{loc}}, r]$	$[z_{\text{loc}}, \Phi, v_{\text{p,d}}]$	$[y_{\text{loc}}, z_{\text{loc}}, b, h, v_{\text{p,d}}]$
\mathbf{U}	$[0.2, 0.2, 0.06]$	$[0.15, 80, 4500]$	$[0.15, 0.15, 0.25,$ $0.25, 4000]$
\mathbf{L}	$[-0.2, -0.2, 0.02]$	$[-0.15, -80, 2000]$	$[-0.15, -0.15, 0.03,$ $0.03, 2000]$
N_{c}	200	200	200
p_0	0.8	0.8	0.9
p_e	0.01	0.01	0.1
N_{k}	3	3	4
\mathbf{P}_0^m	$\text{diag}(0.005^2, 0.005^2,$ $0.002^2)$	$\text{diag}(0.0065^2, 3.5^2,$ $50^2)$	$\text{diag}(0.006^2, 0.006^2,$ $0.006^2, 0.006^2, 35^2)$
\mathbf{Q}	$0.3\mathbf{P}_0^m$	$0.3\mathbf{P}_0^m$	$0.3\mathbf{P}_0^m$
\mathbf{s}_{min}	$0.8\mathbf{s}_{\text{u}}$	$0.8\mathbf{s}_{\text{u}}$	$0.5\mathbf{s}_{\text{u}}$
\mathbf{R}	$0.2\mathbf{s}_{\text{u}} \cdot \mathbf{I}_{\text{r}}$	$0.2\mathbf{s}_{\text{u}} \cdot \mathbf{I}_{\text{r}}$	$0.1\mathbf{s}_{\text{u}} \cdot \mathbf{I}_{\text{r}}$

Table 7.1.: Input parameter configurations for UHSA

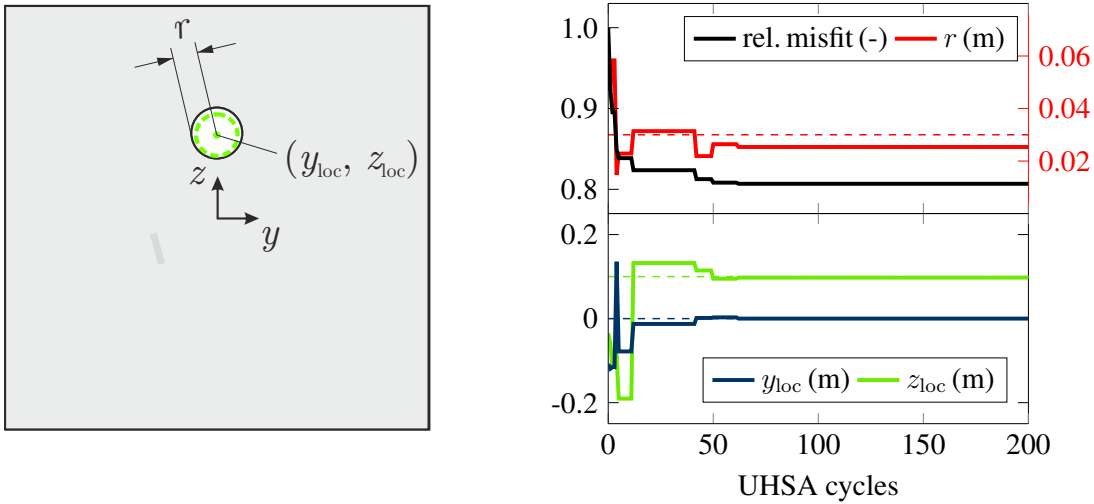
7.3.1. Hole localization

For the imaging of the hole in specimen 1, three inversion parameters are set to describe the disturbance – two location parameters y_{loc} , z_{loc} and one size parameter, which is set to be the radius r of the hole. The definition of the parameters is illustrated in Figure 7.6a. With comparatively small values for p_0 and p_e , the UHSA cycles are set relatively strict, meaning that many parameter configurations are rejected during the course of UHSA. Due to the low number of inversion parameters, this is expected to be sufficient. For the same reason, the grade of local exploration is set weak with only three UKF cycles. \mathbf{s}_{min} and \mathbf{R} are tuned so that the jumps between the UKF cycles remain small in order to obtain a high precision. UHSA is run for 200 cycles. Table 7.2 shows the final values of the determined parameters compared to the expected true value as well as the absolute error. The shape of the reconstructed disturbance is illustrated in Figure 7.6a by the green dashed circle.

inv. parameter	exp. true value	inv. result	abs. error
y_{loc} (m)	0	0.0001	0.0001
z_{loc} (m)	0.1	0.0976	0.0024
r (m)	0.03	0.0254	0.0046

Table 7.2.: Inversion results of specimen 1: inversion parameters, expected true values, inversion results and absolute error

The resulting absolute errors as well as the shape of the determined disturbance show that the parameters are determined precisely. However, the radius of the disturbance is slightly underestimated. The reasons for that lie, on the one hand, in the numerous sources of error explained in List 7.1, with its main reasons evolving from modeling errors. On the other hand, the frequency spectrum of the ultrasonic transducer is quite limited around 90 kHz, where a broad frequency range would make the inversion problem better posed. However, the results are satisfactory. The course of the relative misfit functional as well as the pa-



(a) Geometry in grey with inversion parameters; determined shape of the disturbance illustrated by the green dashed circle

(b) Course of the relative misfit and parameter configurations over the number of UHSA cycles. The dashed lines illustrate the respective estimated true values.

Figure 7.6.: Specimen 1 – geometry with parameters and inversion results

parameter configurations over the number of UHSA cycles are shown in Figure 7.6b. Here, it is observed that a good value for the radius r is already found after 12 cycles, which then diverges from the expected true result (red dashed line) in the next jump. This may seem confusing, but as the misfit landscape is highly multimodal, certain values may improve and then worsen throughout the inversion process because the other inversion parameters are not well estimated. The decisive factor is always the combination of all inversion parameters and the corresponding misfit functional. After 62 cycles or 812 forward simulations per source, the final result is reached. During the 200 UHSA cycles, 1528 forward simulations

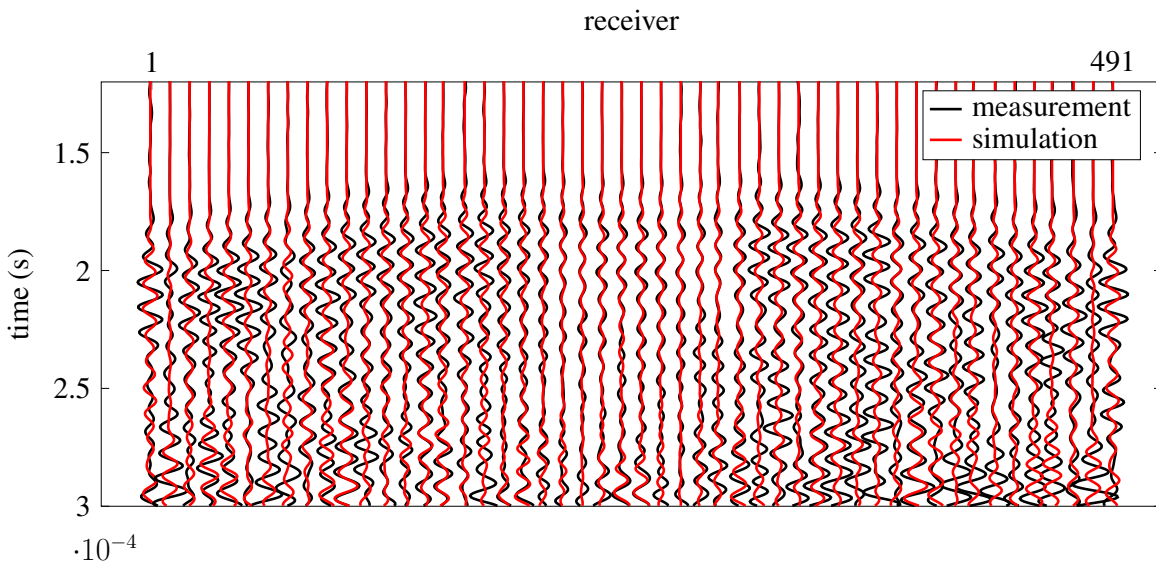
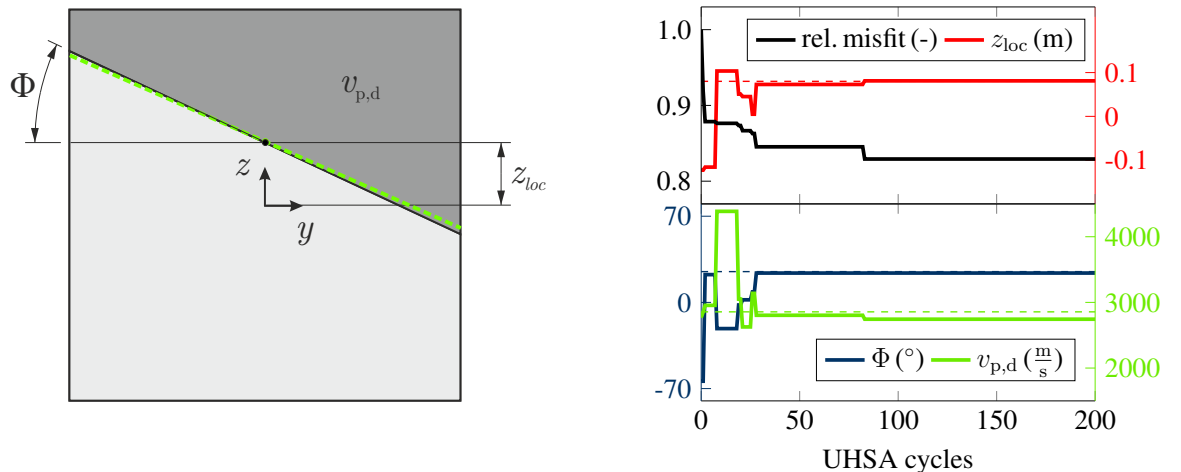


Figure 7.7.: Ultrasonic (black) and simulated (red) waveforms for every 10th receiver of the measurement setup acquired with source S_1 on specimen 1 (see Figure 6.2). The synthetic waveforms are computed with the optimum parameter configuration found by UHSA.

per source are required. The UHSA acceptance rate is 0.325, meaning that approximately one-third of the parameter configuration proposals are accepted for local UKF minimization. The computation time is 18 hours on a 26-core computer with 2.4 GHz each and 96 GB RAM. With the optimum parameter configuration, synthetic waveforms are computed and compared to the measurements in Figure 7.7, exemplary for every 10th receiver of the measurement setup acquired with source S_1 on specimen 1. Despite the numerous sources of error, it is observed that the experimental and synthetic waveforms show a high degree of accordance in both phases and even amplitudes. Modeling errors in terms of geometry, wave velocities and the estimated source signature are the main reasons for errors in phases. Measurement errors are expected to have a high contribution to amplitude mismatches since laser reflections may be poor if encountering uneven and porous locations, leading to correct phases but inaccurate amplitudes. Observing the middle receiver points in Figure 7.7, the impact of the hole is directly visible due to reduced amplitudes.

7.3.2. Detection of a linear material change

For the imaging of the linear material change in specimen 2, three inversion parameters are set. The location of the disturbance is described with coordinate z_{loc} according to the coordinate system in Figure 7.8a, while parameter Φ describes its angle. The material properties are, as previously explained, reduced to the compressional wave velocity $v_{p,d}$. Since the number of inversion parameters is again three, the general settings for UHSA as well as the settings for the UKF of scenario 1 are maintained. Again, UHSA is run for 200 cycles. The final values of the determined parameters, the expected true value as well as the absolute error are shown in Table 7.3. The shape of the reconstructed disturbance is illustrated in Figure 7.8a by the green dashed line.



(a) Geometry in grey with inversion parameters; determined shape of the disturbance illustrated by the green dashed line

(b) Course of the relative misfit and parameter configurations over the number of UHSA cycles. The dashed lines illustrate the respective estimated true values.

Figure 7.8.: Specimen 2 – geometry with parameters and inversion results

It is observed that the geometry of the disturbance is determined highly accurate. Moreover, also v_p is determined quite accurately, although it is slightly underestimated. The source of

inv. parameter	exp. true value	inv. result	abs. error
z_{loc} (m)	0.08	0.0811	0.0011
Φ ($^\circ$)	25	23.8384	1.1616
$v_{\text{p,d}}$ (m/s)	2856	2744	112

Table 7.3.: Inversion results of specimen 2: inversion parameters, expected true values and inversion result

this error is again a combination of the reasons listed in List 7.1, with a strong aspect being also an inaccurate estimation of the expected true value. Figure 7.8b shows the course of the relative misfit functional and the parameter configurations over the number of UHSA cycles compared to the expected true values. Already in a very early stage of the UHSA inversion, the angle Φ and the compressional wave velocity $v_{\text{p,d}}$ are estimated well. However, the location of the disturbance is distant from the expected true value, leading to incorrect arrival times and a high misfit functional. Thus, the algorithm jumps to a parameter configuration with a lower misfit value and diverges from the expected true values for Φ and $v_{\text{p,d}}$. After 28 UHSA cycles or 395 forward simulations per source only, a satisfying parameter configuration is obtained. The best result is found after 83 cycles or 1110 forward simulations per source. At this stage, the compressional wave velocity diverges from the expected true result, which is most likely due to a wrong estimation of the latter as well as modeling errors. During the 200 cycles, 1419 forward simulations per source are required with an acceptance rate of 0.325. The computation time is 16 hours on a 26-core computer with 2.4 GHz each and 96 GB RAM.

UHSA is compared to PSO in Section 6.3.1, where UHSA turns out to be more effective in the presence of two inversion parameters. In this subsection, it is compared to another optimization algorithm – genetic algorithm (GA) – in the presence of the three inversion parameters describing the disturbance in specimen 2. Same as UHSA, GA is a metaheuristic global search algorithm. A detailed description of GA as well as the historical context of the algorithm is provided by Mitchell (1998). GA is widely studied on numerous applications and there exist numerous comparisons to SA (Kerr & Mullen, 2019) (Ingber & Rosen, 1992), which is included in UHSA. There are even hybrid GA-SA approaches for the application to optimization problems (Goldberg *et al.*, 1990). In this work, a standard GA is set up with the same conditions as for UHSA. The investigations are performed on specimen 2 as this scenario is seen to have a higher relevance than the scenario for specimen 1 since also material properties are determined. For specimen 3, the comparison is not performed because of expected long computation times due to the higher number of inversion parameters. GA is conducted with a uniform crossover and a rather small Gaussian mutation within the borders which are also used for UHSA. The population size is tuned to 200 with 50 mating parents. 12 generations are computed in total, resulting in 2000 forward simulations per source. The courses of the relative misfit functionals over the number of forward simulations per source for both GA and UHSA are illustrated in Figure 7.9. Figure 7.10 shows the course of the relative misfit and parameter configurations of GA over the number of forward simulations per source compared to the expected true values.

Note that also here it is observed that single parameters converge to the expected true value and then diverge again until the convergence of all of the parameters is secured. In GA, this effect becomes even more visible due to the uniform crossover and resulting large jumps. In order to make a comparison of the courses of the inversion parameters of GA and UHSA,

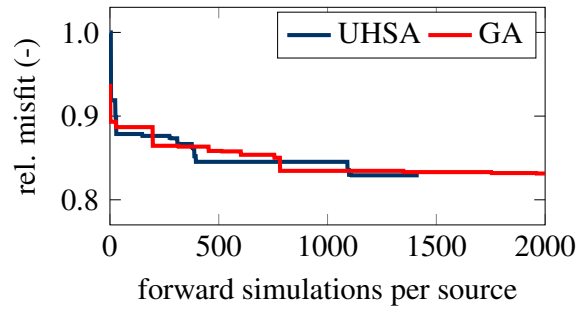


Figure 7.9.: Courses of the normalized misfit functionals of UHSA and GA over the number of forward simulations per source. The misfit functionals are normalized with the value of the initial model of UHSA.

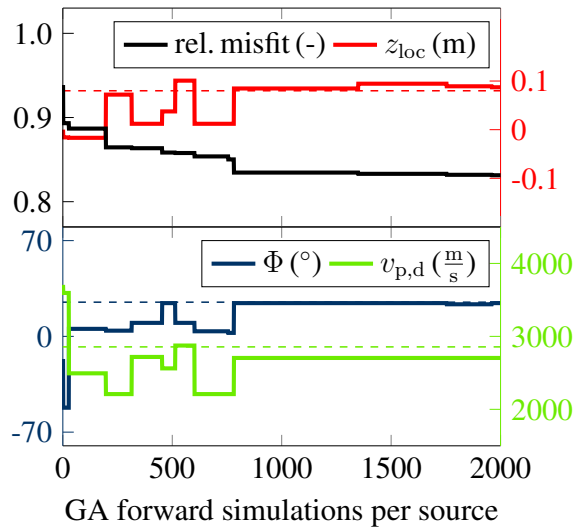


Figure 7.10.: Course of the parameter configurations over the number of forward simulations per source for GA. The dashed lines illustrate the estimated true values.

readers are again referred to Figure 7.8b. The first 200 parameter configurations for GA are selected randomly. Thus, by coincidence, the initial model of GA is slightly better than the initial model of UHSA. However, this does not have an impact on the inversion result as GA is based on random and global exploration. As described previously, a satisfying result of UHSA is found after 395 forward simulations per source. In Figure 7.9 and Figure 7.10 it is observed that GA requires nearly twice as many forward simulations per source to come to a result close to the expected true values. However, at this stage, the misfit functional becomes lower than the minimum misfit value reached by UHSA. After 1110 forward simulations per source, the misfit of UHSA becomes lower again. GA cannot reach this value during the overall inversion, although it comes close to it. The determined parameters of GA are $z_{\text{loc}} = 0.0872 \text{ m}$, $\Phi = 24.3167^\circ$, $v_p = 2704 \frac{\text{m}}{\text{s}}$ and thus, the final result does not differ noteworthy from the determined parameters of UHSA. Summarized, it is observed that UHSA can also outperform GA for this example. UHSA brings a satisfying result during a lower number of simulations and furthermore, a smaller minimum is found after 1419 forward simulations per source, which cannot be reached after the 2000 forward simulations per source of GA.

7.3.3. Detection of a rectangular disturbance

In order to image the rectangular disturbance in specimen 3, five inversion parameters are set. The center of the rectangle is specified by two location coordinates y_{loc} and z_{loc} according to the coordinate system in Figure 7.11, while parameters b and h specify the width and height of the rectangle. The compressional wave velocity is, same as in the previous section, specified with parameter $v_{p,d}$. The general preferences of UHSA are set less strict than in the previous scenarios, meaning that more cycles are accepted for UKF minimization. The necessity for this lies in the higher number of inversion parameters in this scenario, which makes the global minimum harder to find. Similarly, local exploration is set more intense. Same as in the previous scenarios, UHSA is run for 200 UHSA cycles. The final values of the determined parameters, the expected true value as well as the absolute error are shown in Table 7.4. The shape of the reconstructed disturbance is illustrated in Figure 7.11 by the green dashed rectangle.

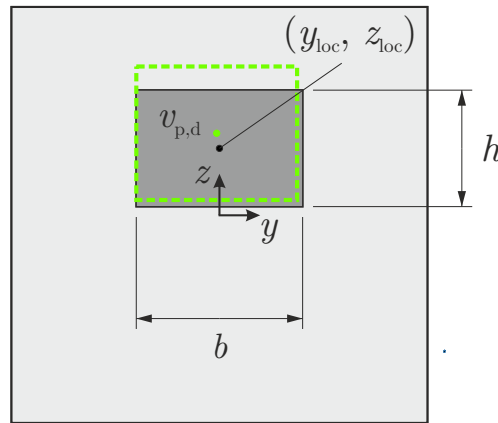


Figure 7.11.: Specimen 3 – geometry with parameters and inversion result: Geometry in grey; determined shape of the disturbance illustrated by the green dashed rectangle.

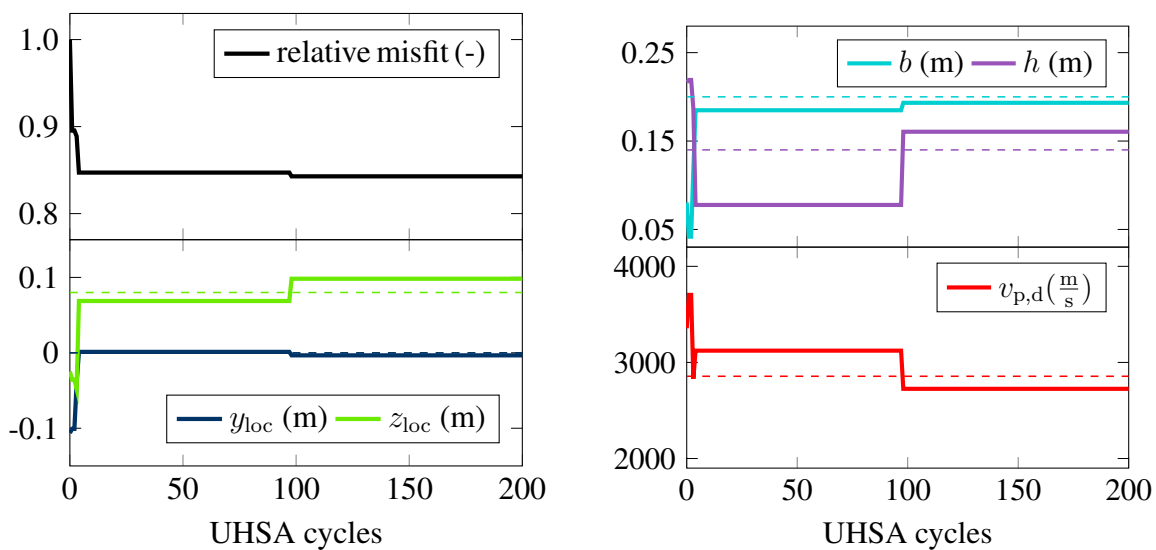


Figure 7.12.: Course of the relative misfit functional and parameter configurations over the number of UHSA cycles. The dashed lines illustrate the respective estimated true values.

inv. parameter	exp. true value	inv. result	abs. error
y_{loc} [m]	0	-0.0033	0.0033
z_{loc} [m]	0.08	0.0982	0.0182
b [m]	0.20	0.1933	0.0067
h [m]	0.14	0.1605	0.0205
$v_{p,d}$ [m/s]	2856	2725	131

Table 7.4.: Inversion results of specimen 3: inversion parameters, expected true values and inversion result

Also in this scenario, all of the inversion parameters are determined with a satisfying precision, but absolute errors larger than in the previous two examples exist. The largest deviations occur in the determination of parameters z_{loc} and h with errors of about two centimeters each. Also in this example, reasons for this are the sources of error listed in List 7.1. Furthermore, the borders of the disturbance in the experimental model are slightly curved, meaning that the parametrization is not able to fully describe the disturbance. The reason for this lies in the manufacturing process, where the background material is let into the mold when the disturbance material is still wet. Another consequence of the merging is that reflections coming from the disturbance are suspected to be weak, which also may cause a small error. Furthermore, due to the higher number of parameters, the inversion scenario is more difficult, meaning that the actual global minimum may be more distant from the estimated minimum than in the previous two examples. Figure 7.12 shows the course of the relative misfit functional and the parameter configurations over the number of UHSA cycles. It is observed that a good approximation of the position is achieved in a very early

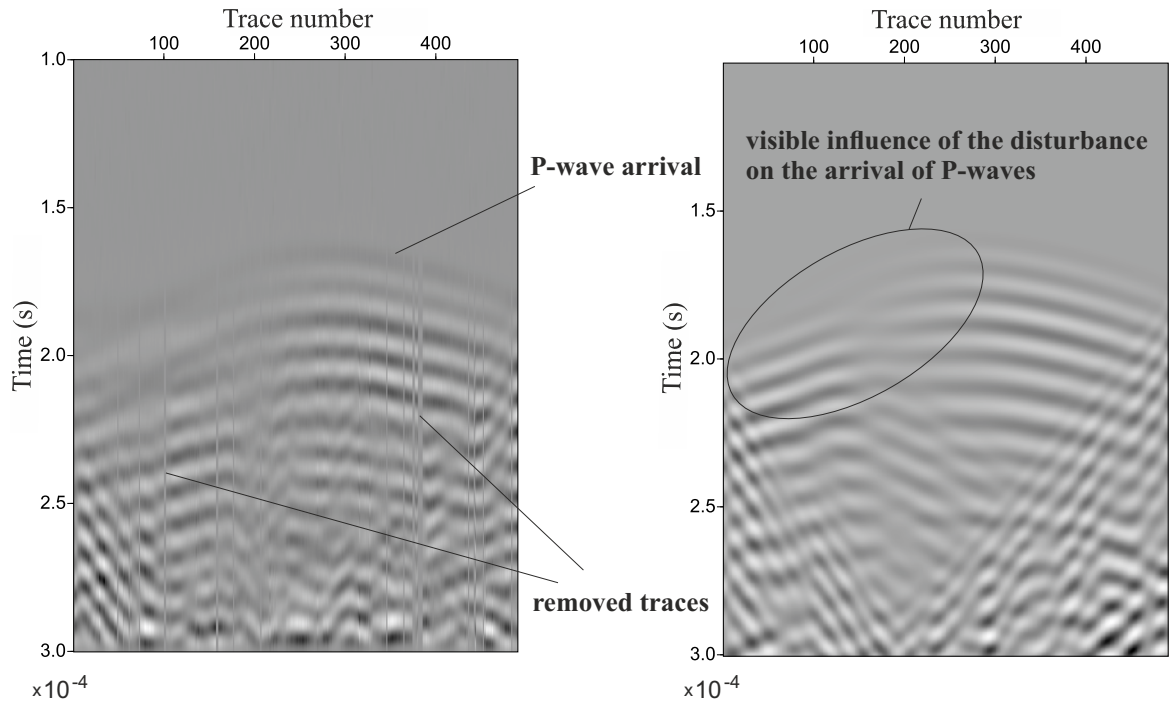


Figure 7.13.: Experimental (left) and simulated data (right) for the measurement setup generated with source S_2 on specimen 3. Traces from left to right are acquired along the red line in Figure 7.1c from top to bottom. The synthetic data is gained with the final results of UHSA (Table 7.4).

stage of the inversion; however, the error in the determined shape is large at this stage. After 98 annealing cycles (2899 forward simulations per source) the final result is found. In total, 4767 forward simulations per source are required with an acceptance rate of 0.605. The computation time is 36 hours on a 26-core computer with 2.4 GHz each and 96 GB RAM. Figure 7.13 shows the experimental ultrasonic data (left) compared to the synthetic data (right) for the measurement setup generated with source S_2 . The traces from left to right correspond to the measurements acquired along the red dashed line in Figure 7.1c from top to bottom. In the ultrasonic data set, the previously described removal of noisy traces is visible. The influence of the disturbance can be observed best in the arrival of the direct (P-)waves. A high degree of accordance of the two data sets is observed especially for the first periods. For later periods, it decreases since the sources of error List 7.1 have a higher impact when also indirect waves come into play.

7.4. Short summary and discussion

In the second stage of experimental validation, UHSA it applied in order to image disturbances in concrete plates. Ultrasonic data is successfully acquired with techniques evaluated in Section 4.3 and a forward model is constructed with similar methods as in Chapter 6, where however the source function is measured directly. Positions, shapes, and material properties of the disturbances are determined with a high precision and UHSA can outperform a standard GA algorithm in terms of computational effort as well as in terms of converging to a lower minimum. Obviously, the conducted scenarios cannot be compared to field models in terms of geometries and source-receiver configurations, but still, concrete may be regarded as a rock-like structure, which is one step closer to field scenarios. Furthermore, for the latter two scenarios, the parametrization of the disturbance can be compared to parametrizations which may come up in mechanized tunneling in the form of a boulder or a layer change, respectively. Although simplifications are made concerning the density of the disturbance and the shear wave velocity, the inversions succeed, which reveals a hint that the simplifications might also be made during an application in mechanized tunneling. Same as in the previous examples of this work, meaningful results are reached at an early stage during inversion, showing that a first prediction could be performed early.

8. Imaging of a layer change in a concrete block

The scenarios of the previous chapter served as a first validation of the developed methods with rock-like materials, where however the shapes of the experimental models differed significantly from actual tunneling setups. Therefore, an experimental model with more similarities to tunneling models is to be constructed. A specimen is designed in such a way that a 2D numerical model can be set up in order to approximate the measured waveforms. The resulting decrease in computational effort allows to make investigations on source-receiver configurations as well as to validate both UHSA and UKF-PaLS with different of those source-receiver configurations. The chapter starts, same as in the previous chapters, with the experiment and the forward modeling, before the inversion scenarios are performed. After that, the comparability of the small-scale experiment to field models is analyzed. The results of this chapter are already published in Trapp & Nestorović (2021); however, the work is rewritten and the pictures and figures are changed or edited substantially.

8.1. The experiment

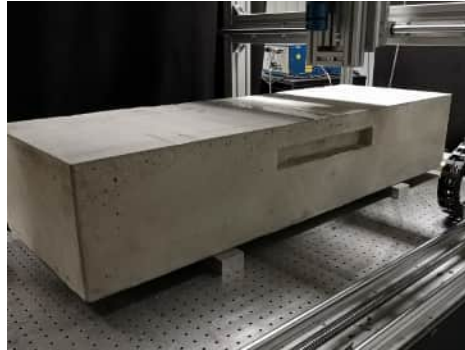


Figure 8.1.: Picture of the specimen

The manufactured specimen is a concrete block into which a linear material change is incorporated (see Figure 8.1). A 3D visualization is illustrated in Figure 8.2a and the 2D cross-section at $y = 0$ is shown in Figure 8.2b. The cross-section incorporates a 2D layer change with a material recess at the left side ($x = 0$), which is to illustrate an excavated tunnel. For stability reasons during the construction, the tunnel representation is not extended throughout the whole y -dimension. The large dimension in y -direction enables a simulation in 2D for a certain time window. The background material, denoted with M1 in Figure 8.2a, consists of a concrete mixture. For the creation of the disturbance material M2, mortar for brickwork is added to the concrete mixture in the ratio *concrete/mortar* 1/0.7. The ingredients of the two construction materials are the ones described in Section 7.1. The construction process is carried out as follows: in a first step, the mold is built. In a next step, the disturbance material M2 is given into the mold, where a wooden plank secures the positioning. After a few hours of dry time, the wooden plank is removed and the background

material is added. At this stage, the disturbance material has a non-dissolving structure but is still slightly wet, which secures a good connection between the two materials. The disadvantage of this procedure is that the interface layer may be assumed to be not perfectly clear since the two materials slightly merge. Therefore, the UHSA parametrization as well as the expected true model considered for an evaluation of the results will not be completely correct.

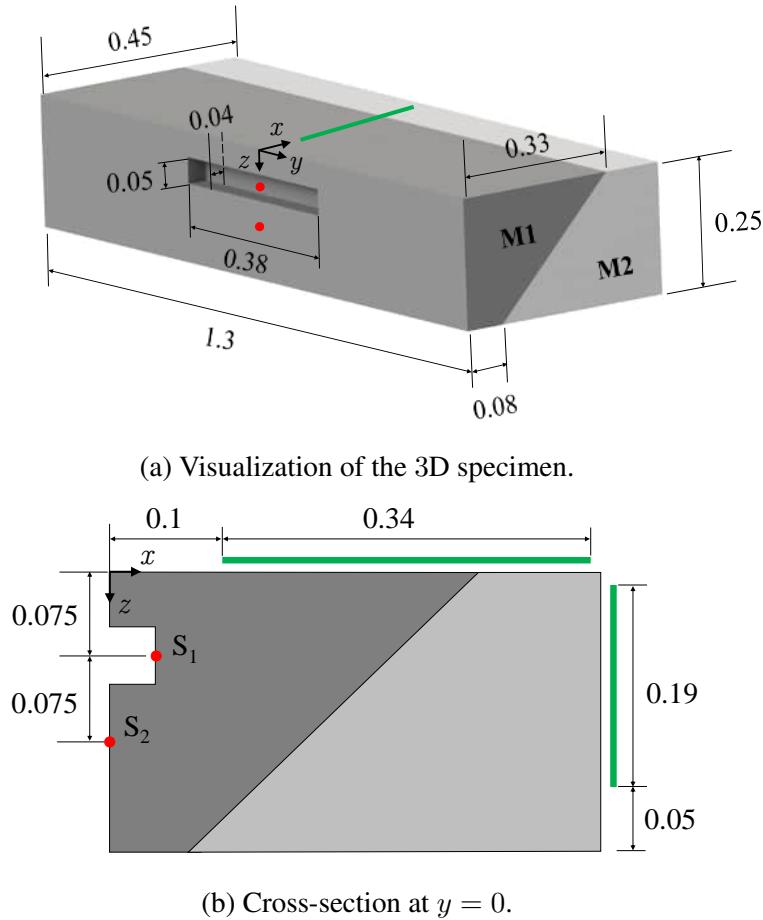


Figure 8.2.: Experimental setup with measurement configurations. Dimensions are in m. The red dots indicate the locations of the sources and the green lines indicate the locations of laser measurements. The background material properties are estimated to lie at $v_{p,b} = 4240 \frac{m}{s}$, $v_{s,b} = 2640 \frac{m}{s}$; the disturbance material properties are estimated to lie at $v_{p,d} = 3900 \frac{m}{s}$, $v_{s,d} = 2380 \frac{m}{s}$.

The specimen is placed on four small metallic blocks comparatively distant from the cross-section at $y = 0$ (see Figure 8.1). Since the signal is cut when reflections arrive from the model sides, the bearing is not expected to have any impact on the data. The ultrasonic measurements are aimed to be acquired in the xz -plane at $y = 0$ according to Figure 8.2b. Two source locations S_1 and S_2 are specified, illustrated with the red dots. The reason for the positioning of S_2 at the surface at $x = 0$ rather than choosing another position inside the tunnel lies in the thickness of the transducer, which does not allow a significant ranging inside the excavation. The ultrasonic sender is transducer B 0.1NN, where tone burst signals are to be utilized as source functions, same as for the scenarios conducted in the previous chapter and for the reasons explained in Section 4.2. However, in this case, two source functions are utilized for each sender location – those are a 80 kHz and a 100 kHz 3.5-cycle Hanning windowed tone burst signal – resulting in four measurement sets being referred to

as $S_1(80 \text{ kHz})$, $S_1(100 \text{ kHz})$, $S_2(80 \text{ kHz})$ and $S_2(100 \text{ kHz})$ in the following. The idea is that with additional measurements, the results are expected to improve since more information is processed. Furthermore, the limited frequency range of the transducer can be more or less fully covered, which is to be shown in the following.

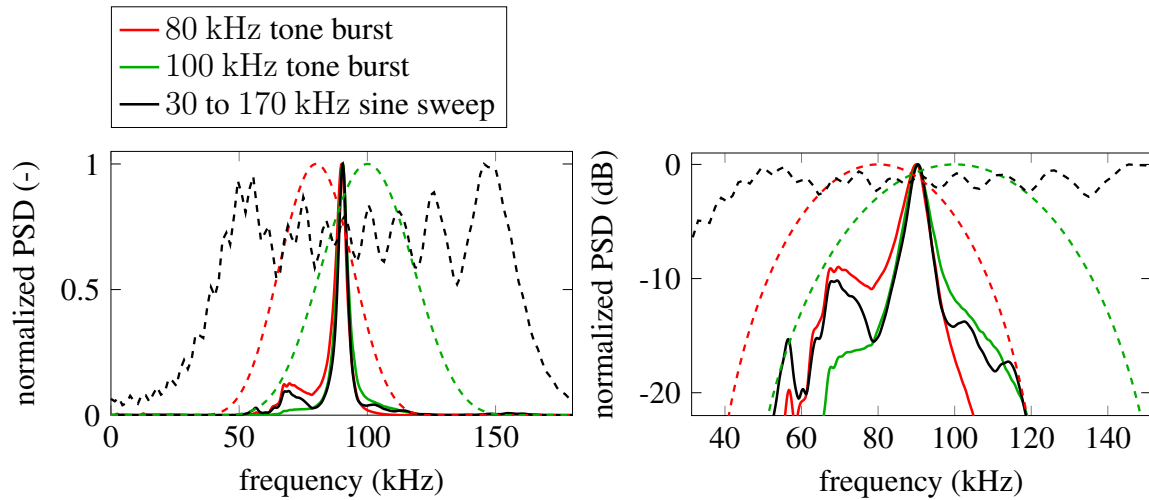


Figure 8.3.: Normalized power spectral densities (raw and dB scale) of the source responses recorded directly with a second transducer. The dashed lines indicate the power spectral densities of the ideal source signals.

Figure 8.3 shows the normalized PSDs (raw and in dB scale) of ideal source functions illustrated by solid lines and the corresponding measured source responses illustrated by dashed lines, where the latter are recorded with a transducer-to-transducer measurement according to the procedure explained on page 75. In order to investigate the frequency range of the transducer again with a more or less constant amplitude spectrum, a sine sweep is triggered during a time window of $2 \cdot 10^{-4} \text{ s}$ with a sweep from 30 kHz to 170 kHz, which are frequencies around the determined frequency range of the transducer (see Section 4.2). Preliminary investigations of various source functions show that the 80 kHz tone burst signal (red solid) and the 100 kHz tone burst signal (green solid) cover the overall range of the sine sweep well. This is observed in the red line and the green line, which in combination cover the area of the black line well (better visible when observing the PSDs in dB scale). Therefore, these two functions are selected as signal inputs. The laser measurements are acquired along the green line in Figure 8.2b in distances of 1 mm. 341 measurements are acquired at the top surface $z = 0$ and 191 receivers are acquired at the right surface $x = 0.45 \text{ m}$, resulting in 532 receiver points in total for each source function. The reflection is improved with aluminum tape, where the corresponding validation and evaluation is described in Section 4.3. Accordingly, measurements are acquired about 100 times and stacked. Waveforms are bandpass filtered with cutoff frequencies of 10 kHz and 150 kHz to reduce noise. Same as in the previous chapter, traces are observed carefully and removed if they are apparently noisy.

A topic that needs to be considered is that the conducted experiment is to be modeled in 2D, where self-evidently the experiment can only be conducted in 3D. The transformation of 3D data to 2D makes up an own research field, where methods are often being referred to as 2.5D approaches (Auer *et al.*, 2013; Igel, 2017). A first issue to pay attention to is that the 2D simulation model can only describe the 3D experimental model approximately if the 3D model is most widely represented with the 2D model out-of-plane extension. Thereby, it is important that no or little reflections arrive from out-of-plane, which in the current case can

be expected if the waveform signals are cut before reflections arrive from the model sides in y -direction. The only irregularity that occurs in the experiment is the representative tunnel excavation, which is not fully extended. However, the impact is tested beforehand by a comparison of the waveforms of two 3D simulation models (one with a fully extended tunnel and one according to the excavation above) and evaluated negligible (see also Figure 8.4). Larger errors are to be expected for other reasons: an extension of the 2D model into the third dimension implies that a 2D point source becomes a line source. Furthermore, 2D waveforms decay with $1/\sqrt{x}$ where 3D waveforms decay with $1/x$ due to the geometrical spreading (Auer *et al.*, 2013). In the experiment, the line source could be dissembled by a superposition of measured waveforms corresponding to plenty of point sources distributed in y -direction. However, measurement errors, inhomogeneities, and deviations of the specimen from its ideal shape lead to the assumption that this procedure would rather have an adverse effect. Furthermore, a huge expense would have to be paid in order to acquire the numerous measurement sets. Many approaches exist which seek to compensate the transformation mismatch, where a common and simple approach is to apply a \sqrt{t} -filter as for example applied by Bretaudeau *et al.* (2013) and Mulder *et al.* (2010). This approach is conducted in this work and approximately compensates for the amplitude mismatch by applying a multiplication of each trace with \sqrt{t} (Williamson & Pratt, 1995; Auer *et al.*, 2013). Figure 8.4 shows \sqrt{t} -filtered 3D simulation data generated with a model of the shape of the experimental model (Figure 8.2a, including also the tunnel excavation) with homogeneous material properties M1 compared to corresponding 2D simulation data. The source is placed at position S_1 and induces a 80 kHz tone burst signal; receivers are placed at the top surface $z = 0$ at positions $x = \{0.1, 0.2, 0.3\}$ m and at the right surface $x = 0.45$ m at $z = \{0.05, 0.15\}$ m. During the observation time induced by the limited y -direction, the two synthetic sets show a comparatively small mismatch and hence, no further action is taken concerning data transformation. Nonetheless, a part of upcoming inversion errors may be ascribed to the 2D computation.

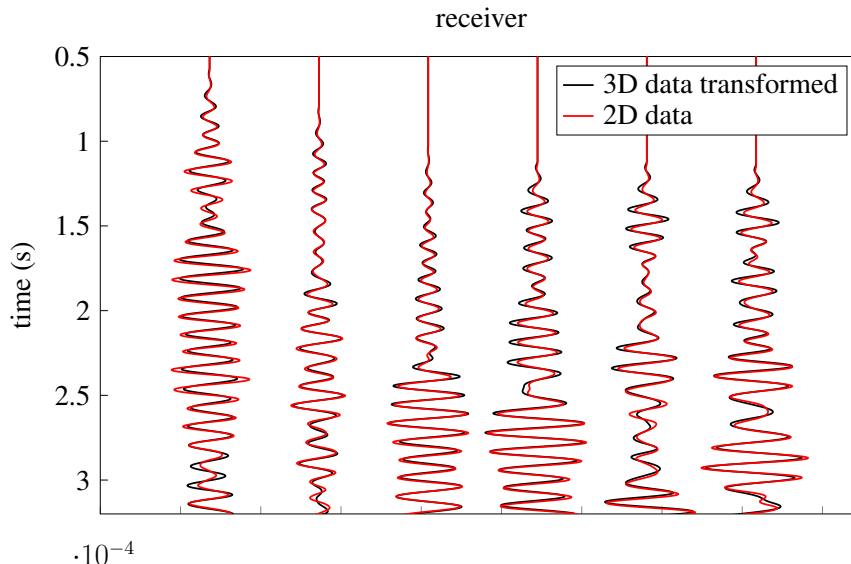


Figure 8.4.: Transformed 3D simulation data of the spatial experimental model compared to 2D simulation data. Traces are normalized with the maxima of the third records from left.

8.2. The forward model

As explained above, the simulations corresponding to the described experimental setup may be performed in 2D with the gain of a reduced computation time. The dimensions of the specimen are carefully measured at $y = 0$ and the geometrical model is built and implemented into Gmsh, where all model boundaries obtain free boundary conditions. Same as for the scenarios of the previous two chapters, great challenges lie in the determination of the background material properties and the source signature, where the strategies of the two previous chapters are combined for the estimation of the latter. The first estimation of the source signature is supplied by a transducer-on-source measurement which is aligned to a laser-on-source measurement on the time axis, where the procedure was described in Section 7.2 in more detail. With this source signal, the material properties are estimated. For that purpose, a homogeneous simulation model is set up whose waveform data is to be compared to the measurement data. For a comparison, only the first 60 receivers (that are the receivers from $x = 0.1$ m to $x = 0.16$ m) of all of the 4 source-receiver sets are utilized within a reduced time window since the impact of the disturbance on these data sets can be expected to be small. In the case of the assumption of an isotropic and homogeneous material, the background material can be fully described by two wave velocities v_p and v_s and the two attenuation values Q_κ and Q_μ (see Section 2.6). Similar to the procedures in the previous chapters, a database with a gridded variation of the 4 material properties is created and the misfit functionals are computed. It is observed that the functional becomes smaller for higher values of Q_κ and Q_μ and thus, also in this scenario, the material is chosen to be elastic. In the subsequent step, the pair of material properties with the lowest misfit functional is selected for the background material M1, which is $v_{p,b} = 4240 \frac{\text{m}}{\text{s}}$ and $v_{s,b} = 2640 \frac{\text{m}}{\text{s}}$. According to Eq. 2.9, the corresponding Poisson's ratio amounts to $\nu_b = 0.1834$, which is a realistic value for concrete. In the next step, the source function is to be further improved where the procedure explained in Section 6.2 is utilized. Note that this method is only applicable because the correlation between the synthetic waveforms and the experimental waveforms is already high (contrary to the example in Section 7.2). The source functions are determined both for the 80 kHz tone burst signal and the 100 kHz tone burst signal with the measurement and simulation wavelets of the 10th receiver released by source S_1 . The reference receiver is picked because the agreement between synthetic and measured data is evaluated high here. Figure 8.5 shows the synthetic waveforms corresponding to a simulation with an homogeneous model with the determined material properties and the estimated source signature (red) compared to the ultrasonic data (black), exemplary for the first 20 receivers triggered with source S_1 (80 kHz). Since the match of the simulated and experimental waveforms is evaluated to be high for the first receivers, it is assumed that the material properties and the source signature are estimated well and thus are utilized for inversion. The observation time window is set so that no reflected waves arrive from the model boundaries in maximum y -dimension $y_{\text{max}} = 1.3$ m as follows:

$$t = \frac{y_{\text{max}}}{v_{p,b}} + t_{\text{delay}} \approx 3.2 \cdot 10^{-4} \text{ s}, \quad (8.1)$$

where $v_{p,b} = 4240 \frac{\text{m}}{\text{s}}$ is the maximum estimated wave velocity of the specimen in terms of material properties, which is the compressional wave velocity of the background material since the disturbance material wave velocities are lower. t_{delay} is the time delay of the measurement system (occurring e.g. due to the signal travel time in cables) which is estimated to $t_{\text{delay}} = 1.5 \cdot 10^{-5}$ s. The discretization of the simulation mesh is set according to Eq. 2.12 with $f_{\text{max}} = 150$ kHz, where this is also the value chosen in the previous chapter.

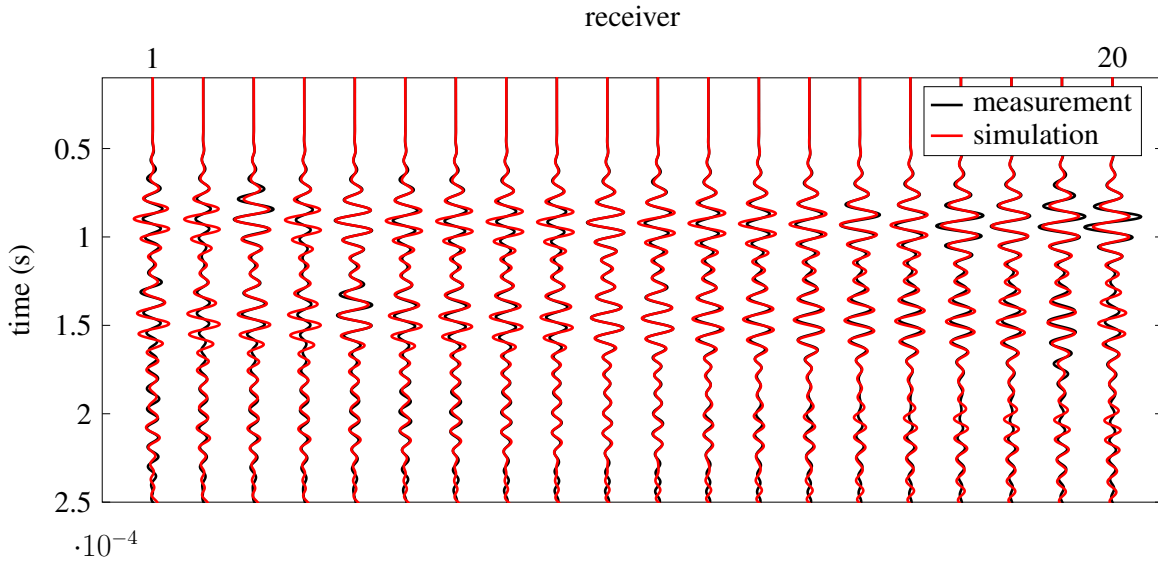


Figure 8.5.: Ultrasonic (black) and synthetic (red) waveforms, exemplary for the first 20 receivers triggered with source S1(80 kHz). The simulation data is generated with the estimated source function and the determined material properties. Amplitudes are normalized with the maximum displacement values at the 10th receiver.

The material properties of the disturbance material are estimated as well in order to obtain a reference value, amounting to $v_{p,d} = 3900 \frac{\text{m}}{\text{s}}$ and $v_{s,d} = 2380 \frac{\text{m}}{\text{s}}$ and resulting in a Poisson's ratio of $\nu_d = 0.2033$. Each forward run in the following requires the computation of the signal responses both to the 80 kHz and the 100 kHz source signal for two source locations. In order to perform only one simulation per source location, a simulation with a dirac delta is performed. With its signal response, the waveforms corresponding to arbitrary source functions can be computed without any significant computational effort.

8.3. Full waveform inversion

In the following, an investigation on source-receiver configurations and source functions is performed, before UHSA and UKF-PaLS are applied to the acquired data. For the former, a database with simulation data is created containing variations in positions, angles and material properties of the disturbance. After generating the database, the misfit functionals can be computed comparatively fast. Based on the results, it is evaluated with which source-receiver configurations and with which source functions an inversion seems possible. Afterwards, UHSA and UKF-PaLS are applied based on these findings. Same as in the prior chapter, the background material density is set to the same value as the disturbance material density and furthermore, amplitudes in the simulation are scaled so that the amplitudes are similar to the measurements at measurement points with a rather low displacement. The justification and the effects of these procedures were treated on page 77.

8.3.1. Source-receiver configurations and source functions

The aim of this section is to investigate the effects of different source-receiver configurations and source functions on the inversion results. Therefore, a parametrization of the disturbance is set up, which is illustrated in Figure 8.6.

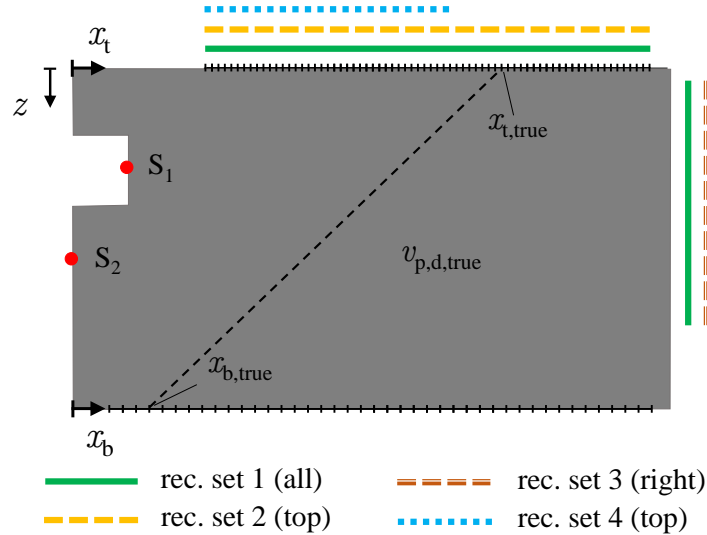


Figure 8.6.: Receiver configurations and parametrization for the database creation

The disturbance is parametrized with a connection of a coordinate at the top model border x_t with a coordinate at the bottom model border x_b and a compressional wave velocity $v_{p,d}$. For the database creation, the shear wave velocity of the disturbance is computed with the assumption $\nu_b = \nu_d = 0.1834$, which is necessary in order to keep the computation time of the database within a realizable frame. x_t is varied in the interval $[0.1, 0.44]$ m with a gridding of 0.005 m and x_b is varied in the interval $[0.03, 0.44]$ m with a gridding of 0.01 m. The compressional wave velocity $v_{p,d}$ is varied in the interval $[3500, 4400]$ $\frac{\text{m}}{\text{s}}$ with a gridding in steps of 50 $\frac{\text{m}}{\text{s}}$. The variations of x_t and x_b and its expected true locations $x_{t,true}$ and $x_{b,true}$ are illustrated in Figure 8.6. The reason for the finer gridding of x_t compared to x_b is a higher change in the misfit functional if x_t is varied since most of the receivers are placed at the top. Therefore, the precision of the result for the top parameter is expected to be higher, but however can only be higher if the gridding is finer. For the creation of the database, 55062 simulations are conducted for each source location, leading to 110124 simulations in total. As the simulations and the data processing are run in parallel, only 82 hours of computation time are consumed on a 26-core computer with 2.4 GHz each and 96 GB RAM. The number of elements during the database creation varies around 3500 to 4000 since for every function evaluation, the model is remeshed. The misfit functionals are evaluated throughout the database for different combinations of receiver sets, source locations and source functions. The investigated receiver sets are illustrated in Figure 8.6. Receiver set 1 includes all seismic receivers locations, receiver set 2 contains those at the top surface only. Receiver set 3 includes the receiver locations at the right side only and receiver set 4 contains those at the top surface given $z = 0$ and $x \leq 0.3$ m, which are receivers placed on the background material only with a distance of 0.03 m to $x_{t,true}$. Table 8.1 shows the parameter configurations with the lowest misfit functional for receiver sets 1-4 in dependency of the source locations and the source functions in the form $x_t, x_b, v_{p,d}$. The source locations are changed horizontally in the respective table with sender position S_1 , sender position S_2 , and both positions combined in terms of summing up the misfit functionals. The source

functions are changed vertically with the 80 kHz tone burst signal, the 100 kHz tone burst signal and a combination of the two source functions. As described in the previous two sections, the expected true values are $x_{t,true} = 0.33$ m, $x_{b,true} = 0.08$ m, $v_{p,2,true} = 3900 \frac{\text{m}}{\text{s}}$.

Receiver set 1	S_1	S_2	both
80 kHz	0.33, 0.06, 3850	0.34, 0.05, 3850	0.33, 0.06, 3850
100 kHz	0.195, 0.04, 4100	0.34, 0.05, 3850	0.33, 0.06, 3850
both	0.33, 0.06, 3850	0.34, 0.05, 3850	0.33, 0.06, 3850

Receiver set 2	S_1	S_2	both
80 kHz	0.33, 0.06, 3850	0.34, 0.05, 3850	0.33, 0.06, 3850
100 kHz	0.30, 0.06, 3850	0.22, 0.04, 3650	0.30, 0.06, 3850
both	0.30, 0.06, 3850	0.34, 0.05, 3850	0.33, 0.06, 3850

Receiver set 3	S_1	S_2	both
80 kHz	0.11, 0.19, 4050	0.42, 0.28, 3700	0.44, 0.17, 3800
100 kHz	0.44, 0.2, 3650	0.255, 0.04, 3550	0.44, 0.2, 3650
both	0.11, 0.19, 4050	0.255, 0.04, 3550	0.43, 0.2, 3700

Receiver set 4	S_1	S_2	both
80 kHz	0.29, 0.06, 3950	0.21, 0.1, 3600	0.29, 0.06, 3950
100 kHz	0.29, 0.06, 3950	0.295, 0.03, 4350	0.29, 0.06, 3950
both	0.29, 0.06, 3950	0.295, 0.03, 4350	0.29, 0.06, 3950

Table 8.1.: Parameter configurations with the lowest misfit functional for receiver sets 1 to 4 in dependency of the source locations (horizontally) and the source functions (vertically). The parameters are given in the form $x_t, x_b, v_{p,d}$, where the expected true values are $x_{t,true} = 0.33$ m, $x_{b,true} = 0.08$ m, $v_{p,2,true} = 3900 \frac{\text{m}}{\text{s}}$

For receiver set 1 it is observed that there is only one combination of source-receiver configurations and source functions that is not able to satisfactorily determine a parameter configuration close to the expected true configuration, namely $S_1(100 \text{ kHz})$. All of the other parameters lie close to the expected true values. However, the bottom border position x_b is not determined as precisely as the other values, which was expected since seismic receivers are placed at the top border and the right border only, where less information from the bottom side is included in the misfit functional. The wrong approximation of $S_1(100 \text{ kHz})$ may be partly explained with the consideration that synthetic travel times at receivers are similar to the true travel times if the disturbance occurs more left (related to the true shape in Figure 8.6), but with wave velocities closer to $v_{p,b}$. Therefore, results are more sensitive to errors, where the reasons for a wrong approximation are thereby numerous and may be explained with the sources of error described in the previous chapter already in List 7.1, but also with the gridding and the material property simplification that no $v_{s,d}$ is computed. The investigations clearly show that the utilization of either multiple source locations or multiple source functions are preferable since the use of either eliminates the error.

For the results of receiver set 2, a similar situation applies – only one combination, namely $S_2(100 \text{ kHz})$ is not able to determine a parameter configuration close to the true parameter configuration. The reasons for this are again those explained above. Once more it is shown that the utilization of multiple source functions or source locations can be highly profitable.

It is noted that not only x_t is determined well, but also x_b , although the receivers are only placed at the top surface.

The results shown in the third table reveal that with receiver set 3, a determination in terms of position of the disturbance and material properties is not possible. However, the resulting angle of the layer change is most often close to the real angle. For most of the cases, the wrong configurations may be justified with a similar argumentation as above, where travel times are similar to true travel times if the disturbance occurs more right, but with wave velocities deviating significantly from $v_{p,b}$. In this case, even multiple source locations cannot improve the results as both sources have a similar 'point of view' to the receivers. The combination with modeling and measurement errors leads to wrong results.

The results of receiver set 4 are surprisingly good in most entries regarding the small information coming in by seismic receivers, although x_t is underestimated. However, the results need to be considered critically. In receiver set 4, receivers are placed until $x = 0.3$ m on the background material only. Thus, waveform agreement between experiment and simulation may be expected to be high if $x_t \gtrsim 0.3$ m since in this case no direct waves are affected by the disturbance. Still, x_b and $v_{p,d}$ are determined well for the location of sender 1 and for the combinations of both senders, which is probably because of reflections of the model sides rather than because of reflections from the disturbance. Reflections from the disturbance layer are suspected to be weak due to the manufacturing process described in Section 8.1, leading to an interface layer that is not clear. Receiver set 4 is considered rather not suitable for an inversion for the current case.

The investigations of this section show that receiver sets 1 and 2 are able to satisfactorily reconstruct the disturbance with the given parametrization if either multiple source functions or multiple source locations are utilized. Receiver sets 3 and 4 are not suitable. Since the material property simplification and the gridding exacerbate the conditions for the inversion in this section, it can already be suspected that UHSA can reconstruct the structure if a similar parametrization of the disturbance is implemented. For UKF-PaLS, this needs to be tested. In order to not go beyond the scope of this work, only data sets using both source locations and both source functions are utilized for receiver sets 1 and 2, which are tested with both UHSA and UKF-PaLS in the following.

8.3.2. UHSA

Based on the findings of the previous section, UHSA is applied to receiver sets 1 and 2 including both source locations and source functions. The parametrization of the model is chosen similar to the parametrization chosen in the previous section, with the only difference that the full elastic material property set is determined. Consequently, the inversion parameters are set to x_t , x_b , $v_{p,d}$ and ν_d , where again a Poisson's ratio is chosen for the reasons described on page 45. Accordingly, the dimension of the inverse problem amounts to $n = 4$, resulting in $2 \cdot n + 1 = 9$ sigma points to compute during each UKF cycle. The allowed boundaries of inversion parameters and the general settings of UHSA for both upcoming scenarios are given in Table 8.2. The settings cause an intense exploration of parameter configurations since many cycles are accepted during a high number of UHSA cycles. The number of elements varies, same as in the previous section, around 3500 to 4000 as for every function evaluation, the model is remeshed. The courses of the misfit functional

and the inversion parameters over the number of UHSA cycles compared to the expected true values are shown in Figure 8.7. Table 8.3 shows the inversion results of UHSA for both receiver sets compared to the expected true values.

Parameter	Configuration
\mathbf{m}	$(x_t, x_b, v_{p,d}, \nu_d)$
\mathbf{U}	$[0.44, 0.44, 4500, 0.25]$
\mathbf{L}	$[0.1, 0.02, 3400, 0.1]$
N_c	200
p_0	0.9
p_e	0.1
N_k	4
\mathbf{P}_0^m	$\text{diag}(0.008^2, 0.008^2, 30^2, 0.003^2)$
\mathbf{Q}	$0.1\mathbf{P}_0^m$
\mathbf{s}_{min}	$0 \cdot \mathbf{s}_u$
\mathbf{R}	$0.2\mathbf{s}_u \cdot \mathbf{I}_T$

Table 8.2.: Input parameter configurations for both scenarios of UHSA

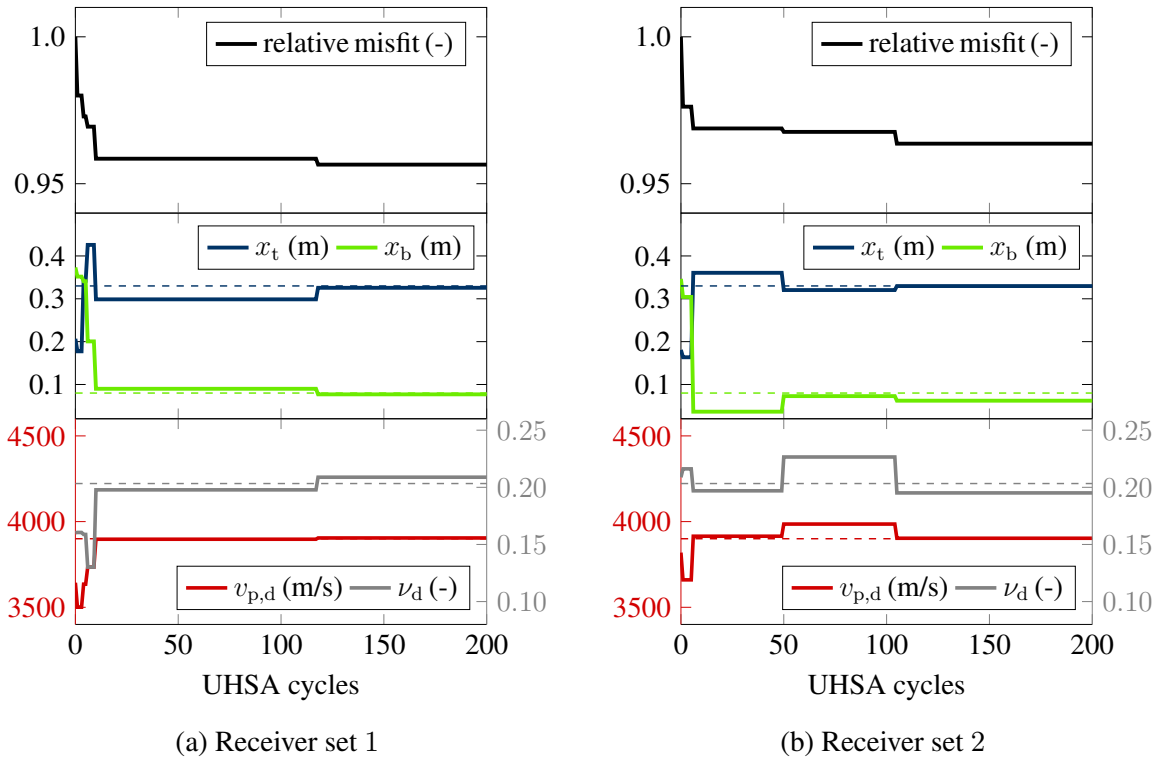


Figure 8.7.: Courses of the relative misfit functionals and inversion parameters over the number of UHSA cycles for receiver sets 1 and 2. The dashed lines illustrate the respective estimated true values.

For receiver set 1, each of the inversion parameters is determined highly precise, meaning that both the geometry and the material properties are determined with values close to the expected true values. Observing Figure 8.7a, it is found that a result close to the expected true values is already estimated early after 11 UHSA cycles. The final result is reached after 118 cycles. In total, 3762 forward simulations per source are consumed in about 12 hours computation time on a 26-core computer with 2.4 GHz each and 96 GM RAM. The

parameter	exp. true value	UHSA (rec. set 1)	UHSA (rec. set 2)
x_t [m]	0.33	0.3256	0.3297
x_b [m]	0.08	0.0770	0.0622
$v_{p,d}$ [m/s]	3900	3904	3903
ν_d	0.2033	0.2088	0.1951

Table 8.3.: inversion results of UHSA: expected true value and inversion results

inversion results for receiver set 2 are close to the expected true values as well; however, the result is, as was to be expected, a little less precise for x_b . The reason for this is that receivers are only placed at the top surface, which decreases the resolution at the bottom border. A parameter configuration close to the expected true configuration is already found after 50 iterations. The best result is reached after 105 cycles during 3933 forward simulations per source. Also here, the inversion requires 12 hours of computation time. To be summarized, the determined parameter configurations for both source-receiver configurations are close to being exact, where for both cases meaningful optima are found during an early stage of inversion.

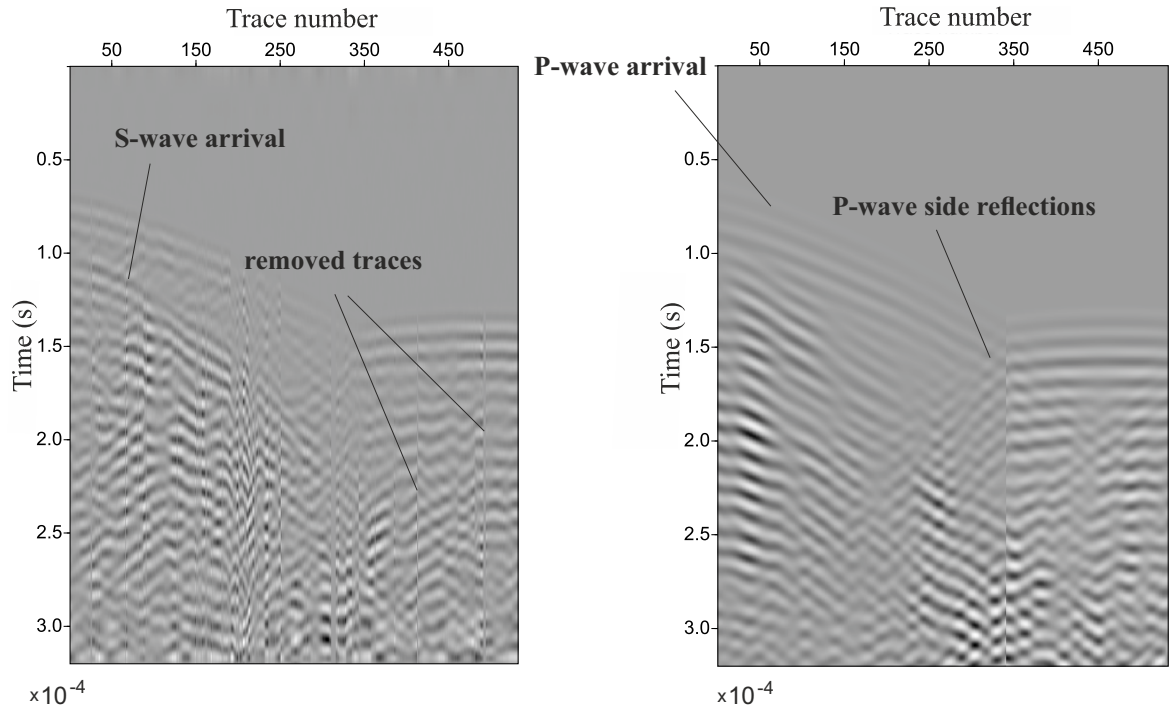


Figure 8.8.: Ultrasonic measurements (left) and simulation data (right) for receiver set 1 generated with source S_2 (100 kHz). The synthetic data is generated with the inversion result of UHSA (see Table 8.3).

Figure 8.8 shows the experimental data and the outcome of UHSA for receiver set 1 generated with source S_2 (100 kHz). The traces from left to right are acquired along the green line in Figure 8.2b from left to right and then from top to bottom. The two data sets show a high grade of similarity. In both the ultrasonic and the synthetic data set, the arrivals of the compressional waves and shear waves are visible. For later waveforms, the grade of similarity decreases since modeling errors have a larger impact. The removal of apparently noisy traces, which is described in Section 8.1, is visible in the ultrasonic data set.

8.3.3. UKF-PaLS

In the following, UKF-PaLS is applied, where same as in the previous section, two inversion scenarios are set up – one for receiver set 1 and one for receiver set 2, including both source locations and both source functions. The model domain is meshed with 3025 elements. The locations of $N_b = 12 \times 18 = 216$ bumps with 0.02 m distance to each other are defined covering the whole model from $x = 0.1$ m to $x = 0.44$ m. This induces a high resolution with a large region of investigation, meaning that no prior knowledge about the location or the size of the disturbance is implemented. Same as in the previous section, the material properties are defined in the form of $v_{p,d}$ and ν_d . Therefore, the dimension of the problem amounts to $n = 434$ (with 216 dimensions for α , 216 dimensions for β , 1 for $v_{p,d}$ and 1 for ν_d), resulting in $2 \cdot n + 1 = 868$ sigma points to compute in each iteration. The initial model parameters and the input parameter configuration are given in Table 8.4. The parameters are set with the aim to perform rather slow inversions in order to observe the changes of the reconstruction and in order to maximize the precision of the result. The corresponding initial model is shown in Figure 8.9.

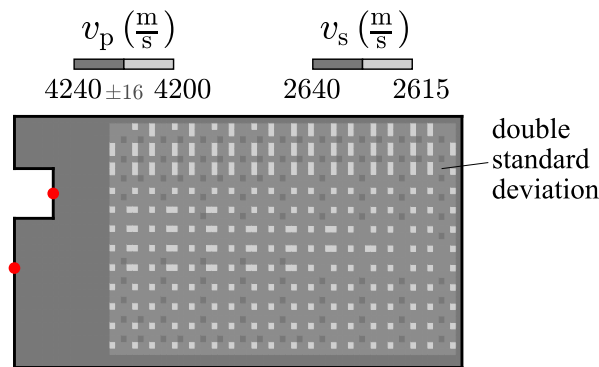
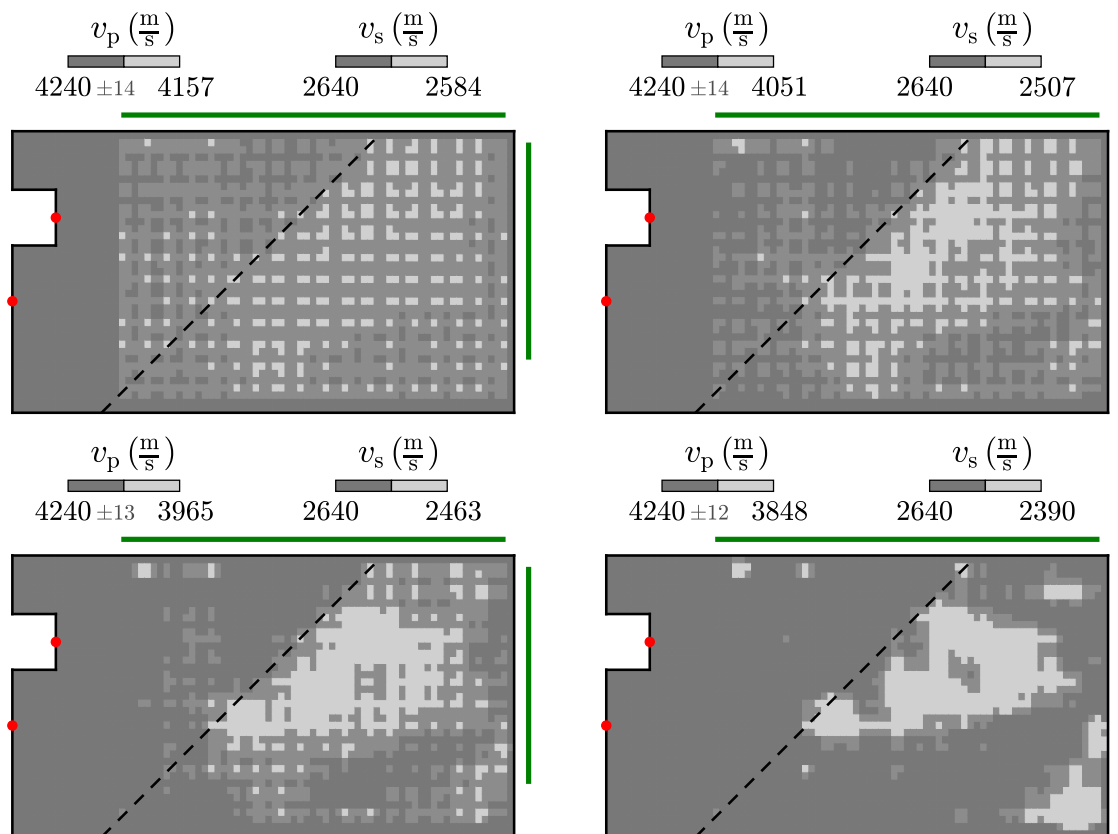
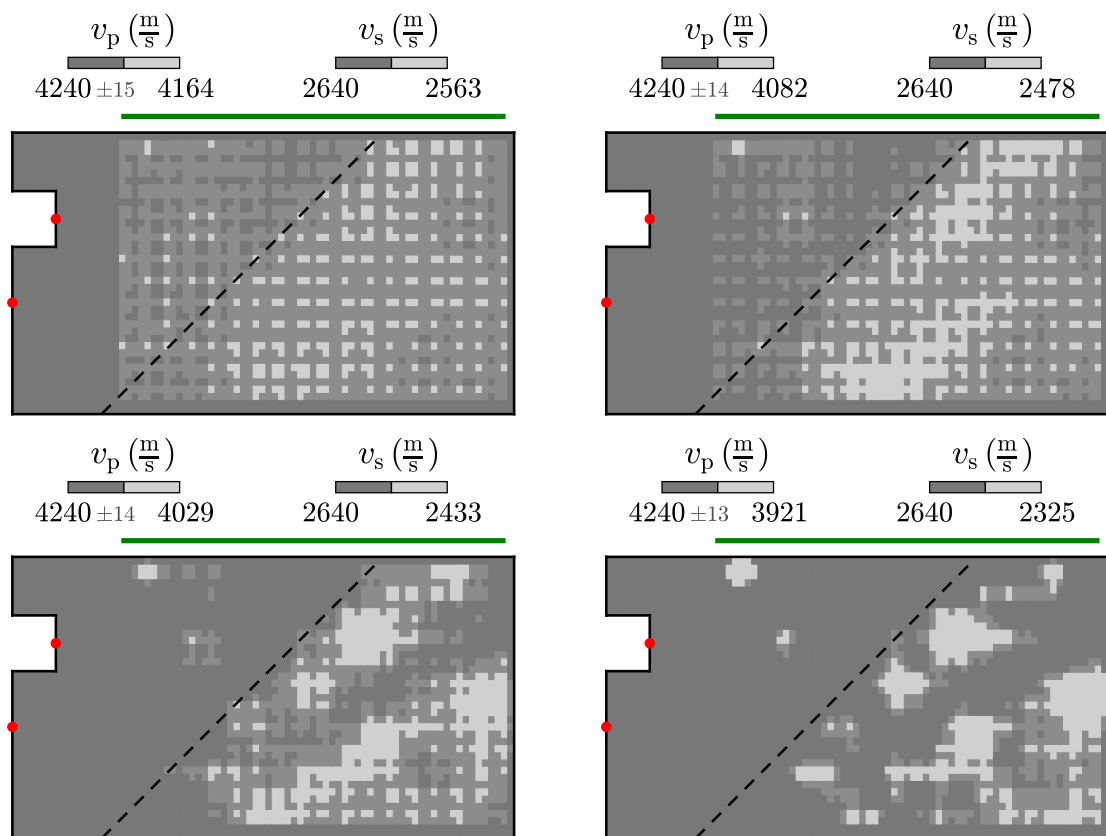


Figure 8.9.: Initial model for both scenarios. The double standard deviations of the initial parameters are plotted in medium dark grey (see marking).

Same as in Chapter 5, the shear wave velocity is illustrated (although the Poisson's ratio is determined) for the purpose of a better overview. Similarly, also the double standard deviations in positive direction are plotted in a medium dark grey tone (see marking in the figure). It is visible that the uncertainty regions occupy a large part of the model, which is different compared to the initial model shown in Figure 5.3 since in the current case, the field of bumps is much denser. Inside the field of the uncertainty region, there are some few elements plotted in dark grey, which are in most cases elements lying on diagonals between elements with disturbance material properties. The reason lies in the radial/circular influence of the radial basis functions, which do affect these darker grey elements least. For both inversion scenarios, UKF-PaLS is run for 20 iterations. Due to the limited spectrum of the transducer, the implementation of a multi-scale approach makes only a minor sense and is therefore not included in the upcoming results. It is, however, also tested but does not bring a significant change of the inversion results. Figure 8.10a shows the models corresponding to the UKF estimates achieved with receiver sets 1 after 5, 8, 11 and 20 iterations compared to the expected true position of the layer change illustrated by black dashed lines. Already after iteration 5, it is visible that the bumps inside the actual disturbance domain increase in size while the bumps inside the actual background domain vanish. At this stage, the effect of vanishing bumps is most visible in direction from the sources to the top receivers. The uncertainty measure is for most of the model domain still visible, although it also vanishes



(a) Receiver set 1: Estimates after 5, 8, 11, 20 iterations (left to right, top to bottom)



(b) Receiver set 2: Estimates after 4, 6, 11, 20 iterations (left to right, top to bottom)

Figure 8.10.: UKF estimates of the respective iterations with double standard deviations in medium dark grey. The expected true geometry is illustrated by black dashed lines. The red dots illustrate the seismic sources, the green lines illustrate the locations of seismic receivers.

Parameter	Configuration
N_b	216
\mathbf{m}_0	$\{\boldsymbol{\alpha}_0, \boldsymbol{\beta}_0, (v_{p,d})_0, (\nu_d)_0\}$
$\boldsymbol{\alpha}_0$	$1 \cdot \mathbf{J}_{N_b,1}$
$\boldsymbol{\beta}_0$	$7 \cdot \mathbf{J}_{N_b,1}$
$(v_{p,d})_0$	$4200 \frac{\text{m}}{\text{s}}$
$(\nu_d)_0$	0.1834
c	0.9
N_k	20
\mathbf{P}_0^m	$\text{diag}(\mathbf{P}_0^\alpha, \mathbf{P}_0^\beta, P_0^{v_{p,d}}, P_0^{\nu_d})$
\mathbf{P}_0^α	$0.15^2 \cdot \mathbf{J}_{N_b,1}$
\mathbf{P}_0^β	$0.2^2 \cdot \mathbf{J}_{N_b,1}$
$P_0^{v_{p,d}}$	8^2
$P_0^{\nu_d}$	0.0015^2
\mathbf{s}_{\min}	$0 \cdot s_u$
\mathbf{R}	$0.015 s_u \cdot \mathbf{I}_r$
\mathbf{Q}	$0.1 \mathbf{P}_0^m$

Table 8.4.: Initial model parameters and input parameter configuration for UKF-PaLS. $\mathbf{J}_{N_b,1}$ is a vector of ones of the size of the number of bumps $\mathbb{R}^{N_b \times 1}$

at some locations inside the actual background domain. After iterations 8 and 11, the structure of the disturbance becomes clearly visible, while nearly all of the bumps lying in the actual background domain vanish. Also the uncertainty measure in terms of the medium grey areas shrinks in these regions, while it is present in the region where the disturbance is located. However, the disturbance becomes most visible in its core; at the model boundaries in the actual disturbance region, the bumps and uncertainties also vanish. That becomes even more visible after iteration 20. The reasons are again for the main part a combination of the sources of error listed in List 7.1. The uncertainties locally extend the region of the disturbance, where they completely vanish in the region where the background domain is located. Therefore, the uncertainty measure is found useful also for these cases since it extends the area of possible disturbances correctly. In the context of mechanized tunneling, the inversion results would be satisfactory since the detection of the body of the disturbance is more important than reconstructing its exact shape. Furthermore, in direction of the tunnel axis, the reconstruction is most exact, which is most important. The determined material properties lie close to the expected true values $v_{p,d,\text{true}} = 3900$ and $v_{s,d,\text{true}} = 2380$. The double standard deviation of the compressional wave velocity changes only slightly during the iterations, which is a consequence of the settings (inducing a slow inversion). During FWI, $20(2n+1) = 17360$ forward runs are computed during 12 hours on a 26-core computer with 2.4 GHz each and 96 GB RAM with all UKF iterations parallelized. For receiver set 2, the models corresponding to the UKF estimates after 4, 6, 11 and 20 iterations are shown in Figure 8.10b. The disturbance is already visible after 6 iterations with a surprisingly good coverage of the whole disturbance domain, although seismic receivers are placed at the top surface only. Until iteration 20, the determined structure rather departs from the expected true structure although the misfit functional decreases. Reasons for that are once more the numerous sources of error from List 7.1. However, also here the location of the disturbance is satisfactorily estimated in direction of the tunnel axis. The uncertainty measure again increases the area of possible disturbances correctly and is therefore found useful. Furthermore, material properties are well estimated. Same as above, the computation takes 12 hours

with all processes parallelized. An error that can be observed in both of the scenarios is that during inversion, areas of disturbance material grow below the left-most surface receivers. The expected reason is that the material properties were determined within a reduced time window. When the core of the disturbance occurs during later iterations, reflected synthetic waves from the internal boundaries arrive at these receivers, where the areas of material probably correct for the occurring mismatch.

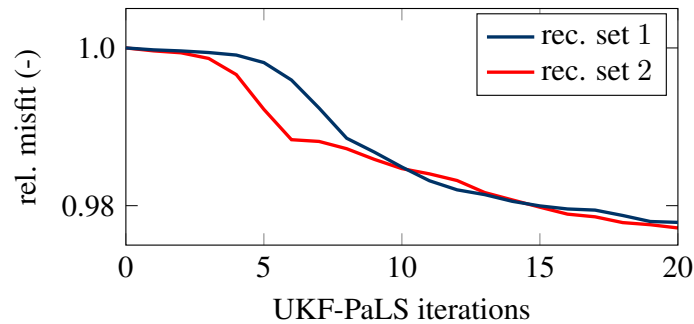


Figure 8.11.: Courses of the relative misfit functionals over the number of iterations of UKF-PaLS for receivers sets 1 and 2. The plotted value refers to the corresponding UKF estimate.

The changes of the misfit functionals during the courses of UKF-PaLS for both receiver sets are shown in Figure 8.11. In both cases, the largest change in the misfit functional occurs approximately between iterations 5 and 15 as in these iterations, the bumps melt to a structure. After iteration 15, the magnitude of the slope decreases since the structure does not change greatly anymore. Due to the UKF settings which are set slow, smoother curves occur than in the other examples for UKF-PaLS in this work. A tendency to converge is observed. For both scenarios, the computation of further iterations is tested, but does not significantly change the appearance of the disturbance anymore. In order to save computational power, it is expected that the reduction of bumps and a tuning of the UKF settings to a more fast inversion would also bring a success (or even bring better results in the case of further reduced dimensionality).

8.4. Comparability to large-scale models

The experimental small-scale model in this chapter is constructed with the aim to obtain a surrogate model with properties that are similar to a real tunneling field model. Thereby, concrete can already be seen as a rock-like structure. Furthermore, the cross-section of the constructed specimen has similarities to a 2D representation of a subsoil segment including a layer change and a tunnel excavated a few meters from a tunnel construction site. Related to the scaling factor, which was introduced in Section 4.1, a factor of 300 would scale the conducted experiment to a shallow tunnel scenario with a tunnel diameter of 12 m with the same amount of overburden. Accordingly, the corresponding source function would be centered at about 330 Hz (for the 100 kHz tone burst), inducing wavelengths around 7-13 m for this frequency. A scenario like this is a reasonable field scenario and the synthetic examples in Chapter 5 and Chapter 9 include scenarios in very similar dimensions. However, for the sake of constructional and technical restrictions, the small-scale model cannot describe an absolutely realistic surrogate model. The main reasons for this are geometrical restrictions of the small-scale model, which lead to reflections from the boundaries in

the plane of measurement. On the one hand, these reflections simplify the inverse problem since the reflected seismic waves carry additional information about the disturbance. On the other hand, modeling errors, especially from an inaccurately modeled geometry, increase due to the reflections, making the inversion more prone to failure. Another aspect that makes a comparison more difficult is that the background material and the disturbance material are expected to be melted within a rather thick interface layer. Thus, reflections from the disturbance are expected to be weak, which would probably be different in a real tunneling scenario. An aspect that exacerbates the inversion scenarios in the small-scale case is that small inhomogeneities and geometrical errors are expected to have a significant adverse effect, while in the large-scale case, inhomogeneities and geometrical errors in similar dimensions have a small effect because of operating wavelengths lying in the meter scale. However, additional modeling challenges may come up in field scenarios, where a homogeneous, isotropic and elastic model may not be sufficient anymore. The expected challenges in mechanized tunneling will be discussed in Section 10.2. Another question is if the consideration of a 3D tunneling scenario will have adverse effects on the performance of the inversion. With the third dimension, also the wave propagation problem is different since 3D waves are considered, also leading to 3D tunnel surface waves. However, their simulation is a modeling issue and does not necessarily increase the difficulty of the inverse problem but rather the computational demand. The numerical study in Section 5.2 reveals a good 3D performance if no modeling and measurement errors are included; however, applications to real field scenarios are still to be tested. To be summarized, there are some aspects that make a direct comparison difficult. However, since severe modeling and measurement errors are naturally included in the small-scale surrogate scenarios and since furthermore the geometry is partly comparable to a representative 2D field example, the scenarios of this chapter are evaluated to be suitable for a validation of the FWI methods with relation to mechanized tunneling. The findings regarding source-receiver configurations and source functions are to be discussed in the next paragraph.

The applied sources and receivers show different properties to field sources and receivers in terms of configurations, locations and functions. The FWI methods achieve good results with receiver sets 1 and 2. To some extent, receiver set 1 may be compared to a set with receivers placed at the Earth's surface and in a borehole and receiver set 2 to a set with receivers placed at the Earth's surface only. The usage of seismic receivers in boreholes is not usual, but also not impossible and could be highly beneficial for FWI in mechanized tunneling since direct information of disturbances would be included in waveforms in the form of transmitted waves. 'Tunnel' receivers, unfortunately, cannot be utilized in the small-scale model due to the dimensions of the sender and its fixture, whereas in field scenarios these receivers are the most common. Depending on the field scenario, additional seismic receivers placed at the Earth's surface could also be used, especially in urban and flat areas. Since the inversion results for the example of the concrete block are satisfying if the receivers are only placed at the surface, this may also apply for a real field scenario. A combination with seismic receivers inside the tunnel is expected to bring even better results as receivers are placed in multiple directions then. In Chapter 5, various 2D and 3D scenarios are investigated on different source-receiver configurations, where the reconstruction of objects was successful also if receivers were placed inside the tunnel only. Probably, this might also apply for real scenarios; however, this is to be tested. Regarding source functions it is found that the utilization of multiple source functions is useful since more information is induced without a significant increase in computation time (if an impulse function is used for the forward run). In the case of mechanized tunneling, broadband signals probably replace the need for the recording of measurements to multiple source functions. If the source func-

tion is known, signal responses to arbitrary source functions can be computed and used for FWI. Regarding source locations, it is found that the inclusion of a second source is advantageous. This probably also applies for field cases, since multiple sources bring a different 'point of view'. However, the computational effort is proportional to the number of sources and therefore, the number of sources needs to be limited. The results of Chapter 5 reveal that with the parameter reduction methods, two sources could suffice in order to achieve a high resolution of the disturbance domain, which should also apply for UHSA due to the lower dimensionality. Issues concerning sources and receivers regarding their quantity, their positioning, and the type of source with an application in mechanized tunneling will be discussed in Section 10.3.

8.5. Short summary and discussion

In the third and last stage of experimental validation, both UHSA and the UKF-controlled level-set method are tested on a model with certain similarities to a representative 2D field model. Therefore, a concrete specimen including a layer change is constructed, ultrasonic data are acquired and an adequate forward model is set up. Given the parametrization of a linear change, UHSA determines the structure as well as the material properties with a precision which is close to being exact. UKF-PaLS determines the structure with a satisfying precision and without the implementation of prior knowledge. Also for the experimental example, an uncertainty quantification delivers additional value since it correctly images where potential disturbances are missed by the inversion. Investigations concerning source-receiver configurations and source functions are conducted, where it is found that the usage of multiple source locations more or less distant to one another as well as multiple source functions may be advantageous for a successful FWI and that receivers placed at the (Earth's) surface only can already represent a favorable measurement setup. Although the findings cannot fully be related to a field scenario, the experiment is evaluated suitable for a validation of UHSA and UKF-PaLS with relation to mechanized tunneling. In combination with the numerical results of Chapter 5, which include more realistic tunnel settings, it is found that the methods show an ability to reconstruct the disturbance domain precisely even with a limited distribution of sources and receivers.

9. A three-stage concept

In Riedel *et al.* (2022), a three-stage concept is presented, where a supervised machine learning algorithm (SML), UHSA, and the adjoint method are combined in order to improve the accuracy of the anomaly detection. Here, the concept as well as the results are shortly summarized with a stronger focus on UHSA.

9.1. Reconstruction of a boulder

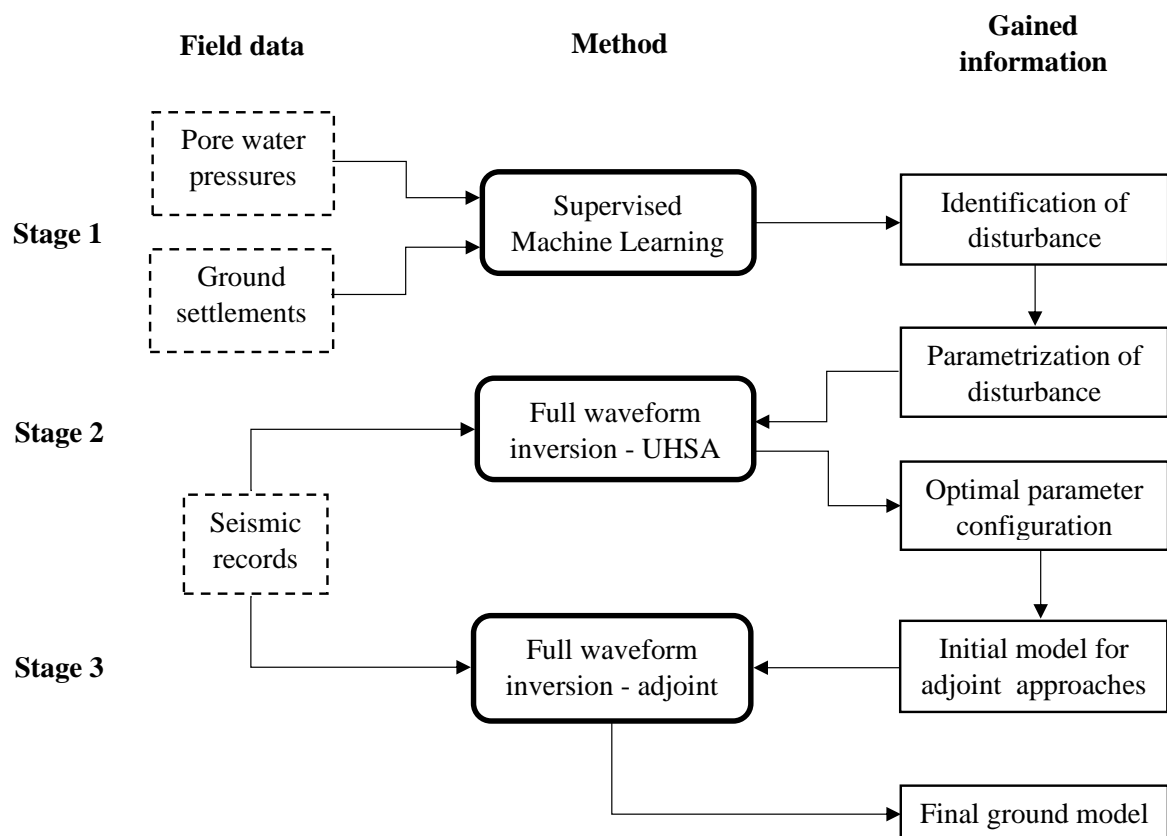


Figure 9.1.: Workflow of the three-stage concept.

As previously explained, UHSA relies on prior knowledge implemented in the form of a user-defined parametrization, where the knowledge can be gained from various sources (see Section 1.4). In the current approach, it is gained from an SML approach. The three-stage concept is illustrated in Figure 9.1. In a first step, the SML approach continuously analyzes ground settlements and pore water pressures during TBM advancement in order to identify a potential disturbance in front of the TBM. The collected data is represented in features, which are defined as certain representations of the measurements explained in Riedel *et al.* (2022). The measured data and the anomalies are classified into various scenarios such as

a layer change, an interlayer or a boulder. The algorithm analyzes the features and makes a prediction about the class (the type of disturbance). This prediction may optimally be used for UHSA, since the type of disturbance can be implemented in the form of a corresponding parametrization. Furthermore, the SML algorithm may deliver knowledge about the possible location, the size or the material properties of the disturbance in the form of uncertainties which accordingly can be implemented into UHSA as well. If a disturbance is predicted with a sufficiently high probability, the TBM stops and a seismic survey is conducted in order to acquire data to which UHSA is subsequently applied. The result of UHSA might already be sufficient. However, it is probable that it cannot describe the real disturbance in its entirety and in this case, adjoint FWI is utilized in order to gain a more detailed image. In this case, the final model of UHSA is used as an initial model for adjoint FWI, which considers the whole spatial distribution of the ground properties. In the three-stage concept, a time-domain and a frequency-domain approach are presented.

According to the previously described workflow, a test scenario is set up. The investigated scenario assumes a tunnel with a diameter of 8.5 m with an equal value of overburden. The anomaly is chosen to be a boulder, which is, before applying the SML procedure, located 69 m in front of the tunnel face. The rest of the model is chosen to be homogeneous. For a more detailed definition of the model and further information, readers are referred to Riedel *et al.* (2022).

9.1.1. Supervised machine learning

In order to be able to apply SML, data needs to be available, from which a pattern may be derived. This data is generated synthetically with a finite element software. For that purpose, four different scenarios are observed, that are a fully homogeneous model, an interlayer, a layer change and a boulder. For these scenarios, various models are set up with varying ground and anomaly properties. For each of the models, excavation steps with 1.5 m are computed, recording pore water pressures and ground settlements. After generating the data sets, 80 % are randomly chosen as a training set and 20% are used for validation. Different methods are tested; however, the best performance could be achieved with the K-Nearest Neighbors method (Cover & Hart, 1967) combined with kriging of the input variables (Mahmoudi & Hölter, 2021). With the data of the reference model described above, the correct class could be identified out of the four stated classes above, which is the boulder class. The boulder is specified to be 39 m ahead of the TBM with a higher elasticity than the background model. However, the exact size, shape, and material properties cannot be determined since this would require more investigations with huge data sets. For the detailed reconstruction of the boulder, FWI is to be applied.

9.1.2. Acquisition of seismic data

In the synthetic test scenario, the TBM is assumed to stop in order to make seismic measurements. The real model is created with a spherical disturbance with a diameter of $d_{\text{sphere}} = 14.888$ m. The center of the sphere is located 46 m ahead of the tunnel face, meaning that the closest location is 38.556 m ahead. From the background model of the SML approach, seismic velocities are derived with $v_{p,b} = 136.38 \frac{\text{m}}{\text{s}}$ and $v_{s,b} = 83.52 \frac{\text{m}}{\text{s}}$ and

implemented as background material properties. Note that the elastic parameters are derived from unconsolidated soil which was used for the SML approach. This leads to uncommonly low wave velocities for the FWI stage, which are still used in order to keep the material properties consistent within the case study. The disturbance obtains material properties of $v_{p,d} = 418.33 \frac{\text{m}}{\text{s}}$, $v_{s,d} = 223.61 \frac{\text{m}}{\text{s}}$. The density is assumed to be constant with $\rho = 2000 \frac{\text{kg}}{\text{m}^3}$. Two seismic sources are utilized, where one source is placed at the tunnel face and one is placed at the Earth's surface. The source functions are Ricker wavelets with central frequencies of 8 kHz and the signals are induced in normal direction of the respective surface. 42 seismic receivers are placed at the tunnel walls, the tunnel face, and at the Earth's surface according to Figure 9.2. Free and absorbing boundaries are applied as explained in Section 2.2.

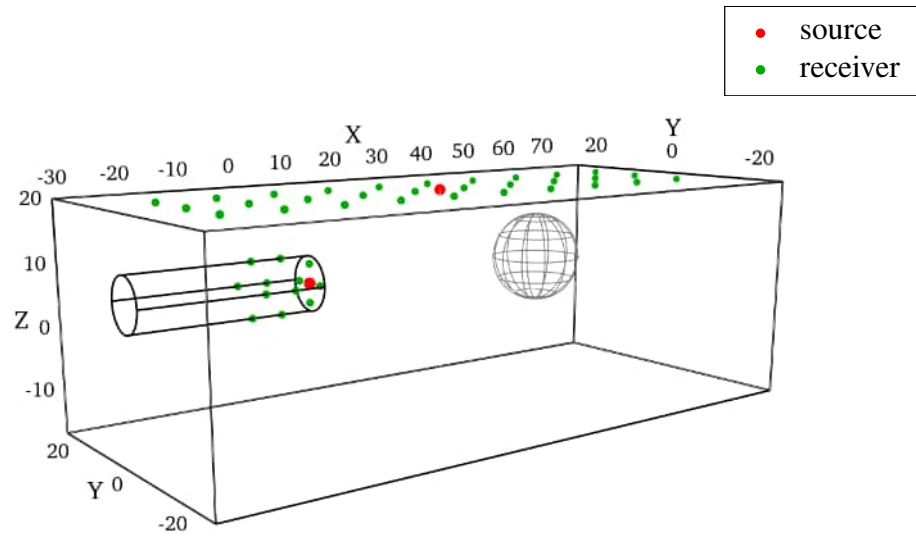


Figure 9.2.: Model used for the creation of seismic data with its spherical disturbance and source and receiver locations.

9.1.3. UHSA FWI

After generating the synthetic measurements, UHSA is prepared. Based on the prediction of the pattern recognition, a parametrization of the disturbance is derived. Here, a difficulty is included to test if the inversion still works: it is falsely assumed that the boulder has the shape of a cube instead of a sphere. Accordingly, a parametrization is implemented, specifying the distance of the cube to the tunnel front x_{loc} , its edge length l_{cube} and the material properties in the form of the compressional wave velocity $v_{p,d}$ and the Poisson's ratio ν_d . The UHSA settings and input parameter configurations are given in Table 9.2. Due to the good primary prediction, the boundaries can be set rather small. Therefore,

Model	Shape	x_{loc} (m)	l_{cube}, d_{sphere} (m)	$v_{p,d}$ ($\frac{\text{m}}{\text{s}}$)	ν_d	$v_{s,d}$ ($\frac{\text{m}}{\text{s}}$)
Real	Sphere	46	14.888	418.33	0.3	223.61
UHSA	Cube	45.7815	11.4772	412.358	0.325	209.9624

Table 9.1.: Inversion results of UHSA compared to parameters describing the disturbance of the real model.

also the number of UHSA cycles is set relatively small with 15 cycles. The number of UKF cycles is set so that a precise local search is conducted. Table 9.1 shows the final values of UHSA for x_{loc} , l_{cube} , v_p and ν compared directly with the center of the sphere, its diameter and its material properties. The shear wave velocity is computed with the help of the compressional wave velocity and the Poisson's ratio and also compared to the true value. It is observed that x_{loc} is determined without a significant mismatch to the center of the sphere. Also the material properties differ only slightly. The edge length and the sphere diameter, however, are difficult to compare since the shapes of the assumed and the real disturbance differ significantly. Still, the volumes are in a similar region with $V_{sphere} = 1728 \text{ m}^3$ and $V_{cube} = 1512 \text{ m}^3$. Figure 9.3 shows the course of the relative misfit as well as

Parameter	Configuration
\mathbf{m}	$(x_{loc}, l_{cube}, v_{p,d}, \nu_d)$
\mathbf{U}	[51, 16, 600, 0.35]
\mathbf{L}	[41, 10, 100, 0.15]
N_c	15
p_0	0.9
p_e	0.1
N_k	6
\mathbf{P}_0^m	$\text{diag}(0.3^2, 0.15^2, 10^2, 0.015^2)$
\mathbf{Q}	$0.1 \mathbf{P}_0^m$
\mathbf{s}_{min}	$0 \cdot \mathbf{s}_u$
\mathbf{R}	$0.2 \mathbf{s}_u \cdot \mathbf{I}_T$

Table 9.2.: Input parameter configurations for UHSA

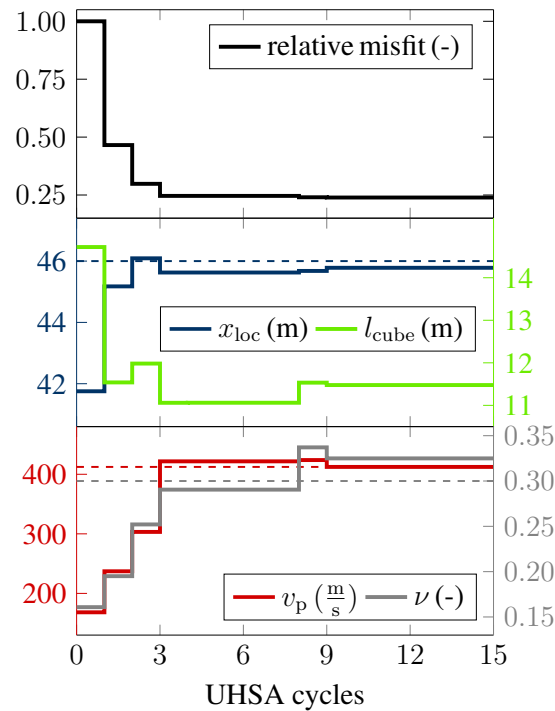


Figure 9.3.: Courses of the relative misfits and inversion parameters over the number of UHSA cycles. The dashed lines illustrate the respective true values of the parametrization of the sphere.

the inversion parameters over the number of UHSA cycles. The dashed lines illustrate the location of the sphere and its material properties as these values may be directly compared. After three UHSA cycles only, the inversion achieves a satisfying result already. The result for the Poisson's ratio departs slightly from the true Poisson's ratio after eight cycles, which is most likely due to the incorrect parametrization of the boulder. During the inversion, 556 simulations per source are consumed during 39 hours of computation time on a 26-core computer with 2.4 GHz each and 96 GB RAM.

9.1.4. Adjoint FWI

In the third and last stage of the proposed concept, the resulting model of UHSA is utilized as an initial model for adjoint FWI. Thereby, two approaches are tested: one in time-domain and one in frequency-domain. For the time-domain approach, 193 iterations are conducted with a multi-scale approach implemented in the form of a low-pass filter increasing stepwise from 7 Hz to 20 Hz during the inversion. For the frequency-domain approach, 27 frequency groups in the range from 1.27 Hz to 17.51 Hz are utilized with up to 10 iterations for each group. Figure 9.4 shows the results of the three FWI approaches.

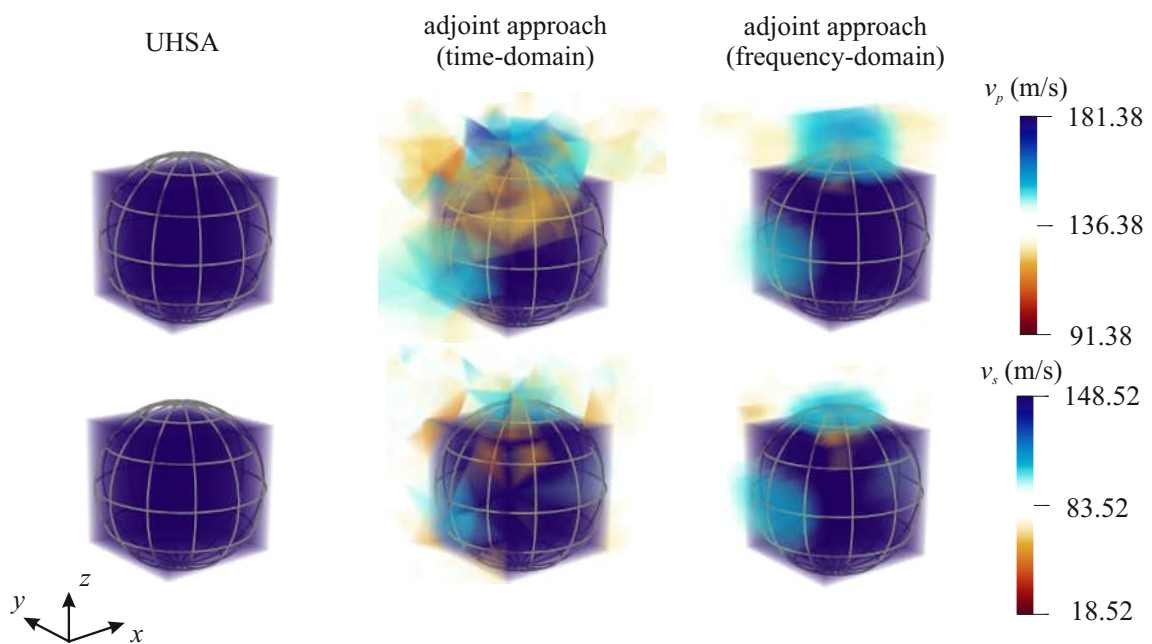


Figure 9.4.: Results of UHSA (left) with results of the time-domain approach (middle) and the frequency-domain approach (right). The upper row shows the determined P-wave velocity, the bottom row shows the determined S-wave velocity. The grey grid lines indicate the shape of the real boulder.

The determined compressional wave velocity is illustrated in the upper row and the determined shear wave velocity in the bottom row. In the left column, the results of UHSA are visualized, which are, as previously explained, implemented as the initial model for the adjoint approaches. The middle column shows the results of the time-domain approach, where the results of the frequency-domain approach are illustrated on the right side. The perspective is the same as in Figure 9.2. In the time-domain approach, both the compressional wave velocity and the shear wave velocity increase (seen from the tunnel perspective

in x -direction) in front of the front face and over the top face, indicating the shape of the sphere. Similarly, both wave velocities decrease at the corners of the cube at these surfaces, indicating that the cuboid representation is incorrect here. At the remaining surfaces, the shape of the sphere does not appear since less information of reflected or refracted waves is arriving at the seismic receivers from these locations. The shear wave representation is distinctly sharper due to the smaller wavelength. For the frequency-domain approach, practically the same applies as for the time-domain approach: in front of the front face and over the top face, both the compressional wave velocity and the shear wave velocity increase and at the front corners, velocities decrease.

9.2. Short summary and discussion

The novel hybrid concept is tested successfully with synthetic data. In the context of UHSA, the big gain of the concept is the transfer of prior knowledge from SML in the form of a disturbance type, which can be used to implement a parametrization of the disturbance. It is found that UHSA may still work if the parametrization of the disturbance is not perfectly adequate, since in this work it is assumed that it is of cuboid shape although it is spherical in the reference model. Still, the location, the material properties, and even the size of the boulder are well determined. An application of an adjoint approach to the result of UHSA can increase the level of detail. Concerning computation times, SML can be applied during a short time in the case that data is available and in the case that the training phase of SML is already conducted. The computation time of UHSA is strongly reduced by implementing the uncertainties of the SML algorithm in the form of boundaries of the inversion parameters. Also the adjoint method can profit from the transfer of results concerning computation time since the misfit functional of the initial model is already closer to the global optimum. However, there are still some issues to be investigated. For the SML approach, difficulties come up if more complex ground scenarios are observed since the type of disturbance needs to be defined in a class, lacking to give a prediction if the type of disturbance deviates from that class. Furthermore, isotropic material without attenuation is considered in this work. Anelastic ground behavior would make the hybrid approach more challenging and more time-consuming for all of the three methods. Further issues are listed in Riedel *et al.* (2022). In summary, the results of this work show that the hybrid concept can be useful for exploration during tunneling since the combination of the methods brings a more detailed image than each method can bring separately.

10. Discussion

10.1. Comparability of the experiments to large-scale scenarios and their additional value

The small-scale experiment is constructed with the aim to validate the FWI methods with experimental data. The experiments cannot fully be compared to tunneling field experiments, where one reason is that reflections occur at the model boundaries. However, the last stage of experimental validation shows certain similarities to a representative 2D field model, where the results are intensively analyzed and where relations to field applications are discussed. Each of the scenarios brings a significant gain compared to synthetic scenarios since real data is used for the inversion. This data naturally contains noise from different sources as well as measurement errors, for instance due to the measurement on porous surfaces. Similarly, modeling errors occur when building the forward model, for instance when geometries are measured, material properties are estimated or the source function is determined. Potential sources of error are listed in List 7.1. All of these error types also occur in field scenarios but not in synthetic data, which illustrates the value of the small-scale experiment. Some of the challenges might be more demanding on the small-scale while others are more demanding on the large-scale. For the latter, several additional challenges will come up which are to be discussed in the following section.

10.2. Challenges in mechanized tunneling

Considering field examples during mechanized tunneling, challenges will occur regarding the forward modeling and the acquisition of measurements. Some of these challenges also appear in the small-scale case, others do not. Also on the large-scale, a knowledge of the source signature is crucial. On the small-scale, a direct measurement of the source function remains difficult since a measurement instrument would have to be found which can be employed as an interlayer between the structure and the transducer and which at the same time enables a high accuracy and sensitivity without seriously altering the system. On the large-scale, a direct measurement of the source signal could be more easily achievable since applied forces are higher and therefore easier to measure. If not, performing a similar determination procedure like described in Section 6.2 is conceivable. Another challenge is the precise determination of the material properties of the tunnel surroundings. An advantage on the large-scale is that measurements may be acquired in multiple directions, from multiple locations and on longer distances. This may increase the precision compared to the small-scale, where the properties are determined on the basis of data acquired in one direction and on a distance of a few centimeters only. A procedure like performed in the small-scale scenarios seems beneficial, where a database with a gridded variation of material properties is constructed and a misfit functional is evaluated in order to find the background velocities.

The advantage of this procedure is that the data needs to be generated only once since the diameter of the tunnel and the boundary conditions stay constant. If the background material changes during excavation, the material properties could be determined close to real-time with a simple evaluation of the data. A determination on the basis of travel times is rather not suggested due to a lack of precision. When building the forward model, another question to be considered is if the TBM (or parts of it) need to be modeled or if its influence can be disregarded, which can only be reliably answered if on-site measurements are available. On the large-scale, phenomena like attenuation, anisotropies and poroelasticity may have to be considered, where modeling strategies are to be evolved. For the case of attenuation, two quality factors are to be determined prior to inversion, increasing the difficulty of the modeling. Lamert & Friederich (2018) investigate the influence on the inversion result if the attenuation factors are determined slightly inaccurate and find that an approximate estimation of the quality factors may be sufficient. This might be a beneficial finding for an application during mechanized tunneling. Besides the knowledge of material properties, also a precise knowledge of the geometry is crucial for model building, where for instance the amount of overburden, the shape of the tunnel, the shape of the Earth's surface as well as exact positions of sources and receivers are to be determined. Also here, strategies have to be developed. Same as in the small-scale case, a stacking of the measurements may be useful in order to increase the signal-to-noise ratio. However, it is not useful in the case that the measurements are poorly repeatable, for instance during TBM advance. When processing the measurements, noise of operating machines or urban noise needs to be considered. The application of filters like bandpass filters is useful in order to remove unwanted frequencies. In order to remove parts of seismic waveforms, additional filters like f-k-filters may come into play. The removal of apparently poor traces also seems reasonable in the large-scale case.

10.3. Sources and receivers

A planning concerning sources and receivers needs to be performed in terms of their quantity, their positioning and the type of source. Concerning the quantity of sources and receivers, it is advisable to bear in mind that the calculation time increases proportionally to the number of sources and that the number of receivers does not change the computation time significantly (only for data evaluation). Therefore, a large number of receivers and a small number of sources is desirable. The experiment in Chapter 8 shows that the usage of two sources more or less distant to each other is advantageous compared to the usage of only one source. A higher number of sources is always beneficial for the inversion and its number may be adapted to the possible computation time. Seismic receivers can be deployed as numerous as possible with regard on the constructional effort.

The placement of sources and receivers is dependent on which type of tunnel is considered: a shallow or a deep tunnel. In the case of deep tunnels, the Earth's surface probably cannot be considered for a positioning. On the one hand, applied source forces may be too weak to transfer a significant amount of energy towards the surface; on the other hand, the model domain may become too large for a fast inversion if considering the whole region from tunnel to Earth's surface for FWI. In the case of shallow tunnels, sources and receivers placed at the Earth's surface can bring a significant advantage since also transmitted waves carrying direct information about the anomalies are included in the data, where these waves also

carry a higher amount of energy than reflected waves. Furthermore, a source placed at the Earth's surface brings a different angle of transmitted waves, which can be highly beneficial for the inversion since the rear surfaces of disturbances may be better resolved or since also regions may be covered, which instead would be lying in the 'shadow' of disturbances. The synthetic scenarios of Chapter 5 show successful results with sources and receivers placed in the tunnel only, with only slight differences to the results with surface receivers. Nevertheless, the advantage of surface receivers may increase if measurement errors and more severe modeling errors come into play. Also the application of a borehole containing sources and receivers could be considered, which would be highly beneficial due to a high amount of transmitted waves. However, this might not always be applicable or be too expensive. Concerning the placement of sources inside the tunnel, Lamert (2019) shows that a placement at the tunnel face brings better results than a placement at tunnel walls (during an inversion with an adjoint FWI approach). However, the placement is also a constructional question. If receivers are to be placed at the tunnel face, this needs to be considered when building the TBM. To be summarized, sources are, if possible, located best at tunnel faces and the Earth's surface. Receivers should be arranged all over the domain or wherever possible.

Source mechanisms that are typically deployed during mechanized tunneling are explosives (Sattel *et al.*, 1992), pneumatic impulse hammers (Borm *et al.*, 2003) and seismic vibrators (Borm *et al.*, 2003). Furthermore, vibrations induced by the cutting head of the TBM may be utilized for FWI (Petronio *et al.*, 2007). In each case, it is beneficial to use a broadband source signal, which is in most cases already naturally induced. Another important criterion for the choice of a source function is that the source function can be precisely determined. In this context, a source estimation of explosives could be more difficult than of sources that are able to induce a controlled source function. If the vibrations of the cutting head shall be used, difficulties could occur in terms of modeling source locations and functions. If a controlled source function can be used, a Ricker function is suggested due to its successful deployment in various studies concerning FWI in general (e.g. Gebraad *et al.* 2020, Bretaudeau *et al.* 2013) but also concerning tunneling applications (e.g. Bohlen *et al.* 2007, Bharadwaj *et al.* 2017). In the case of well-known source functions for broadband signals like sweeps or impulses, the signal response to a Ricker source signal can be computed and made use of for FWI. The findings of Chapter 8 show that the usage of multiple source functions is useful for FWI, where signal responses to arbitrary source functions can be computed without a significant computational effort if the forward simulation is conducted with a dirac source.

10.4. Gains and restrictions of the applied FWI methods

During the course of this work, UHSA and UKF-PaLS reveal a good performance during synthetic and experimental examples, where the optima are in most cases found during an early stage of the inversion – showing that a prediction could be performed early or that the number of iterations could be substantially reduced. The high precision of the results is a consequence of the dimensionality reduction since it reduces the non-uniqueness of the inverse problem and the complexity of the misfit functional. However, the dimensionality reduction is also connected to restrictions.

The great restriction of UHSA is the need for prior knowledge in order to implement a user-defined parametrization of the disturbance. As explained in Chapter 1, this knowledge

may be available from several sources. Prior investigations are already conducted during planning of the tunnel trajectory by, for instance, extrapolation from the Earth's surface, additional geophysical measurements, exploratory drillings and prior seismic surveys. Other sources can be geophysical measurements or approaches like the SML approach described in Chapter 9. Similarly, also classical seismic tomography methods can be a source of prior knowledge. If a parametrization cannot be implemented, UHSA is difficult to apply. If it can be implemented, UHSA conducts a global search with respect to the defined parametrization of the disturbance – meaning that the algorithm will find the parameter configuration with the minimum misfit if the parametrization is correct and the number of cycles is high enough. Hence, the parametrization is a restriction of the method, but a gain in the case that it can adequately be implemented. Besides the restriction of the need for prior knowledge, another restriction of UHSA is that complex structures like irregular boulders are difficult to parametrize and therefore cannot fully be imaged. However, the results of Chapter 9 show that UHSA can still work in terms of locating the object and approximating its size if the parametrization of the disturbance is slightly wrong (since in this case, a cube instead of a sphere was modeled). Furthermore, for the examples in this work, the structure is remeshed prior to every forward run in order to obtain precise model boundaries. In the context of complex 3D tunneling scenarios, a meshing with hexahedral elements may not be possible anymore. In such a case, either a forward solver allowing for a meshing with tetrahedral elements is to be chosen (leading to an increase of computation time). Or, another option is not to remesh the model every forward simulation, but to use a static mesh and to assign material properties to the elements which fall into the criteria of the background or the disturbance domain. In such a case, a slight loss of precision is to be expected since the resolution would be dependent on the chosen mesh. Hybrid methods like the one proposed in Chapter 9 are conceivable. Same as for UKF-PaLS, uncertainty quantification could also be applied for UHSA. However, it is not very meaningful for UHSA since the configuration with the minimum misfit is already found with a high precision due to its global search nature and since the number of inversion parameters is strongly restricted. Therefore, it is left out of this study.

UKF-PaLS is less limited than UHSA, allowing to flexibly define the shapes of the disturbance with an adjustable number of model parameters. However, the dimensionality reduction also comes with some restrictions. For the examples in this work, the number of disturbance materials is limited to one. Nevertheless, for most disturbances, inverting for only one material may be expected to be sufficient since rapid material changes in excavation direction can be detected. If not, material properties could also be coupled to the radial basis functions in order to increase the possible sets of material properties. Furthermore, a region of investigation and a resolution are to be selected by positioning the bumps. However, the region of investigation may also spread over the whole model domain, and the resolution may be selected densely as the example in Section 8.3.3 shows. A setting of these properties could be based on prior knowledge or on the desired region of investigation or resolution. Another idea to decouple the method from these restrictions is to implement translational degrees of freedom to single bumps or to the whole grid of bumps. An implementation of the latter would only add 2 (2D) or 3 (3D) additional degrees of freedom to the inversion, where the region of investigation would be enlarged and the density of bumps inside this region could be reduced. Similarly, also the issue that the inversion result is worsened if bumps occur only at the edges (or even outside) of actual disturbances (see Section 6.3.2) would be solved. Same as for UHSA, hybrid methods are conceivable in which UKF-PaLS may provide an improved initial model for adjoint methods, where the latter can image further details. For UKF-PaLS, the covariance of the model parameters can

be utilized for an uncertainty quantification in order to reveal where anomalies are potentially missed by the inversion. This work introduces an uncertainty measure defined as the double standard deviation of the covariance matrix of the model parameters. The numerical 2D scenarios of Section 5.1 show that uncertainties often occur at locations of the model which are not well covered with transmitted waves, where knowing these locations would be beneficial for a tunneling application. Similarly, in the 2D experimental examples in Section 8.3.3, the uncertainty measure extends the region of the disturbance correctly. The gain of the uncertainty estimation is to be tested for 3D scenarios also. In this work, it is left out since the limited region of investigation hinders a valuable evaluation.

10.5. Computation time

The use of the spectral element method makes the computation time of the applied inversion scenarios comparatively small. Nonetheless, considering a 3D domain leads to a drastic increase of computation time induced by the third dimension but also by a more irregular meshing with varying element sizes due to the 3D tunnel. In this work, a 3D tunnel is considered in Section 5.2 for UKF-PaLS and in Section 9.1.2 for UHSA.

The computation time of UHSA is strongly dependent on the number of inversion parameters and its applied boundaries and thus, on the quantity of prior knowledge. Due to strong prior knowledge, the UHSA scenario conducted in Section 9.1.2 consumes a relatively low number of forward simulations. On a powerful computer, the computation time for a forward simulation could be reduced many times over and furthermore, all forward simulations during an UKF iteration can be parallelized. Therefore, with a reduced parameter set like the one applied, an application of UHSA during mechanized tunneling could soon be achieved.

The computation time of UKF-PaLS is dependent on the chosen number of bumps. The examples in Chapter 5 show examples of how bumps could be distributed in an application during mechanized tunneling. The resulting inversion times are (with almost two weeks on the high-performance cluster) way too long for an application during mechanized tunneling. However, also here, an application on more powerful computers will become possible in a couple of years. One advantage of UKF-PaLS is the possible parallelization of all simulations per source during one iteration. Since a single simulation already takes only a couple of minutes on the utilized cluster, the 25 iterations could be computed during a small amount of time if large computational resources would be available. Furthermore, it is notably to say that satisfactory results were already available after much less iterations than the applied 25 iterations.

To be summarized, the computational resources might be too expensive for an application during mechanized tunneling nowadays but with exponentially increasing computational power, the methods might be applied in a few years. Another great potential for a fast prediction is the creation of metamodels with SML models as performed in Trapp *et al.* (2019), which are summarized again in the next section.

10.6. Supervised machine learning for the creation of metamodels

In Trapp *et al.* (2019), a SML algorithm for the creation of metamodels is introduced by the co-authors Can Bogoclu and Dirk Roos. This approach creates a metamodel based on gridded simulation data in order to completely replace the simulation model. Firstly, a parametrization of the disturbance domain is selected, which can be the one selected for UHSA, the level-set representation or some other parametrization. Then, a database of simulation data with a gridded variation of inversion parameters is created. With respect to the simulation data, a multi output deep Gaussian covariance network (DGCN) is trained, constituting a surrogate model which outputs the waveforms for a given set of parameters. The surrogate model is not dependent on the measurement – thus, if prior to drilling, the background material properties are known and future boundary conditions can be estimated, the creation of the metamodel can be conducted prior to drilling and a forward run can be delivered close to real-time. In the case that the tunnel shape and the tunnel surroundings do not change, which can be the case considering even surfaces or deep tunnels, even one universal SML model could be used for the prediction. This is also a great advantage in regard of continuously acquired measurements during excavation since no new simulation needs to be generated for new sets of measurements. The optimization can be performed with UHSA or the UKF, but also with greedy optimization methods like PSO due to the small duration of a forward run. In Trapp *et al.* (2019), the DGCN is successfully applied to the measurement data acquired on the aluminum block in Chapter 6, where the same parametrization of the drilling as for UHSA is utilized. Only 128 forward simulations are needed in order to obtain a reliable metamodel. The performance for a higher number of parameters needs to be tested in future works, especially in regard of the required number of samples.

11. Summary and conclusion

This thesis considers two full waveform inversion methods based on dimensionality reduction and Bayesian inference for a potential application during mechanized tunneling. Both methods provide precise results, with meaningful reconstructions usually being determined in the early stages of the inversion. Although the dimensionality reduction induces restrictions, the methods are shown to perform well even when the parametrization of the disturbance domain is not chosen fully optimal and when substantial errors are induced in the frame of real measurements. With exponentially growing computational resources, full waveform inversion during mechanized tunneling may become applicable in a few years. In this context, the methods provide an alternative to common adjoint methods, where also a combination or a parallel application of both types of methods is conceivable in order to compensate for the restrictions and weaknesses of each other. The following paragraph summarizes the main achievements and findings of this work. The last paragraph identifies open research questions.

The further development of the methods as well as their application to seismic data are the major goals of this work (see Section 1.5). In Chapter 5, UKF-PaLS is extended to three dimensions and a multi-scale approach is implemented, achieving promising results in two as well as in three dimensions. It is shown that uncertainty quantification can deliver a prediction of where anomalies could potentially be missed by the inversion. Furthermore, the method is shown to perform well even if sources and receivers are placed inside the tunnel only. Chapters 6,7 and 8 represent the experimental stage of this work, where ultrasonic seismic data are acquired on various specimens with which both methods are validated. The additional value of this stage is that – same as in field scenarios – noise, measurement errors and later modeling errors are naturally included. After the deployment of measurement strategies (Chapter 4), adequate methods for the forward modeling are evolved for the corresponding application scenarios, where the determinations of material properties and the source functions are the most important ones. Despite measurement and modeling errors which are still included, all of the inversion scenarios are deployed successfully which demonstrates the robustness of the methods against these types of errors. The final phase of experimental validation in Chapter 8 deals with a scenario that is somewhat close to a representative tunneling scenario, so that an intensive comparison is made where the findings are related to large-scale applications. Hybrid methods are conceivable for both methods and in Chapter 9, UHSA is recommended as part of a hybrid scheme that includes both a supervised machine learning and an adjoint approach. The discussion part in Chapter 10 analyzes the results of the thesis and outlines challenges and suggestions for field applications.

The investigations reveal that the application of the two applied methods can be useful for advance exploration during mechanized tunneling. For a full validation of the methods, field data from tunnel construction sites must be taken into account. Besides this kind of validation, subjects of future studies may include an improvement of UKF-PaLS by the implementation of translational degrees of freedom to the bumps (see Section 8.3.3) and the implementation of Tikhonov regularization (see Section 5.3). Further synthetic three-

dimensional scenarios are to be tested if more computational resources are available. In the case the latter applies, research on Bayesian full waveform inversion with a less intense dimensionality reduction can be considered as well, for instance in the form of gridded velocity models. The optimization can be performed with the unscented Kalman filter; however, other methods should also be considered, with e.g. Markov chain Monte Carlo being a common and promising approach. Furthermore, great potential lies in further studying the use of supervised machine learning for the creation of metamodels, where the methods could also be useful for various applications – even beyond engineering or geotechnical applications.

A. Appendix A

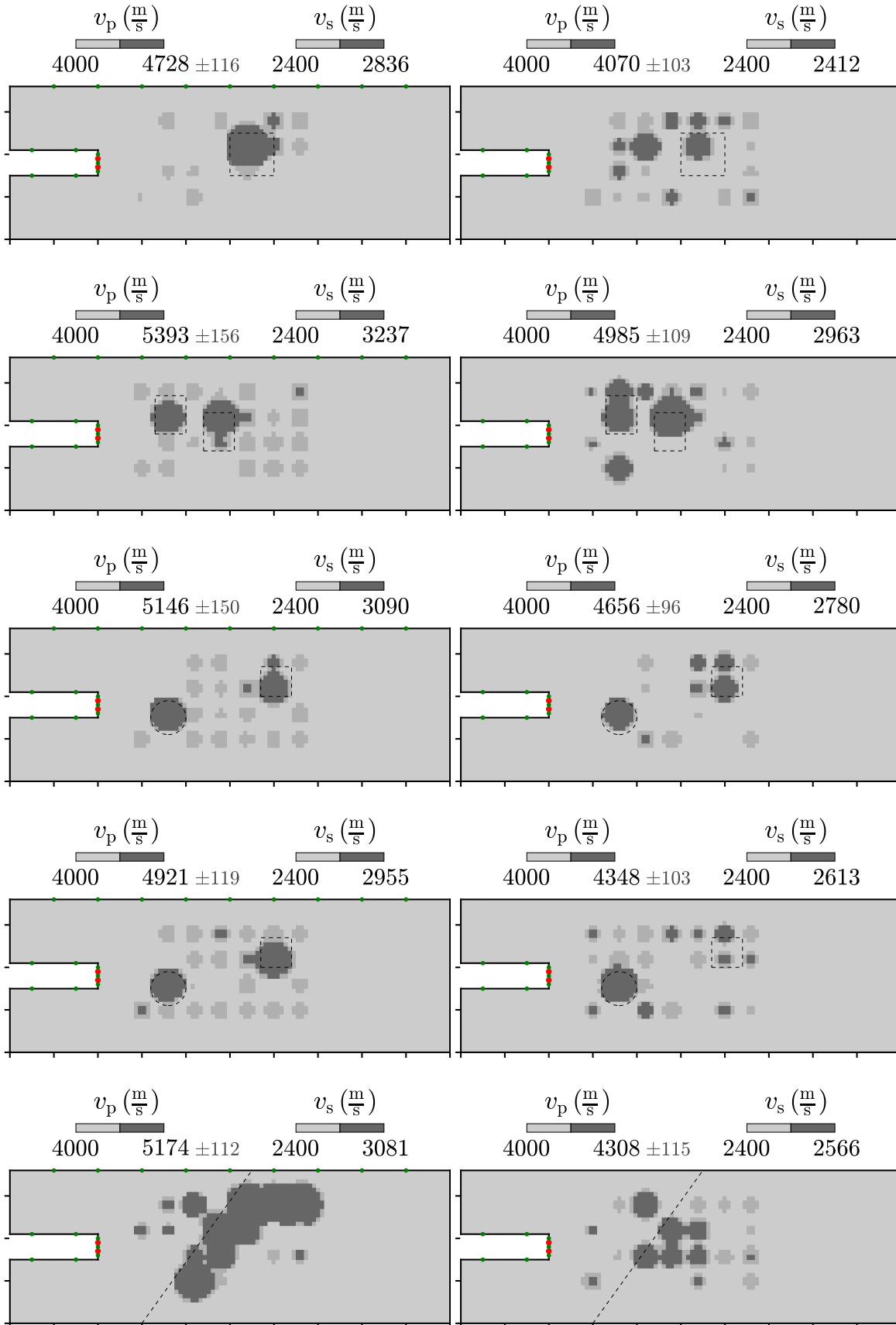


Figure A.1.: Scenarios 1.1 – 5.2 (Section 5.1.2) – Best estimates and double standard deviations in medium dark grey after 5 iterations.

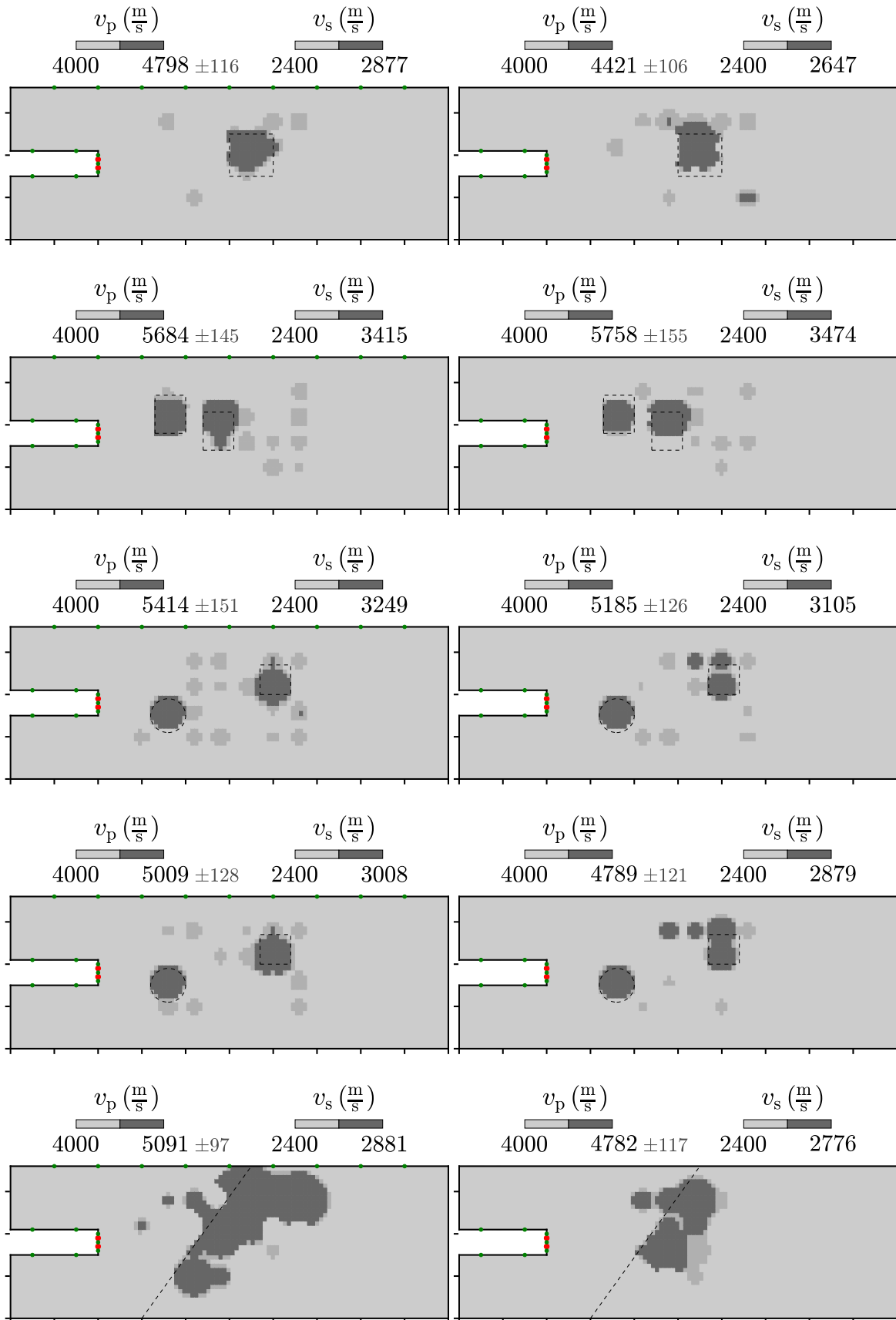


Figure A.2.: Scenarios 1.1 – 5.2 (Section 5.1.2) – Best estimates and double standard deviations in medium dark grey after 10 iterations.

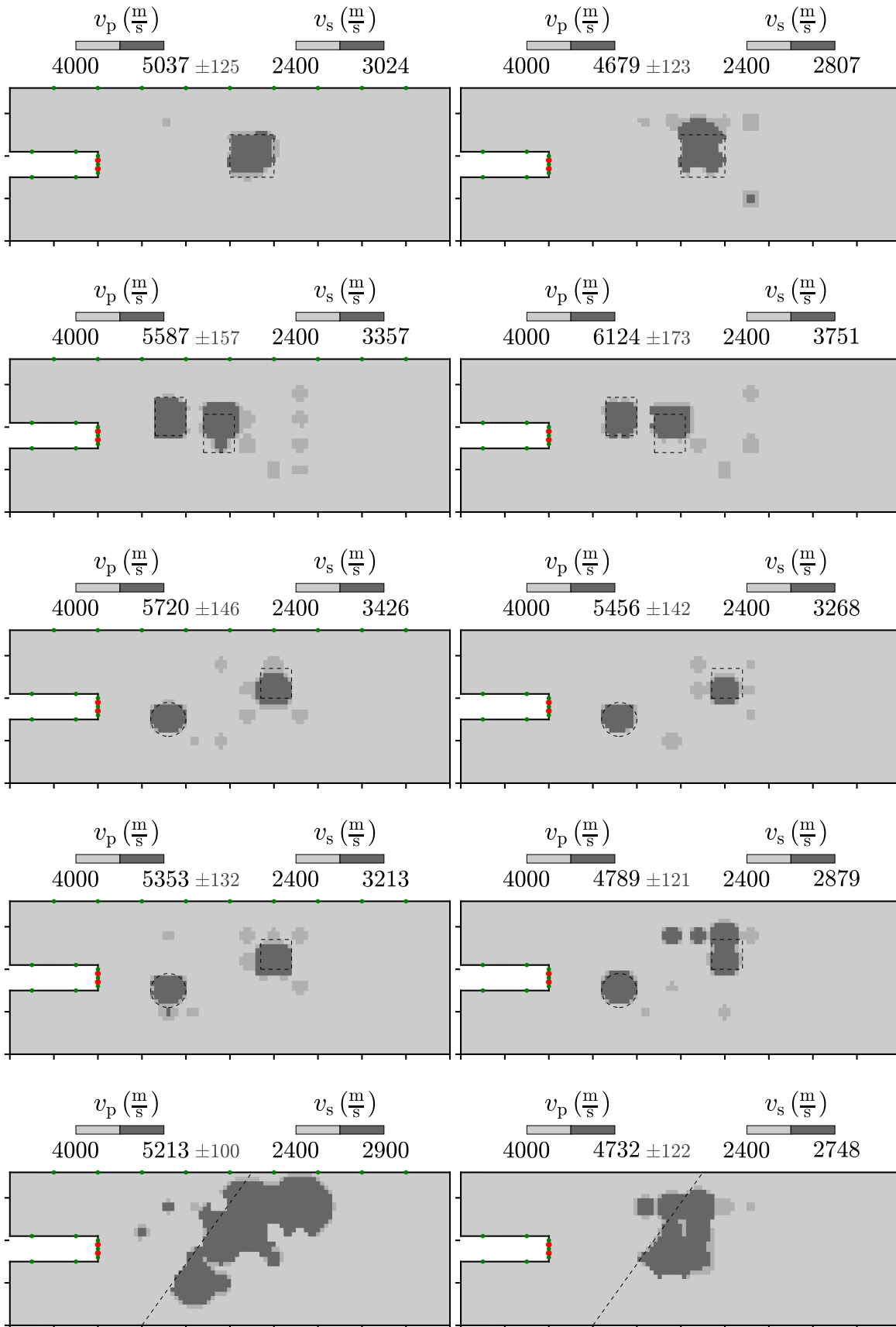


Figure A.3.: Scenarios 1.1 – 5.2 (Section 5.1.2) – Best estimates and double standard deviations in medium dark grey after 15 iterations.

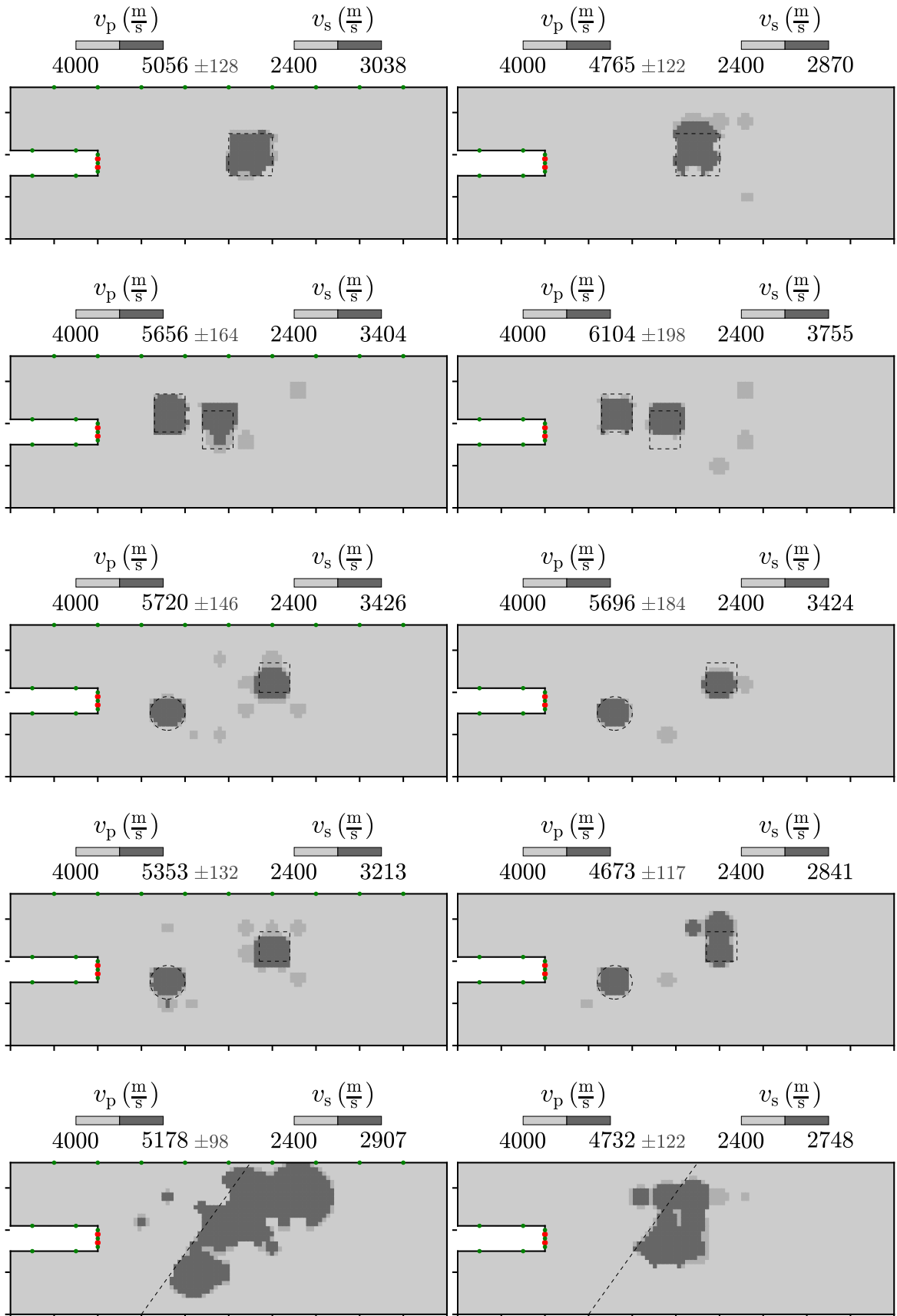


Figure A.4.: Scenarios 1.1 – 5.2 (Section 5.1.2) – Best estimates and double standard deviations in medium dark grey after 20 iterations.

B. Appendix B

Section 5.2: Results for scenario 1

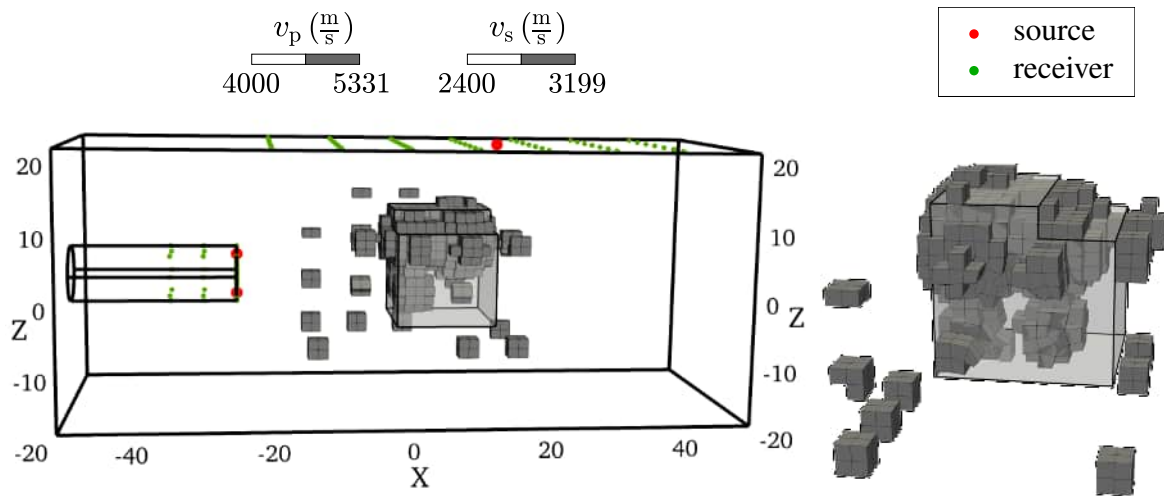


Figure B.1.: Inversion result for scenario 1 from two points of view: Model corresponding to parameter configuration with minimum misfit **after 5 iterations** compared to borders of the true disturbance in light grey.

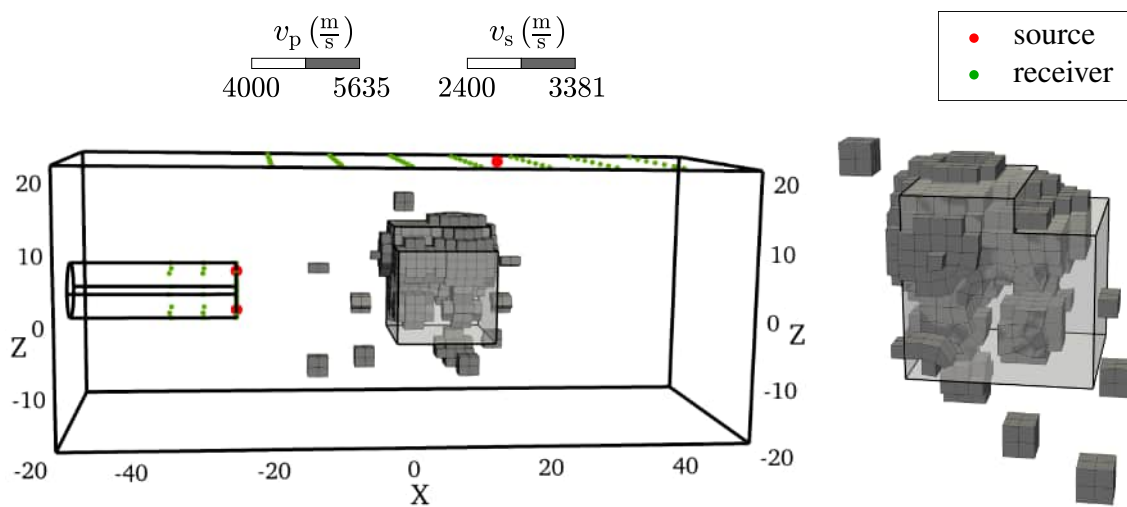


Figure B.2.: Inversion result for scenario 1 from two points of view: Model corresponding to parameter configuration with minimum misfit **after 10 iterations** compared to borders of the true disturbance in light grey.

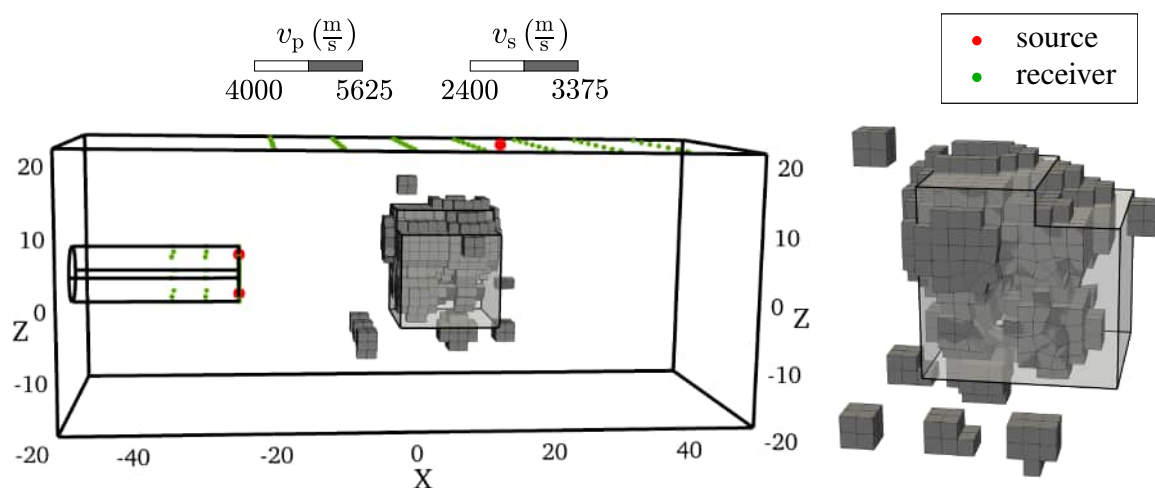


Figure B.3.: Inversion result for scenario 1 from two points of view: Model corresponding to parameter configuration with minimum misfit **after 15 iterations** compared to borders of the true disturbance in light grey.

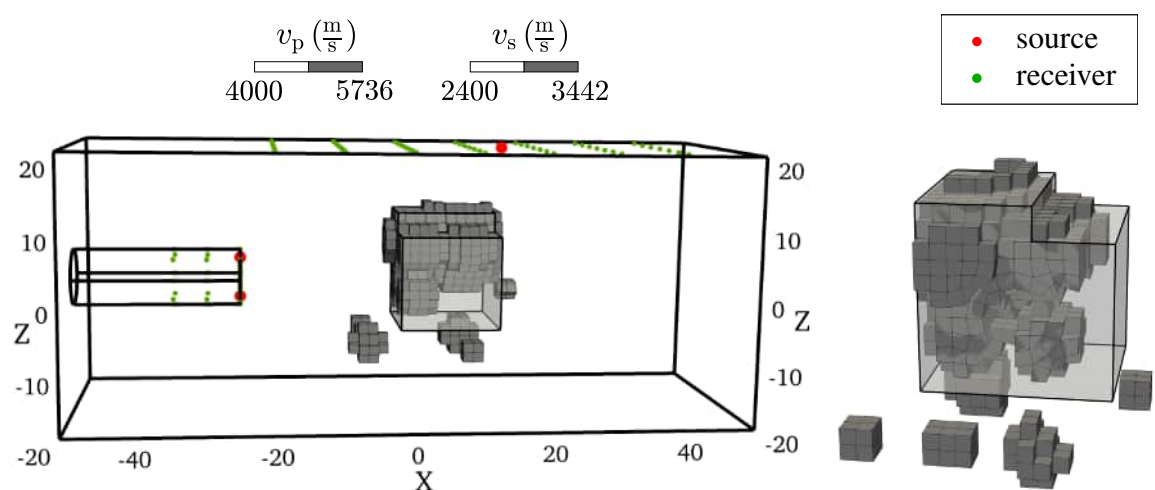


Figure B.4.: Inversion result for scenario 1 from two points of view: Model corresponding to parameter configuration with minimum misfit **after 20 iterations** compared to borders of the true disturbance in light grey.

Section 5.2: Results for scenario 2

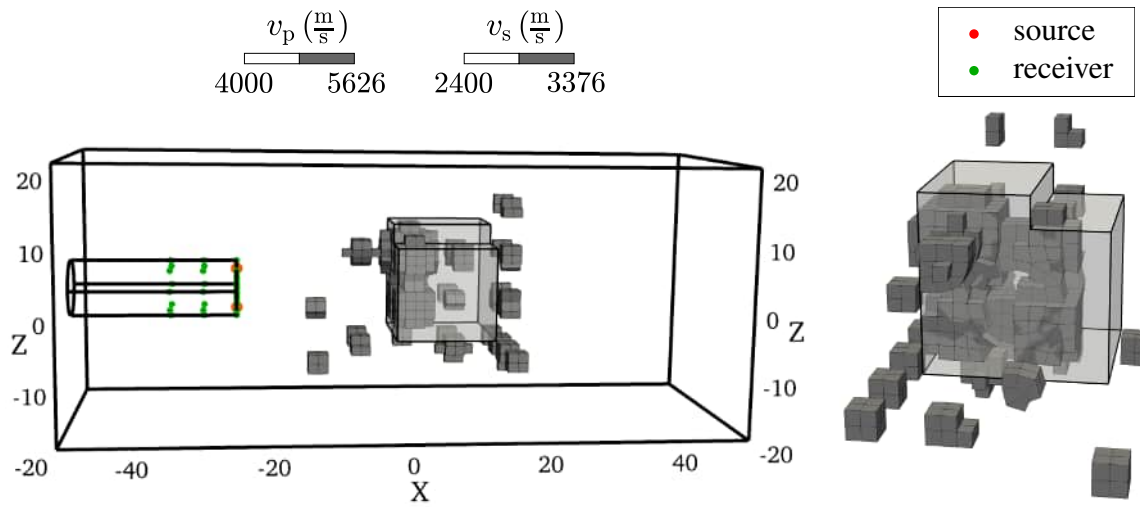


Figure B.5.: Inversion result for scenario 1 from two points of view: Model corresponding to parameter configuration with minimum misfit **after 5 iterations** compared to borders of the true disturbance in light grey.

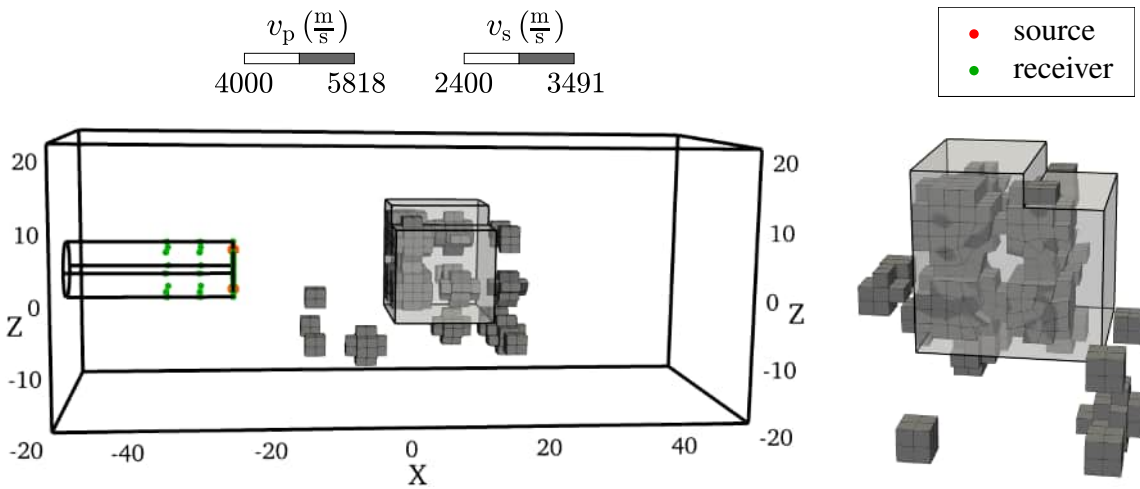


Figure B.6.: Inversion result for scenario 1 from two points of view: Model corresponding to parameter configuration with minimum misfit **after 10 iterations** compared to borders of the true disturbance in light grey.

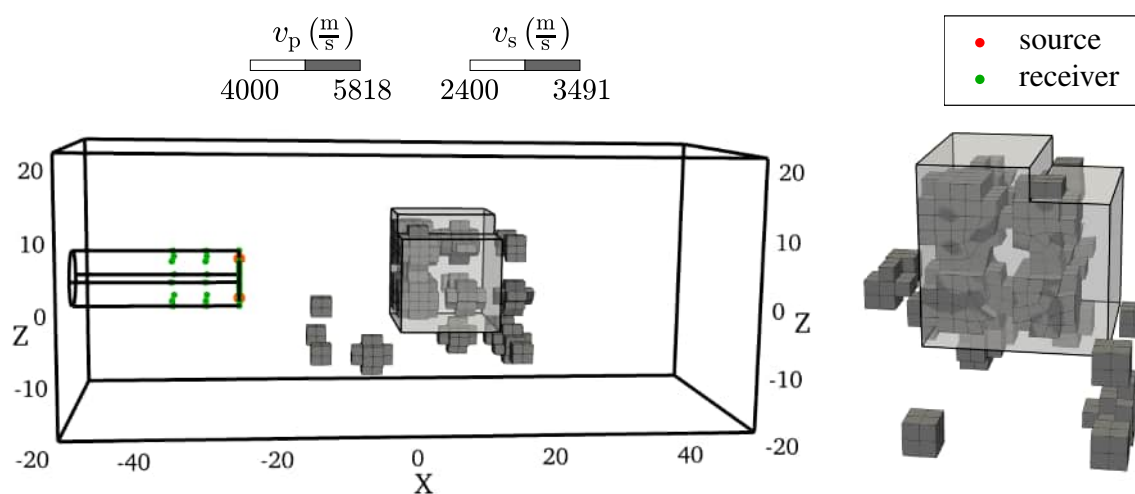


Figure B.7.: Inversion result for scenario 1 from two points of view: Model corresponding to parameter configuration with minimum misfit **after 15 iterations** compared to borders of the true disturbance in light grey. Note that this model is the same as plotted in the previous figure since no model with a lower misfit functional is found during iterations 10-15.

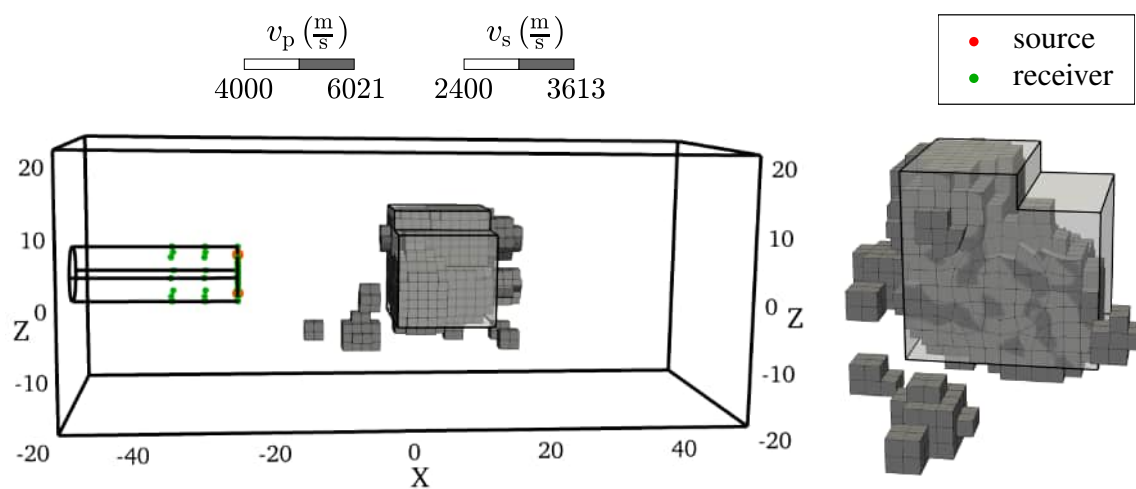


Figure B.8.: Inversion result for scenario 1 from two points of view: Model corresponding to parameter configuration with minimum misfit **after 20 iterations** compared to borders of the true disturbance in light grey.

References

- Aghasi, Alireza, Kilmer, Misha, & Miller, Eric L. 2011. Parametric level set methods for inverse problems. *SIAM Journal on Imaging Sciences*, **4**(2), 618–650.
- American Fork, UT: csimsoft. 2015. *Trelis (Version 15.2) [Computer software]*.
- Attarian, Adam, Batzel, Jerry J., Matzuka, Brett, & Tran, Hien. 2013. Application of the unscented Kalman filtering to parameter estimation. *Pages 75–88 of: Mathematical Modeling and Validation in Physiology*. Springer.
- Auer, Ludwig, Nuber, André Marc, Greenhalgh, Stewart Alan, Maurer, Hansruedi, & Marelli, Stefano. 2013. A critical appraisal of asymptotic 3D-to-2D data transformation in full-waveform seismic crosshole tomography. *Geophysics*, **78**(6), R235–R247.
- Balling, Richard J. 1991. Optimal steel frame design by simulated annealing. *Journal of Structural Engineering*, **117**(6), 1780–1795.
- Barton, Nick. 2006. *Rock quality, seismic velocity, attenuation and anisotropy*. CRC press.
- Berenger, Jean-Pierre, *et al.* 1994. A perfectly matched layer for the absorption of electromagnetic waves. *Journal of computational physics*, **114**(2), 185–200.
- Bergmeister, Konrad, & Reinhold, Chris. 2017. Learning and optimization from the exploratory tunnel–Brenner Base Tunnel: Lernen und Optimieren vom Erkundungsstollen–Brenner Basistunnel. *Geomechanics and Tunnelling*, **10**(5), 467–476.
- Bharadwaj, Pawan, Drijkoningen, Guy, Mulder, W., Thorbecke, Jan, Neducza, Boriszlav, & Jenneskens, Rob. 2017. A shear-wave seismic system using full-waveform inversion to look ahead of a tunnel-boring machine. *Near Surface Geophysics*, **15**(3), 210–225.
- Blum, Christian, & Roli, Andrea. 2003. Metaheuristics in combinatorial optimization: Overview and conceptual comparison. *ACM Computing Surveys (CSUR)*, **35**(3), 268–308.
- Bohlen, Thomas, Lorang, Ulrich, Rabbel, Wolfgang, Müller, Christof, Giese, Rüdiger, Lüth, Stefan, & Jetschny, Stefan. 2007. Rayleigh-to-shear wave conversion at the tunnel face—From 3D-FD modeling to ahead-of-drill exploration. *Geophysics*, **72**(6), T67–T79.
- Borm, G., Bohlen, T., Giese, R., Klose, C., Mielitz, S., & Otto, P. 2003. ISIS—Integrated Seismic Imaging System for the geological prediction ahead of underground construction. *In: 65th EAGE Conference & Exhibition*.
- Bretonneau, François, Leparoux, Donatienne, Durand, Olivier, & Abraham, Odile. 2011. Small-scale modeling of onshore seismic experiment: A tool to validate numerical modeling and seismic imaging methods. *Geophysics*, **76**(5), T101–T112.

- Bretherton, François, Brossier, Romain, Leparoux, Donatienne, Abraham, Odile, & Virieux, Jean. 2013. 2D elastic full-waveform imaging of the near-surface: application to synthetic and physical modelling data sets. *Near Surface Geophysics*, **11**(3), 307–316.
- Colli, Lorenzo, Fichtner, Andreas, & Bunge, Hans-Peter. 2013. Full waveform tomography of the upper mantle in the South Atlantic region: Imaging a westward fluxing shallow asthenosphere? *Tectonophysics*, **604**, 26–40.
- Colton, David L., Kress, Rainer, & Kress, Rainer. 1998. *Inverse acoustic and electromagnetic scattering theory*. Vol. 93. Springer.
- Computational Infrastructure for Geodynamics. 2020. *SPECFEM3D Cartesian User Manual*. Retrieved from <https://geodynamics.org/cig/software/specfem3d>.
- Cover, Thomas, & Hart, Peter. 1967. Nearest neighbor pattern classification. *IEEE transactions on information theory*, **13**(1), 21–27.
- Dahlen, F., & Tromp, Jeroen. 1998. *Theoretical global seismology*. Princeton university press.
- Dickmann, T., & Sander, B. 1996. Drivage concurrent tunnel seismic prediction. *Felsbau-rock and Soil Engineering*, **14**(1), 406–411.
- Eberhart, Russell, & Kennedy, James. 1995. A new optimizer using particle swarm theory. *Pages 39–43 of: MHS'95. Proceedings of the Sixth International Symposium on Micro Machine and Human Science*. Ieee.
- Fichtner, Andreas. 2010. *Full seismic waveform modelling and inversion*. Springer Science & Business Media.
- Fichtner, Andreas, & Villaseñor, Antonio. 2015. Crust and upper mantle of the western Mediterranean—Constraints from full-waveform inversion. *Earth and Planetary Science Letters*, **428**, 52–62.
- French, Scott W., & Romanowicz, Barbara. 2015. Broad plumes rooted at the base of the Earth's mantle beneath major hotspots. *Nature*, **525**(7567), 95–99.
- Freund, L. Ben. 1998. *Dynamic fracture mechanics*. Cambridge university press.
- Garrett, Aaron. 2014. inspyred: Bio-inspired Algorithms in Python. URL: <https://pypi.python.org/pypi/inspyred>.
- Gebraad, Lars, Boehm, Christian, & Fichtner, Andreas. 2020. Bayesian elastic full-waveform inversion using Hamiltonian Monte Carlo. *Journal of Geophysical Research: Solid Earth*, **125**(3), e2019JB018428.
- Gercek, H. 2007. Poisson's ratio values for rocks. *International Journal of Rock Mechanics and Mining Sciences*, **44**(1), 1–13.
- Geuzaine, Christophe, & Remacle, J.-F. 2007. Gmsh: a three-dimensional finite element mesh generator with built-in pre-and post-processing facilities. *Pages 1309–1331 of: Proceedings of the Second Workshop on Grid Generation for Numerical Computations, Tetrahedron II*.

- Goldberg, David E., *et al.* 1990. A note on Boltzmann tournament selection for genetic algorithms and population-oriented simulated annealing. *Complex Systems*, **4**(4), 445–460.
- Hunziker, Jürg, Laloy, Eric, & Linde, Niklas. 2019. Bayesian full-waveform tomography with application to crosshole ground penetrating radar data. *Geophysical Journal International*, **218**(2), 913–931.
- Igel, Heiner. 2017. *Computational seismology: a practical introduction*. Oxford University Press.
- Ingber, Lester. 1993. Simulated annealing: Practice versus theory. *Mathematical and computer modelling*, **18**(11), 29–57.
- Ingber, Lester, & Rosen, Bruce. 1992. Genetic algorithms and very fast simulated reannealing: A comparison. *Mathematical and computer modelling*, **16**(11), 87–100.
- Jetschny, Stefan. 2010. Seismic prediction and imaging of geological structures ahead of a tunnel using surface waves.
- Julier, Simon, Uhlmann, Jeffrey, & Durrant-Whyte, Hugh F. 2000. A new method for the nonlinear transformation of means and covariances in filters and estimators. *IEEE Transactions on automatic control*, **45**(3), 477–482.
- Julier, Simon J., & Uhlmann, Jeffrey K. 1997. New extension of the Kalman filter to nonlinear systems. *Pages 182–194 of: Signal processing, sensor fusion, and target recognition VI*, vol. 3068. International Society for Optics and Photonics.
- Julier, Simon J., & Uhlmann, Jeffrey K. 2004. Unscented filtering and nonlinear estimation. *Proceedings of the IEEE*, **92**(3), 401–422.
- Kaipio, Jari, & Somersalo, Erkki. 2006. *Statistical and computational inverse problems*. Vol. 160. Springer Science & Business Media.
- Kalman, Rudolph Emil. 1960. A new approach to linear filtering and prediction problems. *Journal of Fluids Engineering*, **82**(1), 35–45.
- Kerr, Alexander, & Mullen, Kieran. 2019. A comparison of genetic algorithms and simulated annealing in maximizing the thermal conductance of harmonic lattices. *Computational Materials Science*, **157**, 31–36.
- Kirkpatrick, Scott, Vecchi, M., *et al.* 1983. Optimization by simulated annealing. *science*, **220**(4598), 671–680.
- Kneib, G., Kassel, A., & Lorenz, K. 2000. Automatic seismic prediction ahead of the tunnel boring machine. *First Break*, **18**(7), 295–302.
- Knopoff. 1964. Q. *Reviews of Geophysics* **2**(4), 645–654.
- Komatitsch, D., Vilotte, J.-P., Tromp, J., Ampuero, J.-P., Bai, K., Basini, P., Blitz, C., Bozdog, E., Casarotti, E., Charles, J., Chen, M., Galvez, P., Goddeke, D., Hjørleifsdottir, V., Labarta, J., Le Goff, N., Le Loher, P., Lefebvre, M., Liu, Q., Luo, Y., Maggi, A., Magnoni, F., Martin, R., Matzen, R., McRitchie, D., Meschede, M., Messmer, P., Michea, D., Nadh Somala, S., Nissen-Meyer, T., Peter, D., Rietmann, M., de Andrade, E.S., Savage, B., Schuberth, B., Sieminski, A., Strand, L., Tape, C., Xie, Z., & Zhu, H. 2012. *SPECFEM3D Cartesian v2.0.2 [software]*.

- Komatitsch, Dimitri, & Vilotte, Jean-Pierre. 1998. The spectral element method: An efficient tool to simulate the seismic response of 2D and 3D geological structures. *Bulletin of the seismological society of America*, **88**(2), 368–392.
- Lamert, Andre. 2019. *Tunnel Reconnaissance by Seismic Full Waveform Inversion Numerical Development and Experimental Validation*. Ph.D. thesis, PhD thesis, Ruhr-Universität Bochum.
- Lamert, Andre, & Friederich, Wolfgang. 2018. Full Waveform Inversion for Advance Exploration of Ground Properties in Mechanized Tunneling. *International Journal of Civil Engineering*, 1–14.
- Lamert, Andre, Nguyen, Luan T., Friederich, Wolfgang, & Nestorović, Tamara. 2018. Imaging disturbance zones ahead of a tunnel by elastic full-waveform inversion: Adjoint gradient based inversion vs. parameter space reduction using a level-set method. *Underground Space*, **3**(1), 21–33.
- Lei, Wenjie. 2019. *Global Seismic Full-Waveform Inversion*. Ph.D. thesis, Princeton University.
- Mahmoudi, E., & Hölter, R. 2021. A model adaptation framework for mechanised tunnelling. *Pages 1–33 of: Modelling in geotechnical engineering*. Elsevier, AP.
- Maidl, Bernhard, Herrenknecht, Martin, Maidl, Ulrich, & Wehrmeyer, Gerhard. 2011. *Maschinellem Tunnelbau im Schildvortrieb*. John Wiley & Sons.
- Martin, James, Wilcox, Lucas C., Burstedde, Carsten, & Ghattas, Omar. 2012. A stochastic Newton MCMC method for large-scale statistical inverse problems with application to seismic inversion. *SIAM Journal on Scientific Computing*, **34**(3), A1460–A1487.
- MATLAB. 2019. *9.7.0.1190202 (R2019b)*. Natick, Massachusetts: The MathWorks Inc.
- Metropolis, Nicholas, Rosenbluth, Arianna W., Rosenbluth, Marshall N., Teller, Augusta H., & Teller, Edward. 1953. Equation of state calculations by fast computing machines. *The journal of chemical physics*, **21**(6), 1087–1092.
- Mitchell, Melanie. 1998. *An introduction to genetic algorithms*. MIT press.
- Mouhat, Félix, & Coudert, François-Xavier. 2014. Necessary and sufficient elastic stability conditions in various crystal systems. *Physical review B*, **90**(22), 224104.
- Mulder, W., Perkins, C., & Van De Rijzen, M. 2010. 2D acoustic full waveform inversion of a land seismic line. *Pages cp–161 of: 72nd EAGE Conference and Exhibition incorporating SPE EUROPEC 2010*. European Association of Geoscientists & Engineers.
- Musayev, Khayal, Hackl, Klaus, & Baitsch, Matthias. 2013. Frequency Domain Waveform Inversion in a Tunnel Environment. *PAMM*, **13**(1), 323–324.
- Nguyen, Luan T., & Nestorović, Tamara. 2016. Unscented hybrid simulated annealing for fast inversion of tunnel seismic waves. *Computer Methods in Applied Mechanics and Engineering*, **301**, 281–299.
- Nguyen, Luan T., & Nestorović, Tamara. 2018. Reconstructing disturbance zones ahead of the tunnel face by elastic waveform inversion supported by a parametric level-set representation. *Soil Dynamics and Earthquake Engineering*, **115**, 606–621.

- Ohm, Jens-Rainer, & Lüke, Hans Dieter. 2015. *Signalübertragung: Grundlagen der digitalen und analogen Nachrichtenübertragungssysteme*. Springer-Verlag.
- Otto, Richard, Button, E., Bretterebner, Helfried, & Schwab, Peter. 2002. The application of TRT (true reflection tomography) at the Unterwald tunnel. *Felsbau*, **20**(2), 51–56.
- Petronio, Lorenzo, Poletto, Flavio, & Schleifer, Andrea. 2007. Interface prediction ahead of the excavation front by the tunnel-seismic-while-drilling (TSWD) method. *Geophysics*, **72**(4), G39–G44.
- Pratt, R. Gerhard, & Worthington, M.H. 1990. Inverse theory applied to multi-source cross-hole tomography. Part 1: acoust wave-equation method 1. *Geophysical prospecting*, **38**(3), 287–310.
- Rao, Jing, Ratassepp, Madis, & Fan, Zheng. 2016. Guided wave tomography based on full waveform inversion. *IEEE transactions on ultrasonics, ferroelectrics, and frequency control*, **63**(5), 737–745.
- Riedel, Christopher, Musayev, Khayal, Baitsch, Matthias, Zhu, Hehua, & Hackl, Klaus. 2021a. Acoustic waveform inversion in frequency domain: Application to a tunnel environment. *Underground Space*, **6**(5), 560–576.
- Riedel, Christopher, Musayev, Khayal, Baitsch, Matthias, & Hackl, Klaus. 2021b. Seismic exploration in tunneling using full waveform inversion with a frequency domain model. *PAMM*, **20**(1), e202000141.
- Riedel, Christopher, Mahmoudi, Elham, Trapp, Maximilian, Lamert, Andre, Hölter, Raoul, Zhao, Chenyang, Musayev, Khayal, Baitsch, Matthias, König, Markus, Hackl, Klaus, Nestorović, Tamara, & Friederich, Wolfgang. 2022. A hybrid exploration approach for the prediction of geological changes ahead of mechanized tunnel excavation. *Journal of Applied Geophysics*, 104684.
- Romdhane, Anouar, Grandjean, Gilles, Brossier, Romain, Réjiba, Fayçal, Operto, Stéphane, & Virieux, Jean. 2011. Shallow-structure characterization by 2D elastic full-waveform inversion. *Geophysics*, **76**(3), R81–R93.
- Sajeva, Angelo, Aleardi, Mattia, Stucchi, Eusebio, Bienati, Nicola, & Mazzotti, Alfredo. 2016. Estimation of acoustic macro models using a genetic full-waveform inversion: Applications to the Marmousi model. *Geophysics*, **81**(4), R173–R184.
- Sattel, G., Frey, P., & Amberg, R. 1992. Prediction ahead of the tunnel face by seismic methods-pilot project in Centovalli Tunnel, Locarno, Switzerland. *First Break*, **10**(1), 19–25.
- Schiemenz, Alan, & Igel, Heiner. 2013. Accelerated 3-D full-waveform inversion using simultaneously encoded sources in the time domain: Application to Valhall ocean-bottom cable data. *Geophysical Journal International*, **195**(3), 1970–1988.
- Schmitt, J., Gattermann, J., & Stahlmann, J. 2004. Hohlraumerkundung im Tunnelbau. *Messen in der Geotechnik*, 173–200.
- Simon, Dan. 2006. *Optimal state estimation: Kalman, H infinity, and nonlinear approaches*. John Wiley & Sons.

- Sirgue, Laurent, Barkved, O., Dellinger, J., Etgen, J., Albertin, U., & Kommedal, J. 2010. Thematic set: Full waveform inversion: The next leap forward in imaging at Valhall. *First Break*, **28**(4).
- Smith, James A., Borisov, Dmitry, Cudney, Harley, Miller, Richard D., Modrak, Ryan, Moran, Mark, Peterie, Shelby L., Sloan, Steven D., Tromp, Jeroen, & Wang, Yao. 2019. Tunnel detection at Yuma Proving Ground, Arizona, USA-Part 2: 3D full-waveform inversion experiments Tunnel detection at YPG-Part 2: 3D FWI. *Geophysics*, **84**(1), B95–B108.
- Stacey, Richard. 1988. Improved transparent boundary formulations for the elastic-wave equation. *Bulletin of the Seismological Society of America*, **78**(6), 2089–2097.
- Tarantola, Albert. 1984. Inversion of seismic reflection data in the acoustic approximation. *Geophysics*, **49**(8), 1259–1266.
- Tarantola, Albert. 2005. *Inverse problem theory and methods for model parameter estimation*. SIAM.
- Tikhonov, A., & Arsenin, V. 1963. Solution of incorrectly formulated problems and the regularization method: Soviet Mathematics–Doklady.
- Trapp, Maximilian, & Nestorović, Tamara. 2020. Reconstruction of structural anomalies out of seismic measurements by means of a non-deterministic full waveform inversion approach for application in mechanized tunneling. *Journal of Applied Geophysics*, 104180.
- Trapp, Maximilian, & Nestorović, Tamara. 2021. Non-gradient full waveform inversion approaches for exploration during mechanized tunneling applied to surrogate laboratory measurements. *Tunnelling and Underground Space Technology*, 104252.
- Trapp, Maximilian, Bogoclu, Can, Nestorović, Tamara, & Roos, Dirk. 2019. Intelligent optimization and machine learning algorithms for structural anomaly detection using seismic signals. *Mechanical Systems and Signal Processing*, **133**, 106250.
- Tromp, J., Komatitsch, D., & Liu, Q. 2008. Spectral-element and adjoint methods in seismology. *Communications in Computational Physics*, **3**(1), 1–32.
- Udias, Agustin, & Buforn, Elisa. 2017. *Principles of seismology*. Cambridge University Press.
- Virieux, Jean, & Operto, Stéphane. 2009. An overview of full-waveform inversion in exploration geophysics. *Geophysics*, **74**(6), WCC1–WCC26.
- Visser, Gerhard, Guo, Peng, & Saygin, Erdinc. 2019. Bayesian transdimensional seismic full-waveform inversion with a dipping layer parameterization. *Geophysics*, **84**(6), R845–R858.
- Wang, Jian, Yang, Dinghui, Jing, Hao, & Wu, Hao. 2019. Full waveform inversion based on the ensemble Kalman filter method using uniform sampling without replacement. *Science Bulletin*, **64**(5), 321–330.
- Wendland, Holger. 1995. Piecewise polynomial, positive definite and compactly supported radial functions of minimal degree. *Advances in computational Mathematics*, **4**(1), 389–396.

-
- Williamson, Paul R., & Pratt, R. Gerhard. 1995. A critical review of acoustic wave modeling procedures in 2.5 dimensions. *Geophysics*, **60**(2), 591–595.
- Zienkiewicz, Olgierd Cecil, Taylor, Robert Leroy, & Zhu, Jian Z. 2005. *The finite element method: its basis and fundamentals*. Elsevier.

Curriculum Vitae

Personal Information

Name: Maximilian Trapp
Place of Residence: Essen, Germany
Date of Birth: April 24, 1991

Employment

since 05/2017 Research Assistant
Research Group Mechanics of Adaptive Systems
Ruhr University Bochum

Education

05/2017 - 05/2022 Ph.D. Student
Faculty of Civil and Environmental Engineering
Ruhr University Bochum

10/2014 - 11/2016 Master of Science
Mechanical Engineering
Ruhr University Bochum

10/2010 - 07/2014 Bachelor of Science
Mechanical Engineering
Ruhr University Bochum

Journal Publications

Trapp, Maximilian, & Nestorović, Tamara. 2021. Non-gradient full waveform inversion approaches for exploration during mechanized tunneling applied to surrogate laboratory measurements. *Tunnelling and Underground Space Technology*, 104252.

Trapp, Maximilian, & Nestorović, Tamara. 2020. Reconstruction of structural anomalies out of seismic measurements by means of a non-deterministic full waveform inversion approach for application in mechanized tunneling. *Journal of Applied Geophysics*, 104180.

Trapp, Maximilian, Bogoclu, Can, Nestorović, Tamara, & Roos, Dirk. 2019. Intelligent optimization and machine learning algorithms for structural anomaly detection using seismic signals. *Mechanical Systems and Signal Processing*, 133, 106250.

Riedel, Christopher, Mahmoudi, Elham, Trapp, Maximilian, Lamert, Andre, Hölter, Raul, Zhao, Chenyang, Musayev, Khayal, Baitsch, Matthias, König, Markus, Hackl, Klaus, Nestorović, Tamara, & Friederich, Wolfgang. 2022. A hybrid exploration approach for the prediction of geological changes ahead of mechanized tunnel excavation. *Journal of Applied Geophysics*, 104684.

Conference Publications

Trapp, Maximilian, & Nestorović, Tamara. 2022. Bayesian full waveform inversion designed for exploration during mechanized tunneling – A small-scale experiment. *In: Second EAGE Conference on Seismic Inversion*, vol. 2022. European Association of Geoscientists & Engineers.

**Mitteilungen aus dem Institut für Mechanik
RUHR-UNIVERSITÄT BOCHUM
Nr. 189**

ISBN 978-3-935892-67-4